Alma Mater Studiorum – Università di Bologna

DOTTORATO DI RICERCA IN

Ingegneria Civile, Chimica, Ambientale e dei Materiali

Ciclo XXXII

Settore Concorsuale: 09/D3

Settore Scientifico Disciplinare: ING-IND/25

Computational Fluid Dynamics Analysis of Two-Phase Chemical and Biochemical Reactors

Presentata da: Francesco Maluta

Coordinatore Dottorato **Supervisore**

Prof. Luca Vittuari **Prof.ssa Giuseppina Montante**

Esame finale anno 2020

Abstract

In this work, the numerical analysis of turbulent two-phase processes in stirred tanks and bioreactors is performed with a computational fluid dynamics (CFD) approach. The modelling of the turbulent two-phase phenomena is achieved in the context of the Reynolds Averaged Navier-Stokes (RANS) equations and the Two-Fluid Model (TFM). Different modelling strategies are studied, tested and developed to improve the prediction of mixing phenomena, interphase interactions and bio-chemical reactions in chemical and process equipment. The systems studied in this work are a dilute immiscible liquid-liquid dispersion and dense solid-liquid suspensions, both in stirred tanks of standard geometry, a gas-liquid system consisting of a dual impeller vortex ingesting fermenter for the production of biohydrogen, analyzed in two different configurations of the supports for the attached growth of biomass, and two different bioreactors, of different scale and configuration, subject to substrate concentration segregation. Purposely collected experimental data and data from the literature were extensively used to validate the numerical results and either confirmed the goodness of the models and the modelling techniques, helped the definition of the limits and the uncertainties of the model formulations or guided the development of new models.

The study of Liquid-Liquid dispersions in stirred tanks revealed that since grid effects on the turbulent dissipation rate are relevant, the choice of the breakup kernel parameters depends on the grid refinements. A novel scalar correction for the breakup kernel derived from local quantities is proposed.

Simulating the Solid-Liquid suspension in stirred tanks, it was found that the so-called granular model formulation was uninfluential in the prediction of the solid distribution in the stirred tank for solid volume fractions up to 0.15 and in the operating conditions considered, provided that a packing limit was included. Unsatisfactorily agreement was obtained between experimental and numerical radial concentration profiles in the investigated incomplete suspension conditions, since the turbulent dispersion models would require more advanced multiphase turbulence models.

A modelling strategy for the fermentative production and stripping of biohydrogen in the self-ingesting stirred tank reactor was developed. A local specific interfacial area model was implemented, and it was instrumental in proposing geometrical changes to the bioreactor. The performances of two reactor configurations were tested with a local and an instantaneous analysis of the reaction rate, the interphase hydrogen fluxes and the two-phase fluid dynamics confirming that the two-impeller configuration allows the circulation of stripping gas to enhance recovery.

The fermentation of *Escherichia coli* in bioreactors was studied with a probabilistic mixing model for substrate segregation. The developed mixing model was compared against experimental and numerical literature results revealing that a simplified fluid dynamic description could suffice when just substrate segregation is important. A model tying the maintenance rate of a cell population to the substrate concentration distribution was developed, implemented, validated against experimental data and discussed both from a Lagrangian and from a Eulerian perspective.

In all cases, particular attention was devoted to the precision of the numerical solution, and to the validation with experimental data to quantify the appropriateness of the models and the accuracy of the CFD predictions.

Résumé

Dans ce travail, l'analyse numérique des processus diphasiques turbulents dans les cuves agitées et les bioréacteurs est réalisée avec une approche de la mécanique des fluides numérique (CFD). La modélisation des phénomènes diphasiques turbulents est réalisée dans le cadre des équations de Navier-Stokes moyennes de Reynolds (RANS) et du modèle à deux fluides (TFM). Différentes stratégies de modélisation sont étudiées, testées et développées pour améliorer la prédiction des phénomènes de mélange, des interactions interphasiques et des réactions biochimiques dans les équipements chimiques et de process. Les systèmes étudiés dans ce travail sont une dispersion liquide-liquide diluée non miscible et des suspensions solides-liquides denses, à la fois dans des cuves agitées de géométrie standard, un système gaz-liquide composé d'un fermenteur à double vortex à turbine pour la production de bio-hydrogène, analysé dans deux configurations différentes des supports pour la croissance attachée de la biomasse, et deux bioréacteurs différents, d'échelle et de configuration différentes, soumis à la ségrégation de la concentration du substrat. Les données expérimentales collectées à dessein et les données de la littérature ont été largement utilisées pour valider les résultats numériques et ont soit confirmé la qualité des modèles et des techniques de modélisation, aidé à la définition des limites et des incertitudes des formulations des modèles, soit guidé le développement de nouveaux modèles.

L'étude des dispersions liquide-liquide dans des cuves agitées a révélé que, puisque les effets du réseau sur le taux de dissipation turbulent sont pertinents, le choix des paramètres du noyau de rupture dépend des raffinements du réseau. Une nouvelle correction scalaire du noyau de rupture dérivé des quantités locales est proposée.

Simulant la suspension solide-liquide dans des cuves agitées, il a été constaté que la formulation dite granulaire n'était pas influente dans la prédiction de la distribution des solides dans la cuve agitée pour des fractions volumiques solides jusqu'à 0,15 et dans les conditions de fonctionnement considérées, à condition qu’une limite d'emballage ait été incluse. Un accord insatisfaisant a été obtenu entre les profils de concentration radiale expérimentaux et numériques dans les condi-

tions de suspension incomplètes étudiées, car les modèles de dispersion turbulente nécessiteraient des modèles de turbulence polyphasiques plus avancés.

Une stratégie de modélisation pour la production fermentative et le stripage de bio-hydrogène dans le réacteur agité auto-ingérant a été développée. Un modèle de zone interfaciale spécifique locale a été mis en œuvre, et il a contribué à proposer des changements géométriques au bioréacteur. Les performances de deux configurations de réacteurs ont été testées avec une analyse locale et instantanée de la vitesse de réaction, des flux d'hydrogène entre phases et de la dynamique des fluides à deux phases confirmant que la configuration à deux turbines permet la circulation du gaz de stripping pour améliorer la récupération.

La fermentation d'Escherichia coli dans des bioréacteurs a été étudiée avec un modèle de mélange probabiliste pour la ségrégation du substrat. Le modèle de mélange développé a été comparé aux résultats de la littérature expérimentale et numérique révélant qu'une description simplifiée de l’hydrodynamique pourrait suffire lorsque seule la ségrégation du substrat est importante. Un modèle liant le taux de maintien d'une population cellulaire à la distribution des concentrations de substrat a été développé, mis en œuvre, validé par rapport aux données expérimentales et discuté à la fois du point de vue lagrangien et du point de vue eulérien.

Dans tous les cas, une attention particulière a été portée à la précision de la solution numérique et à la validation avec des données expérimentales pour quantifier la pertinence des modèles et la précision des prédictions CFD.

Index

Chapter 1 Introduction 1

1.1 Computational Fluid Dynamics in Chemical Engineering 1

1.2 Multiphase flow modelling 3

1.3 Research Objectives 4

1.4 References 6

Chapter 2 Mathematical models 9

2.1 Introduction 9

2.2 Single-phase Reynolds Averaged Navier-Stokes equations 11

2.3 Derivation of the two-fluid model 14

2.4 Closure models for the two-phase model 19

2.5 Nomenclature 23

2.6 References 25

Chapter 3 Liquid-Liquid dispersions in stirred tanks 27

3.1 Introduction 29

3.2 Investigated System 32

3.3 Governing equations 33

3.3.1 Two-fluid model 34

3.3.2 Population Balance Model 35
3.3.3 Quadrature Based Method of Moment 38
3.4 Numerical solution procedure 39
3.5 Grid convergence study 40
3.6 Comparison between Weak and Offline Coupling 42
3.7 Results 43
3.7.1 Analysis of the two-phase turbulent field 43
3.7.2 Analysis of the Drop Size Distribution 49
3.8 Discussion 52
3.9 Conclusions 56
3.10 Acknowledgments 57
3.11 Nomenclature 58
3.12 References 60

Chapter 4 Solid-Liquid suspension in stirred tanks 65
4.1 Introduction 66
4.2 Investigated systems 69
4.3 CFD simulations 71
4.3.1 Governing equations 71
4.3.2 Numerical solution procedure 77
4.3.3 Grid convergence study 79
4.4 Results and discussion 82
4.4.1 Complete suspension conditions 83
4.4.1.a Comparison of the 'mixture' k-ε and the 'mixture' Reynolds Stress turbulence models 84

4.4.1.b Comparison of Eulerian-Granular and Eulerian-Eulerian Models *86*
4.4.1.c Effect of turbulent dispersion, drag and lift forces *87*
4.4.1.d Comparison with the experimental data *88*
4.4.2 Incomplete suspension conditions 92
4.4.2.a Comparison of the 'mixture' k-ε and the 'mixture' Reynolds Stress turbulence models *92*
4.4.2.b Comparison of Eulerian-Granular and Eulerian-Eulerian Models *93*
4.4.2.c Effect of the turbulent dispersion force *96*
4.4.2.d Effect of the drag force *97*
4.4.2.e Comparison with the experimental data *98*
4.5 Conclusions 100
4.6 Nomenclature 102
4.7 References 104

Chapter 5 Biohydrogen production in stirred fermenters 109
5.1 Introduction 111
5.2 Geometry of the bioreactor 113
5.3 The CFD model equations 116
5.4 Fermentation kinetic model 119
5.5 Mass transfer model 123
5.5.1 Local mass transfer coefficient: k_La 124
5.6 Computational domain and solution procedure 126
5.7 Results and discussion 127

5.7.1 Fluid dynamics 127
5.7.2 Mass transfer coefficients 129
5.7.3 Hydrogen production and stripping: supports inside the draft tube 133
5.7.4 Hydrogen production and stripping: supports outside the draft tube 137
5.8 Conclusions 141
5.9 Nomenclature 143
5.10 References 145

Chapter 6 *Escherichia coli* fermentation in bioreactors 149
6.1 Introduction 150
6.2 The experiments 153
6.3 Mathematical model 155
6.3.1 General aspects 155
6.3.2 New considerations 158
6.3.2.a Effect of substrate fluctuations on the maintenance rate 158
6.3.2.b The Interaction by Exchange with the Mean mixing model 159
6.3.3 Implementation in ADENON 161
6.4 Simulation set-up 163
6.4.1 Large scale fed-batch 163
6.4.2 Two stage bioreactor STR+PFR 164
6.4.3 Biological constants 165
6.5 Results 166

6.5.1 Constant maintenance rate 167
6.5.1.a Simulating the Xu experiment.....167
6.5.1.b Simulating the Neubauer experiment 169
6.5.2 Changes in the maintenance rate.....172
6.6 Discussion 175
6.6.1 Time evolution of the maintenance rate.....175
6.6.2 Lagrangian formulation of the m model.....177
6.6.3 Further considerations on the coupling with oxygen availability.....182
6.7 Conclusions..... 183
6.8 Appendix A..... 185
6.9 Nomenclature..... 188
6.10 References..... 190

Chapter 7 Conclusions 195

Chapter 1

Introduction

1.1 Computational Fluid Dynamics in Chemical Engineering

Computational Fluid Dynamics (CFD) deals with the simultaneous numerical solution of the momentum conservation, mass conservation and energy conservation differential equations that govern the motion of fluids. CFD simulations generally rely on the finite volume method to derive algebraic equations from the general conservation differential equations (Versteeg & Malalasekera, 2007). In the finite volume method, the differential equations are integrated in the whole discretized finite control volume and then the terms in the equations are substitute with their approximations (Bouchut, 2004).

CFD is being used in a great variety of applications, some of those are the flow and heat transfer in industrial processes, the aerodynamics of ground and airborne vehicles, the ventilation, heating, and cooling flows in buildings, etc. (Bakker, 2002). Specifically, CFD helps in the design and the optimization of the processes,

thanks, for instance, to the local and instantaneous results that can be collected in any point of the computational domain, to the possibility to model the full scale equipment, minimizing the uncertainties related to the scale-up and to safely simulate the flow behaviour of hazardous fluids (Brenner, 2009).

CFD in chemical and process engineering has become an important tool to studying, designing, troubleshooting and prototyping unit operation equipment. A recent overview of some of the latest development and application of CFD models in chemical engineering can be found in Nunhez, et al., (2019) and some examples include applications for oil transport Siqueira, et al., (2019), flashing spray jets de Oliveira, et al., (2019), T-shaped micromixers Galletti, et al., (2019), jacketed stirred tanks Daza, et al., (2019), non-Newtonian fluid flow around a Taylor bubble (Sontti & Atta, 2019), etc. From this short list, some of the common aspects of the CFD in chemical engineering are worthy of attention, namely the important role of turbulence, the different scales involved, the modelling of non-Newtonian fluids, the motion of geometrical parts, the heat exchange dynamics, but two of the most characterizing aspects are probably the variety of physical behaviors considered (such as chemical and biochemical reactions, interphase mass transfer, phase transitions, species transport) and the simultaneous presence of *multiple phases*.

In the context of CFD, the governing conservation equations are often coupled with specific models to catch the different physical behaviors studied. In some specific cases, those models are well established, and the choice is limited to few options thoroughly documented in the literature (turbulence modelling, species diffusion, chemical reactions). On the other hand, a large number of computational and numerical models exists to describe, for instance, the breakup frequency of the bubbles and droplets in turbulent dispersions (Liao & Lucas, 2009) or the fluid-particle interaction forces (Lettieri & Mazzei, 2009). The choice of the modelling strategy is often not unique, intrinsically system dependent and the formulation of new models and *computational techniques* is essential to obtain realistic predictions.

1.2 Multiphase flow modelling

The simultaneous motion of multiple phases is handled in CFD codes with a different set of properties for each of the phases, that allow the calculation of different magnitudes of the forces acting on the continuous and dispersed phases. Several multiphase models are implemented in the CFD codes and they are well documented in the literature (Prosperetti & Tryggvason, 2007).

In this section some context regarding three of the most widespread families of multiphase models are shortly listed, namely: the Euler-Lagrange approach, the Euler-Euler approach and the Volume of Fluid (VOF) (Marshall & Bakker, 2004).

In the Euler-Lagrange approach, the continuous fluid phase is described by means of the Navier-Stokes equations in an Eulerian frame, while the dispersed phase elements are described in a Lagrangian frame. The trajectory for each element is calculated through the integration of the force balance acting on the element (drops, particles, bubbles). Solving Newton's second law of motion for each particle in the system, can quickly lead to prohibitively large computational times. An alternative approach contemplates to compute the trajectories of only a subset of particle, representative of all particles, resulting in a semi-deterministic (deterministic-stochastic) approach (Subramaniam, 2000).

The Euler-Euler approach adopts an Eulerian vision for all the phases considered. The phases are all mathematically described as interpenetrating continua. Each phase is governed by its conservation equations with similar formulations for all phases. Constitutive relations derived from empirical observations are used to mathematically close the set of conservation equations, making the modelling of the multiphase system dependent on the operating conditions, on the phases involved in the process and on their volume fraction.

As the Euler-Euler approach, the VOF as well treats the phases as fluids in an Eulerian frame. The main difference with the Euler-Euler approach is that the fluids are well segregated, each with its own properties and a single momentum conservation equation is shared by the fluids. Each phase is followed in the domain and a single finite volume contains either one of the phases or the interface between them. This approach makes the VOF model especially advantageous when there is the need to track the phase interface evolution.

Many multiphase models exist in the literature, including hybrid description of the phases, depending on their volume fraction. One of the most promising model is the so-called GENeralized TwO Phase flow model (GENTOP) (Hänsch, et al., 2012; Krepper, et al., 2011) that potentially allows the interface tracking due to large inhomogeneities and the description of the dispersed phase at the same time. The application of this model is now just limited to the gas-liquid systems with large and finely dispersed bubbles and it is based on a number of coefficients and parameters that need appropriate tuning.

1.3 Research Objectives

In this work, CFD is exploited to investigate different turbulent two-phase processes in mechanically stirred tanks and bioreactors. The turbulent phenomena are described in the context of the Reynolds Averaged Navier-Stokes (RANS) equations, while the two-phase fluid mechanics is modelled with an Euler-Euler approach, with the so-called Two-Fluid Model (TFM).

The objective of this research is to study the two-phase fluid dynamics in chemical and process equipment and to develop modelling strategies to describe the relevant physics in the system, testing the limitations of the Eulerian-Eulerian method. Different interphase closure models are studied and tested to improve the prediction of mixing phenomena, interphase interactions and bio-chemical reactions. Particular attention is devoted to determining the ordered discretization error (Grid Convergence study) to assess the *precision* of the solution, and to the validation with experimental data to quantify the *accuracy* of the CFD predictions.

In particular, in this work the following aspects are addressed:

- a dilute immiscible liquid-liquid mixture in a stirred tank of standard geometry was studied and the droplet dispersion was described by means of a Population Balance Model solved with the Quadrature Method of Moments. The effect of the turbulence dissipation rate and its correct prediction on the droplet breakup kernel is assessed (Chapter 3);
- dense solid-liquid suspensions in a flat-bottomed fully-baffled tank stirred with a mixed-flow impeller were analyzed. The effects of the turbulence

modelling, the interphase momentum transfer terms and the coupling between the phases on dense solid-liquid suspensions were assessed and the impact of the different terms on the solid distribution and suspension was quantified (Chapter 4). The work described in this chapter has been published in Maluta, et al., (2019a) during the PhD;

- the production of hydrogen in an attached growth bioreactor in which two impellers entrained gas from the head space and distributed it to strip the product from the liquid phase was modelled. The turbulent gas-liquid fluid dynamics, the interphase mass transfer mechanism and the product removal from the gas current were implemented in a comprehensive modelling strategy, comparing two geometrical configurations (Chapter 5). This work has been published in Maluta, et al., (2019b);
- a lab scale and an industrial scale fermentation processes were investigated and glucose concentration fluctuations on the metabolic maintenance cost of a population of *Escherichia coli* were modelled with an Eulerian model. The segregations were described simplifying the fluid dynamics by means of a probabilistic approach based on the Interaction by Exchange with the Mean (IEM) mixing model (Chapter 6). This study is presented as submitted to the *Biochemical Engineering Journal*.

Moreover, in Chapter 2 the mathematical modelling framework in which this research work is inscribed is presented, with particular emphasis in the derivation of the TFM and the role of its closure models.

In Chapter 7 the results obtained in the present thesis are summarised and the limitations of the RANS Eulerian-Eulerian approach are presented.

1.4 References

Bakker, A. (2002). Introduction to CFD. Retrieved from http://www.bakker.org/dartmouth06/engs150/01-intro.pdf

Bouchut, F. (2004). *Nonlinear Stability of Finite Volume Methods for Hyperbolic Conservation Laws* (1st ed.). Basel: Birkhäuser Basel. https://doi.org/10.1007/b93802

Brenner, G. (2009). CFD in Process Engineering. In *Notes on Numerical Fluid Mechanics and Multidisciplinary Design* (Vol. 100, pp. 351–359). Springer, Berlin, Heidelberg. https://doi.org/10.1007/978-3-540-70805-6_27

Daza, S. A., Prada, R. J., Nunhez, J. R., & Castilho, G. J. (2019). Nusselt number correlation for a jacketed stirred tank using computational fluid dynamics. *The Canadian Journal of Chemical Engineering*, *97*(2), 586–593. https://doi.org/10.1002/cjce.23385

de Oliveira, T. C. L., Pereira Neto, A. T., & Alves, J. J. N. (2019). CFD simulation of flashing jet applied to area classification. *The Canadian Journal of Chemical Engineering*, *97*(2), 465–476. https://doi.org/10.1002/cjce.23343

Galletti, C., Mariotti, A., Siconolfi, L., Mauri, R., & Brunazzi, E. (2019). Numerical investigation of flow regimes in T-shaped micromixers: Benchmark between finite volume and spectral element methods. *The Canadian Journal of Chemical Engineering*, *97*(2), 528–541. https://doi.org/10.1002/cjce.23321

Hänsch, S., Lucas, D., Krepper, E., & Höhne, T. (2012). A multi-field two-fluid concept for transitions between different scales of interfacial structures. *International Journal of Multiphase Flow*, *47*, 171–182. https://doi.org/10.1016/J.IJMULTIPHASEFLOW.2012.07.007

Krepper, E., Beyer, M., Lucas, D., & Schmidtke, M. (2011). A population balance approach considering heat and mass transfer—Experiments and CFD simulations. *Nuclear Engineering and Design*, *241*(8), 2889–2897. https://doi.org/10.1016/j.nucengdes.2011.05.003

Lettieri, P., & Mazzei, L. (2009). Challenges and Issues on the CFD Modeling of Fluidized Beds: A Review. *The Journal of Computational Multiphase Flows*, *1*(2), 83–131. https://doi.org/10.1260/175748209789563937

Liao, Y., & Lucas, D. (2009). A literature review of theoretical models for drop and bubble breakup in turbulent dispersions. *Chemical Engineering Science*, *64*(15), 3389–3406. https://doi.org/10.1016/j.ces.2009.04.026

Maluta, F., Paglianti, A., & Montante, G. (2019a). RANS-based predictions of dense solid–liquid suspensions in turbulent stirred tanks. *Chemical Engineering Research and Design*, *147*, 470–482. https://doi.org/10.1016/j.cherd.2019.05.015

Maluta, F., Paglianti, A., & Montante, G. (2019b). Modelling of biohydrogen production in stirred fermenters by Computational Fluid Dynamics. *Process Safety and Environmental Protection*, *125*, 342–357. https://doi.org/10.1016/j.psep.2018.09.020

Marshall, E. M., & Bakker, A. (2004). Computational Fluid Mixing. In E. L. Paul, V. A. Atiemo-Obeng, & S. M. Kresta (Eds.), *HANDBOOK OF INDUSTRIAL MIXING Science and practice*. Hoboken, New Jersey, USA: John Wiley & Sons Inc.

Nunhez, J. R., Derksen, J. J., & Ranade, V. V. (2019). CFD in Chemical Engineering: Process Design Symposium at the 10 th World Congress of Chemical Engineering (WCCE10). *The Canadian Journal of Chemical Engineering*, *97*(2), 442–443. https://doi.org/10.1002/cjce.23364

Prosperetti, A., & Tryggvason, G. (2007). *Computational Methods for Multiphase Flow*. (A. Prosperetti & G. Tryggvason, Eds.), *Computational Methods for Multiphase Flow* (Vol. 9780521847). Cambridge: Cambridge University Press. https://doi.org/10.1017/CBO9780511607486

Siqueira, F. C. S., Farias, I. S., Moraes Júnior, D., & dos S. Vianna, A. (2019). CFD simulation of annular oil flow wrapped with water. *The Canadian Journal of Chemical Engineering*, *97*(2), 444–451. https://doi.org/10.1002/cjce.23326

Sontti, S. G., & Atta, A. (2019). CFD study on Taylor bubble characteristics in Carreau-Yasuda shear thinning liquids. *The Canadian Journal of Chemical Engineering*, *97*(2), 616–624. https://doi.org/10.1002/cjce.23311

Subramaniam, S. (2000). Statistical representation of a spray as a point process. *Physics of Fluids*, *12*(10), 2413. https://doi.org/10.1063/1.1288266

Versteeg, H. K., & Malalasekera, W. (2007). *An Introduction to Computional Fluid Dynamics: The Finite Volume Method*. Pearson Education.

Chapter 2
Mathematical models

2.1 Introduction

The governing equations of fluid flow are the conservation of mass, momentum and energy. A local conservation law for a generic quantity is usually mathematically written as a partial differential equation (PDE) describing the evolution of the amount of the quantity in a control volume. According to the conservation law, the conserved quantity in a control volume can only change by the total net amount deriving from the balance of inlet and outlet flows and the source and sink terms (Bird, et al., 1960).

The local conservation equations for the generic single-phase laminar isothermal fluid flow can be derived from the mass and momentum balance within a generic stationary control volume and, when the continuum hypothesis holds, they read as:

$$\frac{\partial \rho}{\partial t} + \nabla \cdot \rho \boldsymbol{u} = 0 \tag{2.1}$$

$$\frac{\partial \rho \boldsymbol{u}}{\partial t} + \nabla \cdot \rho \boldsymbol{u}\boldsymbol{u} = -\nabla p - \nabla \cdot \boldsymbol{\tau} + \rho \boldsymbol{g} \tag{2.2}$$

Where ρ and $\boldsymbol{u}$ are the local instantaneous fluid density and velocity vector, respectively, p is the local instantaneous pressure, $\boldsymbol{\tau}$ is the local instantaneous viscous stress tensor and $\boldsymbol{g}$ is the gravitational acceleration.

In the simplifying but common conditions of incompressible flow of a fluid exhibiting a Newtonian behaviour, Eq. (2.1) and Eq. (2.2) become:

$$\rho \nabla \cdot (\boldsymbol{u}) = 0 \tag{2.3}$$

$$\rho \left[\frac{\partial \boldsymbol{u}}{\partial t} + \nabla \cdot (\boldsymbol{u}\boldsymbol{u}) \right] = -\nabla p - \nabla \cdot \boldsymbol{\tau} + \rho \boldsymbol{g} \tag{2.4}$$

$$\boldsymbol{\tau} = -\mu \left(\boldsymbol{u} + \nabla \boldsymbol{u}^{\mathrm{T}} \right) \tag{2.5}$$

Where Eq. (2.5) is the so-called Stokes's stress constitutive equation, which is an expression used for incompressible viscous fluids. Eq. (2.3) – Eq. (2.5) are the Navier–Stokes (NS) equations for a Newtonian fluid of constant density and the rigorous derivation of those equations can be easily found in literature (Bird et al., 1960). In this Chapter, just the derivation of the single-phase Reynolds Averaged Navier-Stokes (RANS) equations (Section 2.2) and the two fluid model (Section 2.3) with some general remarks on its closure problem (Section 2.4) are presented. More information on the fluid mechanics related equations can be found in Bird et al., (1960) and in Rutherford, (1989).

The PDEs describing the conserved mass and momentum for the incompressible, isothermal, Newtonian fluid are very general and some analytical solutions exist for a limited number of simplified problems. Moreover, in general the exact solutions may not be indefinitely stable as turbulence develops. In practical terms, approximate solutions are typically obtained with numerical methods implemented in various computer software. One of the oldest numerical method is based on the spatial discretization of the PDEs and their approximation with a local Taylor expansion (Finite Difference Method, FDM, detailed in Smith, (1985)), even though nowadays the Finite Element Method (FEM, detailed in Zienkiewicz & Taylor, (2000)) and the Finite Volume Method (FVM, detailed in Versteeg & Malalasekera, (2007)) are the most adopted methods. The FEM and FVM allow to readily discretize complex geometries in multiple dimensions, unlike the FDM, thanks to the use of an integral formulation of the PDEs. In this work, the formulation of the discretized conservation equations and their solution was achieved by means of two commercial CFD codes based on the FVM, ANSY*S* Fluent v.17.0 and OpenFOAM v.5.0. Details on the implementation of the numerical methods can be found in ANSYS Inc., (2016) and The OpenFOAM Foundation, (2016) respectively.

As already mentioned, CFD provides an approximate solution of the conservation equations that, in their Navier-Stokes formulation, are relatively generic in nature, making their application to specific problems rather diverse. The CFD predictions are therefore tightly tied to the *mathematical modelling* that allows their application to specific problems and to the *numerical methods* that allow the discretized formulation and solution of the PDEs. In this Chapter the discussion is focused on the mathematical modelling since it has been more central in this thesis work, with respect to the numerical methods.

2.2 Single-phase Reynolds Averaged Navier-Stokes equations

Eq. (2.3) and Eq. (2.4) are stable just up to some threshold Reynolds numbers that depends on the system configuration. Beyond those threshold values, the solutions present oscillations and fluctuations around an average value. In order to characterize such kind of randomly fluctuating flows, different approaches exist. One of the most adopted, it is to consider the variables in the NS equations averaged on a time period, Q, that is large with respect to the time scale of the random fluctuations and small with respect to the time scale of the evolution of the mean variables. Such average strategy is called Reynolds average. For the general incompressible flow, the Reynolds averaged quantities become:

$$\boldsymbol{U} = \frac{1}{Q}\int_{t-Q/2}^{t+Q/2} \boldsymbol{u}(\boldsymbol{x},t)dt \tag{2.6}$$

$$P = \frac{1}{Q}\int_{t-Q/2}^{t+Q/2} p(\boldsymbol{x},t)dt \tag{2.7}$$

$$\boldsymbol{T} = \frac{1}{Q}\int_{t-Q/2}^{t+Q/2} \boldsymbol{\tau}(\boldsymbol{x},t)dt \tag{2.8}$$

The mean integral variables are also called expectation value of the variable, and the deviation from their values, or fluctuations, are defined as:

$$\boldsymbol{u}' = \boldsymbol{u} - \boldsymbol{U} \tag{2.9}$$

$$p' = p - P \tag{2.10}$$

$$\boldsymbol{\tau}' = \boldsymbol{\tau} - \boldsymbol{T} \tag{2.11}$$

This procedure is called Reynolds decomposition and it bears an important corollary of the fluctuations, specifically that the mean of the fluctuating quantity is equal to zero.

Writing Eq. (2.3) and Eq. (2.4) in terms of mean integral and fluctuating variables we obtain:

$$\nabla \cdot [\rho(\boldsymbol{U} - \boldsymbol{u}')] = 0 \tag{2.12}$$

$$\frac{\partial \rho(\boldsymbol{U}+\boldsymbol{u}')}{\partial t} + \nabla \cdot [\rho(\boldsymbol{U} + \boldsymbol{u}')(\boldsymbol{U} + \boldsymbol{u}')] = -\nabla(P - p') - \nabla \cdot (\boldsymbol{T} - \boldsymbol{\tau}') + \rho \boldsymbol{g} \tag{2.13}$$

As already stated, when the solution of the NS equations becomes unstable, we are usually interested in the mean behavior of the flow, rather than following each random fluctuation. If we average the terms in Eq. (2.12) and Eq. (2.13) we obtain:

$$\nabla \cdot [\rho \boldsymbol{U}] = 0 \tag{2.14}$$

$$\frac{\partial \rho \boldsymbol{U}}{\partial t} + \nabla \cdot [\rho(\boldsymbol{U}\boldsymbol{U})] = -\nabla P - \nabla \cdot \boldsymbol{T} + \rho \boldsymbol{g} - \nabla \cdot (\rho <\boldsymbol{u}'\boldsymbol{u}'>) \tag{2.15}$$

Where on the right-hand side of Eq. (2.15) an extra term appears, since the average of the nonlinear fluctuations is not nil. The result is an additional stress produced by the fluctuating velocity field, usually referred to as the Reynolds stress. The Eq. (2.14) and Eq. (2.15) are known as the Reynolds Averaged Navier-Stokes (RANS) equations. Since the Reynolds stress accounts for the turbulent fluctuations, it is sometimes indicated with $\boldsymbol{\tau^t}$ and Eq. (2.15) is written as:

$$\frac{\partial \rho \boldsymbol{U}}{\partial t} + \nabla \cdot [\rho(\boldsymbol{U}\boldsymbol{U})] = -\nabla P - \nabla \cdot (\boldsymbol{T} + \boldsymbol{\tau}^{\mathbf{t}}) + \rho \boldsymbol{g} \tag{2.16}$$

In order to solve the RANS equations, the Reynolds stress term needs to be closed with a turbulence model. One of the most used turbulence models is the standard $k - \varepsilon$ turbulence model (Launder & Spalding, 1974) and its popularity is mostly due to its acceptable performances on a wide range of applications, the limited number of additional differential equations and variables introduced and its robustness. The standard $k - \varepsilon$ turbulence model is based on the linear eddy viscosity

approximation (also called Boussinesq hypothesis) and it is a two-equation model, meaning that two transport differential equations are introduced to transport the turbulent related variables: the turbulent kinetic energy, k, and the turbulent energy dissipation rate, ε, respectively. This turbulence model is extensively described in the literature (for instance in Versteeg & Malalasekera, (2007)) and the standard $k-\varepsilon$ turbulence model equations are just briefly reported here.

In the linear-eddy-viscosity-based turbulence models, the Reynolds stress is hypothesized to be proportional to the gradient of velocity, with the proportionality constant being the so-called turbulent viscosity, μ_t, in analogy with the laminar stress tensor.

$$\boldsymbol{\tau}^t = -\mu_t(\nabla \boldsymbol{U} + \nabla \boldsymbol{U}^T) \tag{2.17}$$

The turbulent viscosity is defined as:

$$\mu_t = \rho C_\mu \frac{k^2}{\varepsilon} \tag{2.18}$$

With C_μ being a model constant. The values for the turbulent kinetic energy and the turbulent dissipation rate are obtained from the solution of two transport equations:

$$\frac{\partial \rho k}{\partial t} + \nabla \cdot (\rho k \boldsymbol{U}) = \nabla \cdot \left(\frac{\mu_t}{\sigma_k} \nabla k\right) + 2\mu_t \boldsymbol{E}^2 - \rho\varepsilon \tag{2.19}$$

$$\frac{\partial \rho \varepsilon}{\partial t} + \nabla \cdot (\rho \varepsilon \boldsymbol{U}) = \nabla \cdot \left(\frac{\mu_t}{\sigma_\varepsilon} \nabla \varepsilon\right) + C_{1\varepsilon} \frac{\varepsilon}{k} 2\mu_t \, \boldsymbol{E}^2 - C_{2\varepsilon} \rho \frac{\varepsilon^2}{k} \tag{2.20}$$

Where $\boldsymbol{E}$ is the expectation value of the rate of deformation tensor, that in case of small displacements is defined as $(\nabla \boldsymbol{U} + \nabla \boldsymbol{U}^T)/2$, and σ_k, σ_ε, $C_{1\varepsilon}$ and $C_{2\varepsilon}$ are model constants. The terms in Eq. (2.19) and Eq. (2.20) transport equations are expressed in the form:

$$accumulation + \ advection = diffusion + production\ rate - \\ - destruction\ rate \tag{2.21}$$

The five model constants in the standard $k-\varepsilon$ turbulence model are derived from data fitting for a wide range of turbulent flows and they are reported in Tab. 2.1.

Tab. 2.1 - standard $k-\varepsilon$ turbulence model constants values

$C_\mu = 0.09$	$\sigma_k = 1.00$	$\sigma_\varepsilon = 1.30$	$C_{1\varepsilon} = 1.44$	$C_{2\varepsilon} = 1.92$

2.3 Derivation of the two-fluid model

The modelling of multiphase flows can be achieved with different approaches of increasing complexity, ranging from empirical correlations to the coupled fully resolved solution of the conservation equations for each phase. Two of the most widespread approaches are based on very different assumptions for the dispersed phase. With the *Lagrangian* description of the dispersed phase, the Newton's second law of motion is solved for each element (particles, bubbles, drops, bacteria, …) taking into account the forces acting on it. The *Eulerian* view of the disperse phase assumes a description of the multiphase flow as consisting of as many fluids as the number of phases. The Eulerian description of the dispersed phase coupled with the Eulerian description of the continuous phase is often referred to as Eulerian-Eulerian two-fluid model approach.

For the derivation of the two-fluid model (TFM) (RA)NS equations, we begin by considering a two-phase system such as an aerated reactor, Fig. 2.1, that, for the purpose, can be considered as a tank full of water where bubbles of air are injected from the bottom by means of a holed ring (sparger).

An ideal conductivity probe is positioned in the bulk of the tank and it registers the time evolution of the instantaneous value of the non-dimensional conductivity in a point (or small volume) of the system. The signal, *M*, could be the one shown in Fig. 2.2.

The passage of water in the proximity of the probe produces a high value of the signal, whereas the passage of the gas produces a low value. These values are normalized between 0 and 1. The non-dimensional conductivity can therefore be seen as a *phase indicator function* for the liquid-phase.

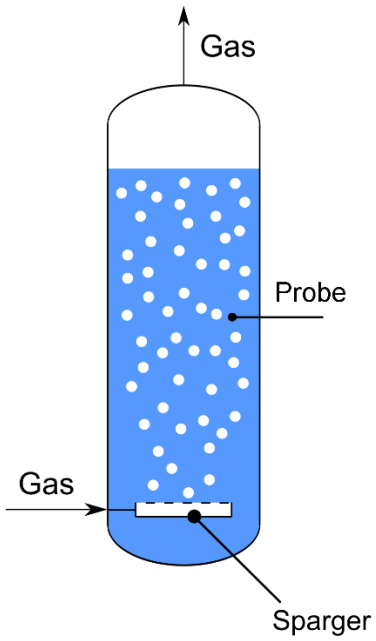

Fig. 2.1 – Example of a two-phase system: aerated reactor

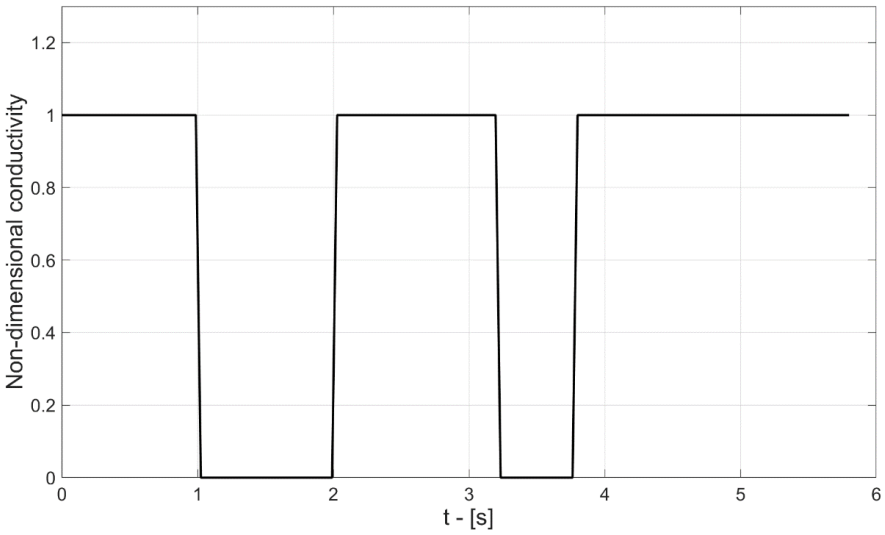

Fig. 2.2 – Signal from the conductivity probe

The phase indicator function can be regarded as a filter, in fact multiplying the phase indicator function by a flow variable, it is possible to derive the phasic quantity, i.e. multiplying the velocity obtained by the measurement of the system in the proximity of the probe by the phase indicator function, the velocity for the liquid phase is found.

Performing many experiments and ensemble averaging the results lead to the statistical probability of finding the phase of interest, j, in the measuring point.

$$\overline{M_j} = \lim_{N\to\infty} \frac{1}{N} \sum_{i=1}^{N} \left(M_j\right)_i = \alpha_j \tag{2.22}$$

Where the subscript j indicates that the quantity is referred to the j-th phase, N is the total number of experiments, and M is the phase indicator function. The quantity α_j is often referred to as the volume fraction of the phase j and one important property is that the sum of the statistical probabilities of all the j phases closes to 1.

Analogously to what was already done in Eq. (2.22), it is possible to define the ensembled average of a generic quantity, ϕ, Eq. (2.23), moreover we can define phase averaged, Eq. (2.24), and phase weighted quantities, Eq. (2.25).

$$\overline{\phi} = \lim_{N\to\infty} \frac{1}{N} \sum_{i=1}^{N} \phi_i \tag{2.23}$$

$$\overline{M_j\phi} = \lim_{N\to\infty} \frac{1}{N} \sum_{i=1}^{N} \left(M_j\phi\right)_i = \overline{\phi}_j \tag{2.24}$$

$$\tilde{\phi}_j = \frac{\overline{M_j\phi}}{\overline{M_j}} = \frac{\overline{M_j\phi}}{\alpha_j} \tag{2.25}$$

Having defined phase-averaged variables, it is possible to derive phase-averaged conservation equations. The first step is to multiply the mass conservation equation, Eq. (2.14), and the momentum conservation equation, Eq. (2.16), by the phase indicator function, M_j.

$$M_j \nabla \cdot [\rho \boldsymbol{U}] = 0 \tag{2.26}$$

$$M_j \frac{\partial \rho \boldsymbol{U}}{\partial t} + M_j \nabla \cdot [\rho(\boldsymbol{U}\boldsymbol{U})] = -M_j \nabla P - M_j \nabla \cdot (\boldsymbol{T} + \boldsymbol{\tau}^{\mathbf{t}}) + M_j \rho \boldsymbol{g} \tag{2.27}$$

From the chain rule, Eq. (2.28) and Eq. (2.29) are found.

$$M_j \frac{\partial}{\partial t}(\rho) = \frac{\partial}{\partial t}\left(M_j \rho\right) - \rho \frac{\partial}{\partial t}\left(M_j\right) \tag{2.28}$$

$$M_j \nabla \cdot (\rho \boldsymbol{U}) = M_j \frac{\partial}{\partial x^i}(\rho U) = \frac{\partial}{\partial x^i}\left(M_j \rho U\right) - \rho U \frac{\partial}{\partial x^i}\left(M_j\right) = \\ = \nabla \cdot \left(M_j \rho \boldsymbol{U}\right) - \rho \boldsymbol{U} \cdot \nabla\left(M_j\right) \tag{2.29}$$

Before deriving the phase averaged conservation equations, it is useful defining the phase indicator function derivatives. Through a detailed analysis of the signal of Fig. 2.2, shown in Fig. 2.3, it is possible to derive an expression for the phase indicator functions derivatives. The area highlighted in blue corresponds to the change of the non-dimensional conductivity in time due to the passage of a bubble on the probe tip. More specifically, the change happens when the probe tip passes through the liquid-gas interface that, for the purpose of this discussion, has thickness δ.

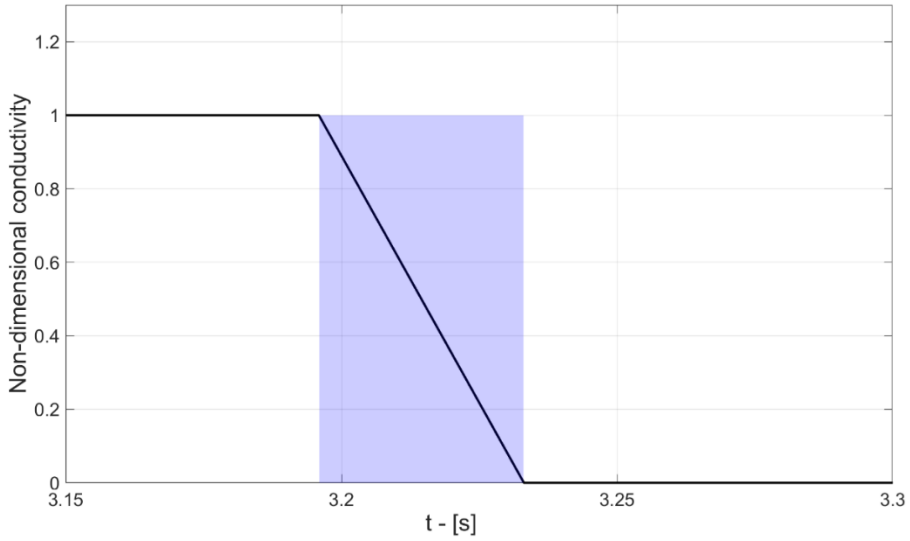

Fig. 2.3 – Signal from the conductivity probe in correspondence of the passage of a bubble

The interface in the system considered is in motion with respect to the fixed probe, due to the rising velocity of the dispersed bubbles in the liquid, therefore it is

possible to define an *interfacial velocity*, v^I. Assuming these hypotheses, the order of magnitude of the phase indicator functions derivatives can be inferred, in fact:

$$\frac{\partial}{\partial t}\left(M_j\right) \propto \frac{1}{\delta/_{v^I}} \tag{2.30}$$

$$\frac{\partial}{\partial x^i}\left(M_j\right) \propto -\frac{1}{\delta} \tag{2.31}$$

Recalling here the conservation equation for the generic variable ϕ:

$$\frac{\partial}{\partial t}(\rho\phi) + \nabla \cdot (\rho \boldsymbol{U}\phi) = -\nabla \cdot \boldsymbol{C}_\phi + \boldsymbol{S}_\phi \tag{2.32}$$

In which with $\boldsymbol{C}_\phi$ are indicated all the fluxes related to the surface of the control volume (except the advection) and with $\boldsymbol{S}_\phi$ are indicated the terms related to the bulk of the control volume (including source/sink terms), we notice that the left hand side (LHS) of Eq. (2.32) relative to the phase indicator function then becomes:

$$\begin{aligned}\frac{\partial}{\partial t}\left(\rho M_j\right) + \nabla \cdot \left(\rho \boldsymbol{U} M_j\right) = M_j \frac{\partial}{\partial t}(\rho) + M_j \nabla \cdot (\rho \boldsymbol{U}) + \\ + \rho \frac{\partial}{\partial t}\left(M_j\right) + \rho \boldsymbol{U} \cdot \nabla\left(M_j\right)\end{aligned} \tag{2.33}$$

Where the first two terms on the RHS of Eq. (2.33) sum up to zero, as shown in Eq. (2.1), resulting in the so called *topological equation***:**

$$\begin{aligned}\frac{\partial}{\partial t}\left(\rho M_j\right) + \nabla \cdot \left(\rho \boldsymbol{U} M_j\right) \propto -\rho v^I \cdot \nabla\left(M_j\right) + \rho \boldsymbol{U} \cdot \nabla\left(M_j\right) = \\ = \rho(\boldsymbol{U} - v^I) \cdot \nabla\left(M_j\right)\end{aligned} \tag{2.34}$$

Ensemble averaging Eq. (2.34) results in:

$$\overline{\frac{\partial}{\partial t}\left(\rho M_j\right)} + \overline{\nabla \cdot \left(\rho \boldsymbol{U} M_j\right)} = \overline{\rho(\boldsymbol{U} - v^I) \cdot \nabla\left(M_j\right)} \tag{2.35}$$

That can be rearranged in Eq. (2.36) due to the properties of the Reynolds averaging, and it can be further arranged in Eq. (2.37):

$$\frac{\partial}{\partial t}\overline{(\rho M_j)} + \nabla \cdot \overline{(\rho \boldsymbol{U} M_j)} = \overline{\rho(\boldsymbol{U} - v^I) \cdot \nabla(M_j)} \tag{2.36}$$

$$\frac{\partial}{\partial t}(\widetilde{\rho_j}\alpha_j) + \nabla \cdot (\alpha_j \widetilde{\rho_j}\widetilde{\boldsymbol{U}_j}) = \overline{\Gamma_j}\frac{\partial}{\partial x^i}(M_j) \propto -\frac{1}{\delta} \tag{2.37}$$

Where the term $\overline{\Gamma_j}$ is the phasic mass source term and it exists only at the interfaces. It represents the mean flow rate per volume in and out of phase (i.e. boiling, condensation, cavitation, ...) and it is related to known quantities via empirical models. Moreover:

$$\sum_{j=1}^{Np} \overline{\Gamma}_j = 0 \tag{2.38}$$

With the same procedure used to derive the phase averaged continuity equation, Eq. (2.37), The momentum conservation equation in Eq. (2.27), results in:

$$\begin{aligned}\frac{\partial}{\partial t}(\alpha_j \widetilde{\rho_j}\widetilde{\boldsymbol{U}_j}) + \nabla \cdot (\alpha_j \widetilde{\rho_j}\widetilde{\boldsymbol{U}_j}\widetilde{\boldsymbol{U}_j}) = \\ = -\nabla(\alpha_j \widetilde{P_j}) - \nabla \cdot (\alpha_j[\widetilde{\boldsymbol{T}_j} + \widetilde{\boldsymbol{\tau}^t_j}]) + \alpha_j \widetilde{\rho_j}\boldsymbol{g} + \overline{\Gamma_j}\widetilde{\boldsymbol{U}_j} + \overline{\boldsymbol{D}_j} + \overline{\boldsymbol{N}_j}\end{aligned} \tag{2.39}$$

With $\overline{\Gamma_j}\widetilde{\boldsymbol{U}_j}$, $\overline{\boldsymbol{D}_j}$ and $\overline{\boldsymbol{N}_j}$ being the interfacial momentum transfer, the viscous (and turbulent) phase interaction and the pressure phase interaction term, respectively. These terms arise from the phase averaging procedure and need an expression to mathematically close the system. This is usually done via empirical closure models.

2.4 Closure models for the two-phase model

In the phase averaged conservation equations, Eq. (2.37) and Eq. (2.39), neglecting at first the phase interaction terms, there are $5 \times Np$ unknowns namely, the three components of the velocity vector, ($\widetilde{U_j}$, $\widetilde{V_j}$ and $\widetilde{W_j}$), the pressure ($\widetilde{P_j}$) and the volume fractions (α_j). The momentum conservation equation consists of $3 \times Np$ scalar equations, it is possible to write one continuity equation for each phase and one volume conservation equation as.

$$\sum_{j=1}^{Np} \alpha_j = 1 \tag{2.40}$$

$Np-1$ additional equations are needed to close the system of differential equations. The assumption commonly accepted is that all the phases share the same local pressure i.e.:

$$\tilde{P}_1 = \tilde{P}_2 = \cdots = \tilde{P}_j = \cdots = \tilde{P}_{Np} = \tilde{P} \tag{2.41}$$

And this hypothesis conveniently leads to $Np-1$equations. More modelling effort is needed to derive empirical closure for the phase interaction terms. Let us consider the system in Fig. 2.4 where a simple closed stationary two-phase system at rest is considered.

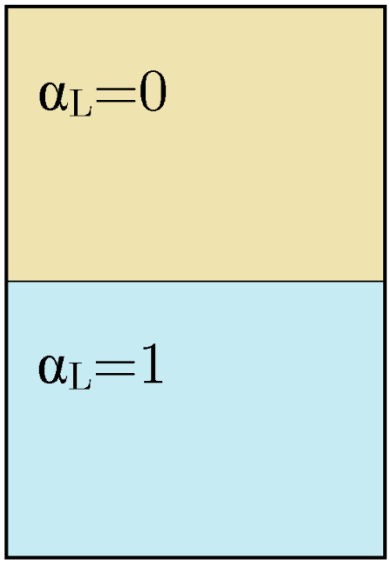

Fig. 2.4 – Closed stationary two-phase system at rest

The two-phases are completely segregated and the momentum conservation equation in a generic point in the system reads:

$$0 = -\nabla(\alpha_j \tilde{P}) + \alpha_j \tilde{\rho_j} \boldsymbol{g} + \overline{\boldsymbol{N}_j} \tag{2.42}$$

Considering now the momentum conservation equation in the bulk of the L-phase, we have that no spatial gradient of the volume fraction of L exists:

$$\nabla(\alpha_j) = 0 \tag{2.43}$$

Therefore, bearing in mind that the interfacial momentum transfer terms depend on the gradient of the phase indicator function, Eq. (2.42) becomes:

$$0 = -\nabla(\alpha_j \tilde{P}) + \alpha_j \widetilde{\rho_j} \boldsymbol{g} + \overline{\boldsymbol{N_j}} = -\alpha_j \nabla(\tilde{P}) + \alpha_j \widetilde{\rho_j} \boldsymbol{g} \tag{2.44}$$

Subtracting Eq. (2.44) to Eq. (2.42) results in:

$$\overline{\boldsymbol{N_j}} = \tilde{P} \nabla(\alpha_j) \tag{2.45}$$

Eq. (2.45) is a model for the pressure force which is not null only at the interface between different phases. Simplifying the notation for the phase weighted variables, modelling the pressure force with Eq. (2.45), assuming the hypothesis of shared pressure and no interfacial mass transfer, Eq. (2.39) becomes:

$$\begin{aligned} \frac{\partial}{\partial t}(\alpha_j \rho_j \boldsymbol{U_j}) + \nabla \cdot (\alpha_j \rho_j \boldsymbol{U_j} \boldsymbol{U_j}) \\ = -\alpha_j \nabla(P) - \nabla \cdot (\alpha_j [\boldsymbol{T_j} + \boldsymbol{\tau^t_j}]) + \alpha_j \rho_j \boldsymbol{g} + \overline{\boldsymbol{D_j}} \end{aligned} \tag{2.46}$$

The last term on the RHS of Eq. (2.46) is the interaction term due to viscous and turbulent interphase forces and it is usually modelled as a sum of different contributions (i.e. interphase drag force, turbulent dispersion force, lift force, particle collisions, …). The overall phase interaction term must close to zero:

$$\sum_{k=1}^{Np} \overline{\boldsymbol{D_j}} = 0 \tag{2.47}$$

Where $\overline{\boldsymbol{D_j}}$ is defined as:

$$\begin{aligned} \overline{\boldsymbol{D_j}} = \sum_{l \neq j}^{Np} \overline{\boldsymbol{D}}_{j \to l_{drag}} + \sum_{l \neq j}^{Np} \overline{\boldsymbol{D}}_{j \to l_{TD}} + \sum_{l \neq j}^{Np} \overline{\boldsymbol{D}}_{j \to l_{lift}} + \\ + \sum_{l \neq j}^{Np} \overline{\boldsymbol{D}}_{j \to l_{collision}} + \dots \end{aligned} \tag{2.48}$$

Different forces require different models that are usually empirically derived for specific systems. For this reason, the relevant interphase force models are discussed in the following chapters.

2.5 Nomenclature

C_μ, σ_k, σ_ε, $C_{1\varepsilon}$, $C_{2\varepsilon}$	$k-\varepsilon$ turbulence model parameters
$\boldsymbol{C_\phi}$	Fluxes related to the surface of the control volume
$\overline{\boldsymbol{D_j}}$	Interaction term due to viscous and turbulent interphase forces
$\boldsymbol{E}$	Expectation value of the rate of deformation tensor
$\boldsymbol{g}$	Gravitational acceleration
k	Turbulent kinetic energy
M_j	Indicator function of the *j-th* phase
$\overline{M_j}$	Ensemble average of the indicator function of the *j-th* phase
N	Total number of experiments
Np	Number of phases
$\overline{\boldsymbol{N_j}}$	Pressure phase interaction term
p	Pressure
p'	Pressure fluctuation
P	Averaged pressure
Q	Time interval
$\boldsymbol{S_\phi}$	Terms related to the bulk of the control volume
t	Time
$\boldsymbol{u}$	Velocity
$\boldsymbol{u'}$	Velocity fluctuation
$\boldsymbol{U}$	Averaged velocity
v^I	Interfacial velocity
$\boldsymbol{x}$	Spatial coordinate vector

Greek letters

α_j	Volume fraction of the *j-th* phase
$\overline{\Gamma_j}$	Phasic mass source term
δ	Interface thickness
ε	Turbulent dissipation rate
μ	Dynamic viscosity
μ_t	Turbulent viscosity
ρ	Density
$\boldsymbol{\tau}$	Viscous stress tensor
$\boldsymbol{\tau^t}$	Reynolds stress
$\boldsymbol{\tau'}$	Viscous stress fluctuation
$\boldsymbol{T}$	Averaged viscous stress

ϕ	Generic quantity
$\overline{\phi}$	Ensemble average of ϕ
$\overline{\phi}_j$	Phase average of ϕ
$\tilde{\phi}_j$	Phase weighted average of ϕ

2.6 References

ANSYS Inc. (2016). *ANSYS Fluent Theory Guide* (17th ed.). Canonsburg, PA. Retrieved from https://support.ansys.com/portal/site/AnsysCustomerPortal/template.fss?file=%2Fsolutions%2Fattach%2FANSYS+Fluent+Theory+Guide.pdf

Bird, R. B., Stewart, W. E., & Lightfoot, E. N. (1960). *Transport Phenomena*. New York: Wiley & Sons, Inc.

Launder, B. E., & Spalding, D. B. (1974). The numerical computation of turbulent flows. *Computer Methods in Applied Mechanics and Engineering*, *3*(2), 269–289. https://doi.org/10.1016/0045-7825(74)90029-2

Rutherford, A. (1989). *Vectors, Tensors and the Basic Equations of Fluid Mechanics* (Dover ed). New York: Dover Publications, Inc.

Smith, G. D. (1985). *Numerical solution of partial differential equations : finite difference methods*. Oxford: Clarendon Press. Retrieved from https://global.oup.com/academic/product/numerical-solution-of-partial-differential-equations-9780198596509?cc=it&lang=en&

The OpenFOAM Foundation. (2016). OpenFOAM v5 User Guide. Retrieved from https://cfd.direct/openfoam/user-guide-v5/

Versteeg, H. K., & Malalasekera, W. (2007). *An Introduction to Computional Fluid Dynamics: The Finite Volume Method*. Pearson Education.

Zienkiewicz, O. C., & Taylor, R. L. (2000). *The finite element method*. Oxford: Butterworth-Heinemann Ltd.

Chapter 3

Liquid-Liquid dispersions in stirred tanks

In this work the droplet size distribution (DSD) of diesel fuel in water in a tank stirred with a Rushton turbine was numerically studied by means of computational fluid dynamics simulations coupled with a population balance model (PBM) considering very dilute (0.1 vol%) and completely dispersed conditions. The PBM was solved with the Quadrature Method of Moments (QMOM) in the context of the two-fluid model. The effect of the turbulent dissipation rate on the breakup frequency was studied with grids of different densities, up to 5.5 million elements, and the analysis highlighted that grid effects are relevant and need to be properly addressed. Results are validated with experimental droplet size data collected by a laser diffraction technique. Based on Particle Image Velocimetry data, the effect of the dispersed phase on the continuous phase mean and fluctuating velocity was found to be negligible, while the flow fields of the two phases were coincident, being the droplet relaxation time even smaller than that of the liquid seeding particles. Therefore, the turbulent dissipation rate from the simulations is compared with experimental and numerical data collected in similar stirred tanks and single-phase flow in previous

investigations. The study confirmed that the adopted breakup kernel is heavily dependent on the model parameters and that their values are system dependent. An alternative way to deal with the underprediction of the turbulent dissipation rate in the breakup kernel in the context of RANS simulations is proposed, based on the spatial distribution of turbulent dissipation rate and breakup frequency.

3.1 Introduction

Several unit operations in the food, pharmaceutical and chemical industry rely on liquid-liquid turbulent dispersions. Emulsification, organic synthesis, and extractions, among the others, are heavily dependent on the properties of the dispersion which rheology, stability and exchange properties are determined by many factors, one of the most important being the drop size distribution (DSD) of the dispersed phase (Afshar Ghotli, et al., 2013; Leng & Calabrese, 2016). The DSD, in fact, has an important role in governing the dispersed phase fluid dynamics in the equipment, that in turn affects the performances of the whole process (Afshar Ghotli et al., 2013; Drumm, et al., 2009; Maaß, et al., 2012).

Computational techniques have become an important aid in studying the evolution of the DSD and its relationships with the fluid dynamics. This study can be performed with different modelling approaches that can be divided into three main categories: fully-resolved (Derksen & Van Den Akker, 2007; Di Miceli Raimondi, et al., 2008), Lagrangian point-particle (Z. Jaworski & Pianko-Oprych, 2002; Rieger, et al., 1996) and Eulerian-Eulerian approaches (Gao, et al., 2016; Hu, et al., 2015). Eulerian-Eulerian methods have the advantage of being computationally cheaper than the other approaches but, at the same time, they do not allow a segregation of the dispersed phase properties (such as size, velocity, interfacial properties, etc.) that are described with a unique value for each and every dispersed element (Buffo, et al., 2013). To overcome this problem, the segregation of the internal properties of interest can be described by means of a population balance model (PBM) that can be solved in a computational fluid dynamics (CFD) framework.

The solution of the PBM can be performed in several ways, one of the oldest being the discretization in classes of the investigated properties (Hounslow, et al., 1988; Kumar & Ramkrishna, 1996), even though nowadays more computationally efficient methods exists, such as the method of moments (MOM) (Hulburt & Katz, 1964), adopted in this work.

The MOM introduces the so-called closure problem, which was solved, many years after the formulation of the MOM, with the adoption of a family of solutions based on a quadrature approximation (QMOM) (McGraw, 1997), described in the book by Marchisio & Fox, (2010).

In order to develop a CFD-PBM fully-predictive model for the DSD, reliable closure models to account for coalescence and breakage are needed. The development of the coalescence and breakage models, also called kernels, should rely on theoretical considerations and universal constants only, and their use should not be subject to tuning to match the experimental trends (Azizi & Taweel, 2011). Nevertheless, said kernels often contain parameters that are tuned for specific configurations or heavily depend on empirical correlations that limit the use of the models themselves (Bakker, et al., 2001). In fact, the kernels are functions of the physical properties of the mixture as well as process variables, therefore in tuning the kernels parameters and testing them in new conditions, the modelist must pay attention to the process conditions. As a result, the formulation of the kernels is achieved through extensive amount of pilot-scale testing that limits the use of the kernels to the parameter ranges derived from the original measurement data set (Azizi & Taweel, 2011).

One of the most important process variables for the breakage and coalescence mechanism is the turbulent intensity acting on the single droplets, that is considered in the kernels by means of the turbulent dissipation rate. In several studies in which the modelling capabilities of PBM model are extended to new conditions, the modelists derived the turbulent dissipation rate from *ad hoc* experiments and an averaged value of the variable was used in the modified kernels (Basavarajappa, et al., 2017; Khadem & Sheibat-Othman, 2019; Lebaz & Sheibat-Othman, 2019). Some of the drawbacks of using an averaged value of the turbulent dissipation rate derived from the experiments are that indirect techniques are often used to evaluate the turbulent dissipation rate that may be subject to uncertainties (Karimi & Andersson, 2020; Lebaz & Sheibat-Othman, 2019) and that a unique value is used instead of a field.

As a matter of fact, the turbulent dissipation rate may change consistently inside the equipment in which the dispersion is studied, therefore it is important to know its spatial distribution for proper calculation of the kernels (Buffo, et al., 2016).

Indeed, the turbulent dissipation rate has a major effect in determining the evolution of the droplets size as well as the ratio between breakage and coalescence rates (Li, et al., 2017) and the prediction of these phenomena by the kernels may be tested varying the dissipation rate by means of numerical sensitivity studies on the PBM (De Bona, et al., 2016).

Experimental values of the turbulent dissipation rate and sensitivity studies are very important in the early stages of the formulation and development of a model but are not suitable for a fully-predictive model formulation. In this regard, a useful aid could come from the CFD.

Deriving the turbulence field from the CFD is an appealing solution but the correct prediction of the turbulent variables is severely dependent on the simulations conditions, especially in the widespread RANS, Eulerian-Eulerian frame (Coroneo, et al., 2011). Jaworski, et al., (2007) pointed out the importance of a correct calculation of the turbulent quantities in the prediction of the DSD and how their underestimation led to larger droplets diameters. Other authors acknowledged and identified the issue of underestimating the turbulent dissipation rate because of a coarse mesh and low order numerical schemes, either without proposing alternative solutions (Drumm et al., 2009; Tang, et al., 2018; Zhang, et al., 2012), by quantifying the error on the turbulent variables and how this affected their results (Alopaeus, et al., 2002; Kálal, et al., 2014), or deriving new experimental-numerical hybrid methods tuned to correctly predict the DSD (Khajeh Naeeni & Pakzad, 2019).

Recently, some authors proposed to introduce in the kernels a scalar correction that takes into account the RANS underprediction of the turbulent dissipation field in the simulation of stirred tanks (Gao et al., 2016; Li, et al., 2017). As noted by the authors, this approach has the drawbacks of being dependent on the system and on the CFD simulations (being based on the experimental power number of the impeller and on the integral of the turbulent dissipation rate on the whole numerical domain) and introducing a uniform correction that may not be representative of the spatial distribution of the turbulent variables. In fact, underpredictions of the turbulent dissipation rate are expected to be higher in those regions of the domain where the turbulence is more intense.

This work focuses on the comparison between the experimental DSD and flow variables of a immiscible liquid-liquid mixture of diesel fuel in water and its prediction by a CFD-PBM simulation with the Alopaeus breakup kernel (Alopaeus et al., 2002). Being the dispersion in very dilute conditions, coalescence mechanisms were neglected. Three dimensional CFD RANS simulations are performed with different grid densities to predict the turbulent field inside the domain and test the kernel without correction coefficients. The CFD-PBM model is solved in OpenFOAM v.5.x with the QMOM implementation described by Buffo et al., (2013) and by Buffo, et

al., (2016). Numerical results are compared against experimental DSD data purposely collected from a tank stirred with a Rushton impeller which geometrical features were closely reproduced in the CFD-PBM simulations.

3.2 Investigated System

The investigated system was a cylindrical, flat bottomed tank with diameter, *T*, and height, H_T, both equal to 0.232m. It was equipped with four equally spaced baffles of width equal to *T*/10. A single Rushton turbine (RT) mounted on a central shaft was used to agitate the system. The diameter of the impeller, *D*, was equal to 0.077m, corresponding to a *T/D* ratio equal to 3, and the off-bottom clearance, *C*, was half of the vessel diameter (*T/C* = 2). The liquid height, H_L, was always maintained at H_T, corresponding to a total volume of 9.8L.

A mixture of commercial diesel fuel with density, ρ_D, equal to 810kg/m^3 and viscosity, μ_D, equal to 3.5×10^{-3}Pa·s (measured at room temperature) in demineralized water with density, ρ_C, and viscosity, μ_C, equal to 998kg/m^3 and 10^{-3} Pa·s respectively, was simulated. The diesel fuel/water interfacial tension was assumed equal to 44.7mN/m, resulting from the difference between water, 72.3mN/m, and the measured diesel fuel surface tension, 27.6mN/m at room temperature.

The diesel fuel drop size distribution obtained from the simulations of the dispersion of 9.7mL of oil, corresponding to a volume fraction of $\alpha_D = 10^{-3}$, at an impeller rotational speed of *N* = 500rpm, to ensure complete dispersion, was studied and the numerical results were compared with the experimental data collected by means of a Spraytec laser diffraction system (Malvern Panalytical). A sample of the mixture was withdrawn from the system at a position of $r/T = 0.35 \pm 0.02$, $z/T = 0.69 \pm 0.04$ (assuming the origin of the axes in the centre of the bottom of the tank) on a plane midway two consecutive baffles and promptly transferred to a *wet sample dispersion unit* (Malvern Panalytical) that recirculated continuously the sample through the Spraytec laser diffraction system. Collecting the intensity of light scattered as the laser beam passes through the sample, the system calculates the size of the droplets that created the scattering pattern and produces a discretized DSD in term of the weighted volume fractions with respect to the total dispersed phase volume in the sample.

The flow fields of the continuous phase with and without droplets and of the diesel fuel droplets were measured by Particle Image Velocimetry (PIV), similarly to previous investigations concerning gas-liquid (Montante, et al., 2008) and solid-liquid (Montante, et al., 2012) in stirred tanks. The data were collected on a portion of the vertical plane located midway between two consecutive baffles. Water was seeded by polymeric particles coated with fluorescent Rhodamine B, that emit the received light of wavelength 532nm at the wavelength of 590nm, while the droplets have the same emission wavelength as the laser light. By using two cameras equipped with optical filters, each camera received the proper light signal. A band-pass filter centred on the orange light wavelength was placed on the continuous phase camera to block the droplets scattered light, while a band-pass filter centred on the green light wavelength was placed on the dispersed phase camera to block the light emitted by the Rhodamine B.

The pulsed Nd:YAG laser (λ=532nm, 15Hz, 65mJ) and the two Charge-Coupled Device cameras (resolution of 1344×1024 pixels) were handled by a Dantec Dynamics system. The area viewed from the two cameras were identical.

The instantaneous velocity vectors were obtained from the cross-correlation images collected in double-frame mode. The time interval between the two laser pulses was set to 270μs, the total number of image pairs was 2000. A vector resolution of 1.7mm was obtained by applying the cross-correlation on an interrogation area size of 32×32 pixels with on overlap of 50%. The instantaneous vectors were discarded if they did not fulfil two conditions, one based on the evaluation of the peak heights in the correlation plane and the other on the velocity magnitude.

3.3 Governing equations

The equations solved in this work to obtain the two-phase flow field inside the stirred tank and the formulation of the PBE are shown in this section. Since the flow regime is fully turbulent ($Re = ND^2 \rho_C/\mu_C \approx 50{,}000$), the RANS two-fluid model equations are solved.

3.3.1 Two-fluid model

The simulations were based on the two-fluid model equations written under incompressible and isothermal hypotheses. The disperse phase continuity and momentum equations specifically solved in this work are:

$$\frac{\partial(\alpha_D \rho_D)}{\partial t} + \nabla \cdot (\alpha_D \rho_D \boldsymbol{u_D}) = 0 \tag{3.1}$$

$$\frac{\partial(\alpha_D \rho_D \boldsymbol{u_D})}{\partial t} + \nabla \cdot (\alpha_D \rho_D \boldsymbol{u_D u_D}) = -\alpha_D \nabla P + \alpha_D \rho_D \boldsymbol{g} + \\ + \nabla \cdot (\boldsymbol{\tau_D} + \boldsymbol{\tau^t}) + \boldsymbol{F}_{drag,CD} \tag{3.2}$$

where α_D is the volume fraction of the disperse phase, $\boldsymbol{u_D}$ is the disperse phase mean velocity vector, P is the pressure, $\boldsymbol{g}$ is the gravity vector and $\boldsymbol{\tau_D}$ is the viscous stress tensor. The Reynolds stress tensor, $\boldsymbol{\tau^t}$, and the interphase drag term, $\boldsymbol{F}_{drag,CD}$, need to be modelled to mathematically close the set of equations.

The Reynolds stress was modelled with the single-phase standard *k*-ε turbulence model with the properties of the continuous phase:

$$\frac{\partial \alpha_C \rho_C k}{\partial t} + \nabla \cdot (\alpha_C \rho_C k \boldsymbol{u_C}) = \nabla \cdot \left(\alpha_C \frac{\mu_t}{\sigma_k} \nabla k\right) + 2\alpha_C \mu_t \boldsymbol{E^2} - \alpha_C \rho_C \varepsilon \tag{3.3}$$

$$\frac{\partial \alpha_C \rho_C \varepsilon}{\partial t} + \nabla \cdot (\alpha_C \rho_C \varepsilon \boldsymbol{u_C}) = \nabla \cdot \left(\alpha_C \frac{\mu_t}{\sigma_\varepsilon} \nabla \varepsilon\right) + \\ + \alpha_C C_{1\varepsilon} \frac{\varepsilon}{k} 2\mu_t \boldsymbol{E}^2 - \alpha_C C_{2\varepsilon} \rho_C \frac{\varepsilon^2}{k} \tag{3.4}$$

Where α_C and ρ_C are the volume fraction and the density of the continuous phase, respectively, k is the turbulent kinetic energy, ε is the turbulent dissipation rate, $\boldsymbol{E}$ is the rate of deformation tensor and $\mu_t = \rho_C \mathrm{C}_\mu \, k^2/\varepsilon$ is the turbulent viscosity. The five model constants σ_k, σ_ε, $C_{1\varepsilon}$, $C_{2\varepsilon}$ and C_μ assume their standard values of 1.00, 1.30, 1.44, 1.92 and 0.09, respectively.

The only interphase momentum exchange term in Eq. (3.2) is the drag force that can be written in the form:

$$\boldsymbol{F}_{drag,CD} = \frac{3}{4} \frac{\alpha_D}{d_D} C_D \rho_C \|\boldsymbol{u_D} - \boldsymbol{u_C}\| (\boldsymbol{u_D} - \boldsymbol{u_C}) \tag{3.5}$$

In Eq.(3.5), d_D is the droplet diameter and C_D is the drag coefficient calculated with the well-known Schiller & Naumann correlation:

$$C_D = 24\left(1 + 0.15Re_p^{0.687}\right)/Re_p \tag{3.6}$$

$$Re_p = \frac{||\boldsymbol{u_D} - \boldsymbol{u_C}||d_D\rho_C}{\mu_C} \tag{3.7}$$

valid for droplets Reynolds numbers, Re_p, smaller than 1000.

As a matter of fact, the drag force magnitude acting on a droplet depends on the drop diameter. When the drop size distribution of the population of droplets (DSD) is relatively narrow, the liquid densities are similar and the size of the droplets is the order of magnitude of micrometers, a widely accepted hypothesis is to consider the drag force acting on each droplet as constant. The constant drag force is obtained with a single diameter value equal to the Sauter mean diameter of the population (Gao et al., 2016). Since the Sauter mean diameter can be defined as the ratio between the third and the second order moment of the DSD, to close the system of equations we need to calculate the DSD moments.

The continuity and momentum conservation equations for the continuous phase are in the same form of Eq. (3.1) and Eq. (3.2) and just the drag force is considered, as previously done for similar systems (Gao et al., 2016; Li, et al., 2017).

3.3.2 Population Balance Model

Considering a generic liquid-liquid system with a continuous and a dispersed phase, the system can be defined in terms of velocities and internal coordinates of the two phases, ξ_C and ξ_D. Internal coordinates of the phases are droplet size, chemical composition, enthalpy, etc. The DSD is defined from the total count of the droplets and their characteristic dimension. In an Eulerian frame, DSD is obtained from the population of droplets which Number Density Function (NDF), n, is defined such that $n(t, \boldsymbol{x}, \boldsymbol{u_D}, \xi_D, \boldsymbol{u_C}, \xi_C)d\boldsymbol{x}d\boldsymbol{u_D}d\xi_D d\boldsymbol{u_C}d\xi_C$ represents the number of particles in the population with velocity in the range $\boldsymbol{u_D}$ and $\boldsymbol{u_D} + d\boldsymbol{u_D}$, with internal coordinate between ξ_D and $\xi_D + d\xi_D$, that at the time t are found within $\boldsymbol{x}$ and $\boldsymbol{x} + d\boldsymbol{x}$ in the continuous phase with velocity in the range $\boldsymbol{u_C}$ and $\boldsymbol{u_C} + d\boldsymbol{u_C}$ and with internal coordinate between ξ_C and $\xi_C + d\xi_C$.

The evolution of the DSD is governed by the Generalized Population Balance Equation (GPBE):

$$\frac{\partial n}{\partial t} + \nabla \cdot (n\boldsymbol{u_D}) + \frac{\partial}{\partial \boldsymbol{u_D}} \cdot [(\boldsymbol{A_D} + \boldsymbol{A_{DC}})n] + \frac{\partial}{\partial \xi_D}(G_D n) + \\ + \frac{\partial}{\partial \boldsymbol{u_C}} \cdot [(\boldsymbol{A_C} + \boldsymbol{A_{CD}})n] + \frac{\partial}{\partial \xi_C}(G_C n) = \boldsymbol{S} \tag{3.8}$$

With $\boldsymbol{A_D}$ and $\boldsymbol{A_{DC}}$ being the disperse phase acceleration vectors due to body forces and due to particle-fluid interaction respectively, and $\boldsymbol{A_C}$ and $\boldsymbol{A_{CD}}$ being the continuous phase acceleration vectors due to body forces and due to fluid-particle interaction respectively. G_D and G_C are the disperse phase and the continuous phase rate of changes of the internal coordinates due to continuous processes, while the source term, $\boldsymbol{S}$, accounts for the discontinuous changes due to discrete events (i.e. breakage, coalescence).

When the momentum transfer due to collisions between droplets can be neglected, when no growth mechanisms exists, when $\boldsymbol{u_D}$ can be locally considered as a function of ξ_D only ($\boldsymbol{u_D}(\xi_D) = \boldsymbol{U_D}$) and when $\boldsymbol{u_C}$ and ξ_C can be considered as constant and equal to $\boldsymbol{U_C}$ and Ξ_C at the time t and in the interval $\boldsymbol{x}$ and $\boldsymbol{x} + d\boldsymbol{x}$, the discrete and continuous phase velocities and the continuous phase internal coordinate can be integrated out of Eq. (3.8), leaving:

$$\frac{\partial n^*}{\partial t} + \nabla \cdot (n^* \boldsymbol{U_D}) = \boldsymbol{S}^* \tag{3.9}$$

With n^* being the reduced number density function, defined as:

$$n(t, \boldsymbol{x}, \boldsymbol{u_D}, \xi_D, \boldsymbol{u_C}, \xi_C) = \\ = n^*(t, \boldsymbol{x}, \xi_D)\delta(\boldsymbol{u_D} - \boldsymbol{U_D})\delta(\boldsymbol{u_C} - \boldsymbol{U_C})\delta(\xi_C - \Xi_C) \tag{3.10}$$

In order to close Eq. (3.10), an expression for the reduced source term, $\boldsymbol{S}^*$ is needed. A common assumption when the dispersed phase volume fraction is small, is to neglect the coalescence events (Maaß et al., 2012; Marchisio & Fox, 2010; Wang & Calabrese, 1986) thus simplifying the reduced source term to account for breakup mechanisms only:

$$\boldsymbol{S}^* = \int_{d_D}^{\infty} \beta(d_D, d')g(d')n(d')dd' - g(d_D)n(d_D) \tag{3.11}$$

Where g is the breakup kernel expressing the breakup frequency and $\beta(d_D, d')$ is the daughter distribution function that gives the size distribution of drops originating from the breakage of a drop of diameter d'. In this work the daughter distribution function proposed by Laakkonen, et al., (2006) was used due to its low computational cost and the fair agreement with more detailed models, (Li, et al., 2017). The daughter distribution function has the following expression (Laakkonen et al., 2006):

$$\beta(d_D, d') = 180\left(\frac{d_D^2}{d'^3}\right)\left(\frac{d_D^3}{d'^3}\right)^2\left(1 - \frac{d_D^3}{d'^3}\right)^2 \tag{3.12}$$

Eq. (3.12) assumes binary breakage based on a statistical distribution in which symmetric breakup is considered as the event with the highest probability.

The Alopaeus breakup kernel (Alopaeus et al., 2002) was used in this work. The kernel assumes a Poisson point process distribution frequency of the eddy-drop collisions in which the turbulent dissipation rate, ε, affects said frequency. Its expression is:

$$g = C_1\varepsilon^{1/3}erfc\left(\sqrt{\frac{C_2\sigma}{\rho_C\varepsilon^{2/3}d_D^{5/3}} + \frac{C_3\mu_C}{\sqrt{\rho_C\rho_D}\varepsilon^{1/3}d_D^{4/3}}}\right) \tag{3.13}$$

With C_1, C_2, C_3 being model constants and σ being the interfacial tension. The constant values were taken equal to 3.68, 0.0775 and 0.2, respectively, being the values for C_1 and C_3 the original values proposed by (Alopaeus et al., 2002) and the value for C_2 being fitted with experimental data for a similar system by Li, et al., (2017).

The closed Eq. (3.9) can now be solved with different strategies, such as, Monte Carlo methods, Method of Characteristics, Class method or with the Method of Moments (MOM).

3.3.3 Quadrature Based Method of Moment

In this work, the MOM was used to determine the NDF. With this strategy, the Eq. (3.9) is not solved directly, instead transport equations for the moments of the reduced NDF are derived and then solved. The reduced NDF moment of order k, M_k, is defined as:

$$M_k = \int_0^\infty n^* d_D^k dd_D \tag{3.14}$$

And applying the moment transform of order k to Eq. (3.9) leads to:

$$\frac{\partial M_k}{\partial t} + \nabla \cdot (M_k \boldsymbol{U_D}) = \\ = \int_0^\infty \left[\int_{d_D}^\infty \beta(d_D, d') g(d') n(d') dd' - g(d_D) n(d_D) \right] d_D^k dd_B \tag{3.15}$$

where the term on the right-hand side of Eq. (3.15) is not closed, meaning that its formulation involves also moments external to the set. To overcome this closure problem, a particular class of MOM is used, called Quadrature Based Method of Moment (QMOM), in which the NDF is simplified with a quadrature approximation:

$$n^* \approx \sum_{i=1}^{N_q} w_i \delta[d_D - d_i] \tag{3.16}$$

Where N_q is the order of the approximation, w_i are the quadrature weights and d_i are the nodes or abscissas of the quadrature. Substituting Eq. (3.16) in Eq. (3.14) leads to:

$$M_k \approx \sum_{i=1}^{N_q} w_i d_i^k \tag{3.17}$$

And substituting the quadrature approximation of the moment of order k in Eq. (3.15):

$$\frac{\partial M_k}{\partial t} + \nabla \cdot (M_k U_D) = \sum_{i=1}^{N_q} w_i g(d_i) \left[\int_0^\infty \beta(d_D, d_i) d_D^k dd_D - d_i^k \right] \tag{3.18}$$

Where the integral between square brackets is analytically solved, once Eq. (3.12) is substituted into the term in square brackets of Eq. (3.18), resulting in:

$$\int_0^\infty \beta(d_D, d_i) d_D^k dd_D = \frac{3240 d_i^k}{(k+9)(k+12)(k+15)} \tag{3.19}$$

Turning integrals of the NDF moments transport equations into summations, the QMOM approach eliminates the closure problem, once a method for obtaining the quadrature nodes and weights is adopted.
In this work, the quadrature nodes and weights are obtained from the first 6 moments $(M_0, M_1, \dots, M_5)$ of the NDF using the well-known Product-Difference algorithm, as described by Marchisio & Fox, (2010).

3.4 Numerical solution procedure

In this work, the QMOM approach implemented in OpenFOAM as described by Buffo et al., (2013) and by Buffo, et al., (2016) was adopted in conjunction with a modified version of the OpenFOAM 5.0 solver `twoPhaseEulerFoam`. Six NDF moments were transported, resulting in three quadrature nodes and three weights. The fluid dynamics governing equations presented in Section 3.3 were solved with the default OpenFOAM merged PISO-SIMPLE algorithm (PIMPLE), detailly described by Passalacqua & Fox, (2011).

The time-dependent solution of the CFD equations and the PBM was obtained through two different strategies, called weak coupling (WC) and offline coupling (OC).

The WC strategy was already described by Gao et al., (2016). Two different time scales were calculated, a mixing scale defined as the ratio between the turbulent kinetic energy and the turbulent dissipation rate, and a characteristic breakage time, defined as the inverse of the breakup frequency, g. The time scale analysis revealed that mixing is at least one order of magnitude faster than breakage and the time scale ratio was used to define the WC. For each second of simulated time, the fluid dynamics equations fully coupled with the PBM were solved for just 0.1s of simulated

time. During this time, the following iterative strategy was adopted: the disperse phase volume fraction and the turbulence model equations were solved, the Product-Difference algorithm was then applied with the initial NDF moments, thus allowing the solution of Eq. (3.18). The calculation of the actualized moments resulted in a new value for the Sauter mean diameter, used to update the interphase momentum exchange and then solve the momentum balance and the continuity equations.

The WC results from the fact that during the remaining 0.9s of simulated time, just the PBM equations were solved in a stationary frozen flow-field. After that, the whole procedure was repeated for another second of simulated time.

With the OC strategy, on the other hand, the PBM equations are solved to convergence in a stationary frozen flow-field. In the following simulated time, just the moments are transported until the Sauter mean diameters, monitored in several sampling points in the tank volume, reach a stationary value.

The rotation of the impeller was accounted for with the so-called Multiple Reference Frame approach (MRF) and the boundary conditions and numerical schemes used for each variable are reported in Tab. 3.1 and Tab. 3.2, respectively.

3.5 Grid convergence study

The tank geometry was built with ANSY*S* Design-Modeler, three different structured meshes with hexahedral elements were generated with ANSY*S* ICEM to evaluate the grid convergence of the solution (Roache, 1998).

Tab. 3.1 – Boundary conditions used in the simulations

Variable	Wall Boundary conditions
α_D	Zero Gradient
ε	Zero Gradient
k	Zero Gradient
M_k	Zero Gradient
P	Zero Gradient
$\boldsymbol{u_D}, \boldsymbol{u_C}$	No Slip

Tab. 3.2 – Numerical schemes used in the simulations

Term	Configuration
$\partial/\partial t$	Euler explicit
$\nabla\psi$	cellMDLimited Gauss Linear 0.5
$\nabla\cdot(\boldsymbol{u_D}\alpha_D)$	Gauss vanLeer01
$\nabla\cdot(\boldsymbol{u_C}\alpha_C k)$	Gauss linearUpwind
$\nabla\cdot(\boldsymbol{u_C}\alpha_C \varepsilon)$	Gauss linearUpwind
$\nabla\cdot(\alpha\boldsymbol{uu})$	Gauss limitedLinearV 1
$\nabla\cdot(\boldsymbol{u_D}M_k)$	Gauss upwind
$\nabla^2\psi$	Gauss linear limited 1
ψ_f	linear
$\nabla^\perp\psi$	limited 1

ψ is the generic variable, f denotes the face interpolation operator, $\nabla^\perp$ is the surface normal gradient.

The number of elements of the three meshes, named G1, G2 and G3, was 5.5×10^6, 2.2×10^6 and 0.60×10^6, respectively, resulting in a refinement ratio of 1.45, calculated on the spacing between the grid nodes of the impeller blades ($h_1 = 0.83\ mm$ for G1, $h_2 = 1.10\ mm$ for G2 and $h_3 = 1.60\ mm$ for G3).

A set of *k*-ε single-phase simulations with the three grids was performed and the grid convergence of the solution was evaluated considering the power number, $N_P = P_\varepsilon/\rho_C N^3 D^5$, of the RT at *N* equal to 500rpm, corresponding to a rotational Reynolds number of 4.9×10^4. The impeller power consumption, P_ε, was calculated from the integral of the turbulent dissipation rate over the vessel volume. Underestimations in the prediction of ε result in the underestimation of the breakage rate, for this reason the convergence of the grid based on the turbulent dissipation rate was studied. The value of N_P for a similar impeller is expected to be 5, while the values obtained with the three grids are 4.86 for G1, 4.60 for G2 and 3.71 for G3. The power numbers obtained with the three grids from the torque on the moving walls are 5.09 for G1, 5.05 for G2 and 4.78 for G3. As already found by Coroneo et al. (2011), the power number obtained from the integral of the pressure difference over the front and back of the blades is almost grid independent even with a relatively coarse grid.

For the three grids, the grid convergence index, GCI, (Coleman & Stern, 1997) is 2.79% for G1, 9.48% for G2 and 34.06% for G3, as can be seen in Fig. 3.1, this results in a Richardson extrapolation of N_P equal to 4.97, very close to the experimental value.

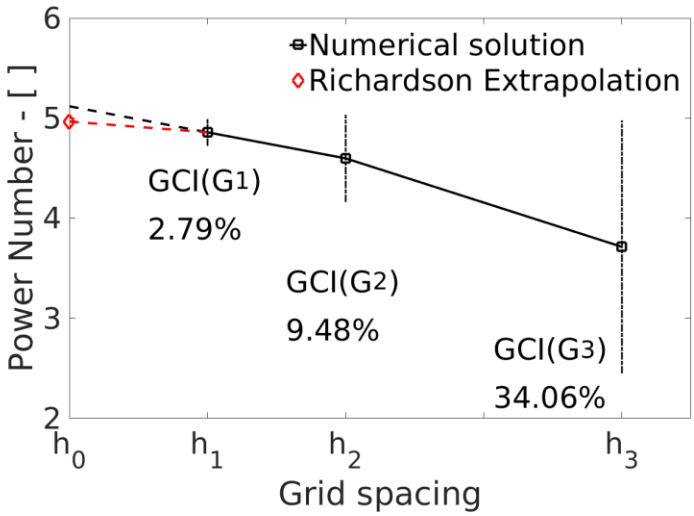

Fig. 3.1 – GCI and Richardson extrapolation for the three grids considered.

3.6 Comparison between Weak and Offline Coupling

The Weak Coupling (WC) and the Offline Coupling (OC) were tested with the coarsest grid G3. The simulation was initialized with the dispersed phase homogeneously distributed inside the volume as droplets of constant diameter equal to 700μm.

The simulation was run with the WC between the CFD and the PBM equations until the fluid dynamic reached the steady state, after approximately 460s of simulated time. Subsequently, the PBM was solved in a frozen flow field by means of the OC. The simulation was stopped after around 25,000s of simulated time, after the Sauter mean diameters monitored in several positions inside the volume reached a constant value of 47.9μm. The simulation with the Weak Coupling between CFD and PBM equations was run for other 100s of simulated time, reaching about 560s

of total simulated time and the time evolution of the Sauter mean diameter as obtained with the WC and the OC was compared to quantify the deviations between the two coupling strategies. In Fig. 3.2, the time evolution of the Sauter mean diameter monitored just below the shaft, as obtained with the WC and the OC between the CFD and the PBM equations is reported, for the first 2,000s of simulated time.

The maximum deviation of the Sauter mean diameter obtained with the OC strategy is about 0.5% of the diameter as obtained with the WC. Given the enormous differences in term of computational time and the overall agreement between the two strategies, just the OC was considered in the remaining part of this study.

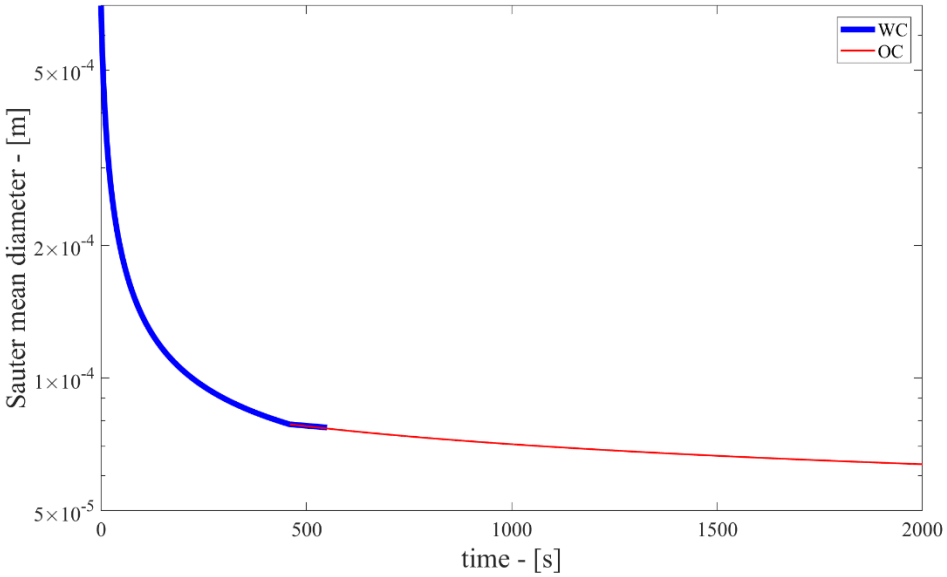

Fig. 3.2 – Time evolution of the Sauter mean diameter monitored just below the shaft, as obtained with the WC and the OC between the CFD and the PBE.

3.7 Results

3.7.1 Analysis of the two-phase turbulent field

Being the turbulent variables paramount in the determination of the breakup frequency, the turbulent velocity field of the continuous phase obtained from the

numerical simulations was examined considering the results of the PIV measurements and compared with experimental data from the literature.

The two-phase PIV measurements showed that the seeding particles and the droplets velocity fields can be well discriminated adopting light filters and that the mean velocities of water and droplets perfectly overlap. Clearly, under the agitation conditions selected for achieving complete droplet dispersions, the droplets and the seeding particles have similar relaxation time and slip velocities, therefore they both follow the continuous phase very closely. For this reason, just the analysis of the continuous phase mean velocity and turbulent characteristics will be considered in this study. Since the diesel fuel volume fraction in the system was very low and the droplets diameters were in the order of tens of micrometers, the first step was to confirm that the dispersed phase had a negligible effect on the continuous phase.

The continuous phase flow field was measured in single phase conditions (SP), with the stirred tank filled with water only, and in two-phase conditions (TP), with 0.1vol% of diesel fuel in water.

Selected axial profiles of the mean and fluctuating velocity components of water measured in TP conditions are shown in Fig. 3.3 and in Fig. 3.4 respectively at different radial coordinates. The velocity components are divided by $v_{tip} = \pi ND$ to make them dimensionless. As expected, Fig. 3.3 shows that the averaged velocity profiles of water with and without dispersed phase almost perfectly overlap.

Negligible differences are also visible for the root mean square (*RMS*) velocity fluctuations of the continuous phase with and without droplets. As can be observed in Fig. 3.4, the profiles at $r/T = 0.22$ perfectly overlap, whereas at $r/T = 0.43$ the water fluctuations in the presence of diesel fuel are around 7% higher than the fluctuations measured with just water.

Having proved that in these operating conditions the presence of the dispersed phase affects both the mean and the turbulent velocity field of the continuous phase significantly less than 10%, the detailed determination of the turbulent dissipation rate was not performed in this work, being the validation of the turbulent flow field possible using single-phase data collected in previous works.

Sharp & Adrian, (2001) studied small scales flow structures by means of PIV in a system similar to the one used in this work. Baldi, et al., (2004) performed a PIV study to determine the turbulent dissipation rate in a tank stirred with a Rushton impeller position at an off-bottom clearance of *T*/3.

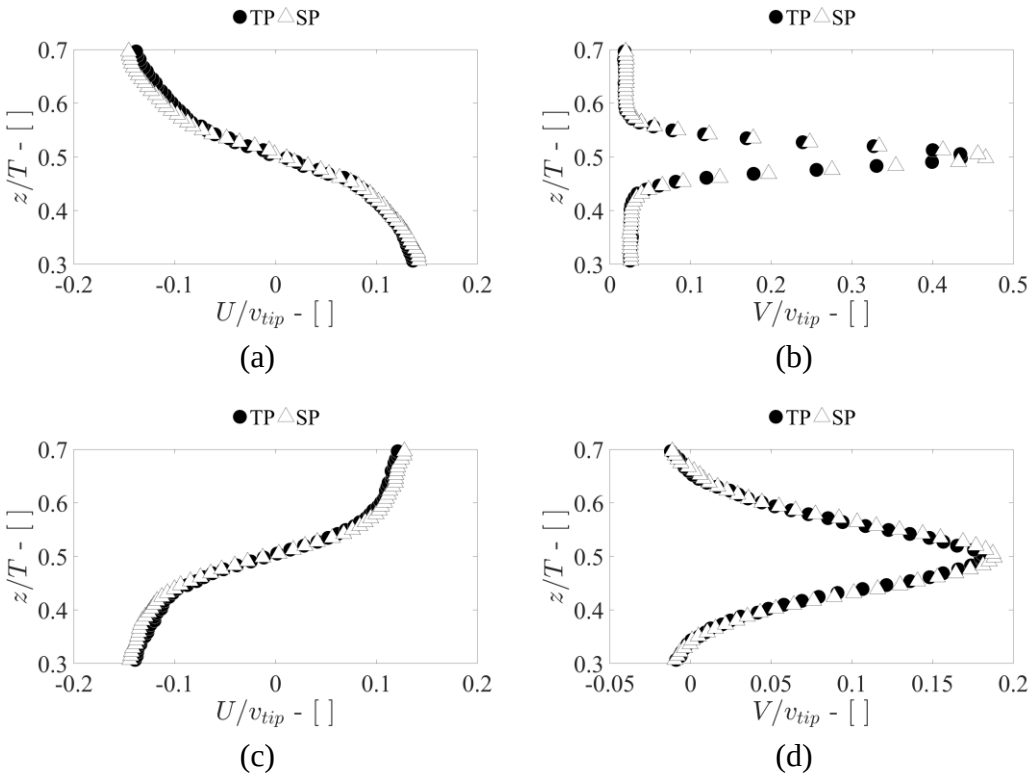

Fig. 3.3 - Axial profile of single-phase (SP) and two-phase (TP) axial (U) and radial (V) non-dimensional average velocities of water. Data are obtained on a plane midway two consecutive baffles at a dimensionless radial coordinate of r/T = 0.22 (a) and (b) and r/T = 0.43 (c) and (d).

Yeoh, et al., (2004) performed RANS and LES studies with a sliding/deforming mesh approach and reported instantaneous and averaged results, while Delafosse, et al., (2008) compared fluctuating and turbulent variables from unsteady RANS simulations and LES simulations with PIV experiments from Escudié & Liné, (2003) and Ducci & Yianneskis, (2005), obtained with an off-bottom clearance of $T/3$.

In Fig. 3.5, data from these authors are shown, along with data collected in the present work with the G1 grid, in terms of non-dimensional turbulent dissipation rate radial profile, collected at an axial coordinate corresponding to the center of the impeller blade. Radial profiles of ε obtained from RANS simulations were not reported in the work by Yeoh et al., (2004).

Fig. 3.5 clearly shows that RANS simulations fail in reproducing the non-monotonic profile of the turbulent dissipation rate along the radial coordinate. The

turbulent dissipation rate predicted in this work compares acceptably with the results from the literature, especially in terms of trend, where the slope of the ε profile closely matches the slope obtained by Delafosse et al., (2008) with RANS simulations and the slope obtained by Yeoh et al., (2004) with LES simulations, the latter just after $r/T = 0.2$.

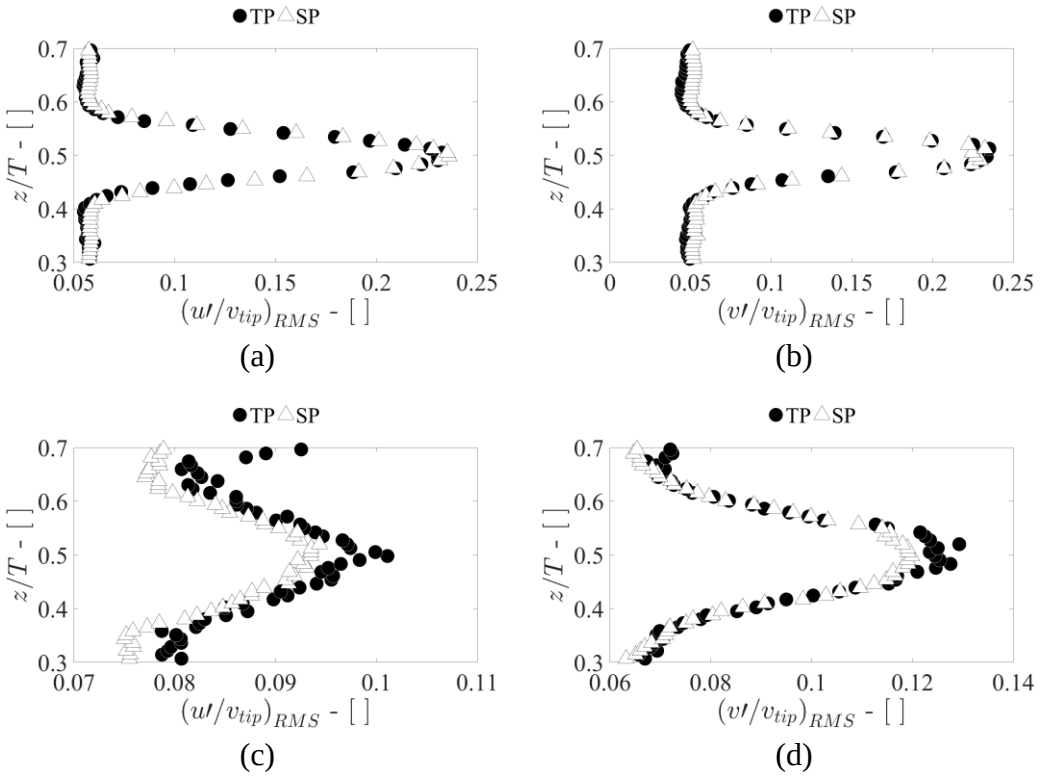

Fig. 3.4 – Axial profile of single-phase (SP) and two-phase (TP) axial (u') and radial (v') non-dimensional RMS of the water fluctuating velocities. Data are obtained on a plane midway two consecutive baffles at a dimensionless radial coordinate of r/T = 0.22 (a) and (b) and r/T = 0.43 (c) and (d).

The simulation performed in this work agrees with the experimental results, within the limits of a factor of two.

Axial profiles of non-dimensional turbulent dissipation rate were also compared with the experimental data obtained from turbulent kinetic energy balance by Escudié & Liné, (2003) and they are shown in Fig. 3.6.

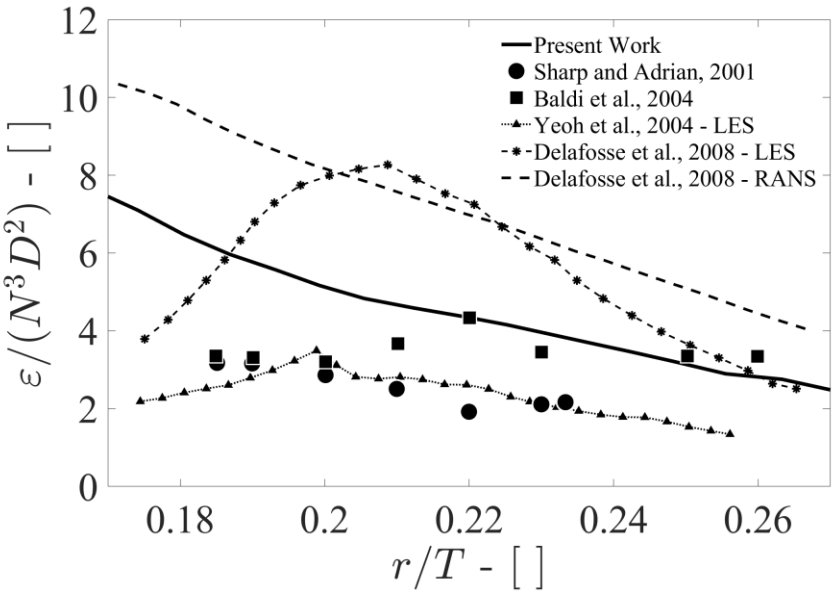

Fig. 3.5 – Comparison between numerical and experimental turbulent dissipation rate radial profiles from the literature and the present work results. Data are collected at an axial coordinate equal to the center of the impeller blade.

Data in Fig. 3.6 are shown in terms of a scaled axial coordinate centered in the midpoint of the impeller blade height and divided by the blade height, w, equal to 0.2D. Numerical results at $r/T = 0.20$ compare very well with the experimental profile, whereas the numerical simulation at $r/T = 0.22$ underpredicts the turbulent dissipation. RANS simulations are known to predict the maximum dissipation rate in the region behind the impeller blades and a monotonic decrease of the variable with the increasing radial coordinate. This monotonic behavior is not observed experimentally, where the maximum dissipation occurs at some distance from the impeller blade, in the discharge jet, that both Baldi et al., (2004) and Escudié & Liné, (2003) detected at $r/T = 0.22$.

In Fig. 3.6b it is possible to see the upward inclination of the discharge jet produced by the asymmetric axial position of the impeller that is observed both experimentally and numerically with LES simulations while it is not predicted with the RANS simulations.

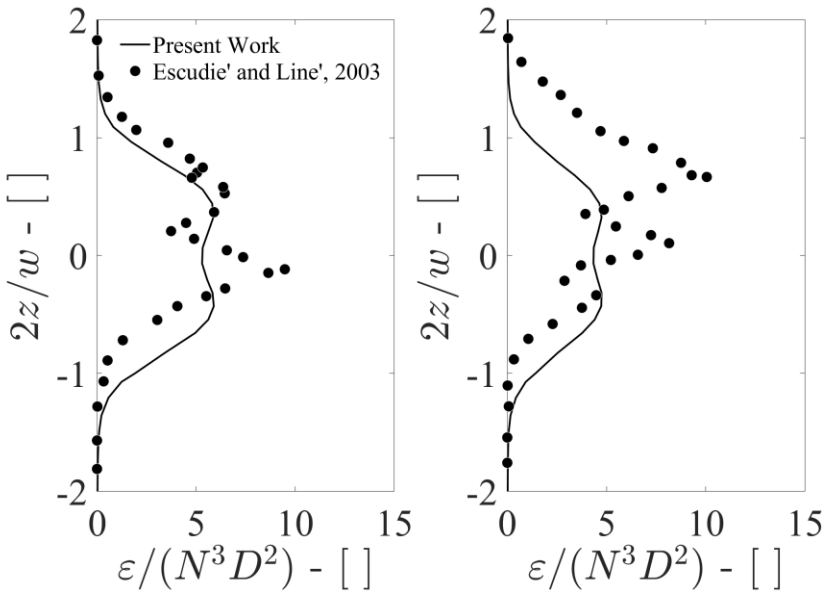

Fig. 3.6 – Non dimensional turbulent dissipation rate axial profiles obtained at a non dimensional radial coordinate of $r/T = 0.20$(a) and of $r/T = 0.22$(b).

The maximum value of the turbulence dissipation rate obtained with the simulations with the G1 grid was compared with the experimental data by Escudié & Liné, (2003), Baldi & Yianneskis, (2004), Ducci & Yianneskis, (2005) and with the RANS simulations of Delafosse et al., (2008), as already done by the latter author. Results are shown in Tab. 3.3, where the radial position of the maximum value is reported as well.

Tab. 3.3 – Maximum energy dissipation rate and its position as obtained from experimental and numerical works from the literature and the present work. Numerical data collected behind the impeller blades are reported within brackets.

	Escudié & Liné, (2003)	**Baldi & Yianneskis, (2004)**	**Ducci & Yianneskis, (2005)**	**Delafosse et al., (2008)**	**Present work**
$\frac{\varepsilon_{max}}{N^3D^2}$	14	10.5	9.4	11	(84) 10.2
r/T	0.22	0.224	0.225	0.16	(0.08) 0.17

The maximum turbulent dissipation rate obtained in this work is found at a non-dimensional coordinate of $r/T = 0.08$, that is located behind the impeller blades. The associated maximum non-dimensional turbulent dissipation rate is $\frac{\varepsilon_{max}}{N^3 D^2} = 84$ that is around 8 times higher than the value found in the experiments.

Excluding the zone behind the impeller blades (that is difficult to probe with optical techniques) a maximum value of 10.2 is measured, that is in fair agreement with the results from the literature. As already recalled, RANS simulations fail in predicting the non-monotonic profile of turbulent dissipation rate and its maximum value is therefore found at radial coordinates smaller than those experimentally measured.

Overall, despite the known limitations of the RANS approach with the MRF description of the impeller rotation, the averaged two-phase flow field and turbulent field results obtained with G1 are in good agreement with the single phase experimental and numerical results from the literature.

3.7.2 Analysis of the Drop Size Distribution

As explained in Section 3.2, an experimental campaign was performed to provide results with which validate the numerical data. Results on the DSD were collected at different impeller speeds, ranging from 500rpm to 800rpm.

Fig. 3.7 shows the experimental DSD obtained from triplicate measurements at N = 500 rpm, where the distribution probability is expressed in terms of volume fraction with respect to the total dispersed-phase volume in the sample.

The experimental measurements of the DSD show good reproducibility, as shown by the low standard deviations for each diameter category, that range from 1.4×10^{-4} to 3.8×10^{-3}. The corresponding coefficients of variations for each diameter category range from 0.8% to 23.4% for the droplets with average diameters equal to 8.00×10^{-5} m and to 1.47×10^{-4} m respectively. The experiments confirmed that the size of the droplets is of the order of tens of micrometers and that the DSD is relatively narrow. The experimental DSD is then used to validate the numerical results obtained with the modelling procedure described in Section 3.3.

Since the experiments provided the DSD of the droplets in the sample, a method to reconstruct the NDF in the postprocessing calculations was used.

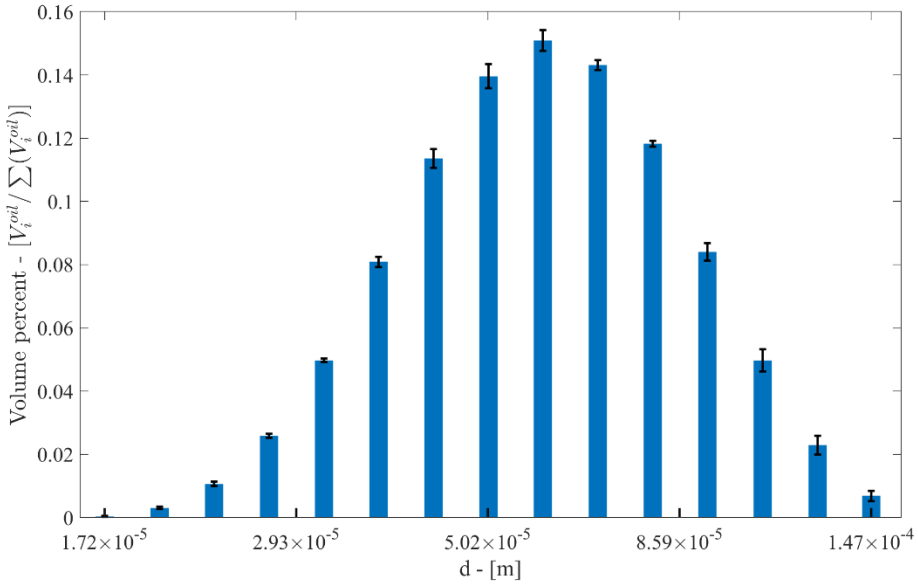

Fig. 3.7 – Experimental DSD obtained from triplicate measurements at N = 500rpm and error bars in terms of standard deviations

The EQMOM with a gamma distribution as a kernel density function was used, in the postprocessing stage, to obtain the continuous DSD from the moment set available from the calculation (Marchisio & Fox, 2010). The results obtained with the coarsest mesh G3 are shown in Fig. 3.8.

The DSD is obtained through an average over the volume enveloped by the square toroid generated through a rotation around the tank axis of the rectangular sampling position described in Section 3.2. Having described the rotation of the impeller with the simplified MRF approach, this averaging procedure was adopted in order to obtain data at different blade-baffle relative positions. The DSD obtained from the simulation was discretized in the same diameter bins used in the experimental DSD, for an easier comparison. The DSD is expressed in terms of volume fraction, to match the experimental data. Despite an underestimation of the power consumed by the impeller, P_ε, the DSD from the simulation is in acceptable agreement with the experimental one.

A numerical Sauter mean diameter of 47.9μm was obtained whereas the experimentally measured diameter was equal to equal to 47.6μm. Since an underestimation of the turbulent dissipation rate would lead to larger droplets, having found a

numerical Sauter mean diameter in very good agreement the experimental one suggests that the set of parameters used in the breakage kernel, Eq. (3.13), is not optimized for very fine grids.

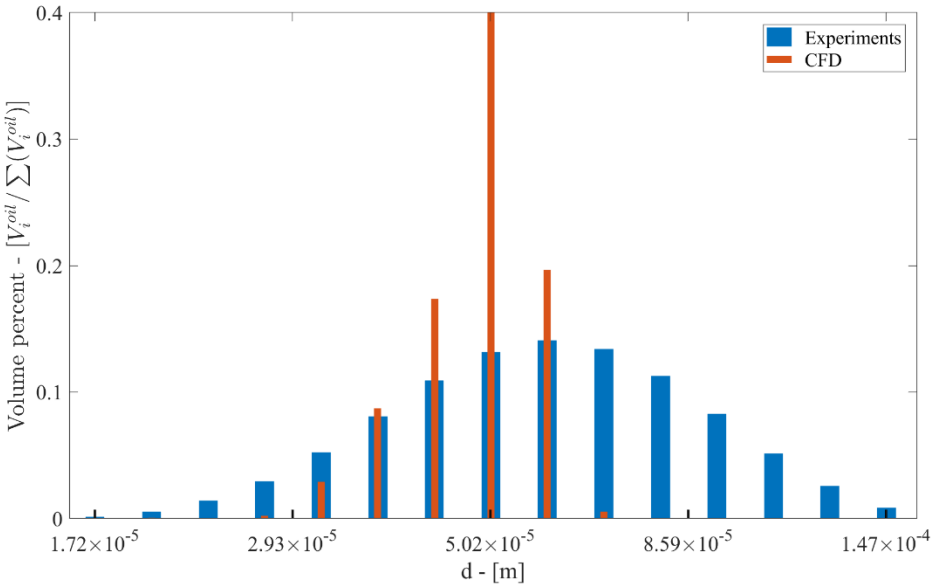

Fig. 3.8 – Comparison between experimental and numerical DSD as obtained with the G3 grid.

The DSD as obtained with the simulation with the finest grid G1 was calculated as well, with the same procedure described above for G3, and it is shown in Fig. 3.9. As expected, in this case a lower Sauter mean diameter of 31.7µm was obtained in the sampling volume since the volume integral of the turbulent dissipation rate was higher, as shown in Section 3.5.

These results confirm the importance of the computational grids on the prediction of the turbulent variables and their subsequent effects on the outcome variables. Although the underprediction of the turbulent dissipation rate can be compensated with an adjustment of the set of parameters of the breakage kernel, the selection of their values results in a loss of fully predictive capabilities of the simulations.

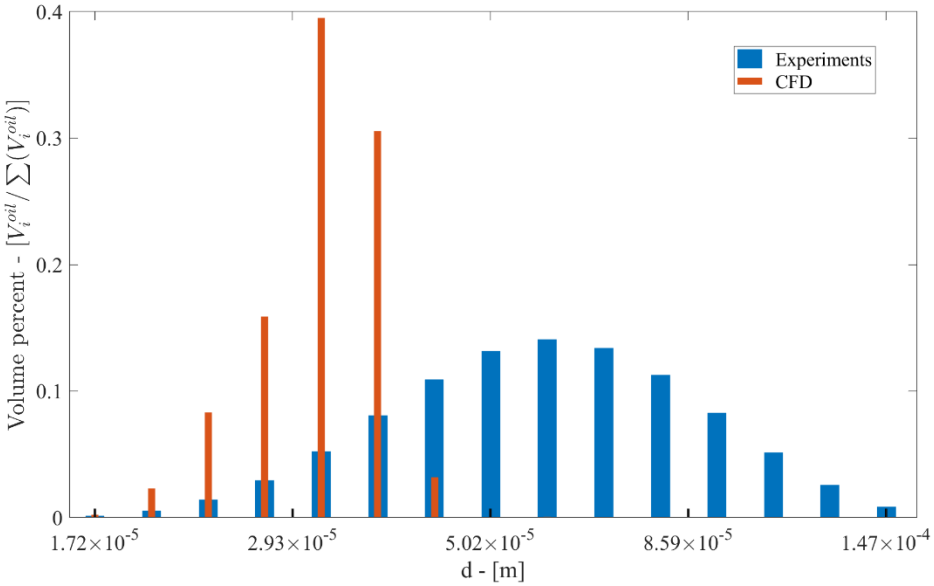

Fig. 3.9 - Comparison between experimental and numerical DSD as obtained with the G1 grid.

3.8 Discussion

As already mentioned, the numerical DSD is obtained through an average over the volume enveloped by the square toroid generated through a rotation around the tank axis of the rectangular sampling position described in Section 3.2, and shown in Fig. 3.10. The turbulent dissipation rate generated by the two grids is also shown in Fig. 3.10 on a plane midway two consecutive baffles. As expected, the spatial distribution of turbulent dissipation rate is remarkably inhomogeneous, and the highest values are limited in the proximity of the impeller.

Large differences are found between the two predictions and the ratio of the average turbulent dissipation rate over the volume enveloped by the square toroid as predicted by the two grids is:

$$\varepsilon(G1)\Big/_{\varepsilon(G3)} \approx 0.077\Big/_{0.065} = 1.20 \tag{3.20}$$

which is very close to the ratio of the power numbers obtained from P_ε:

$$N_P(G1)\Big/_{N_P(G3)} \approx 4.86/_{3.71} = 1.31 \tag{3.21}$$

This result confirms that correcting the turbulent dissipation rate inside the breakage kernels with the ratio of the power number obtained from the simulation and the experimental power number may be a workable approach to avoid long computational time. On the other hand, this correction holds when the parameters in the kernels are optimized for the system in exam.

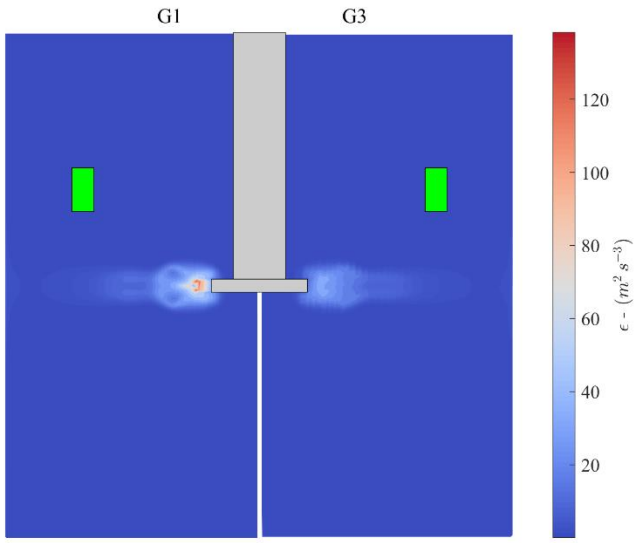

Fig. 3.10 – Comparison between the turbulent dissipation rate field generated with the G1 grid (left) and the G3 grid (right) on a plane midway two consecutive baffles. In green, the section of the square toroid corresponding to the sampling zone.

In Fig. 3.11, the breakup frequency on a plane between two consecutive baffles, as obtained with G1 right after the fluid dynamics inside the system reached the steady state (after approximately 75s), is reported, and in these conditions, the average Sauter mean diameter was of the order of 100μm.

The breakup frequency decreases as the diameter decreases. Since the simulations predict a DSD shifted towards diameters that are smaller than those measured

experimentally, Fig. 3.11 shows the breakup frequency calculated at 75s, when the diameter is larger than the one experimentally measured.

Having found that the breakup frequency is significant just where ε is high, an alternative procedure to derive the breakup kernel parameters would require to optimize their value on a fine grid, where the turbulent variables are more accurately predicted, and then, when solving the PBE on a coarser grid, applying the correction proposed by Gao et al., (2016).

Since for this system the breaking events are meaningful just in the proximity of the impeller, as shown in Fig. 3.11, the correcting factor should be derived from the ratio of the ε volume average obtained either in a region close the impeller or as the ratio of the maximum ε in the system.

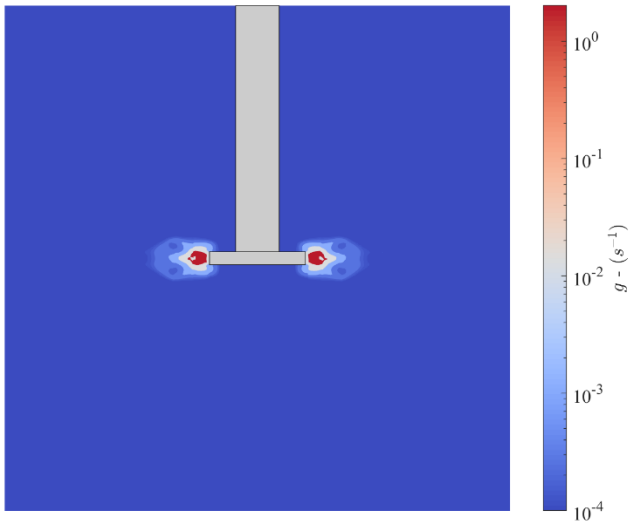

Fig. 3.11 – breakup frequency on a plane midway two consecutive baffles obtained with G1 after 75s of simulated time, when the Sauter mean diameter was of the order of 100μm.

In those scenarios the correcting factors for our system would be:

$$\varepsilon_{impeller}(G1) \Big/ \varepsilon_{impeller}(G3) \approx 24.30 \Big/ 15.16 = 1.60 \tag{3.22}$$

$$\varepsilon_{max}(G1)\Big/_{\varepsilon_{max}(G3)} \approx {}^{291.6}\Big/_{85.2} = 3.42 \tag{3.23}$$

As known, the grid has a non-linear effect on the turbulent dissipation rate and with G3 it is underestimated by 16% in the bulk, by 38% around the impeller and by 71% of the peak maximum value, with respect to G1.

The spatial distribution of the breakage frequency in a stirred tank was already numerically studied by Vonka & Soos, (2015) that stated that "*even a small zone around the impeller can have a significant impact on the DSD*". In their analysis they used a 316,803 elements mesh and found a $\varepsilon_{max}/\langle\varepsilon\rangle$ value of 290 (with $\langle\varepsilon\rangle$ being the volume average of the turbulent dissipation rate) obtained with a $k-\varepsilon$ model with the physical properties of the mixture, that compared well with the value of $\varepsilon_{max}/\langle\varepsilon\rangle = 550$ obtained for a similar system in a previous work with a LES simulation and a 1.6 million elements mesh (Soos, et al., 2013).

The value of $\varepsilon_{max}/\langle\varepsilon\rangle = 550$ agrees with our value of $\varepsilon_{max}/\langle\varepsilon\rangle = 387$ obtained with G1 (the grid with 5,500,000 elements). However, Soos et al., (2013) reported that the power number calculated as the integral of the turbulent dissipation rate on the whole tank volume was underpredicted with respect to the values in the literature, pointing to the fact that the turbulent field may, in fact, have been underpredicted, even with a 1.6 million elements mesh.

The fact that the breakage occurs in the proximity of the impeller and that the droplets are then dispersed in the whole volume is confirmed also by the spatial distribution of the Sauter mean diameter, shown in Fig. 3.12. The Sauter mean diameter is rapidly obtained as the ratio of the third and the second transported moments of the NDF.

Indeed, the diameters range is very narrow despite the large inhomogeneities in the turbulent dissipation rate field, and the color scale in Fig. 3.12 was expanded to highlight this. Moreover, the droplets in the proximity of the impeller, approximately in the same region where the breakup frequency is higher, are almost imperceptibly but consistently smaller than in the bulk of the tank. This result is a further indication that the correction on the turbulent dissipation rate, which is necessary when using coarse grids that underestimate the turbulent variables, should be based on local quantities rather than volume averaged ones.

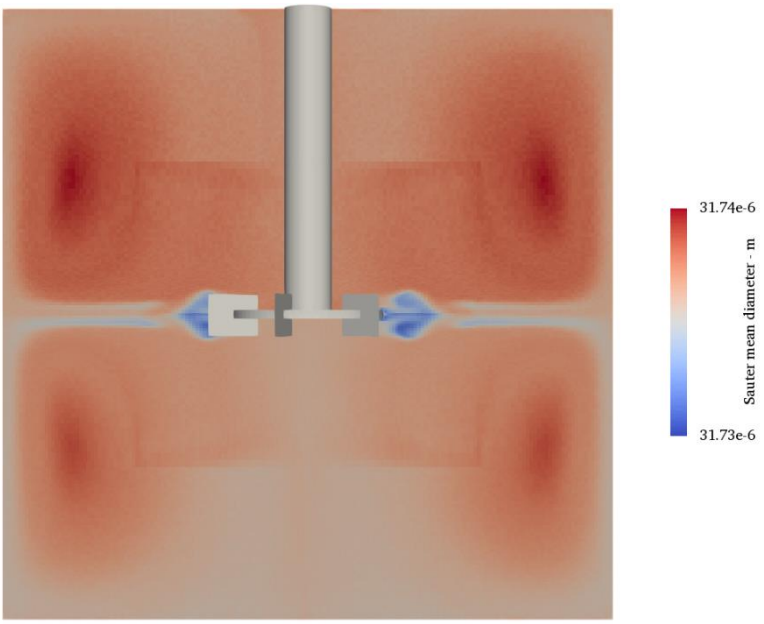

Fig. 3.12 – Sauter mean diameter on a plane between two consecutive baffles, as obtained with G1

3.9 Conclusions

In this work, RANS Eulerian-Eulerian simulations coupled with a PBM for the determination of the DSD of diesel fuel in water in a mechanically stirred tank were run in OpenFOAM. The PBM was solved in the simplified case of negligible coalescence phenomena with the QMOM strategy and the resulting DSDs were compared to experimental data collected from *ad hoc* experiments.

PIV data confirmed that the dispersed phase has a very limited effect on the average and fluctuating velocities of the continuous phase, in these operating conditions.

The turbulent flow field was compared with experimental and numerical single-phase results from the literature and an acceptable agreement was found, despite the well-known limitations of the RANS and the MRF modelling techniques.

The analysis of the Sauter mean diameters and the local DSDs revealed that the simulations underpredict the size of the droplets, suggesting that the parameters of

the breakage kernel found in the literature for similar systems are not optimized for the case under study.

Different computational grids were tested, to explore the effects of the different prediction of the turbulent variables on the numerical results. The adoption of a fine grid that satisfactorily predicted the average turbulent dissipation rate field resulted in a larger underprediction of the DSD, with respect to a coarser grid, meaning that grid effects are relevant and need to be properly addressed before the analysis of the results.

In the discussion section, the turbulent dissipation rate field and the related breakage phenomena were analyzed, confirming the well-known results that relevant inhomogeneities are found in the stirred tank and that the turbulent dissipation rate and the breakup frequency are order of magnitude higher in the proximity of the impeller than in the bulk.

A way to deal with the grid effects is hypothesized, adopting the scalar correction for the turbulent dissipation rate in the breakup kernel proposed by Gao et al., (2016) and deriving it from local quantities rather than volume averaged ones.

3.10 Acknowledgments

We acknowledge the CINECA award under the ISCRA initiative, for the availability of high performance computing resources and support.

3.11 Nomenclature

$\boldsymbol{A_C}$	Continuous phase acceleration due to body forces
$\boldsymbol{A_{CD}}$	Continuous phase acceleration due to phase interaction
$\boldsymbol{A_D}$	Dispersed phase acceleration due to body forces
$\boldsymbol{A_{DC}}$	Dispersed phase acceleration due to phase interaction
C	Off-bottom clearance
C_1, C_2, C_3	Alopaeus breakage kernel parameters
$C_{1\varepsilon}, C_{2\varepsilon}, C_\mu$	$k-\varepsilon$ turbulence model parameters
C_D	Drag coefficient
d_D	Drop diameter
d_i	Nodes of quadrature
D	Impeller diameter
$\boldsymbol{E}$	Rate of deformation
$\boldsymbol{F}_{drag,CD}$	Interphase drag force
$\boldsymbol{g}$	Gravity vector
g	Breakup frequency
$G1, G2, G3$	Finest, intermediate and coarsest grid used for the simulations
G_C	Continuous phase rate of change of ξ_C due to continuous processes
G_D	Dispersed phase rate of change of ξ_D due to continuous processes
h_1, h_2, h_3	G1, G2 and G3 spacing of the nodes on the impeller blade
H_L	Liquid height
H_T	Tank height
k	Turbulent kinetic energy
M_k	Reduced NDF moment of order k
n	Number density function
n^*	Reduced number density function
N	Impeller rotational speed
N_p	Power number
P	Pressure
P_ε	Impeller power consumption from the volume integral of ε
r	Radial coordinate
Re	Reynolds number
Re_p	Particle Reynolds number
$\boldsymbol{S}$	NDF discontinuous changes due to discrete events
$\boldsymbol{S}^*$	Reduced NDF discontinuous changes due to discrete events
t	Time
T	Tank diameter

$\boldsymbol{u_C}$	Continuous phase velocity vector
$\boldsymbol{u_D}$	Dispersed phase velocity vector
u'_{RMS}	Continuous phase RMS of the fluctuating axial velocity
U	Continuous phase average axial velocity
$\boldsymbol{U_C}$	Local constant value of $\boldsymbol{u_C}$
$\boldsymbol{U_D}$	Local constant value of $\boldsymbol{u_D}$
v_{tip}	Impeller tip speed
v'_{RMS}	Continuous phase RMS of the fluctuating radial velocity
V	Continuous phase average radial velocity
w	Impeller blade height
w_i	Weights of quadrature
$\boldsymbol{x}$	Spatial coordinate vector
z	Axial coordinate

Greek letters

α_C	Continuous phase volume fraction
α_D	Dispersed phase volume fraction
β	Daughter distribution function
ε	Turbulent dissipation rate
$\langle\varepsilon\rangle$	Volume averaged turbulent dissipation rate
μ_C	Continuous phase dynamic viscosity
μ_D	Dispersed phase dynamic viscosity
μ_t	Turbulent viscosity
ξ_C	Internal coordinate of the continuous phase
ξ_D	Internal coordinate of the dispersed phase
Ξ_C	Local constant value of ξ_C
ρ_C	Continuous phase density
ρ_D	Dispersed phase density
σ	Interfacial tension
$\sigma_k, \sigma_\varepsilon$	$k-\varepsilon$ turbulence model parameters
$\boldsymbol{\tau_D}$	Dispersed phase viscous stress tensor
$\boldsymbol{\tau^t}$	Reynolds stress tensor
ψ	Generic variable

3.12 References

Afshar Ghotli, R., Raman, A. A. A., Ibrahim, S., & Baroutian, S. (2013). LIQUID-LIQUID MIXING IN STIRRED VESSELS: A REVIEW. *Chemical Engineering Communications*, *200*(5), 595–627. https://doi.org/10.1080/00986445.2012.717313

Alopaeus, V., Koskinen, J., I. Keskinen, K., & Majander, J. (2002). Simulation of the population balances for liquid–liquid systems in a nonideal stirred tank. Part 2—parameter fitting and the use of the multiblock model for dense dispersions. *Chemical Engineering Science*, *57*(10), 1815–1825. https://doi.org/10.1016/S0009-2509(02)00067-2

Azizi, F., & Taweel, A. M. Al. (2011). Turbulently flowing liquid–liquid dispersions. Part I: Drop breakage and coalescence. *Chemical Engineering Journal*, *166*(2), 715–725. https://doi.org/10.1016/j.cej.2010.11.050

Bakker, A., Haidari, A. H., & Oshinowo, L. M. (2001). Realize greater benefits from CFD. *Chemical Engineering Progress*, *97*(3), 45–53.

Baldi, S., Ducci, A., & Yianneskis, M. (2004). Determination of Dissipation Rate in Stirred Vessels Through Direct Measurement of Fluctuating Velocity Gradients. *Chemical Engineering & Technology*, *27*(3), 275–281. https://doi.org/10.1002/ceat.200401979

Baldi, S., & Yianneskis, M. (2004). On the quantification of energy dissipation in the impeller stream of a stirred vessel from fluctuating velocity gradient measurements. *Chemical Engineering Science*, *59*(13), 2659–2671. https://doi.org/10.1016/j.ces.2004.03.021

Basavarajappa, M., Alopaeus, V., Yoon, R.-H., & Miskovic, S. (2017). A high-order moment-conserving method of classes (HMMC) based population balance model for mechanical flotation cells. *Minerals Engineering*, *108*, 36–52. https://doi.org/10.1016/j.mineng.2017.01.015

Buffo, A., De Bona, J., Vanni, M., & Marchisio, D. L. (2016). Simplified volume-averaged models for liquid–liquid dispersions: Correct derivation and comparison with other approaches. *Chemical Engineering Science*, *153*, 382–393. https://doi.org/10.1016/j.ces.2016.07.032

Buffo, A., Marchisio, D. L., Vanni, M., & Renze, P. (2013). Simulation of polydisperse multiphase systems using population balances and example application to bubbly flows. *Chemical Engineering Research and Design*, *91*(10), 1859–1875. https://doi.org/10.1016/j.cherd.2013.06.021

Buffo, A., Vanni, M., & Marchisio, D. L. (2016). On the implementation of moment transport equations in OpenFOAM: Boundedness and realizability. *International Journal of Multiphase Flow*, *85*, 223–235. https://doi.org/10.1016/j.ijmultiphaseflow.2016.06.017

Coleman, H. W., & Stern, F. (1997). Uncertainties and CFD Code Validation. *Journal of*

Fluids Engineering, *119*(4), 795. https://doi.org/10.1115/1.2819500

Coroneo, M., Montante, G., Paglianti, A., & Magelli, F. (2011). CFD prediction of fluid flow and mixing in stirred tanks: Numerical issues about the RANS simulations. *Computers & Chemical Engineering*, *35*(10), 1959–1968. https://doi.org/10.1016/j.compchemeng.2010.12.007

De Bona, J., Buffo, A., Vanni, M., & Marchisio, D. L. (2016). Limitations of simple mass transfer models in polydisperse liquid–liquid dispersions. *Chemical Engineering Journal*, *296*, 112–121. https://doi.org/10.1016/j.cej.2016.03.070

Delafosse, A., Line, A., Morchain, J., & Guiraud, P. (2008). LES and URANS simulations of hydrodynamics in mixing tank: Comparison to PIV experiments. *Chemical Engineering Research and Design*, *86*(12), 1322–1330. https://doi.org/10.1016/j.cherd.2008.07.008

Derksen, J. J., & Van Den Akker, H. E. A. (2007). Multi-Scale Simulations of Stirred Liquid–Liquid Dispersions. *Chemical Engineering Research and Design*, *85*(5), 697–702. https://doi.org/10.1205/cherd06161

Di Miceli Raimondi, N., Prat, L., Gourdon, C., & Cognet, P. (2008). Direct numerical simulations of mass transfer in square microchannels for liquid–liquid slug flow. *Chemical Engineering Science*, *63*(22), 5522–5530. https://doi.org/10.1016/j.ces.2008.07.025

Drumm, C., Attarakih, M. M., & Bart, H.-J. (2009). Coupling of CFD with DPBM for an RDC extractor. *Chemical Engineering Science*, *64*(4), 721–732. https://doi.org/10.1016/j.ces.2008.05.041

Ducci, A., & Yianneskis, M. (2005). Direct determination of energy dissipation in stirred vessels with two-point LDA. *AIChE Journal*, *51*(8), 2133–2149. https://doi.org/10.1002/aic.10468

Escudié, R., & Liné, A. (2003). Experimental analysis of hydrodynamics in a radially agitated tank. *AIChE Journal*, *49*(3), 585–603. https://doi.org/10.1002/aic.690490306

Gao, Z., Li, D., Buffo, A., Podgórska, W., & Marchisio, D. L. (2016). Simulation of droplet breakage in turbulent liquid–liquid dispersions with CFD-PBM: Comparison of breakage kernels. *Chemical Engineering Science*, *142*, 277–288. https://doi.org/10.1016/J.CES.2015.11.040

Hounslow, M. J., Ryall, R. L., & Marshall, V. R. (1988). A discretized population balance for nucleation, growth, and aggregation. *AIChE Journal*, *34*(11), 1821–1832. https://doi.org/10.1002/aic.690341108

Hu, X., Passalacqua, A., & Fox, R. O. (2015). Application of quadrature-based uncertainty quantification to the NETL small-scale challenge problem SSCP-I. *Powder Technology*, *272*, 100–112. https://doi.org/10.1016/j.powtec.2014.11.030

Hulburt, H. M., & Katz, S. (1964). Some problems in particle technology. *Chemical Engineering Science*, *19*(8), 555–574. https://doi.org/10.1016/0009-2509(64)85047-8

Jaworski, Z., & Pianko-Oprych, P. (2002). Two-Phase Laminar Flow Simulations in a

Kenics Static Mixer. *Chemical Engineering Research and Design*, *80*(8), 910–916. https://doi.org/10.1205/026387602321143462

Jaworski, Zdzislaw, Pianko-Oprych, P., Marchisio, D. L., & Nienow, A. W. (2007). CFD Modelling of Turbulent Drop Breakage in a Kenics Static Mixer and Comparison with Experimental Data. *Chemical Engineering Research and Design*, *85*(5), 753–759. https://doi.org/10.1205/cherd06179

Kálal, Z., Jahoda, M., & Fořt, I. (2014). Modelling of the Bubble Size Distribution in an Aerated Stirred Tank: Theoretical and Numerical Comparison of Different Breakup Models. *Chemical and Process Engineering*, *35*(3), 331–348. https://doi.org/10.2478/cpe-2014-0025

Karimi, M., & Andersson, R. (2020). Stochastic simulation of droplet breakup in turbulence. *Chemical Engineering Journal*, *380*, 122502. https://doi.org/10.1016/j.cej.2019.122502

Khadem, B., & Sheibat-Othman, N. (2019). Modeling of double emulsions using population balance equations. *Chemical Engineering Journal*, *366*, 587–597. https://doi.org/10.1016/j.cej.2019.02.092

Khajeh Naeeni, S., & Pakzad, L. (2019). Experimental and numerical investigation on mixing of dilute oil in water dispersions in a stirred tank. *Chemical Engineering Research and Design*, *147*, 493–509. https://doi.org/10.1016/j.cherd.2019.05.024

Kumar, S., & Ramkrishna, D. (1996). On the solution of population balance equations by discretization—I. A fixed pivot technique. *Chemical Engineering Science*, *51*(8), 1311–1332. https://doi.org/10.1016/0009-2509(96)88489-2

Laakkonen, M., Alopaeus, V., & Aittamaa, J. (2006). Validation of bubble breakage, coalescence and mass transfer models for gas–liquid dispersion in agitated vessel. *Chemical Engineering Science*, *61*(1), 218–228. https://doi.org/10.1016/j.ces.2004.11.066

Lebaz, N., & Sheibat-Othman, N. (2019). A population balance model for the prediction of breakage of emulsion droplets in SMX+ static mixers. *Chemical Engineering Journal*, *361*, 625–634. https://doi.org/10.1016/j.cej.2018.12.090

Leng, D. E., & Calabrese, R. V. (2016). Immiscible Liquid-Liquid Systems. In S. M. Kresta, A. W. I. Etchells, D. S. Dickey, & V. A. Atiemo-Obeng (Eds.), *Advances in industrial mixing: a companion to the handbook of industrial mixing* (pp. 457–463). Hoboken, New Jersey: Wiley & Sons, Inc.

Li, D., Buffo, A., Podgórska, W., Marchisio, D. L., & Gao, Z. (2017). Investigation of droplet breakup in liquid–liquid dispersions by CFD–PBM simulations: The influence of the surfactant type. *Chinese Journal of Chemical Engineering*, *25*(10), 1369–1380. https://doi.org/10.1016/J.CJCHE.2017.01.014

Li, D., Gao, Z., Buffo, A., Podgorska, W., & Marchisio, D. L. (2017). Droplet breakage and coalescence in liquid-liquid dispersions: Comparison of different kernels with EQMOM and QMOM. *AIChE Journal*, *63*(6), 2293–2311. https://doi.org/10.1002/aic.15557

Maaß, S., Paul, N., & Kraume, M. (2012). Influence of the dispersed phase fraction on experimental and predicted drop size distributions in breakage dominated stirred systems. *Chemical Engineering Science*, *76*, 140–153. https://doi.org/10.1016/j.ces.2012.03.050

Marchisio, D. L., & Fox, R. O. (2010). *Computational models for polydisperse particulate and multiphase systems*. *Cambridge University Press* (Vol. 9780521858). Cambridge: Cambridge University Press. https://doi.org/10.1017/CBO9781139016599

McGraw, R. (1997). Description of Aerosol Dynamics by the Quadrature Method of Moments. *Aerosol Science and Technology*, *27*(2), 255–265. https://doi.org/10.1080/02786829708965471

Montante, G., Horn, D., & Paglianti, A. (2008). Gas–liquid flow and bubble size distribution in stirred tanks. *Chemical Engineering Science*, *63*(8), 2107–2118. https://doi.org/10.1016/j.ces.2008.01.005

Montante, G., Paglianti, A., & Magelli, F. (2012). Analysis of dilute solid–liquid suspensions in turbulent stirred tanks. *Chemical Engineering Research and Design*, *90*(10), 1448–1456. https://doi.org/10.1016/j.cherd.2012.01.009

Passalacqua, A., & Fox, R. O. (2011). Implementation of an iterative solution procedure for multi-fluid gas-particle flow models on unstructured grids. *Powder Technology*, *213*(1), 174–187. https://doi.org/10.1016/j.powtec.2011.07.030

Rieger, R., Weiss, C., Wigley, G., Bart, H.-J., & Marr, R. (1996). Investigating the process of liquid-liquid extraction by means of computational fluid dynamics. *Computers & Chemical Engineering*, *20*(12), 1467–1475. https://doi.org/10.1016/0098-1354(95)00232-4

Roache, P. J. (1998). *Verification and Validation in Computational Science and Engineering*. Hermosa Publishers, Albuquerque, New Mexico. Retrieved from http://www.hermosa-pub.com/hermosa

Sharp, K. V., & Adrian, R. J. (2001). PIV study of small-scale flow structure around a Rushton turbine. *AIChE Journal*, *47*(4), 766–778. https://doi.org/10.1002/aic.690470403

Soos, M., Kaufmann, R., Winteler, R., Kroupa, M., & Lüthi, B. (2013). Determination of maximum turbulent energy dissipation rate generated by a rushton impeller through large eddy simulation. *AIChE Journal*, *59*(10), 3642–3658. https://doi.org/10.1002/aic.14206

Tang, Q., Ye, S., Wang, Y., & Liu, Z. (2018). A study on liquid-liquid dispersions in a continuous mixer via computational fluid dynamics (CFD) simulation combined with population balance model (PBM). *The Canadian Journal of Chemical Engineering*, *97*(2), cjce.23361. https://doi.org/10.1002/cjce.23361

Vonka, M., & Soos, M. (2015). Characterization of liquid-liquid dispersions with variable viscosity by coupled computational fluid dynamics and population balances. *AIChE Journal*, *61*(8), 2403–2414. https://doi.org/10.1002/aic.14831

Wang, C. Y., & Calabrese, R. V. (1986). Drop breakup in turbulent stirred-tank contactors. Part II: Relative influence of viscosity and interfacial tension. *AIChE Journal*, *32*(4), 667–676. https://doi.org/10.1002/aic.690320417

Yeoh, S. L., Papadakis, G., & Yianneskis, M. (2004). Numerical Simulation of Turbulent Flow Characteristics in a Stirred Vessel Using the LES and RANS Approaches with the Sliding/Deforming Mesh Methodology. *Chemical Engineering Research and Design*, *82*(7), 834–848. https://doi.org/10.1205/0263876041596751

Zhang, J., Xu, S., & Li, W. (2012). High shear mixers: A review of typical applications and studies on power draw, flow pattern, energy dissipation and transfer properties. *Chemical Engineering and Processing: Process Intensification*, *57–58*, 25–41. https://doi.org/10.1016/j.cep.2012.04.004

Chapter 4

Solid-Liquid suspension in stirred tanks

This work is aimed at investigating the impact of different meso-scale models and constitutive equations for the RANS-based two-fluid model simulations of a turbulent solid-liquid stirred vessel with high solids loading. The model assessment is preceded with a grid convergence study, which confirms the variability of the discretization requirements depending on the observed variable. The simulation results demonstrate that for the investigated system the high solids loading contribution modelled by the kinetic theory of granular flows is negligible, both in incomplete and complete suspension conditions. Instead, the particle concentration fluctuations contribution included in the momentum equations dramatically affect the predictions, particularly in incomplete suspension conditions. The evaluation of the models is completed with the comparison of the predicted solids concentration profiles with experimental data measured by Electrical Resistance Tomography. The computational strategy for achieving realistic predictions of the solid distribution both in complete and incomplete suspension conditions is outlined.

4.1 Introduction

In the last 30 years, the role of Computational Fluid Dynamics (CFD) has become increasingly important as an aid both in fundamental research and in industrial design. On the other hand, the numerical simulation of several process problems is still not reliable enough, mostly owing to the lack of suitable CFD models (Liu, 2016). In this regard, solid-liquid suspensions in stirred tanks still pose several challenges. Solid-liquid systems are common in many process industries and the correct description of the related chemical reactions, mass and energy transfer phenomena is strongly linked to the proper prediction of the multiphase flow field and the particle distribution inside the equipment. Notably, the simulation of slurry stirred tanks is particularly complex due to the two-phase turbulence and the interphase interactions (Li et al., 2015). Additional complexity is found at increasing particle concentration, therefore the understanding gained so far on single phase and dilute solid-liquid systems cannot be extended to dense suspensions (Carletti et al., 2014).

This investigation concerns the simulation of solid distribution in a stirred tank in high solids loading and turbulent conditions, in the realm of the two-fluid model formulation of the Reynolds averaged Navier-Stokes (RANS) equations. As recently observed by Van den Akker (2015), this type of simulations is based on a huge number of modelling assumption and numerical issues. Nevertheless, RANS-based two fluid models are still the most affordable tool for investigating industrially relevant problems in complex geometries, large scale apparatus and high solids loading, therefore the improvement of their predictive capability attracts still significant research interest.

The Eulerian-Eulerian two fluid model including different closure relationships has been validated for dense solid-liquid stirred tanks in turbulent regime by various experimental data, including cloud height (e.g. Fletcher & Brown, 2009), just-suspended impeller speed (e.g. Xie & Luo, 2018), particle concentration distribution (e.g. Delafosse, et al., 2018; Kasat, et al., 2008; Liu & Barigou, 2013; Tamburini, et al., 2013; Wadnerkar, et al., 2016), liquid and solid velocities (e.g. Liu & Barigou, 2013; Wadnerkar et al., 2016). Of the different terms included in the momentum equation of the solid phases, the drag force and the turbulent dispersion force are generally the most significant. As for the drag force, the drag coefficient correlations

for single rigid spheres in still fluid have been usually adopted and the effects of hindered settling or of free stream turbulence were found to be either uninfluential or important depending on the investigated conditions. Also, the effect of the turbulent fluctuations of the solid volume fraction was either ignored or included alternatively in the continuity or in the momentum equation depending on the averaging procedure adopted for the equations derivation. Fletcher & Brown (2009) suggested the inclusion of both the drag and the turbulent dispersion forces and highlighted the need of valid formulations for dense solid-liquid stirred tanks. Kasat et al. (2008) included the turbulent dispersion force in the momentum equation and accounted for the turbulent effect on the drag coefficient via the Brucato et al. (1998) correlation. Liu & Barigou (2014) and Mishra & Ein-Mozaffari (2017) considered just the hindered settling effect on the drag law. Tamburini et al. (2014) found that the inclusion of the turbulent dispersion force and of the hindered settling effect can either improve or worsen the results depending on the operating conditions, while the inclusion of the Brucato drag correction was considered generally useful. Recently, Wadnerkar et al. (2016) and Xie & Luo (2018) suggested the adoption of the Granular version of the Eulerian momentum equation for the solid phase for a better prediction of dense solid-liquid stirred tanks. Unsatisfactory predictions of solid spatial distribution were reported by a similar set of model equations by Delafosse et al. (2018) for dense suspensions of light microcarriers particles. The granular model was found not applicable due to numerical issues in other investigations (Mishra & Ein-Mozaffari, 2017; Tamburini et al., 2013)

Overall, significant progresses have been recently made in the development of CFD methods for slurry stirred tanks and in their validation by comparison with experimental data collected in dense suspensions. Unique conclusions on models and constitutive equations to account for the prevailing physical mechanisms and on the reliability of the relevant numerical solution methods in predicting the suspension and the distribution of high concentration particles in stirred equipment are not achieved yet.

The Eulerian-Lagrangian approach has been employed in the study of solid-liquid mixing, alongside the Eulerian-Eulerian approach. With this approach, the force balance on each element of the disperse phase is solved and the fluid flow is solved with different resolution depending on the simulation method, i.e. direct numerical simulations (DNS), large eddy simulations (LES), RANS. The fluid flow resolved

spatial scale can be either in the same order of magnitude or smaller (fully resolved approach) than the characteristic size of the elements of the disperse phase (Tsuji, 2007). Fully resolved turbulent Eulerian-Lagrangian solid-liquid applications are usually limited to small scales and limited number of particles, due to the high computational cost (Ayranci et al., 2013; Derksen, 2003). With the unresolved CFD-DEM (Discrete Element Model) approach, the fluid flow is solved at scales coarser than the particle size, describing the particle-particle interactions with a DEM and coupling the two phases with explicit expressions of the interphase forces, such as drag, lift, wall lubrication (Blais et al., 2016; Zhu et al., 2007). Even though this approach allows to simulate denser suspensions with respect to the fully resolved approach, unresolved CFD-DEM models has seldom been used to assess partially suspended conditions (Blais, 2016).

Recently, Blais et al. (2017) studied the suspension curve of non-dilute concentration of glass particles in a stirred tank with a Large Eddy CFD-DEM approach, with the Rong drag law (Rong et al., 2013) and the Saffman-Mei lift force (Mei, 1992) as interphase forces. They were successful in reproducing the suspension curve and just-suspended speed obtaining good agreement with the experimental measurements obtained with the Pressure Gauge Technique, that were used to validate the code.

Li et al. (2018) performed particle-resolved simulations with Lattice- Boltzmann method of a a dense solid suspension in a stirred tank in transitional regime. The flow fields were fully resolved down to the flow scale around the particles and the suspension dynamics was simulated from the initial state to complete suspension conditions. The authors validated the numerical results with particle image velocimetry (PIV) experimental data finding a good agreement in terms of instantaneous and averaged solids distributions in the stirred tank, averaged liquid velocities and the turbulent fluctuation levels of the liquid.

In the following, the distribution of glass particles in water at agitation conditions below and above the just-suspended impeller speed, N_{js}, is considered. The simulation of the two-phase system starts from the solution of the RANS equations and the Eulerian description of both solid and liquid phases, including a Granular formulation of the momentum equation of the solid phase. The interplay of different particle-particle interactions, fluid-particle interaction and turbulence models is compared with the goal to reproduce the solid suspension and the solid concentration

distribution in the tank. The momentum exchange terms considered in this work are shown in Table 4.1 and they are detailed in Section 4.3.1.

Table 4.1 – Solid-Liquid interaction forces

	Model	**Eq.**
Turbulence	'Mixture' *k-ε* 'Mixture' Reynolds Stress model (RSM)	Eq. (4.2)
Fluid-particle	*Interphase Drag:*	
	Schiller & Naumann	Eq. (4.12)
	Wen & Yu	Eq. (4.15)
	Ergunn	Eq. (4.17)
	Turbulent dispersion:	
	Burns	Eq. (4.18)
	Lift force:	
	Moraga	Eq. (4.20)
Particle-particle	Kinetic theory of granular flows	Eq. (4.8)

The model predictions are presented by means of comparison of global variables and solids concentration profiles. Finally, the results are discussed using experimental observation and solid concentration data as a benchmark for the different models.

4.2 Investigated systems

The simulations concerned the same solid-liquid stirred tank experimentally investigated by Carletti et al. (2014). The vessel was cylindrical, flat bottomed with diameter, *T*, and height, H_T, equal to 0.232 m and 0.28 m, respectively. It was equipped with four equally spaced baffles of width equal to *T*/10. A single 6-blades 45° down-pumping pitched blade turbine (PBT) mounted on a central shaft was used to agitate the system. The diameter of the impeller, *D*, was equal to 0.078 m, corresponding to a *T/D* ratio equal to 3, and the off-bottom clearance, *C*, was a third of

the vessel diameter (T/C = 3). The water height, H_L, was always maintained at 0.25 m, corresponding to a total volume of 10.6 L.

Glass particles of narrow size distribution and mean diameters d_p equal to either 138 μm or 385 μm and density, ρ_S, equal to 2500 kg/m^3 were used. The liquid phase was demineralized water, which density, ρ_L, and viscosity, μ_L, were taken equal to 998 kg/m^3 and 0.001 Pa s respectively in the calculations. The experiments were carried out at room conditions at temperature of 20°C ± 3°C.

Two different cases were simulated among those investigated by Carletti et al. (2014), one well above and the other well below the N_{js} value determined by visual observation. The first case concerned the suspension of the glass particles of mean size equal to 138 μm and mass ratio, X_S, of 24%, corresponding to a mean solid volume fraction, $<\alpha_S>$, of 0.09. The solid-liquid system was stirred at the impeller rotational speed, N, of 900 rpm, that is much higher than the N_{js} value of 540 rpm estimated by visual observation. The second case concerned the suspension of the 385 μm particles at the impeller rotational speed of 500 rpm and mass ratio equal to 43%, corresponding to $<\alpha_S>$ of 0.15. The N_{js} value determined by visual observation in this case was equal to about 700 rpm. Both the complete and the incomplete suspension cases deal with dense suspensions, since the average solid-phase volume fraction is much larger than 10^{-3} (Balachandar & Eaton, 2010). The impeller Reynolds number based on the liquid phase properties is equal to 9×10^4 for the complete suspension and 5×10^4 for the incomplete suspension case.

For the two cases, experimental non-dimensional conductivity maps of the liquid-phase were collected by Electrical Resistance Tomography on four horizontal vessel sections located at the mean axial coordinates, $z_1 = 0.26T$, $z_2 = 0.47T$, $z_3 = 0.69T$ and $z_4 = 0.90T$ from the tank bottom. With respect to the investigation by Carletti et al. (2014), a number of sensor planes connected to the data acquisition system equal to four instead of two was available, thus the measurements were performed on the four planes simultaneously and the measurement uncertainties were reduced.

4.3 CFD simulations

4.3.1 Governing equations

The simulations were based on the two-fluid model equations written under incompressible, isothermal, steady state hypotheses. The solid phase continuity and momentum equations specifically solved in this work are:

$$\nabla \cdot (\alpha_S \rho_S \boldsymbol{u_S}) = 0 \tag{4.1}$$

$$\nabla \cdot (\alpha_S \rho_S \, \boldsymbol{u_S u_S}) = -\alpha_S \nabla P + \alpha_S \rho_S \boldsymbol{g} + \underbrace{\nabla \cdot \boldsymbol{\tau_S}}_{I} - \underbrace{\nabla P_S}_{\text{II}} + \underbrace{\boldsymbol{F}_{TD,S}}_{\text{III}} + \underbrace{\boldsymbol{F}_{drag,SL}}_{\text{IV}} + \underbrace{\boldsymbol{F}_{lift,S}}_{V} \tag{4.2}$$

where α_S is the volume fraction of the solid phase, ρ_S is its density, $\boldsymbol{u_S}$ is the solids mean velocity vector, P is the pressure, $\boldsymbol{g}$ is the gravity vector. On the right-hand side of the momentum equation of the solid phase, the stress term (I), the solid pressure gradient (II), the turbulent dispersion force (III), the interphase drag force (IV) and the lift force (V) require specific models.

The continuity and the momentum conservation equations for the liquid phase are in the same form, apart for the solid pressure gradient, that is nil for the liquid phase.

The stress tensor was divided into two contributions, the laminar viscous stress tensor $\boldsymbol{\tau_S}^{\boldsymbol{l}}$ and the Reynolds stress tensor $\boldsymbol{\tau_S}^{\boldsymbol{t}}$. For the latter, either the 'mixture' k-ε or the 'mixture' Reynolds Stress turbulence model (RSM) was used. In the so-called 'mixture' or 'homogeneous' multiphase turbulence models, the two phases are assumed to share the same turbulent variables, the turbulent model equations do not include any interphase turbulent transport term and the averaged physical properties of the solid-liquid mixture are adopted (e.g. Tamburini, et al., 2011). Other formulations of the multiphase turbulence models were not considered, mainly due to the lack of robust models to account for the interphase turbulent transfer particularly in the case of dense solid-liquid systems and based on the results of previous investigations (Fletcher & Brown, 2009; Tamburini et al., 2014). In the near wall region,

the so-called Standard Wall Function or the Enhanced Wall Treatment, as implemented in FLUENT v17.0, were selected depending on the computational grid size.

The interactions within the solid phase are included by the solid pressure gradient and the solid laminar viscous stress tensor, which formulation is based on the kinetic theory of granular flows, firstly introduced by Jenkins & Savage (1983). Both the solid pressure and the solid laminar viscous stress tensor depend on the granular temperature Θ_S, that is the kinetic energy associated with the particle velocity fluctuations and is calculated from the Boltzmann transport equation for the probability distribution of random particles motion.

In this work, the following Θ_S transport equation is adopted:

$$\frac{3}{2}\nabla\cdot(\rho_S\alpha_S\boldsymbol{u_S}\Theta_S) = (-P_S\,\boldsymbol{I} + \boldsymbol{\tau_S}):\nabla\boldsymbol{u_S} + \nabla\cdot\left(k_{\theta_S}\boldsymbol{\nabla}\Theta_S\right) + \phi_{LS} - \gamma_{\Theta_S} \tag{4.3}$$

where $\boldsymbol{I}$ is the identity tensor, k_{θ_S} is the granular diffusion coefficient, ϕ_{LS} is the kinetic energy exchanged between the liquid and the solid phase and γ_{Θ_S} is the collisional dissipation of energy due to inelastic collisions. For these last three terms, several constitutive equations exist in the literature and as default implementations both in the most common closed and open-source CFD codes (e.g. ANSYS FLUENT, OpenFOAM).

For the granular diffusion coefficient, the equation proposed by Syamlal et al. (1993) was selected, that reads:

$$k_{\theta_S} = \frac{15 d_p \rho_S \alpha_S \sqrt{\Theta_S \pi}}{4(41-33\,\eta)} \times \\ \times\left[1 + \frac{12}{5}\eta^2(4\eta-3)\alpha_S g_{0S} + \frac{16}{15\pi}(41-33\eta)\eta\alpha_S g_{0S}\right] \tag{4.4}$$

where e_S is the coefficient of restitution, $\eta = \frac{1}{2}(1+e_S)$, g_{0S} is the radial distribution function. The coefficient of restitution, accounting for the inelastic collisions between particles, was set equal to 0.9, that is a suitable value for glass beads (Lun et al., 1984).

The radial distribution function, g_{0S}, is an empirical function that goes to infinity when the solid volume fraction reaches its maximum value, thus preventing unphysical particles packing by driving the particle velocity to zero. It is defined as:

$$g_{0S} = \left[1 - \left(\frac{\alpha_S}{\alpha_{S,max}}\right)^{1/3}\right]^{-1} \tag{4.5}$$

where the solids volume fraction at the packing limit, $\alpha_{S,max}$, was set equal to 0.63, being the typical 'filling fraction' of randomly packed spheres of equal diameter.

The collisional dissipation, γ_{Θ_S} and the interphase exchanged kinetic energy, ϕ_{LS}, were modelled with the expression derived by Lun et al. (1984) and Ding & Gidaspow (1990), respectively, as:

$$\gamma_{\Theta_S} = \frac{12(1-e_S^2)g_{0S}}{d_p\sqrt{\pi}}\rho_S\alpha_S^2\Theta_S^{3/2} \tag{4.6}$$

$$\phi_{LS} = -\frac{9}{4}\frac{\alpha_S\rho_L}{d_p}C_D\|\boldsymbol{u_S} - \boldsymbol{u_L}\|\Theta_S \tag{4.7}$$

where C_D is the particle drag coefficient.

The solid pressure,P_S, was calculated as:

$$P_S = \alpha_S\rho_S\Theta_S[1 + 2(1+e_S)\alpha_S g_{0S}] \tag{4.8}$$

For the laminar solid phase stress, the following formulation was adopted:

$$\boldsymbol{\tau_S^l} = -P_S\boldsymbol{I} + \alpha_S\mu_S(\boldsymbol{\nabla u_S} + \boldsymbol{\nabla u_S}^T) + \alpha_S(\lambda_S - 2/3\mu_S)\boldsymbol{\nabla}\cdot\boldsymbol{u_S}\,\boldsymbol{I} \tag{4.9}$$

where μ_S is the solid shear viscosity and λ_S is the solid bulk viscosity.

The solid shear viscosity was calculated following Syamlal et al. (1993) as:

$$\mu_S = 0.5\sqrt{\Theta_S}\alpha_S d_p \rho_S \left\{\frac{\sqrt{\pi}}{3(3-e_S)}\left[1+\frac{2}{5}(1+e_S)(3e_S-1)\alpha_S g_{0S}\right]+ \right. \\ \left. +\frac{8}{5}\frac{\alpha_S g_{0S}(1+e_S)}{\sqrt{\pi}}\right\} \tag{4.10}$$

The bulk viscosity was calculated following Lun et al. (1984) as:

$$\lambda_S = 4/3\alpha_S^2 \rho_S d_p g_{0S}(1+e_S)\sqrt{\Theta_S/\pi} \tag{4.11}$$

Neglecting the solid pressure gradient and the laminar solid stress tensor reduces the two-fluid model equations including the kinetic theory of granular flows, namely the Eulerian-Granular model (E-G), to the classical two-fluid model equations, namely the Eulerian-Eulerian model (E-E). It is worth keeping in mind that the E-G constitutive equations have been derived under a number of assumptions which hold true for the flow of granular materials, where collisions are the principal transport mechanisms, as is the case of fluidized beds. The solid suspensions in stirred tanks hardly adhere to the same assumptions, but the adoption of the above equations is considered, since it was suggested in previous investigations of similar systems (Delafosse et al., 2018; Wadnerkar et al., 2016; Xie & Luo, 2018).

In the context of the two-fluid model, the coupling between the liquid and the solid flow fields is achieved by means of interaction forces between the solid and the liquid phase. In this work the drag, the turbulent dispersion and the lift forces were considered.

The interphase drag force is calculated as:

$$\boldsymbol{F}_{drag,SL} = \frac{3}{4}\frac{\alpha_S}{d_p} C_D \rho_L \|\boldsymbol{u_S} - \boldsymbol{u_L}\|(\boldsymbol{u_S} - \boldsymbol{u_L}) \tag{4.12}$$

where the drag coefficient, C_D, calculation requires a suitable correlation, depending on the particles Reynolds number, Re_p. In this work, the Schiller & Naumann, (1933) correlation was selected, that is:

$$C_D = 24 \times \frac{1+0.15Re_p^{0.687}}{Re_p} \tag{4.13}$$

where the particles Reynolds number is calculated as:

$$Re_p = \frac{||\boldsymbol{u_S} - \boldsymbol{u_L}||d_p\rho_L}{\mu_L} \tag{4.14}$$

Eq. (4.13) holds true for $1 < Re_p < 1000$ and single rigid spheres falling in a still fluid.

To account for the dense particle effects, a combination of the Wen & Yu (1966) correlation and of the Ergun (1952) correlation was proposed by Gidaspow (1994) to describe the drag force in dense fluidized beds. If the local liquid volume fraction is higher than 0.8, the drag force follows the correlation proposed by Wen & Yu (1966):

$$\boldsymbol{F}_{drag,SL} = \frac{3}{4}\frac{\alpha_S}{d_p{\alpha_L}^{1.65}}C_D\rho_L\|\boldsymbol{u_S} - \boldsymbol{u_L}\|(\boldsymbol{u_S} - \boldsymbol{u_L}) \tag{4.15}$$

where the drag coefficient C_D follows the Schiller & Naumann correlation, with the particle Reynolds number corrected with the liquid volume fraction, as:

$$C_D = 24 \times \frac{1+0.15\left(\alpha_L Re_p\right)^{0.687}}{\alpha_L Re_p} \tag{4.16}$$

and where the local liquid volume fraction is lower than 0.8, the correlation proposed by Gidaspow suggests to describe the drag force with the Ergun (1952) equation:

$$\boldsymbol{F}_{drag,SL} = \left(150\frac{\alpha_S^2\mu_L}{\alpha_L d_p^2} + 1.75\frac{\alpha_S\rho_L\|\boldsymbol{u_S}-\boldsymbol{u_L}\|}{d_p}\right)(\boldsymbol{u_S} - \boldsymbol{u_L}) \tag{4.17}$$

The values of the drag coefficient based on the particle terminal velocity in stationary fluids calculated from Eq. (4.13) are 2.53 and 16.67 for the incomplete and complete suspension conditions respectively, whereas the drag coefficient calculated from Eq. (4.16) are 1.48 and 4.12 for the incomplete and complete suspension respectively, as obtained with the mean particle volume fractions of 0.09 and 0.15

respectively. The values are reported to give an indication of the expected variations of the drag force magnitude due to the particle swarm effects.

Drag coefficient corrections accounting for free stream turbulence effects were not studied, since the available correlations apply to very dilute conditions (Brucato et al., 1998).

The turbulent dispersion force arises from the Favre averaging of the interphase drag term. It accounts for the turbulent fluctuations of the particle volume fractions, contributing to the solids transport from high to low volume fraction regions. The following model due to Burns et al. (2004) was used:

$$\boldsymbol{F}_{TD,S} = -\frac{\mu_t}{\sigma_{SL}\rho_L}\frac{3}{4}\frac{\alpha_S}{d_p}C_D\rho_L\|\boldsymbol{u_S}-\boldsymbol{u_L}\|\left(\frac{\boldsymbol{\nabla}\alpha_S}{\alpha_S}-\frac{\boldsymbol{\nabla}\alpha_L}{\alpha_L}\right) \tag{4.18}$$

In Eq. (4.18) σ_{SL} is the turbulent Schmidt number set equal to 0.9 and μ_t is the turbulent viscosity calculated as:

$$\mu_t = 0.09\rho_{mix}\frac{k^2}{\varepsilon} \tag{4.19}$$

with ρ_{mix}being the local density of the solid-liquid mixture, k being the turbulent kinetic energy and ε the turbulent dissipation rate. Eq. (4.18) was chosen because it has been specifically derived for modelling the contribution of the particle volume fraction turbulent fluctuations in Eulerian two-fluid model (Burns et al., 2004). The correlation is based on the eddy diffusivity hypothesis of the term ($\overline{\alpha'\boldsymbol{u}'}$), that appears after the Favre average of the drag force. It is modelled with a linear dependence on the volume fraction gradient, where the linear coefficient is given by μ_t/σ_{SL}. This hypothesis makes the predictions strongly dependent on the turbulent viscosity value, which in turn depends on the two-phase turbulence model.

Finally, the lift force was modelled as:

$$\boldsymbol{F}_{lift,S} = -0.0767\rho_L\alpha_S(\boldsymbol{u_S}-\boldsymbol{u_L})\times(\boldsymbol{\nabla}\times\boldsymbol{u_S}) \tag{4.20}$$

The effect of the terms from I to V in Eq. (4.2) on the solid distribution is presented in detail in Section 4.4.

4.3.2 Numerical solution procedure

The model equations were solved by ANSYS FLUENT v17.0 in the computational domain depicted in Fig. 4.1, that matched closely the stirred tank geometry adopted in the experiments.

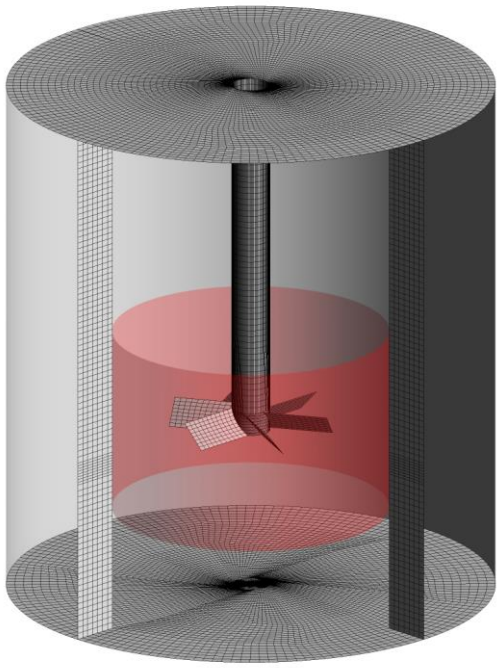

Fig. 4.1 - Stirred tank meshed geometry. The interface between rotating and stationary frame is defined by the red surface.

For accounting for the impeller rotation, the computational domain consisted in two zones, the first containing the impeller and the second defined as the whole vessel volume minus the first fluid zone. The geometry was built in ANSYS DesignModeler, while the meshes were created with ANSYS ICEM. A conformal interface (an interface where each node on one side can be matched with a node on the other side of the interface with a very low tolerance) was defined midway between the tip of the blades and the internal edge of the baffles. A similar criterion was adopted for the lower part of the interface. The upper surface of the interface was defined at an axial coordinate so that the axial distance between the center of the impeller and the

surface itself was equal to the axial distance between the center of the impeller and the lower interface.

The model equations were solved selecting the steady state approximation, by the so-called multiple reference frame (MRF) approach. Based on previous results (Tamburini et al., 2011; Tamburini et al., 2013), the benefits of a reduced computational power required by the steady-state MRF technique, with respect to the transient sliding grid (SG), were deemed to outweigh the slightly increase in prediction accuracy.

No-slip boundary conditions were imposed at the wall for both the liquid and the solids, as the mixture k-ε model requires the same velocity boundary conditions for the two phases.

At the beginning of the calculations, the particles volume fraction was uniformly distributed in the still fluid or in the fully developed single-phase flow field. In particular, the latter initial condition was needed for the solution of the Eulerian-Granular model coupled with the granular temperature transport equation in the form reported in Eq. (4.3), since the numerical solution was not stable adopting the former initial condition.

Steady-state MRF simulations of the two-phase system do not ensure mass conservation in FLUENT v17.0, resulting in the variation of the total volume fraction of the dispersed phase in the tank. Mass conservation was ensured either correcting the overall particle volume fraction at each iteration by a purposely written user defined function (UDF) or by a pseudo-transient approach (Versteeg & Malalasekera, 2007), that allows under-relaxed iterative steady state calculations. The pseudo-transient method led to the convergence of the calculation in a longer computational time with respect to the volume fraction correction at each iteration. It was required for the solution of the Eulerian-Granular model coupled with Eq. (4.3) in order to avoid numerical oscillations of the solution leading to divergence, particularly in the case of incomplete suspension. The adoption of a simplified version of Eq. (4.3), where the diffusion and the convective terms are neglected, significantly reduced the numerical issues and allowed the adoption of the volume fraction correction at each iteration to achieve a stable solution. The pressure-velocity coupling was implemented with the SIMPLE algorithm. The second order upwind discretization scheme and the QUICK scheme were selected for the momentum equations and for the volume fraction respectively.

In all cases, the convergence was assumed to be achieved when all the scaled residuals reached a constant 'low' value (highest value of the residuals below 10^{-3}) and the force measured on the baffles and the average solid volume fraction on selected horizontal planes reached a constant value.

4.3.3 Grid convergence study

A set of three different structured meshes with hexahedral elements was used to evaluate the grid convergence of the solution following the method presented by Roache (1998). The number of cells of the three meshes, named G_1, G_2 and G_3, was 5.87×10^6, 1.87×10^6 and 0.60×10^6, respectively. The corresponding size of the axial discretization on the impeller blades was 0.8, 1.2 and 1.7 mm, respectively.

A set of k-ε single-phase simulations with the three grids was carried out and the grid convergence of the solution was evaluated considering the power number, N_P, and the flow number, Fl, of the PBT at the rotational speed, N, of 900 rpm, corresponding to a rotational Reynolds number of 9×10^4. The impeller power consumption was calculated from the torque on the fixed walls of the tank and from the integral of the turbulent dissipation rate over the vessel volume. The volume flow rate discharged by the impeller was obtained by integrating the axial velocity, u_z, on a horizontal circular section of diameter equal to the impeller located just below it. The N_P values obtained with the three grids as estimated from the torque on the steady walls are 1.58 for G_1, 1.58 for G_2 and 1.57 for G_3, while the values based on the integration of ε range from 1.33 with the coarsest grid to 1.51 with the finest. The Fl values are constant in the three cases considered, with values of 0.88 for G_1 and G_2 and G_3. The experimental values for a similar impeller and configuration are 1.63 for the power number, as found by Chudacek (1985), and 0.73 for the flow number, as reported by Paglianti et al. (2006).

The grid convergence index, GCI, (Coleman & Stern, 1997) for the three grids based on N_P estimated from the torque is equal to 0.8% for G_1, 1.1% for G_2 and 1.2% for G_3. Much higher values are obtained basing the CGI calculation on N_P estimated from the total turbulent dissipation rate: 1.2% for G_1, 4.5% for G_2 and 16.7% for G_3. The results of these preliminary single phase simulations confirm previous findings obtained with a Rushton turbine (Coroneo, et al., 2011), that is the higher effect of the grid resolution on the turbulent variables with respect to the mean flow variables,

as can be observed also on a local basis from the profiles of selected variables along the radial coordinate at the axial elevation of 0.216T shown in Fig. 4.2.

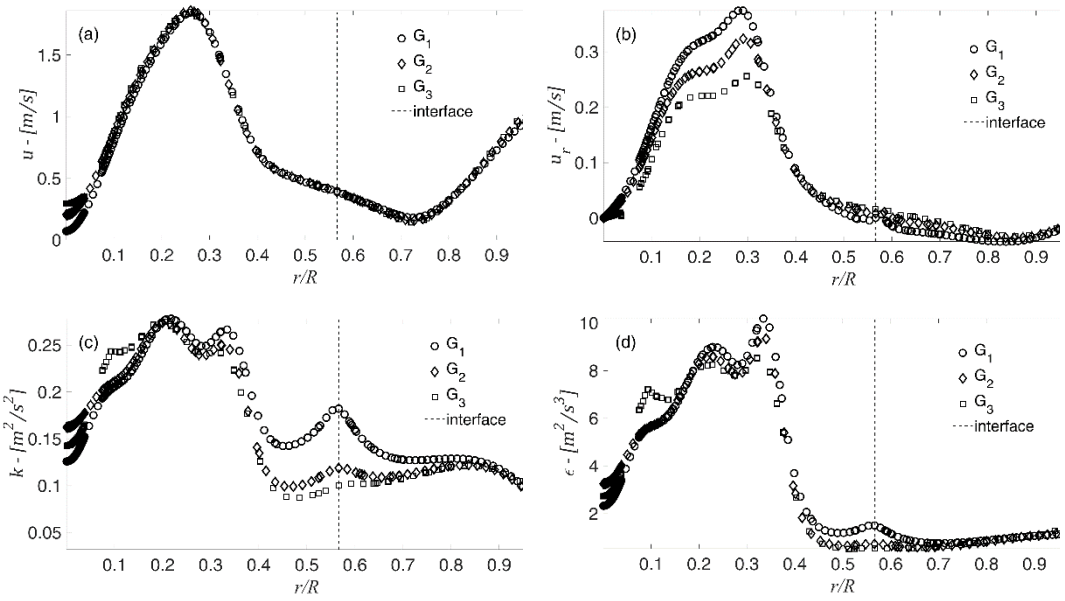

Fig. 4.2 – Velocity magnitude (a), radial velocity (b), turbulent kinetic energy (c) and turbulent dissipation rate (d) on a horizontal line at z=0.05m set mid-way between two baffles.

It is worth observing that at the radial coordinate corresponding to the interface between the two reference frames, depicted in Fig. 4.2 as a vertical dotted line, a perturbation of the k and ε values is clearly visible. The perturbation sharpens as the number of cells increases and it is negligible for the mean velocities. Similar results were found adopting the transient Sliding Mesh method and the OpenFOAM CFD code. This issue was never highlighted before, probably due to the relatively coarse grids typically adopted in RANS based calculations, and it will be worth of further investigation.

The grid dependency of the solid-liquid results was investigated considering the incomplete suspension condition case, that was simulated adopting the Eulerian-Granular formulation of the two-fluid model. In this case, following Guida et al. (2009), the flow number was calculated as the sum of the liquid, $Fl_{(L)}$, and the solid, $Fl_{(S)}$, flow numbers from the volumetric flow rate discharged by the impeller, by integrating the axial velocity weighted by the local phase volume fraction, as:

$$Fl_{(L)} = \frac{1}{ND^3} \int \alpha_L u_{z,L} dA \quad (4.21)$$

$$Fl_{(S)} = \frac{1}{ND^3} \int \alpha_S u_{z,S} dA \quad (4.22)$$

where A is the area of the horizontal circular surface of diameter D located just below the impeller.

As for the results of the single-phase convergence study, the power number calculated from the integration of ε increased noticeably from 0.96 to 1.41 as the number of cells increased, as well as the values calculated from the torque on the fixed walls that ranged from 1.78 to 1.68. The flow numbers had the same value of 0.61 for the liquid and 0.11 for the solid with all the three grids, confirming that the mean flow variables achieve the grid independency with much coarser grids with respect to the turbulent variables also with the two-fluid model.

The comparison of the axial profiles of solid volume fraction, obtained from the average on 25 equally spaced horizontal tank sections, and the radial profiles, obtained from the azimuthal average on the plane at z = 0.11 m, are reported in Fig. 4.3. Overall, with the selected model equations the underestimation of the turbulent dissipation rate significantly affects the solid distribution. As can be observed, the solid distribution in the tank generally follows the same trend as the mean flow variables, similarly to what already found by Tamburini et al., (2013). The axial profiles shown in Fig. 4.3a are almost overlapped at most elevations, while noticeable differences exist in the radial profiles only at selected elevations, as at z = 0.11 m, that are shown in Fig. 4.3b. Since the maximum differences in the distribution of solid volume fraction between the coarsest and the finest grid is about 8%, the mesh G_3 was adopted in the following simulations, being the computational time shorter.

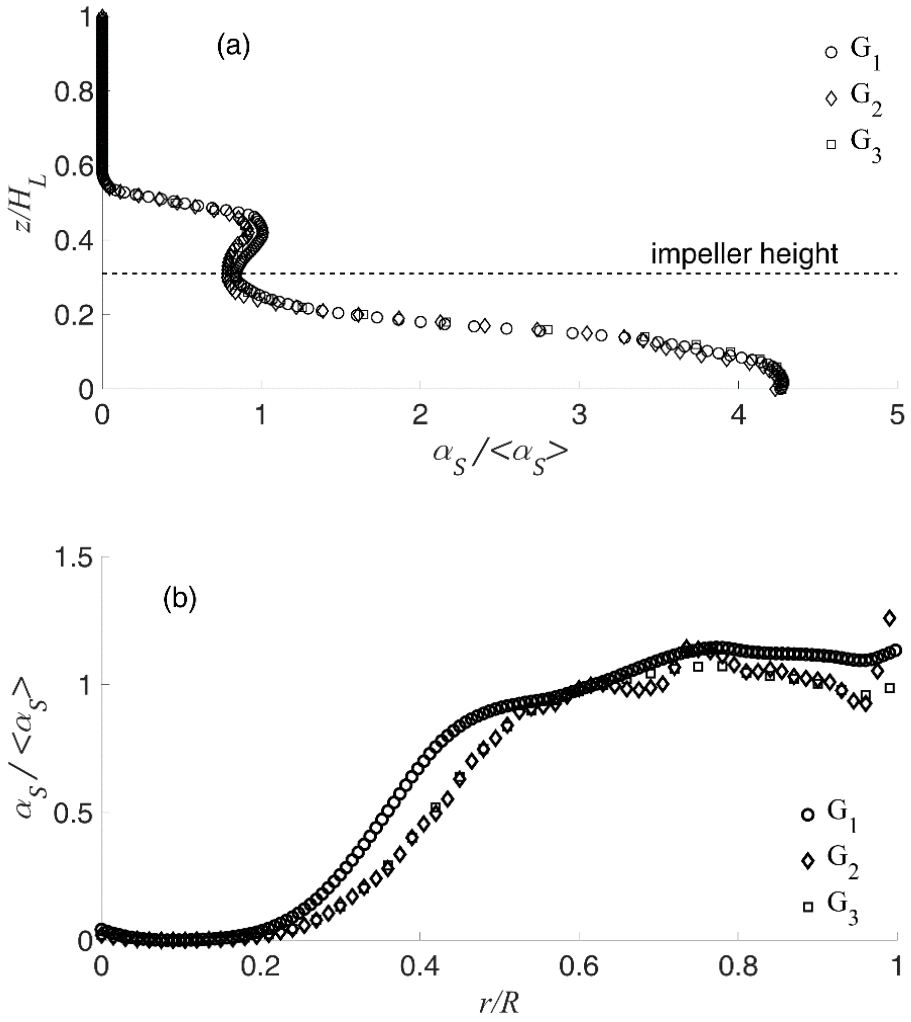

Fig. 4.3 – Axial (a) and radial (b) normalized solid volume fraction as predicted by the three grids in the in-complete suspension case.

4.4 Results and discussion

In the following, the effects of the different models on the solid distribution are compared and quantified. The analysis is based on the comparison of local and global variables. Beside the classical dimensionless power and pumping numbers, two global parameters were considered for estimating the solid suspension features.

The amount of solid suspended by the impeller, S, was estimated by the criterion proposed by Tamburini et al. (2011), as:

$$S = \left(1 - \frac{V_{S,unsuspended}}{V_{total}}\right) \times 100 \tag{4.23}$$

where the unsuspended amount of solid, $V_{S,unsuspended}$, was defined as the volume of the solid phase at the bottom of the tank with a volume fraction equal to the packing limit.

The degree of uniformity of the solid distribution on each horizontal plane investigated experimentally was estimated by coefficient of variation, CoV, as:

$$CoV(z_i) = \sqrt{\frac{\sum_{j=1}^{N_c} a_j \left(\frac{\alpha_{S,j}}{\overline{\alpha_S}(z_i)} - 1\right)^2}{\sum_{j=1}^{N_c} a_j}} \tag{4.24}$$

where a_j is the area of the cell, N_c is the total number of cells on the plane z_i, $\alpha_{s,j}$ is the solid volume fraction on the cell j, $\overline{\alpha_s}(z_i)$ is the mean solid volume fraction on the z_i plane. For each simulation, four CoV values were obtained on four horizontal planes corresponding to the ERT measuring planes z_1, z_2, z_3 and z_4.

4.4.1 Complete suspension conditions

Firstly, the complete suspension case was studied. In these conditions, the effect of the turbulence model (I), solid pressure term (II), turbulent dispersion force (III), drag force (IV), lift force (V) and their interactions on the solid distribution in the simplified situation of unpacked particles and solid-phase dispersed in the whole tank volume were quantified. The simulations were run with the 'mixture' k-ε turbulence model, the E-G model, the turbulent dispersion force, the Gidaspow drag model and without the lift force, unless otherwise stated. This initial set of equations was updated as different aspects were studied.

4.4.1.a Comparison of the 'mixture' k-ε and the 'mixture' Reynolds Stress turbulence models

The results obtained with the 'mixture' versions of the RSM and the *k-ε* turbulence models are presented in this section. The liquid flow fields normalized by the impeller tip speed, V_{tip}, obtained with the two turbulence models are compared in Fig. 4.4. Very similar flow fields were obtained for the solid phase, not shown for brevity, since the slip velocity was of the order of a few cm/s.

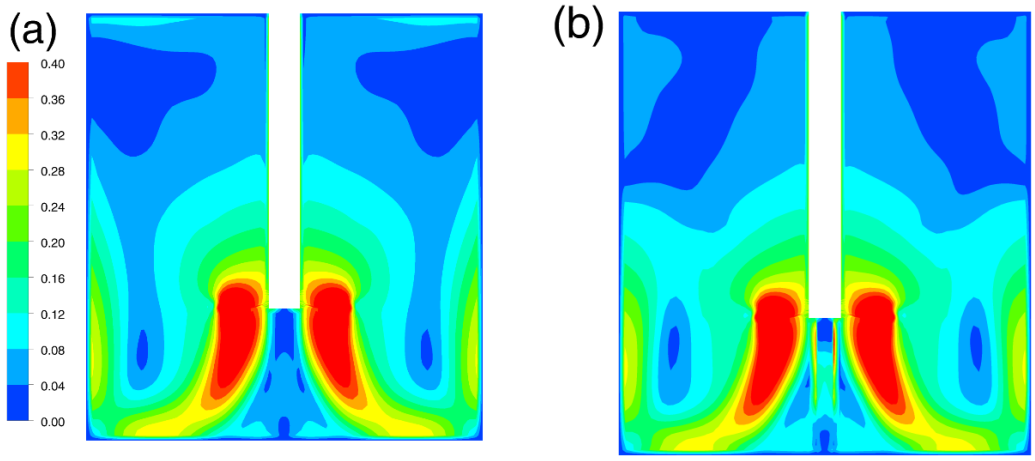

Fig. 4.4 – Velocity magnitude divided by V_{tip}, on a vertical plane mid-way between baffles. (a) E-G/ k-ε simulation, (b) E-G/RSM simulation. Complete suspension case.

By means of example, the map of the norm of the dimensional slip velocity, in m/s, on a plane midway between two consecutive baffles is shown in Fig. 4.5 for the complete suspension case, as obtained with the *k-ε* turbulence model, E-G model, Wen & Yu drag model and with the turbulent dispersion force.

Fig. 4.5 shows that the norm of the slip velocity is almost constant in most of the tank volume, with an average value around 1 cm/s.

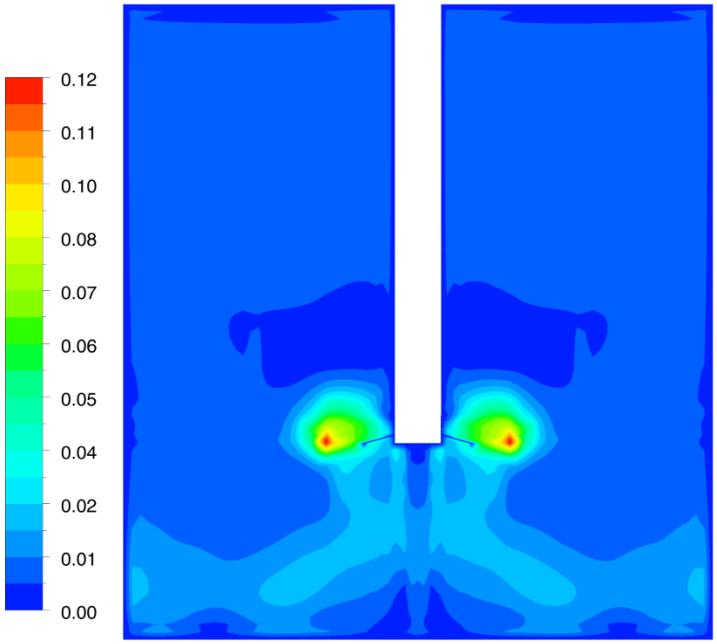

Fig. 4.5 – Norm of the dimensional slip velocity (m/s) contour map as obtained obtained with the k-ε turbulence model, E-G model, Wen & Yu drag model and with the turbulent dispersion force in complete suspension conditions.

The flow numbers obtained in the two cases are equal to 0.80 and 0.81 for the liquid with the k-ε and the RSM, respectively and 0.08 for the solid flow number in both cases.

With the RSM simulation the N_P value of 0.47 was obtained (estimated from the integral of the turbulent dissipation rate), a little above half the power number predicted by the k-ε simulation, that is equal to 0.96, confirming that at equal grid size the predicted turbulent quantities are much lower with the RSM than with the k-ε model (Montante, et al., 2001).

Using either the RSM model or the k-ε model produces small changes in the solid axial distribution as can be observed in Fig. 4.6, where the axial profiles obtained with the two models are shown.

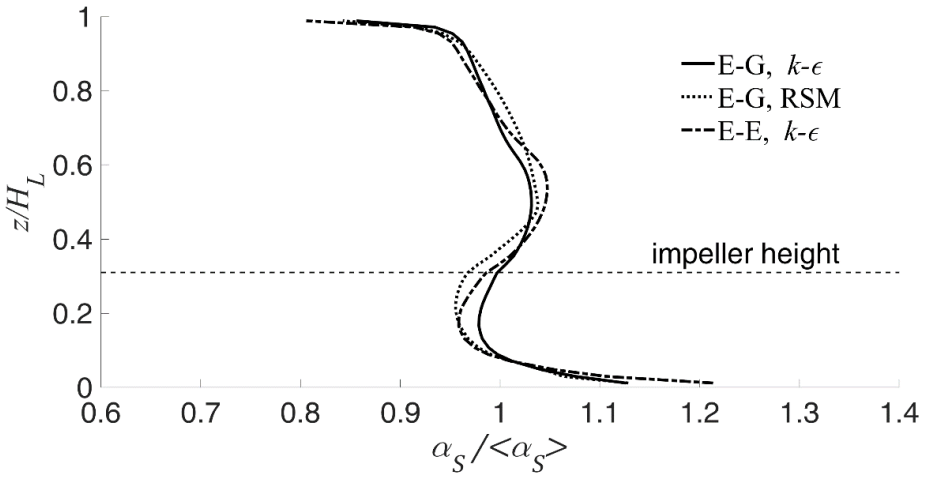

Fig. 4.6 – Axial profile of the normalized volume fraction of the solid phase, as predicted by different models. Complete suspension case.

The global parameters showed that both turbulence models produce complete suspension (S = 100%) and almost uniform particle distribution on the planes, with a small but noticeable higher solid concentration at the bottom of the tank. Nonetheless, the solid phase velocity around the bottom is not zero, pointing to the fact that the particles are not settled. In fact, the maximum CoV, evaluated on the four measuring planes z_1 to z_4, was found on the plane at z/H_L=0.84 and it was equal to 7.75% for the simulation with the k-ε turbulent model and 10.18% for the simulation with the RSM. Being the RSM more computational demanding, the k-ε model was used for the simulations of the complete suspension case.

4.4.1.b Comparison of Eulerian-Granular and Eulerian-Eulerian Models

In the complete suspension conditions, the flow fields generated by the E-G model and the E-E model were very similar and they are not shown for sake of brevity. The two models predicted almost the same values of $Fl_{(S)}$, $Fl_{(L)}$and N_P. The differences on the axial concentration of particles as predicted by the E-E and the E-G are negligible, as can be observed in Fig. 4.6, the suspension index S obtained from the two simulations had the same values of 100% in both cases and the largest difference of the CoV was found on the plane below the impeller, z_1, where the CoV

value for the E-G simulation was equal to 1.71% and the CoV for the E-E simulation was 5.91%.

From these results it may be inferred that the E-E and the E-G model do not provide significant differences on the distribution of the particles at N well above N_{js}, and up to the solid to liquid mass ratio of about 25%, corresponding to 9 vol. % of glass beads in water. In these cases, the E-E formulation of the two-fluid model is strongly suggested instead of the E-G, despite a dense solid-liquid system is considered, since the numerical issues arising in the solution of the complete E-G model may compromise the solution accuracy and in the best case, they give rise to unnecessary long computational time.

4.4.1.c Effect of turbulent dispersion, drag and lift forces

The impact of the interphase momentum transfer via the drag force, the lift force and the turbulent dispersion force on the solid distribution is considered in the following. Of these terms, the contribution of the turbulent dispersion force is discussed first. The flow fields predicted without or with the turbulent dispersion force in the complete suspension case were very similar, as are the power and the flow numbers.

As for the solid volume fraction distributions, that are reported in Fig. 4.7, noticeable differences were obtained with or without turbulent dispersion force. Although the differences between the two profiles are quantitatively relatively small, the inclusion of the turbulent dispersion force smoothened the axial gradients and made the minimum solid volume fraction below the impeller less pronounced. In both cases the suspension coefficient S indicated complete suspension (S = 100%), but the CoV values for the simulation without turbulent dispersion force were generally two to three times higher, on average, with respect to the simulations with the turbulent dispersion force.

The drag laws considered in the complete suspension case, the Schiller & Naumann and the Wen & Yu correlations, produced the same axial distribution of solid particles, as can be observed in Fig. 4.7, where the results obtained with the two C_D laws matched very closely. It is important to notice that in the complete suspension conditions the solid volume fraction never exceeded the value of 0.2, therefore the Gidaspow drag correlation was essentially the Wen & Yu (1966) correlation, with the Schiller & Naumann drag coefficient corrected with the liquid phase volume fraction, as adopted by Derksen (2018).

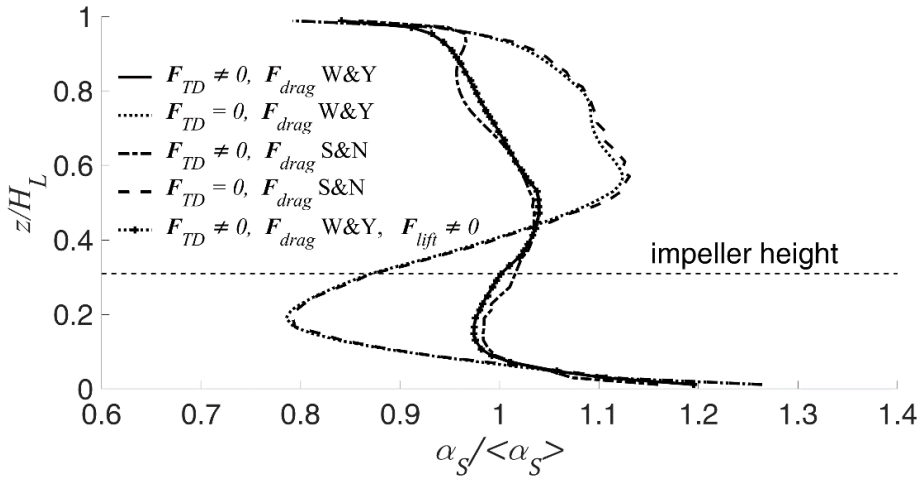

Fig. 4.7 – Axial profile of the normalized solid volume fraction, as predicted with or without the turbulent dispersion force and, the two drag laws of Schiller & Naumann (S&N) and Wen & Yu (W&Y) and without or with the lift force. Complete suspension case.

To the best of our knowledge, the two selected correlations more closely represent the investigated system among those developed so far. The adoption of different correlations was not investigated, since they hold true far outside the physical conditions investigated in this work.

Finally, as already found in previous investigations on dilute (Ljungqvist & Rasmuson, 2001) and dense (Fletcher & Brown, 2009) systems, including the lift force in Eq. (4.2) did not change the axial profile of solid volume fraction, as shown in Fig. 4.7, with the maximum variation of the CoVs well below 1%.

In all cases, the selected models predict complete solid suspension, that was expected, since the impeller speed is much higher than N_{js}. Therefore, a more stringent benchmark is required in order to evaluate the simulations results, that is provided by the ERT data comparison discussed in the following.

4.4.1.d Comparison with the experimental data

The data collected by the ERT technique were used to quantify the predictive capabilities of the simulations. The main limitations of the ERT technique are related to: the extension of the measured volume due to the so called fringe effect, that is

marked for large inhomogeneity in the electrodes region (Lioumbas et al., 2014; Sun & Yang, 2014), the variations due to the free liquid surface oscillations, the loss of accuracy in the centre of the plane with respect to the outer region. Finally, the ERT data resolution is much coarser than that of the CFD data on the planes.

Bearing this in mind, the experimental and computed radial profiles of particle volume fractions on the measurement planes are compared in Fig. 4.8.

For the case of complete suspension, the experimental profiles on the four measurement planes shown that the solid is almost uniformly distributed along the vessel height and that the variations along the vessel radius were also quite small. The comparison of the calculated radial profiles confirms that the E-E and the E-G models provide very similar results. A realistic prediction of particle distribution on the four planes was obtained, particularly when the turbulent dispersion force was included. The major deviations between the experimental data and the predictions were visible on the lower z_1 plane when the turbulent dispersion force was neglected. Smaller differences among the models and a satisfactorily agreement between experiments and simulations were obtained on the z_2 and z_3 planes. The agreement was worse on the upper plane, where the experimental data might be affected by the significant fluctuations of the liquid free surface. Notwithstanding the limitations of the ERT technique, the experimental data provided strong evidence of the reliability of the E-E formulation of the two-fluid model and of the adequacy of the turbulent dispersion contribution for the quantitative prediction of the particle distribution.

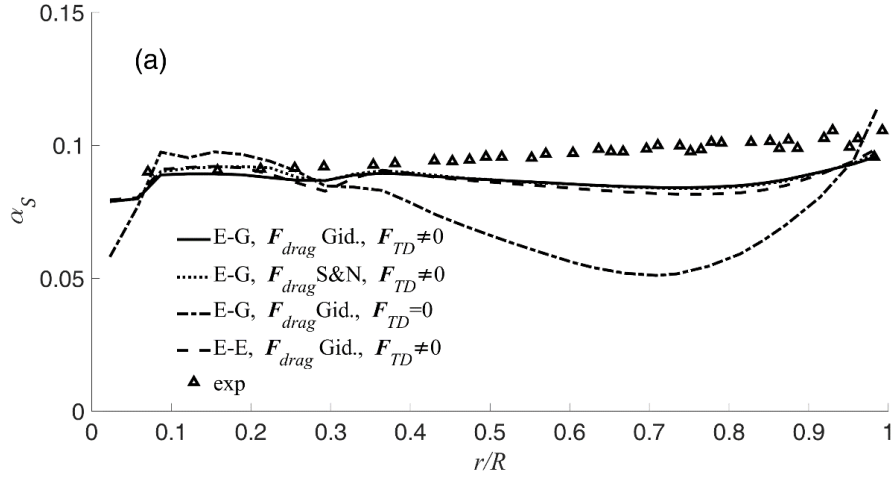
(a)
0.15
0.1
0.05
0
α_S
E-G, F_{drag} Gid., F_{TD}≠0
E-G, F_{drag} S&N, F_{TD}≠0
E-G, F_{drag} Gid., F_{TD}=0
E-E, F_{drag} Gid., F_{TD}≠0
exp
0 0.1 0.2 0.3 0.4 0.5 0.6 0.7 0.8 0.9 1
r/R

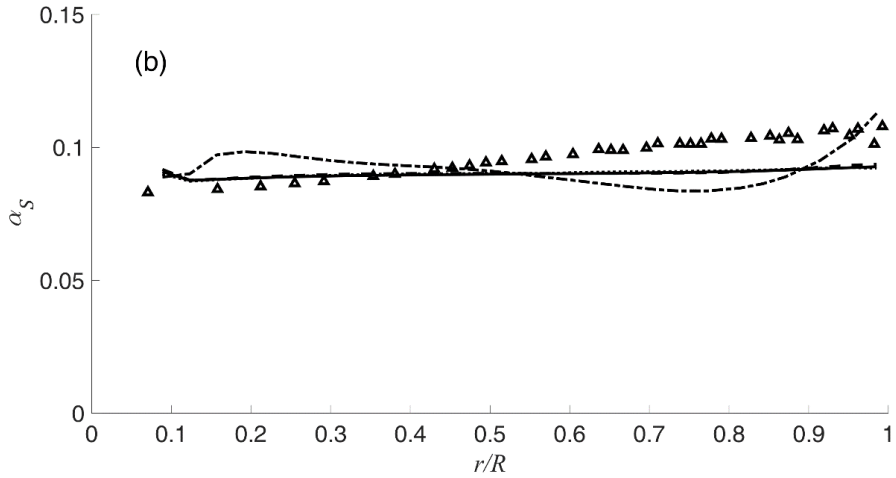
(b)
0.15
0.1
0.05
0
α_S
0 0.1 0.2 0.3 0.4 0.5 0.6 0.7 0.8 0.9 1
r/R

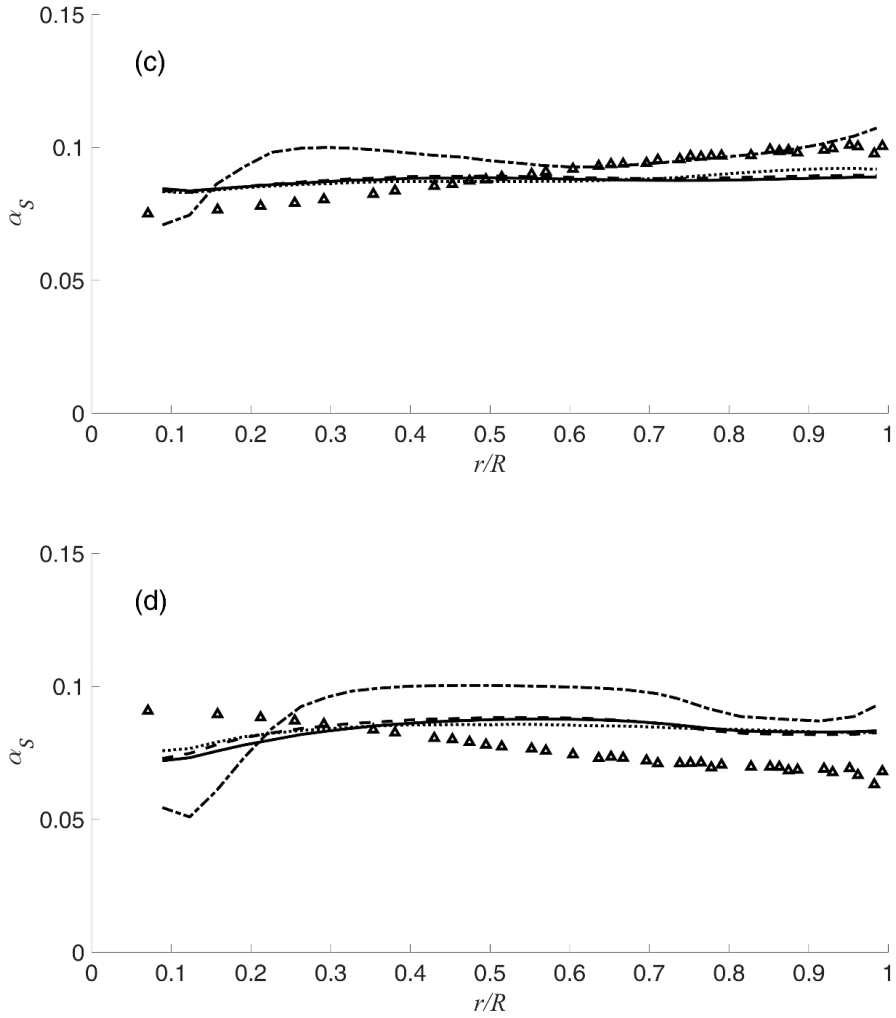

Fig. 4.8 – Radial profiles of solid volume fraction measured on z_1 = 0.06 m (a), z_2= 0.11 m (b), z_3= 0.16 m (c) and z_4= 0.21 m (d) planes and predicted by different simulations.

4.4.2 Incomplete suspension conditions

The simulations were run with the 'mixture' k-ε turbulence model, the E-G model, without the turbulent dispersion force, the Gidaspow drag model and without the lift force, unless otherwise stated. The assessment of the lift force on the results was neglected, having found it uninfluential on the results for the complete suspension case, as well as in the literature.

This initial set of equations was updated as different aspects were studied.

4.4.2.a Comparison of the 'mixture' k-ε and the 'mixture' Reynolds Stress turbulence models

Similarly to what was already found for the complete suspension case, very close mean flow fields were obtained in the incomplete suspension condition with the two turbulence models. The RSM simulation predicted a power number based on the turbulent dissipation rate that was less than half the power number predicted by the k-ε simulations, whereas the pumping numbers were almost coincident. The axial profile of volume fraction of solid slightly changed between 0.2 H_L and 0.5 H_L and in both simulations the predicted solid cloud reached the same height, located around $z/H_L = 0.56$ that was lower than the z_3 plane. The CoV remained basically unchanged on the lowest plane, z_1 ($CoV \approx 60\%$), as well as on the second plane, z_2 ($CoV \approx 34\%$).

As for the complete suspension case, since the RSM did not lead to any remarkable variation on the predictions, the k-ε model was used for investigating the effect of the other terms in the predictions of the incomplete suspension case.

Since the results obtained with the two different models were almost identical, the data are not shown for sake of brevity, whereas the map of the norm of the dimensional slip velocity, in m/s, on a plane midway between two consecutive baffles is shown in Fig. 4.9 for the incomplete suspension case, as obtained with the k-ε turbulence model, E-G model, Wen & Yu drag model and without the turbulent dispersion force.

Fig. 4.9 shows that in the lower part and in the upper part of the tank the slip velocity is nil. In the lower part, both the liquid and the solid particles are still whereas in the upper part the slip velocity is nil due to the absence of solid particles.

In incomplete suspension conditions, noticeable slip velocity gradients are present, with the norm of the slip velocity reaching values up to 12 cm/s.

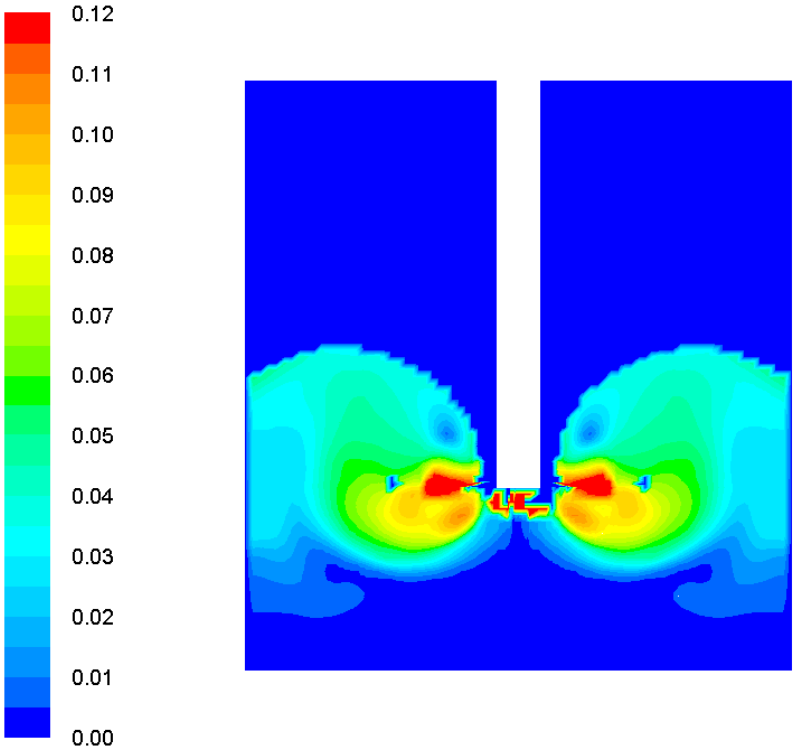

Fig. 4.9 – Norm of the dimensional slip velocity (m/s) contour map as obtained obtained with the k-ε turbulence model, E-G model, Wen & Yu drag model and without the turbulent dispersion force in incomplete suspension conditions.

4.4.2.b Comparison of Eulerian-Granular and Eulerian-Eulerian Models

Since the E-E simulations do not force a limit on the particle packing, for N lower than N_{js}, unphysical concentrations are obtained in the lower part of the tank, as shown in Fig. 4.10a. Despite the different particle distribution in the tank, a similar cloud height was obtained with the E-E and E-G models. The suspension coefficient S with the E-E model was lower (57%) with respect to the E-G model (63%). Clearly, the selection of the E-E model was not appropriate for incomplete suspension, but it

can be adopted as a first simpler tool for evaluating the suspension conditions, when N_{js} is not known a priori.

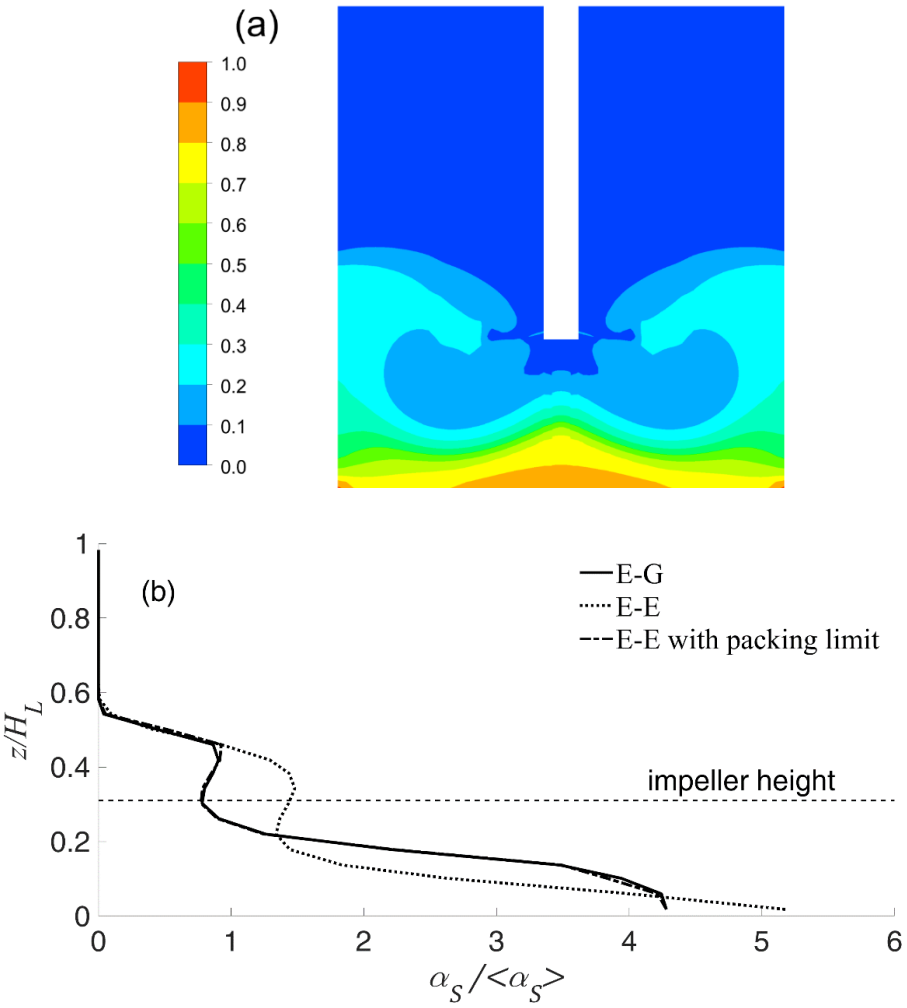

Fig. 4.10 – Solid volume fraction as predicted by the E-E simulation (a) and comparison between the normalized solid axial profiles as predicted by the E-E, E-E with packing limit and E-G model (b). Incomplete suspension case.

The suitability of the E-G formulation was investigated by an additional simulation where just the solid maximum packing limit was fixed, as suggested by Tamburini et al. (2009) and Fletcher & Brown, (2009), who adopted different methods for achieving the limitation. In this work, the default method available in ANSYS

FLUENT v17.0 was used, that retained just the radial distribution function effect at the packing limit, by the solid pressure term in the momentum equation of the solids. In the cells where the solid volume fraction was lower than the packing limit, since all the model constant were set to zero, the solid pressure gradient (Eq. (4.8)) and the laminar solid stress tensor (Eq. (4.9)) were nil.

As for $N > N_{js}$, also for $N < N_{js}$, the application of the kinetic theory of granular flows did not provide a contribution to account for the high solid content, since almost identical results were obtained in the two cases, as shown from the axial profiles of solid volume fraction in Fig. 4.10b and the liquid and solid velocity on the z_1 plane (Fig. 4.11).

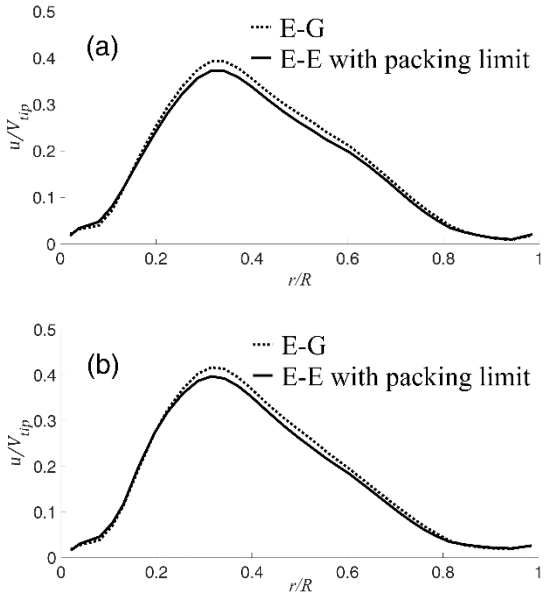

Fig. 4.11 – Velocity magnitude on z_1 plane of the liquid (a) and solid (b) phase divided by V_{tip} as predicted by the E-G and the E-E model with the packing limit. Incomplete suspension case.

As a result, all the contributions included in the E-G model (modified laminar viscosity of the solids and particle-particle interactions) were negligible.

As already observed for the complete suspension case, the E-G formulation of the two-fluid model equation introduced additional numerical complexity without leading to any remarkable effect on the solution. For this reason, the adoption of the

E-E model is suggested also for the incomplete suspension cases at least up to the mass ratio of 43% and 15% by volume of solids, provided that a limitation to the maximum packing limit is included.

4.4.2.c Effect of the turbulent dispersion force

The effect of the turbulent dispersion force on the incomplete suspension case was evaluated adopting the E-E model with the packing limit and the mixture k-ε model. A significantly different impact on the solid suspension was obtained including the turbulent dispersion force, resulting in a much higher fraction of suspended solids, as can be appreciated from the S values that changed from 63% as predicted without the turbulent dispersion force, to 100% when the turbulent dispersion force was included. Concerning the coefficient of variation on the z_1 plane, it changed from 60% without the turbulent dispersion force to 9% when the turbulent dispersion force was considered, whereas the differences were less pronounced on the z_2 plane. As a result of the different amount of suspended solid, the discharge jet produced by the impeller with the two models changed significantly.

The different distribution of solids with the two models is apparent from Fig. 4.12. The high solid fraction packed on the bottom of the tank (Fig. 4.12a) slows the liquid phase, on the contrary, the turbulent dispersion force suspends the great majority of the solid phase (Fig. 4.12b), therefore the liquid is free to flow in the proximity of the bottom of the tank. Being the impeller speed well below N_{js}, the inclusion of the turbulent dispersion force clearly overestimates the effect of the turbulent dispersion arising from the volume fraction fluctuations on the solid suspension.

Interestingly enough, Fig. 4.13 shows that similar heights of the solid cloud were predicted whether the turbulent dispersion force was accounted for or not, meaning that the model validation solely based on the solid cloud height can lead to erroneous conclusions.

The results presented in this section showed that for $N<N_{js}$ the flow field and solid distribution were very sensitive to the turbulent dispersion force, that, with its high intensity and upwards direction close to the tank bottom, provided a significant contribution to the solid suspension.

Eq. (4.18) included the contribution of the solid volume fraction fluctuations not only in the turbulent regions of the stirred tank, but it was artificially introduced also

in the motionless bottom region, where the turbulent viscosity should be equal to zero.

It is apparent that a strategy is required to prevent the turbulent dispersion force to unphysically suspend the solid phase in the regions of settled solids.

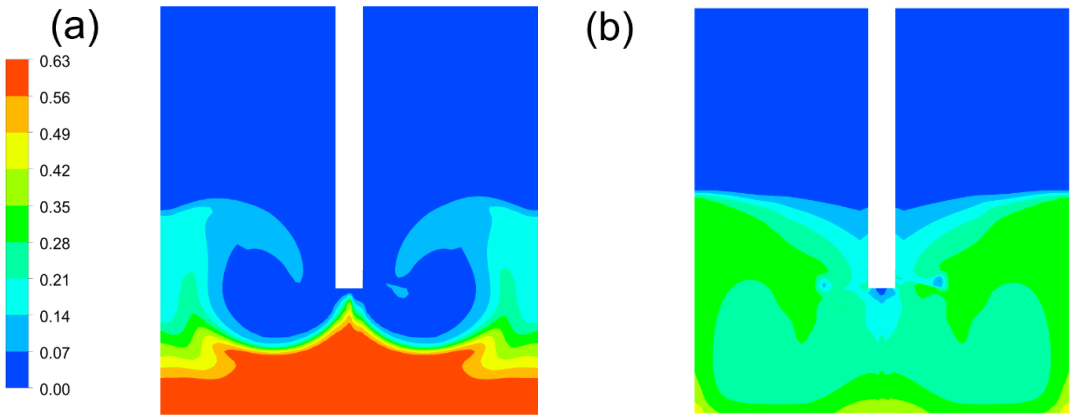

Fig. 4.12 – Solid phase distribution obtained without (a) and with (b) turbulent dispersion force.

4.4.2.d Effect of the drag force

Lastly, the effects of the drag law on the solid distribution in incomplete suspension conditions were considered. The results obtained with the Schiller & Naumann drag law are compared with those obtained applying the Wen & Yu model and the Gidaspow model in Fig. 4.13.

The axial profiles of the non-dimensional solid volume fraction as predicted with the simulations with the three different drag laws were very similar. A small difference in the solid distribution was highlighted by the value of the suspension coefficient that decreased by just 8% with respect to the other two cases, when the Schiller & Naumann drag law is used. As expected from the preliminary estimations of C_D reported in Sec. 3.1, for the examined system, the drag coefficient modification due to the solid volume fraction had little effect on the solid distribution.

4.4.2.e Comparison with the experimental data

The model assessment was repeated also for the incomplete suspension case by the comparison of the simulated radial profiles of solid volume fraction with the experimental data collected by the ERT technique, shown in Fig. 4.14 on the z_1 and z_2 planes only, being the solid fraction nil on the two upper planes. In the incomplete suspension case, the fringe effect is expected to be particularly marked in the lower measurement plane, z_1, due to the proximity of the stagnant solid layer.

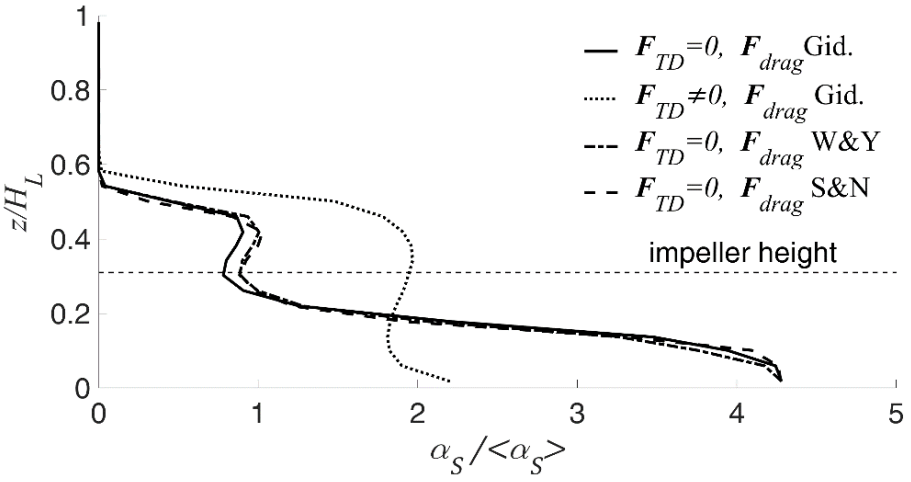

Fig. 4.13 – Axial profile of the solid volume fraction as predicted without and with the turbulent dispersion force and the three drag laws of Schiller & Naumann (S&N), Wen & Yu (W&Y) and Gidaspow (Gid.). Incomplete suspension case.

A preliminary evaluation of the simulations was performed considering the experimental solid cloud height estimated by visual observation between the z_2 and the z_3 plane at $z/H_L = 0.57$. The height of the solid cloud was correctly predicted by each simulation, as can be observed for example in Fig. 4.13. This confirms that the cloud height is an insufficient parameter for a fine estimation of the model prediction capabilities.

The comparison of the simulations with the experimental data shown in Fig. 4.14 confirmed that with the turbulent dispersion force the amount of suspended solid is significantly overpredicted. The other sets of model equations provided all the same results and none of the simulations could reproduce the measured solid distribution.

The comparison clearly suggests that further efforts for including the contribution of the turbulent dispersion by a more suitable formulation in case of packed regions must be devised. Indeed, the experimental solid volume fraction profile on the z_2 plane exhibited less pronounced gradients with respect to the simulated profile obtained neglecting the turbulent dispersion force.

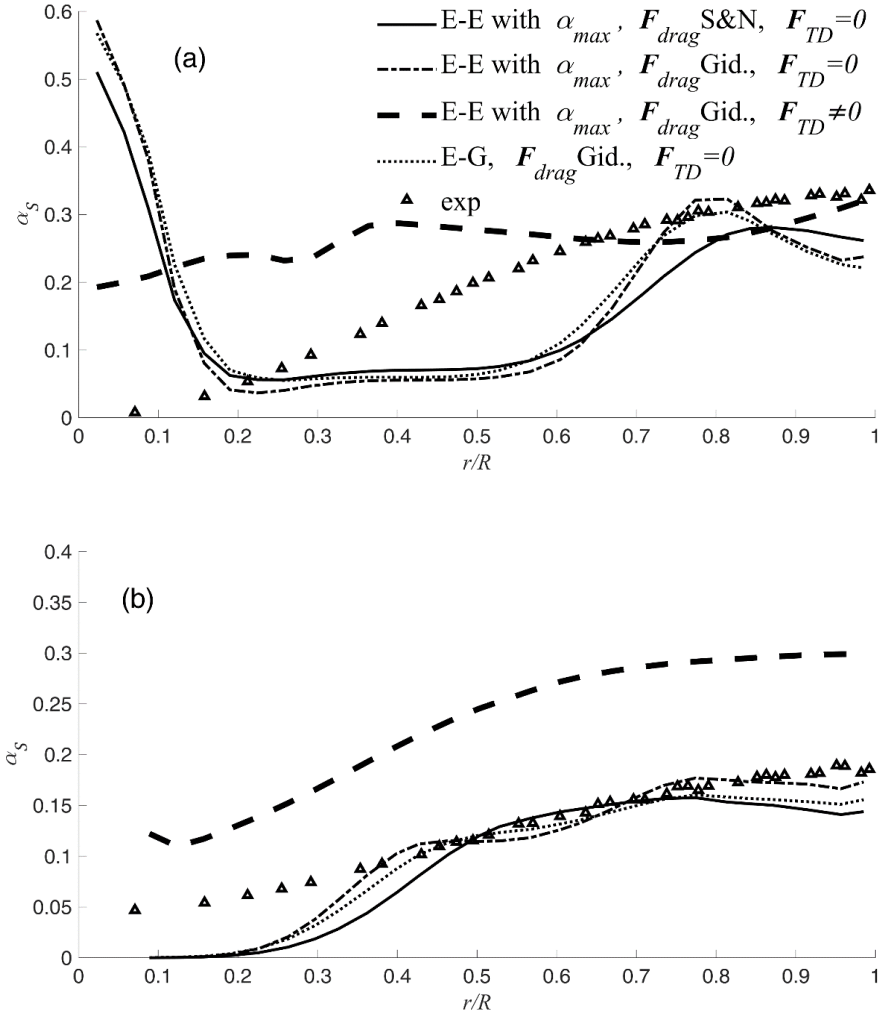

Fig. 4.14 – Radial solid volume fraction profiles measured on z_1 = 0.06 m (a) and z_2 = 0.11 m (b) planes as predicted by different simulations. The experimental radial dimensionless liquid conductivity profiles (exp) are shown as well.

Instead, the shape of the simulated profile obtained including the turbulent dispersion force had a correct trend, but did not provide a quantitative agreement, due to the observed overprediction of the amount of suspended solid. The unsatisfactory agreement of the profiles obtained on the z_1 plane might be a combination of the model deficiencies and the uncertainties of the measurements, due to the mentioned location of the z_1 elevation, situated in the proximity of the interface between the suspended and unsuspended solid.

The overprediction of the suspended solids due to the turbulent dispersion was already observed by Tamburini et al., (2014), who included the turbulent dispersion of the volume fraction in the continuity equation, while satisfactory agreement on the solid distribution was observed with the same modelling method for dilute systems and complete suspension conditions (e.g. Montante et al., 2002), similarly to the results obtained for the complete suspension conditions in this work.

4.5 Conclusions

In this work, the predictive capabilities of RANS-based simulations of incomplete and complete solid suspension in a tank stirred with a single PBT were assessed, considering the Eulerian-Eulerian formulation of the momentum equations for both the phases.

For the solid-liquid systems considered in this work, up to a solid volume fraction equal to 0.15 the momentum equation terms derived from the kinetic theory of granular flows, namely the solid pressure and the solid viscosity, did not provide any contribution in the prediction of the solid distribution in the stirred tank. The Eulerian-Eulerian formulation of the two-fluid model provided reliable radial profiles of solid concentration along the vessel height up to the solid volume fraction of 0.09 and at agitation conditions well above N_{js}.

For agitation condition well below N_{js}, the E-E and the E-G models produced the same results, provided that in both cases a method for fixing a realistic particle packing limit was included, but the numerical solution of the E-G equations exhibit a significantly higher complexity. In the investigated incomplete suspension case, with both the models, the accuracy of the predicted radial concentration profiles was much worse than for the case of complete suspension.

For the drag force, the adoption of the standard drag curve correlations, such as due to Schiller & Naumann, either corrected or not corrected for the hindered settling effects is the option that most strictly adhere to the real physical system. The turbulent dispersion force is found to provide a significant contribution to the suspension and to the distribution of the particles, which is fully appropriate only when the flow regime is turbulent in the whole vessel volume. This result is of great importance not only for RANS simulations, but also for Large Eddy Simulations, since the sub grid scale velocity fluctuations may have an important role in the suspension of the solid particles.

Given the complex physical behaviour of the dense solid-liquid system under investigation and the limitations of the currently available experimental methods for investigating dense and opaque systems, we consider further development of the computational strategy investigated in this work particularly useful, as a feasible predictive tool for industrial operations in solid-liquid stirred tanks and for the analysis of their performances. For more accurate predictions of the solid distribution, specific models to account for particle-particle interactions in stirred tanks are needed and further investigations are required to improve the modelling of the turbulent dispersion due to the particle fluctuations for incomplete suspension conditions.

4.6 Nomenclature

a_j	Area of the cell j, [m^2]
C	Off-bottom clearance, [m]
C_D	Drag coefficient, [-]
CoV	Coefficient of variation, [-]
D	Impeller diameter, [m]
d_p	Particle diameter, [m]
e_S	Coefficient of restitution, [-]
$\boldsymbol{F}_{drag,\,SL}$	Interphase drag force, [N m^{-3}]
$\boldsymbol{F}_{lift,S}$	Lift force, [N m^{-3}]
$\boldsymbol{F}_{TD,\,S}$	Turbulent dispersion force, [N m^{-3}]
Fl	Flow number, [-]
$Fl_{(L)}$	Liquid flow number, [-]
$Fl_{(S)}$	Solid flow number, [-]
$\boldsymbol{g}$	Gravitational acceleration, [m s^{-2}]
g_{0S}	Radial distribution function, [-]
H_L	Liquid height, [m]
H_T	Vessel height, [m]
k	Turbulent kinetic energy, [m^2 s^{-2}]
k_{θ_s}	Granular conductivity coefficient, [-]
N	Impeller rotational speed, [s^{-1}]
N_c	Number of cells in a selected plane, [-]
N_P	Power number, [-]
N_{js}	Just-suspended impeller speed, [s^{-1}]
P	Pressure, [Pa]
P_S	Solid pressure, [Pa]
R	Vessel radius, [m]
r	Radial coordinate, [m]
Re_p	Particle Reynolds number, [-]
S	Suspension coefficient, [-]
T	Vessel diameter, [m]
V_S	Volume of solid phase, [m^3]
$\boldsymbol{u_S}$	Time-averaged velocity of the solid-phase, [m s^{-1}]
$\boldsymbol{u_L}$	Time-averaged velocity of the liquid-phase, [m s^{-1}]
$u_{r,\,i}$	Radial velocity of the i^{th} phase, [m s^{-1}]
V_{tip}	Impeller tip speed, [m s^{-1}]
$u_{z,\,i}$	Axial velocity of the i^{th} phase, [m s^{-1}]
X_S	Solids loading, [kg_{solid} kg_{liquid}^{-1} x 100]

z	Axial coordinate, [m]
z_i	Axial coordinate of the i^{th} plane, [-]

Greek symbols

α_L	Liquid volume fraction, [-]
α_S	Solid volume fraction, [-]
$\alpha_{S,\,max}$	Solid volume fraction at the packing limit, [-]
$\overline{\alpha_S}(z_i)$	Mean solid volume fraction on the i^{th} plane, [-]
$< \alpha_S >$	Mean solid volume fraction in the vessel, [-]
ε	Turbulent kinetic energy dissipation rate, [$m^2\ s^{-3}$]
ϕ_{LS}	Kinetic energy exchange between liquid and solid phases, [$kg\ m^{-1}\ s^{-3}$]
Θ_S	Granular temperature, [$m^2\ s^{-2}$]
γ_{θ_s}	Collisional dissipation energy, [$kg\ m^{-1}\ s^{-3}$]
λ_S	Solid bulk viscosity, [Pa s]
μ_t	Turbulent viscosity, [Pa s]
μ_L	Liquid viscosity, [Pa s]
μ_S	Solid shear viscosity, [Pa s]
ρ_L	Liquid density, [$kg\ m^{-3}$]
ρ_{mix}	Mixture density, [$kg\ m^{-3}$]
ρ_S	Solid density, [$kg\ m^{-3}$]
σ_{SL}	Turbulent Schmidt number, [-]
$\boldsymbol{\tau_S}^{\boldsymbol{l}}$	Laminar solid-phase stress, [Pa]
$\boldsymbol{\tau_S}$	Viscous stress tensor of the solid phase, [Pa]
$\boldsymbol{\tau_S}^{\boldsymbol{t}}$	Reynolds stress tensor of the solid phase, [Pa]

4.7 References

Ayranci, I., Kresta, S. M., & Derksen, J. J. (2013). Experiments and Simulations on Bidisperse Solids Suspension in a Mixing Tank. *Chemical Engineering & Technology*, *36*(11), 1957–1967. https://doi.org/10.1002/ceat.201300409

Balachandar, S., & Eaton, J. K. (2010). Turbulent Dispersed Multiphase Flow. *Annual Review of Fluid Mechanics*, *42*(1), 111–133. https://doi.org/10.1146/annurev.fluid.010908.165243

Blais, B. (2016). *DÉVELOPPEMENT D'UN MODÈLE EULER-LAGRANGE ROBUSTE POUR LASIMULATION DES ÉCOULEMENTS SOLIDE-LIQUIDE DANS LES OPÉRATIONS DEMÉLANGE*. École Polytechnique de Montréal.

Blais, B., Bertrand, O., Fradette, L., & Bertrand, F. (2017). CFD-DEM simulations of early turbulent solid–liquid mixing: Prediction of suspension curve and just-suspended speed. *Chemical Engineering Research and Design*, *123*, 388–406. https://doi.org/10.1016/j.cherd.2017.05.021

Blais, B., Lassaigne, M., Goniva, C., Fradette, L., & Bertrand, F. (2016). Development of an unresolved CFD–DEM model for the flow of viscous suspensions and its application to solid–liquid mixing. *Journal of Computational Physics*, *318*, 201–221. https://doi.org/10.1016/j.jcp.2016.05.008

Brucato, A., Grisafi, F., & Montante, G. (1998). Particle drag coefficients in turbulent fluids. *Chemical Engineering Science*, *53*(18), 3295–3314. https://doi.org/10.1016/S0009-2509(98)00114-6

Burns, A. D., Frank, T., Hamill, I., & Shi, J.-M. M. (2004). The Favre Averaged Drag Model for Turbulent Dispersion in Eulerian Multi-Phase Flows. In *Fifth International Conference on Multiphase Flow, ICMF-2004* (pp. 1–17). Yokohama, Japan. Retrieved from http://www.drthfrank.de/publications/2004/Burns_Frank_ICMF_2004_final.pdf

Carletti, C., Montante, G., Westerlund, T., & Paglianti, A. (2014). Analysis of solid concentration distribution in dense solid–liquid stirred tanks by electrical resistance tomography. *Chemical Engineering Science*, *119*, 53–64. https://doi.org/10.1016/j.ces.2014.07.049

Chudacek, M. W. (1985). Impeller power numbers and impeller flow numbers in profiled bottom tanks. *Industrial & Engineering Chemistry Process Design and Development*, *24*(3), 858–867. https://doi.org/10.1021/i200030a056

Coleman, H. W., & Stern, F. (1997). Uncertainties and CFD Code Validation. *Journal of Fluids Engineering*, *119*(4), 795. https://doi.org/10.1115/1.2819500

Coroneo, M., Montante, G., Paglianti, A., & Magelli, F. (2011). CFD prediction of fluid flow and mixing in stirred tanks: Numerical issues about the RANS simulations. *Computers & Chemical Engineering*, *35*(10), 1959–1968. https://doi.org/10.1016/j.compchemeng.2010.12.007

Delafosse, A., Loubière, C., Calvo, S., Toye, D., & Olmos, E. (2018). Solid-liquid suspension of microcarriers in stirred tank bioreactor – Experimental and numerical analysis. *Chemical Engineering Science*, *180*, 52–63. https://doi.org/10.1016/j.ces.2018.01.001

Derksen, J. J. (2003). Numerical simulation of solids suspension in a stirred tank. *AIChE Journal*, *49*(11), 2700–2714. https://doi.org/10.1002/AIC.690491104

Derksen, J. J. (2018). Eulerian-Lagrangian simulations of settling and agitated dense solid-liquid suspensions – achieving grid convergence. *AIChE Journal*, *64*(3), 1147–1158. https://doi.org/10.1002/aic.16061

Ding, J., & Gidaspow, D. (1990). A bubbling fluidization model using kinetic theory of granular flow. *AIChE Journal*, *36*(4), 523–538. https://doi.org/10.1002/aic.690360404

Ergun, S. (1952). *Fluid flow through packed columns*. *Chem. Eng. Prog.* (Vol. 48).

Fletcher, D. F., & Brown, G. J. (2009). Numerical simulation of solid suspension via mechanical agitation: effect of the modelling approach, turbulence model and hindered settling drag law. *International Journal of Computational Fluid Dynamics*, *23*(2), 173–187. https://doi.org/10.1080/10618560802680211

Gidaspow, D. (1994). *Multiphase Flow and Fluidization: Continuum and Kinetic Theory Descriptions*. Academic Press.

Guida, A., Nienow, A. W., & Barigou, M. (2009). PEPT measurements of solid–liquid flow field and spatial phase distribution in concentrated monodisperse stirred suspensions. *Chemical Engineering Science*, *65*(6), 1905–1914. https://doi.org/10.1016/j.ces.2009.11.005

Jenkins, J. T., & Savage, S. B. (1983). A theory for the rapid flow of identical, smooth, nearly elastic, spherical particles. *Journal of Fluid Mechanics*, *130*, 187–202. https://doi.org/10.1017/S0022112083001044

Kasat, G. R., Khopkar, A. R., Ranade, V. V., & Pandit, A. B. (2008). CFD simulation of liquid-phase mixing in solid–liquid stirred reactor. *Chemical Engineering Science*, *63*(15), 3877–3885. https://doi.org/10.1016/j.ces.2008.04.018

Li, G., Li, Z., Gao, Z., Wang, J., Bao, Y., & Derksen, J. J. (2018). Particle image velocimetry experiments and direct numerical simulations of solids suspension in transitional stirred tank flow. *Chemical Engineering Science*, *191*, 288–299. https://doi.org/10.1016/j.ces.2018.06.073

Li, Z., Derksen, J. J., & Gao, Z. (2015). Models and applications for simulating turbulent solid–liquid suspensions in stirred tanks. *Journal of Chemical Engineering of Japan*, *48*(5), 329–336. https://doi.org/10.1252/jcej.14we056

Lioumbas, J. S., Chatzidafni, A., & Karapantsios, T. D. (2014). Spatial considerations on electrical resistance tomography measurements. *Measurement Science and Technology*, *25*(5), 055303. https://doi.org/10.1088/0957-0233/25/5/055303

Liu, L., & Barigou, M. (2013). Numerical modelling of velocity field and phase

distribution in dense monodisperse solid–liquid suspensions under different regimes of agitation: CFD and PEPT experiments. *Chemical Engineering Science*, *101*, 837–850. https://doi.org/10.1016/j.ces.2013.05.066

Liu, L., & Barigou, M. (2014). Experimentally validated computational fluid dynamics simulations of multicomponent hydrodynamics and phase distribution in agitated high solid fraction binary suspensions. *Industrial and Engineering Chemistry Research*, *53*(2), 895–908. https://doi.org/10.1021/ie3032586

Liu, M. (2016). CFD Modeling of Stirred Tank Reactors. In S. M. Kresta, A. W. Etchells III, V. A. Atiemo-Obeng, & D. S. Dickey (Eds.), *Advances in industrial mixing: a companion to the handbook of industrial mixing* (pp. 123–148). John Wiley & Sons, Ltd.

Ljungqvist, M., & Rasmuson, A. (2001). Numerical Simulation of the Two-Phase Flow in an Axially Stirred Vessel. *Trans IChemE*, *79*. https://doi.org/10.1205/02638760152424307

Lun, C. K. K., Savage, S. B., Jeffrey, D. J., & Chepurniy, N. (1984). Kinetic theories for granular flow: inelastic particles in Couette flow and slightly inelastic particles in a general flowfield. *Journal of Fluid Mechanics*, *140*(1), 223. https://doi.org/10.1017/S0022112084000586

Mei, R. (1992). An approximate expression for the shear lift force on a spherical particle at finite reynolds number. *International Journal of Multiphase Flow*, *18*(1), 145–147. https://doi.org/10.1016/0301-9322(92)90012-6

Mishra, P., & Ein-Mozaffari, F. (2017). Using computational fluid dynamics to analyze the performance of the Maxblend impeller in solid-liquid mixing operations. *International Journal of Multiphase Flow*, *91*, 194–207. https://doi.org/10.1016/j.ijmultiphaseflow.2017.01.009

Montante, G., Lee, K. C., Brucato, A., & Yianneskis, M. (2001). Numerical simulations of the dependency of flow pattern on impeller clearance in stirred vessels. *Chemical Engineering Science*, *56*(12), 3751–3770. https://doi.org/10.1016/S0009-2509(01)00089-6

Montante, Giuseppina, Pinelli, D., & Magelli, F. (2002). Diagnosis of Solid Distribution in Vessels Stirred with Multiple PBTs and Comparison of Two Modelling Approaches. *The Canadian Journal of Chemical Engineering*, *80*(4), 1–9. https://doi.org/10.1002/cjce.5450800408

Paglianti, A., Montante, G., & Magelli, F. (2006). Novel experiments and a mechanistic model for macroinstabilities in stirred tanks. *AIChE Journal*, *52*(2), 426–437. https://doi.org/10.1002/aic.10634

Roache, P. J. (1998). *Verification and Validation in Computational Science and Engineering*. Hermosa Publishers, Albuquerque, New Mexico. Retrieved from http://www.hermosa-pub.com/hermosa

Rong, L. W., Dong, K. J., & Yu, A. B. (2013). Lattice-Boltzmann simulation of fluid flow through packed beds of uniform spheres: Effect of porosity. *Chemical Engineering*

Science, *99*, 44–58. https://doi.org/10.1016/j.ces.2013.05.036

Schiller, L., & Naumann, A. (1933). Über die grundlegenden berechnungen bei der schwerkraftbereitung. *Zeitschrift Des Vereines Deutscher Fngenieure*, *77*(12), 318--321.

Sun, J., & Yang, W. (2014). Evaluation of fringe effect of electrical resistance tomography sensor. *Measurement*, *53*, 145–160. Retrieved from https://ac.els-cdn.com/S0263224114001432/1-s2.0-S0263224114001432-main.pdf?_tid=666956ca-a684-48c6-a7cc-f2bfff03caf0&acdnat=1531310827_d39db07f4f8f29e4277c85d8a35f5a1c

Syamlal, M., Rogers, W., & O`Brien, T. J. (1993). *MFIX documentation theory guide*. Oak Ridge, TN. https://doi.org/10.2172/10145548

Tamburini, A., Cipollina, A., Micale, G., Brucato, A., & Ciofalo, M. (2011). CFD simulations of dense solid–liquid suspensions in baffled stirred tanks: Prediction of suspension curves. *Chemical Engineering Journal*, *178*, 324–341. https://doi.org/10.1016/j.cej.2011.10.016

Tamburini, A., Cipollina, A., Micale, G., Brucato, A., & Ciofalo, M. (2013). CFD simulations of dense solid–liquid suspensions in baffled stirred tanks: Prediction of solid particle distribution. *Chemical Engineering Journal*, *223*, 875–890. https://doi.org/10.1016/j.cej.2013.03.048

Tamburini, A., Cipollina, A., Micale, G., Brucato, A., & Ciofalo, M. (2014). Influence of drag and turbulence modelling on CFD predictions of solid liquid suspensions in stirred vessels. *Chemical Engineering Research and Design*, *92*(6), 1045–1063. https://doi.org/10.1016/j.cherd.2013.10.020

Tamburini, A., Cipollina, A., Micale, G., Ciofalo, M., & Brucato, A. (2009). Dense solid–liquid off-bottom suspension dynamics: Simulation and experiment. *Chemical Engineering Research and Design*, *87*(4), 587–597. https://doi.org/10.1016/j.cherd.2008.12.024

Tsuji, Y. (2007). Multi-scale modeling of dense phase gas–particle flow. *Chemical Engineering Science*, *62*(13), 3410–3418. https://doi.org/10.1016/j.ces.2006.12.090

Van den Akker, H. E. A. (2015). Mesoscale Flow Structures and Fluid–Particle Interactions. In *Advances in Chemical Engineering, Volume 46* (Vol. 46, pp. 281–354). Elsevier Inc. https://doi.org/10.1016/bs.ache.2015.10.010

Versteeg, H. K., & Malalasekera, W. (2007). *An Introduction to Computional Fluid Dynamics: The Finite Volume Method*. Pearson Education.

Wadnerkar, D., Tade, M. O., Pareek, V. K., & Utikar, R. P. (2016). CFD simulation of solid–liquid stirred tanks for low to dense solid loading systems. *Particuology*, *29*, 16–33. https://doi.org/10.1016/j.partic.2016.01.012

Wen, C. Y., & Yu, Y. H. (1966). Mechanics of fluidization. *Chemical Engineering Progress, Symposium Series*, *62*(1), 100–111.

Xie, L., & Luo, Z. H. (2018). Modeling and simulation of the influences of particle-

particle interactions on dense solid–liquid suspensions in stirred vessels. *Chemical Engineering Science*, *176*, 439–453. https://doi.org/10.1016/j.ces.2017.11.017

Zhu, H. P., Zhou, Z. Y., Yang, R. Y., & Yu, A. B. (2007). Discrete particle simulation of particulate systems: Theoretical developments. *Chemical Engineering Science*, *62*(13), 3378–3396. https://doi.org/10.1016/j.ces.2006.12.089

Chapter 5

Biohydrogen production in stirred fermenters

A bioreactor for the production of hydrogen from the dark fermentation of organics is studied by a comprehensive modelling strategy. The bioreactor is a dual impeller vortex ingesting stirred tank working under batch and attached growth conditions. Two geometrical configurations of the reactor are investigated: one devised to ensure an effective fluid dynamics behavior and the other proposed to increase the hydrogen productivity. The turbulent gas-liquid fluid dynamics, the production and the recovery of H_2 from the liquid phase are predicted by the numerical solution of the two-phase Reynolds averaged Navier-Stokes equations and the species mass transport equations, including a simplified kinetic model for the fermentative hydrogen production found in literature and a local interphase mass transfer model for the hydrogen stripping from the aqueous to the gas phase. A simplified model for the description of the interfacial area in the context of the two-fluid model is also proposed. This work suggests a method for the predictive simulations of a complex biological process via numerical modelling based on Computational Fluid Dynamics. The main outcome of the proposed investigation method is a detailed

estimation of the different relevant variables and their interaction on a local basis, providing a viable tool for the optimization and the scale-up of bioreactors.

5.1 Introduction

In the last years, hydrogen has been recognized as one of the most energy dense and environmental friendly fuels, being a promising alternative to conventional fossil fuels (Bharathiraja, et al., 2016) although, more than 85% of hydrogen produced worldwide is derived from the steam reforming of petroleum derivatives (Mohsin, et al., 2018). Biological production of H_2 can be a cost-effective alternative to the current industrial methods (Cammack, et al., 2001) and microbial processes for hydrogen production can be split into two different categories, based on the H_2 synthesis: dark anaerobic production by bacteria and photoproduction by cyanobacteria and algae (Markov, 2012). The dark fermentation of waste organics is one of the most promising sources of biohydrogen and a key technology to obtaining hydrogen from crop residues, livestock waste and food waste and limiting the use of fossil fuels sources (Guo, et al., 2016).

As fermentation is industrially conducted in bioreactors, fluid mixing and interphase mass transfer inside bioreactors are increasingly studied aspects, together with the biochemical, microbiological factors and start-up behavior, as important features for enhancing biohydrogen production (Bakonyi, et al., 2014; Kumar et al., 2016). The suspended-cell continuous stirred tank reactor (CSTR) is the most popular solution for dark fermentation, however, the goal of improving hydrogen production led to the development of a number of different bioreactor geometries and processes such as expanded granular sludge bed (ESGB) reactors (Cisneros-Pérez et al., 2015; Guo et al., 2008), membrane bioreactors (Li & Fang, 2007; Oh, et al., 2004), fixed-bed reactors (Chang, et al., 2002; Kumar & Buitrón, 2017), just to name a few (Show, et al., 2008).

The difficulties in studying industrial scale reactors require that relationships between design, operating variables and performances of bioreactors should be predictable when performing a scale-up from the laboratory to the production scale, because hydrogen productivity and energy efficiency exhibit important variations depending on the process scale (Manish & Banerjee, 2008; Wang, et al., 2010). Computational Fluid Dynamics (CFD) has been recently establishing itself as a viable approach for the design and the optimization of biohydrogen fermenters (Ding, et al., 2010; Ri, et al., 2017; Wang et al., 2010).

Despite CFD increasing use in the field of bioreactors modelling, the integration of physical and biological processes still poses great challenges (Wu, 2013). The variation of the parameters of the biological models with the reactor scale (Morchain, et al., 2014), the reliable prediction of the relevant hydrodynamics variables with affordable computational times (Delafosse et al., 2014) and the coupling of fluid dynamics, mass transfer and kinetic variables (Elqotbi, et al., 2013) are, among others, complex aspects that have started being investigated by CFD in the recent past. The value of CFD for moving from trial and error procedures to more rational approaches for the design and the scale-up of biohydrogen fermenters has been specifically highlighted, together with the requirement of further multiphase flow model developments (Ren, et al., 2011).

This work deals with the modelling of a stirred bioreactor for the fermentative production of hydrogen from organics, in different configurations. In particular, the attached-growth dark fermentation in a dual impeller vortex-ingesting batch stirred bioreactor is considered. The final goal of the vortex-ingesting configuration is to drive the stripping gas towards a membrane separation unit for pure H_2 recovery without adding any external device. The hydrodynamics features of this special bioreactor were already investigated experimentally (Montante, et al., 2013a), for one of the two configurations proposed. It was proven that with the selected configuration, the process hydrodynamics requirements, such as effective fluid mixing and gas recirculation to strip the dissolved gaseous fermentation products, are fulfilled. The objective of this work is to present a comprehensive modelling strategy for the prediction of fluid flow features, H_2 production and mass transfer in the bioreactor to be confidently adopted for scale-up, providing a complete route for the prediction and the optimization of the bioreactor performances. The modelling challenges for the reliable simulations of the bioreactors are addressed. The issues which may arise from the adoption of standard CFD tools, without the assessment of the underlying hypothesis, are highlighted.

5.2 Geometry of the bioreactor

In this work, we have studied two different configurations of a batch stirred bioreactor for the production of hydrogen through dark fermentation. The stirred bioreactor consisted of a four-baffled, flat-bottomed cylindrical vessel of diameter $T = 0.232m$ and height $H = 2T$, provided with a co-axial draft tube of internal diameter equal to $0.40T$ and height of $1.36T$. The vessel was closed with a flat lid, on which the draft tube and the external tube for gas recirculation were fixed. The liquid passage from the external volume of the vessel to the inside of the draft tube was ensured by four equally spaced $26mm$ ($0.112T$) holes placed at $45°$ with respect to the baffles at a distance of $0.135m$ ($0.58T$) from the vessel top. An additional $28mm$ ($0.12T$) hole was made at $60mm$ ($0.26T$) from the vessel top to ensure gas recirculation from the external zone. A draft tube with a diameter to tank diameter ratio of 0.4 was selected for ensuring a mixture velocity in the draft tube greater than the bubble rising velocity, thus promoting gas ingestion. Two down-pumping impellers were selected for the agitation: the lower agitator was a four-bladed $45°$ pitched blade turbine (4PBT) of diameter equal to $9.4cm$ ($0.41T$), placed just outside the draft tube at the distance $0.6T$ from the vessel base, the upper one was a six-bladed $45°$ PBT (6-PBT) of diameter equal to $T/3$, placed inside the draft tube at a distance of $18cm$ ($0.77T$) above the lower 4-PBT. The gas-liquid regime was obtained by allowing vortex ingestion from the vessel headspace.

This configuration of the reactor allows to remove the produced hydrogen from the liquid medium through the stripping with the gas in the headspace of the vessel. The gas is entrained in the liquid phase by the vortex and it is recirculated through the liquid phase without the need to introduce a compressor to sparge the gas in the medium. As pointed out by (Bakonyi, et al., 2017) in their experimental analysis of a gas separation membrane bioreactor, the hydrogen recovery through a membrane resulted in a significantly higher H_2 production.

For this purpose, the reactor is designed to be coupled with a membrane separation module, in the upper part of the external pipe in Fig. 5.1 and in Fig. 5.2, for hydrogen recovery.

The reactor can work with an internal pressure higher than the atmospheric pressure, to enhance the driving force for the membrane separation. In principle, the reactor could work under vacuum conditions in order to lower hydrogen concentration in the liquid phase. Anyhow, in these operating conditions, the use of a vacuum pump counters the benefits arising from the lack of a compressor to circulate the gas.

The first configuration presented is the one previously experimentally investigated by (Montante, et al., 2013a). The reactor is equipped with supports for the attached growth of bacteria (in green in Fig. 5.1), which are placed inside the draft tube only.

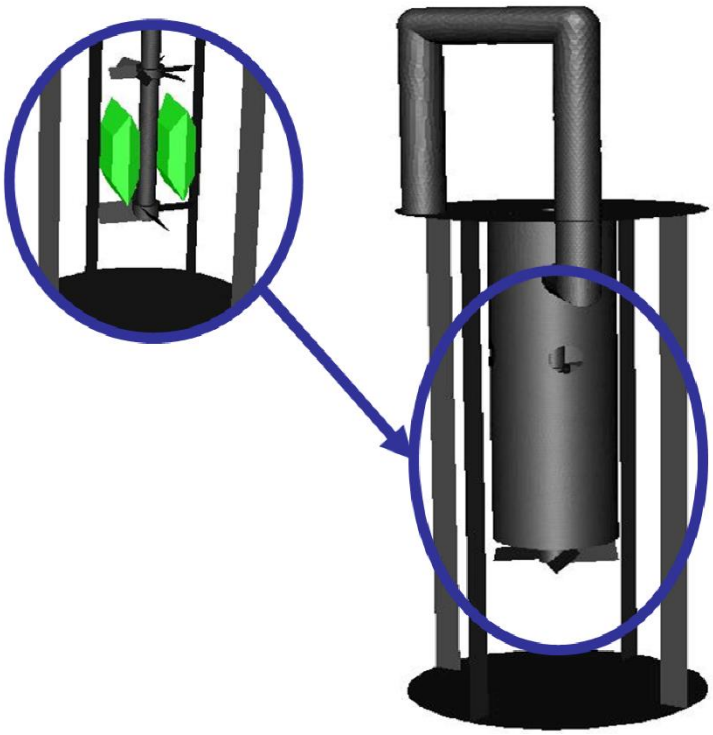

Fig. 5.1 – Bioreactor geometry, the part inside the draft tube is shown in the top-left circle.

In Fig. 5.1, the bioreactor is drawn without the cylindrical vertical wall enclosing the whole geometry, to show the internal baffles, recirculation pipe and draft tube. The focus on the top left circle is a cutaway drawing of the part enclosed by the draft tube, where the shaft, the two different impellers and the supports for the attached

growth of biomass are clearly visible. This configuration was adopted to keep the reactor volume outside the draft tube optically accessible and thus allowing the study of the flow field by means of the particle image velocimetry. More details on the experimental characterization of this reactor configuration can be found in (Montante, et al., 2013a).

A second configuration, shown in Fig. 5.2, was proposed to increase the hydrogen productivity and it consists in the same bioreactor where the supports for the attached growth fermentation are positioned outside the draft tube.

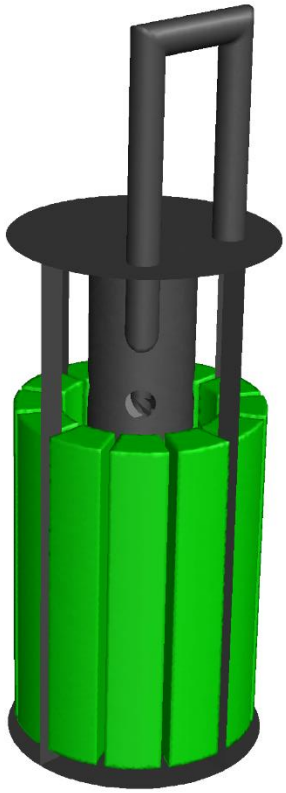

Fig. 5.2 - Bioreactor geometry, in this different configuration the biomass supports are positioned outside the draft tube

It is important to point out that just the first configuration was experimentally studied, whereas the second configuration was just studied from a computational perspective.

The different overall volume of the supports and their position inside the reactor is the main difference between the two geometries considered. In the configuration with the supports inside the draft tube, the total volume of the structures is $0.23L$ while it is $5.88L$ in the configuration with the supports outside the draft tube.

5.3 The CFD model equations

To simulate the gas-liquid bioreactors we have selected the two-fluid model, considering therefore the two fluids (liquid phase and gas phase) as interpenetrating continua interacting through the interphase transfer terms. Pure water ($\rho_L = 998 kg\ m^{-3}$, $\mu_L = 0.001 Pa\ s$) and pure nitrogen ($\rho_G \approx 1 kg\ m^{-3}$) were chosen as the two fluids at room conditions ($T = 20°C$ *and* $P = 101325 Pa$). Being the reactor in a turbulent regime, the continuity and momentum conservation equations (Navier-Stokes equations) for each fluid were Reynolds averaged, Eq. (5.1), and the system of differential equations was closed with the $k-\varepsilon$ turbulence model, with phase-averaged quantities, to extend the model to multiphase flows.

$$\frac{\partial}{\partial t}(\rho_i \alpha_i) + \nabla \cdot (\alpha_i \rho_i \boldsymbol{U_i}) \tag{5.1a}$$

$$\frac{\partial}{\partial t}(\alpha_i \rho_i \boldsymbol{U_i}) + \nabla \cdot (\alpha_i \rho_i \boldsymbol{U_i U_i}) = -\alpha_i \nabla(P) - \nabla \cdot (\alpha_i [\boldsymbol{T_i} + \boldsymbol{\tau^t}_i]) + \alpha_i \rho_i \boldsymbol{g} + \boldsymbol{F}_{drag}\{-S_i\} \tag{5.1b}$$

In Eq. (5.1), the subscript *i* indicates that the variable refers to the phase *i*, so α_i is the volume fraction of phase *i*, ρ_i is the density of phase *i* ($kg\ m^{-3}$) and so forth. The other variables are: the time-averaged velocity vector $\boldsymbol{U_i}$ (m s^{-1}), P the time-averaged pressure (Pa), $\boldsymbol{T_i}$ the time-averaged viscous stress tensor (Pa) and $\boldsymbol{g}$ the gravitational acceleration (m s^{-2}), the Reynolds stress tensor (Pa), is the term that accounts for turbulent fluctuations and it is modelled with the $k-\varepsilon$ turbulence model and the term in curly brackets is a momentum sink term used to model the pressure drops inside the porous supports. The liquid and gas phase momentum equations are coupled by means of an interphase momentum exchange term, $\boldsymbol{F}_{drag}$ ($Pa\ m^{-1}$), which

represents the time-averaged interphase drag term. This term depends on a coefficient (C_D, the drag coefficient) which is modelled with the Schiller and Naumann correlation, Eq. (5.2).

$$C_D = 24\left(1 + 0.15\,Re_p^{0.687}\right)/Re_p \tag{5.2}$$

In Eq. (5.2), Re_p is the particle Reynolds number calculated as:

$$Re_p = \boldsymbol{U_S} d_B \rho_L / \mu_L \tag{5.3}$$

where $\boldsymbol{U_S}$, the slip velocity (m s^{-1}), is defined as the difference between the velocities of the two different fluids and ρ_L and μ_L are the density and viscosity of the liquid phase, respectively. To solve Eq. (5.3) we need to provide the diameter of the bubble (d_B, [m]). A rigorous modelling approach would require that the local bubble diameter was calculated from the solution of a local population balance equation. Based on previous preliminary results on the two-phase fluid dynamics inside the reactor (Montante, et al., 2013a), the bubbles were considered as rigid spheres and a constant diameter of 0.5 mm was assumed. The same approach was adopted in a previous work (Montante, et al., 2013b) and the CFD results were validated for some classes of bubble diameters in mono- and bi- dispersed conditions ranging from 0.25 mm to 1.10 mm. It resulted that the bioreactor fluid dynamics was satisfactorily predicted, and that the accuracy of the simulations increased when multiple bubble classes were considered. In Fig. 5.3, the comparison between experimental data obtained with the particle image velocimetry (PIV) and the two-phase CFD simulation with monodispersed bubbles with $d_B = 0.5mm$ is shown.

The supports geometry considered for the simulations differs from the real support geometry used in the experiments, therefore a perfect agreement between the two flow-fields is not achievable, nonetheless, the jet velocity module is satisfactorily predicted.

A convection-diffusion equation for each of the k^{th} species was solved in order to model the species transport in each phase *i*.

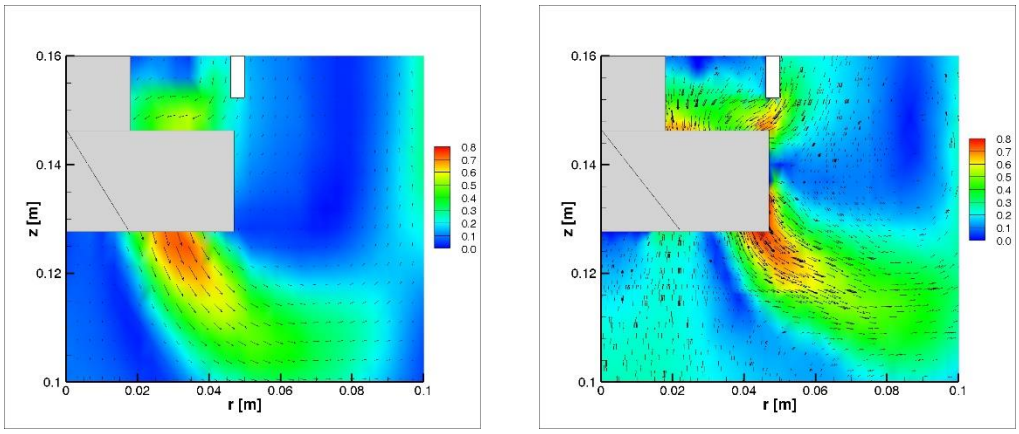

(a) (b)

Fig. 5.3 – Non-dimensional liquid-velocity at the lower impeller, as measured from the experimental data (a), and obtained from the CFD simulation with mono-dispersed bubbles with d_B = 0.5mm (b).

The conservation equation for each component assumes the following form:

$$\frac{\partial}{\partial t}\left(\alpha_i \rho_i Y_i^k\right) + \nabla \cdot \left(\alpha_i \rho_i \boldsymbol{U_i} Y_i^k\right) = -\nabla \cdot \left(\alpha_i \boldsymbol{J}_i^k\right) + \alpha_i R_i^k + \left(\dot{m}_{ij}^k - \dot{m}_{ji}^k\right) \tag{5.4}$$

Where Y_i^k is the mass fraction of the k^{th} component in phase i, $\boldsymbol{J}_i^k$ is the diffusion flux of the k^{th} component (kg m^{-2} s^{-1}), R_i^k is the net rate of production of species k by chemical reactions (kg m^{-3} s^{-1}) and $\dot{m}_{ij}^k$ quantifies the mass transfer of component k from phase i to phase j (kg s^{-1}). In Eq. (5.4), the terms on the LHS represent the rate of change in time and the advection of the mass of the k^{th} species in phase i, respectively. The first term on the RHS of Eq. (5.4) is modelled with a modified version of Fick's first law of diffusion, to take the turbulent diffusion into account:

$$\boldsymbol{J}_i^k = -\left(\rho_i D_i^k + \frac{\mu_t}{Sc_t}\right) \nabla Y_i^k \tag{5.5}$$

with D_i^k being the mass diffusion coefficient for species k in phase i ($m^2\,s^{-1}$), μ_t being the turbulent viscosity ($Pa\ s$) and Sc_t the turbulent Schmidt number equals to $\frac{\mu_t}{\rho D_t}$, where D_t is the turbulent diffusivity.

The second term in the RHS of Eq. (5.4) describes the biochemical reaction rate and it is illustrated in Section 5.4, whereas the third term is treated in detail in Section 5.5 and it expresses the mass transfer rate between the two different phases.

The term $\alpha_i R_i^k$ in Eq. (5.4) allows us to define a volumetric reaction rate that takes place just in the liquid phase on the surface of the porous supports of the system. The porous structure was modelled by adding a sink in the momentum balance equations, Eq. (5.1b) described by Eq. (5.6).

$$S_i = \frac{\mu_i}{\Gamma} \boldsymbol{U_i} + \frac{C_2}{2} \rho_i \boldsymbol{U_i}^2 \tag{5.6}$$

In Eq. (5.6) $1/\Gamma$ is the viscous resistance (m^{-2}) and C_2 is the inertial resistance (m^{-1}). The porous material was assumed isotropic, therefore a single value for each of the porous resistances was considered in each spatial direction. $1/\Gamma$ was taken equal to 228400m^{-2} and the value of C_2 was assumed to be 210m^{-1}, based on the known pressure drops of the Biomax ceramic porous carrier used in previous works (Alberini, 2013; Frascari et al., 2013).

5.4 Fermentation kinetic model

Dark fermentation has proved to be the most realistic technique for industrial scale bioreactors due to the relatively low energy requirements, the substantial hydrogen production rates and the possibility to ferment organic matter in liquid and solid wastes (Sivagurunathan et al., 2016). Despite the many advantages of the dark fermentation, moderate H_2 yields are obtained, mostly due to the conspicuous co-formation of soluble metabolites: mainly volatile organic acids and alcohols. The net effect is that a considerable amount of chemical energy stored in the fermentation raw material is diverted to by-product formation and remains unexploited (Sivagurunathan et al., 2016). The energy-rich effluents can be subjected to anaerobic digestion processes to obtain biomethane, photofermentative treatments or undergo microbial electrohydrogenesis (Bakonyi et al., 2018; Nathao, et al., 2013; Ren et al., 2011). The dark fermentation process not only produces soluble metabolites,

but also CO_2 among the others. This can lead to difficulties during the gas separation, that would require the use of one or more membranes to purify the H_2 current.

As shown in Section 5.3, we need to model the biochemical reaction kinetic in order to close the species transport equation, Eq. (5.4). A characterized bioreaction for the production of hydrogen was found in literature (Frascari et al., 2013) and, among the different experimental schemes presented in the document, we selected the case of hydrogen production from the fermentation of glucose by attached cells of *Thermotoga neapolitana*.

The use of a stripping gas to lower the H_2 concentration in the reactor volume has proven to have beneficial effects in the biohydrogen production through dark fermentation (Munro et al., 2009). For this reason, N_2 is used as a stripping gas, as already done by Frascari et al. (2013) and by Nguyen et al. (2010) for the *T. neapolitana* dark fermentation. The use of CO_2 as stripping gas is also documented (Łukajtis et al., 2018) but it may cause local pH variation resulting in suboptimal production of biohydrogen (Munro et al., 2009). Moreover, using nitrogen as stripping gas does not require an additional gas feed, being the N_2 gas already employed to displace the oxygen in the broth, at the beginning of the fermentation.

Being the exact bioreaction scheme extremely complex and beyond the scope of our modelling effort, we decided to simplify the reaction with the following expression:

$$Glucose \rightarrow Hydrogen + Acetic\ Acid \tag{5.7}$$

Being the goal of this work to present a comprehensive model strategy of the fluid-dynamics, reaction and mass-transfer rates, we decided to simplify the bioreaction mechanism. Implementing a more realistic scheme does not require a deep change in the modelling procedure (see Fig. 5.4), provided data are available for the implementation.

In fact, the conservation equations, as shown in Section 5.3, require that just the mass is conserved (in both time and space) without regard for the number and type of atoms transported, therefore the simplification introduced in Eq. (5.7) does not affect the generality of the conservation equations.

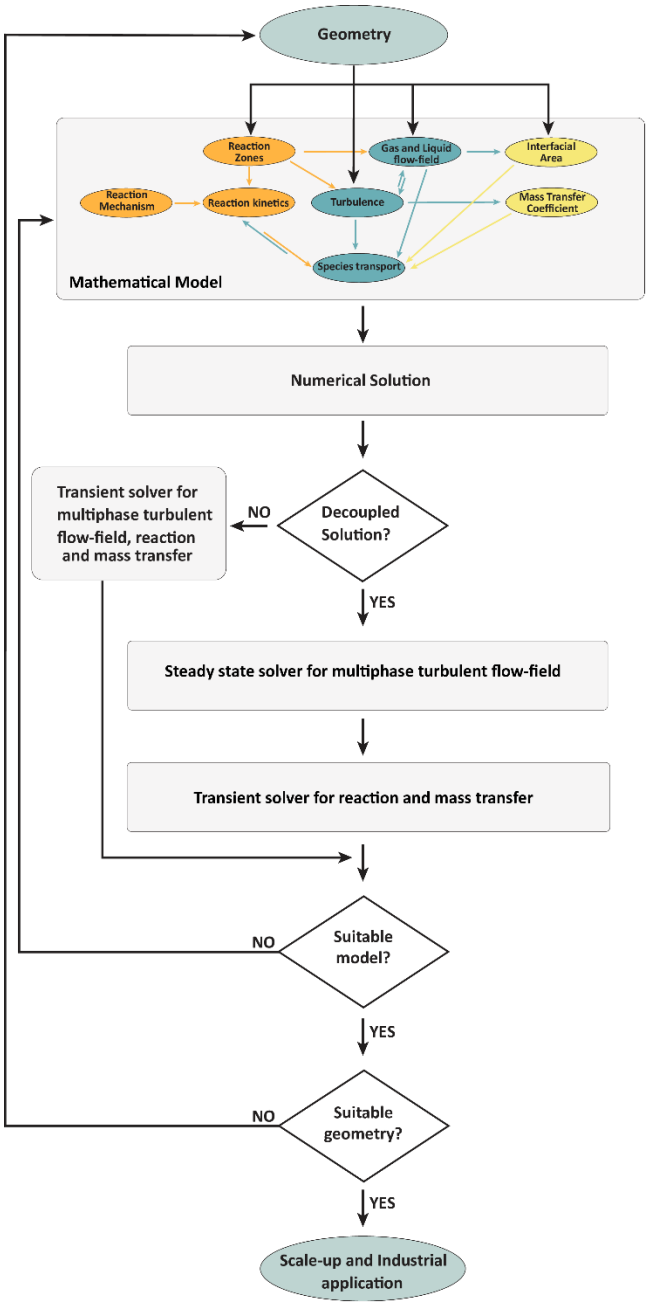

Fig. 5.4 – Scheme of the model formulation and solution procedure.

A H_2/substrate yield of $7.2 mmol_{H_2}\, g_{sugars}^{-1}$ was experimentally reported by Frascari et al., (2013), from which the hydrogen stoichiometric coefficient for the simplified reaction was obtained. The acetic acid stoichiometric coefficient was derived from the mass conservation equation, and the resulting reaction is:

$$1\ Glucose \rightarrow 1.30\ Hydrogen + 2.96\ Acetic\ Acid \tag{5.8}$$

Once again it should be pointed that the conservation equations (implemented in the software) require that only the mass is conserved. The initial concentration of glucose in the liquid phase was taken from Frascari et al., (2013) equal to $7.5 g\ L^{-1}$, corresponding to $4.15E-02 kmol\ m^{-3}$.

Frascari et al., (2013) modelled the biohydrogen production from glucose by attached cells of *T. neapolitana* with Andrews model of substrate inhibition:

$$q_L^{H_2} = q_{L,max}^{H_2} \times \frac{S}{K_S + S + S^2/K_I} \tag{5.9}$$

where $q_{L,max}^{H_2}\left(mmol_{H_2} g_{protein}^{-1} h^{-1}\right)$ is the maximum H_2 specific production rate, S is the substrate concentration ($g_{sugar} L^{-1}$), K_S is the half-saturation constant ($g_{sugar}\ L^{-1}$) and K_I is the inhibition constant ($g_{sugar}\ L^{-1}$).

The rate of production of H_2 must be converted in SI units, in order to close the conservation equations implemented in the CFD software.

While the conversion in SI units is straightforward for the two constants of the model and the substrate concentration, some more data is needed for the conversion of the maximum H_2 specific production rate. In fact, if we examine Tab. 5.1, we notice that $q_{L,max}{}^{H_2}$ is defined per unit mass of bacteria in term of grams of proteins in the cells, since the biomass concentration was quantified with the Lowry protein assay.

Tab. 5.1 – Kinetic parameters obtained by Frascari et al., (2013)

Parameter	Original value	Converted value	
$q_{L,max}^{H_2}$	6.1 $mmol\ g^{-1}\ h^{-1}$	$5.1E-07$	$kmol\ kg^{-1}\ s^{-1}$
K_S	0.09 $g\ L^{-1}$	$5.0E-04$	$kmol\ m^{-3}$
K_I	90 $g\ L^{-1}$	$5.0E-01$	$kmol\ m^{-3}$

Alberini, (2013) found that the protein content is about 30% of the dry weight of *T. neapolitana* therefore, once we can estimate the cell concentration in the attached-growth supports, we can obtain $\hat{q}_{L,max}^{H_2}$, the maximum H_2 production rate in SI units of $kmol\ kg^{-1}\ s^{-1}$. The reaction rate in SI units becomes:

$$R_L^{H_2} = R = \hat{q}_{L,max}^{H_2} \times \frac{C_L^S}{K_S + C_L^S + (C_L^S)^2 / K_I} \times CC \times PM_{H_2} \tag{5.10}$$

where $R_L^{H_2}$ is the H_2 production rate, ($kg\ m^{-3}\ s^{-1}$), C_L^S is the substrate molar concentration in the liquid phase ($kmol\ m^{-3}$), CC is the concentration of *T. neapolitana* in the supports, assumed to be $10.5 kg\ m^{-3}$ and PM_{H_2} is the molecular weight of hydrogen ($kg\ kmol^{-1}$). In the work of Alberini, (2013), it is possible to find the porous support data and the biomass concentration on the support. This information is reported in Tab. 5.2.

Tab. 5.2 – Porous support data by Alberini, (2013)

Name	**Biomax**
Porosity	67%
Density	777 $kg\ m^{-3}$
Material	Ceramic
Biomass concentration on the support	10.5 $kg_{cells}\ m_{bulk}^{-3}$

5.5 Mass transfer model

Improving H_2 desorption results in favorable thermodynamic conditions for H_2 production, in fact when the rate of hydrogen production exceeds the interphase mass transfer high H_2 concentrations may be encountered in the reactor. This phenomenon is called *supersaturation* and it can cause unwanted changes in the microbial community that results in lower hydrogen production (Bakonyi et al., 2017). Hydrogen stripping from the liquid medium can mitigate the issues related to hydrogen supersaturation.

The interphase molar flux of hydrogen, $\dot{n}_{L\to G}^{H_2}$ ($kmol\ m^{-3}\ s^{-1}$) was modelled according to Eq. (5.11):

$$\dot{n}_{L\to G}^{H_2} = N = k_L a(C_L - C_L^I) \tag{5.11}$$

where k_L is the liquid-side mass transfer coefficient ($m\ s^{-1}$), a is the interfacial area (m^2), $C_L{}^I$ is the molar concentration of hydrogen in the liquid phase at the interface between L and G ($kmol\ m^{-3}$) and C_L is the molar concentration of hydrogen in the liquid phase ($kmol\ m^{-3}$).

Eq. (5.11) is solved locally for each cell in the computational domain, for this reason a local description of the terms in the RHS of Eq. (5.11) is needed. The molar concentration of each species is derived from the species transport equations, already described in Section 5.3, hence no further modelling is required to have the local concentration of hydrogen.

For the evaluation of H_2 concentration at the gas-liquid interface, the gas phase mass transfer resistance has been neglected due to the H_2 low solubility in the liquid phase. Therefore:

$$C_L^I = (P/\mathcal{H})\, C_G \tag{5.12}$$

with P being the pressure, C_G the molar concentration of H_2 in the gas phase and $\mathcal{H}$ being the Henry's constant.

5.5.1 Local mass transfer coefficient: $k_L a$

As also described by Gimbun, et al., (2009) and more recently by Bach et al., (2017), we used the expression for the liquid-side mass transfer coefficient derived by Lamont & Scott, (1970) under the assumption that small-scale turbulent structures affect the mass transfer rate. The eddy cell model (Lamont & Scott, 1970) uses the isotropic turbulence theory of Kolmogorov to refine the surface renewal model (Danckwerts, 1951), obtaining this expression for k_L:

$$k_L = K D_L^{0.5} \left(\frac{\epsilon_L}{\nu_L}\right)^{0.25} \tag{5.13}$$

with D_L being the diffusion coefficient ($m^2\ s^{-1}$), ϵ_L being the turbulent dissipation rate in the liquid phase ($m^2\ s^{-3}$), ν_L the liquid dynamic viscosity ($m^2\ s^{-1}$) and K the dimensionless constant of the model, equals to 0.4. The turbulent dissipation rate was obtained from the solution of the RANS equations together with the two-phase turbulence model equations.

The interfacial area is the total area of contact between the gas and the liquid phase. From this definition is clear that the two-fluid model cannot predict the interfacial area since it describes the phases of the multiphase flow as interpenetrating continua. The phasic volume fractions, denoted here by α_L and α_G, represent the space occupied by each phase and the laws of conservation of mass and momentum are satisfied by each phase individually. To calculate the interfacial area a closure model is needed.

Hänsch, et al. (2012) reported that after a critical volume fraction $\alpha_G^{cr} = 0.3$, coalescence rate increases sharply and the bubbly flow transitions to a flow with resolved structures, in both vertical and horizontal flows. For this reason, different modelling approaches were used to define the interfacial area, depending on the local volume fraction. When α_G is below α_G^{cr}, it was hypothesized that only bubbles with the assigned diameter of $d_B = 0.5mm$ were present, resulting in an interfacial area (per unit volume of the grid cell) of:

$$a = 6\alpha_G / d_B \tag{5.14}$$

When $\alpha_G^{cr} < \alpha_G < 0.5$, it was assumed that the sharp increase in coalescence rate formed a single bubble in the grid cell, resulting in an interfacial area per unit volume of:

$$a = 4\pi \frac{\left(\frac{3}{4\pi}\alpha_G\right)^{2/3}}{\left(6\sqrt{2}V_{cell}\right)^{1/3}} \tag{5.15}$$

where V_{cell} is the volume of the grid cell (m^3).

On the other hand, when α_G exceeds 0.5, we assumed that some type of phase inversion takes place and the water phase forms a drop-like structure with interfacial area per unit volume of:

$$a = 4\pi \frac{\left(\frac{3}{4\pi}\alpha_L\right)^{2/3}}{\left(6\sqrt{2}V_{cell}\right)^{1/3}} \tag{5.16}$$

This simplified approach allows to close the set of equations needed to model the interphase mass transfer in the context of the two-fluid model.

5.6 Computational domain and solution procedure

The CFD software ANSYS Fluent 17.0 was adopted for the simulations. The model equations were solved in two computational domains, one for each geometrical configuration. The two geometries were discretized with 1.68 million tetrahedral cells (the configuration with the supports inside the draft tube) and with 2.30 million tetrahedral cells (the configuration with the supports outside the draft tube), using the software ANSYS ICEM CFD 17.0. The discretized geometries (meshes) were divided into four different blocks: one for the supports, two for the fluids close to the impellers and one for the remaining fluid, in order to describe the porous support and for dealing with the relative motion of the rotating impeller and the steady baffles and supports (by using the "multiple reference frame" algorithm, MRF). Still and ungassed liquid was considered as the initial condition for the simulations, with the liquid level fixed at $H = 1.55T$, corresponding to an overall gas volume fraction of approximately 22%. Firstly, just the two-phase turbulent fluid flow was solved with a steady state solver and, when solution converged, the chemical reaction, species transport and interphase mass transport were solved with an unsteady solver in a "fixed" flow field, in order to reduce the computational time. Having decoupled the fluid dynamics from the species transport allowed us to use a fairly large time step equal to $0.1s$: the underlying assumption is that the product formation does not affect the flow field in the system. A sink term for the hydrogen in the gas phase was introduced in the outer part of the pipe, to simulate product removal from a membrane module. With the workstations available in our facility, approximately an hour and a half were required to simulate 1 second of process.

A simplified flowchart of the solution procedure is reported in Fig. 5.4. The block called “mathematical model” is detailed to highlight the different models presented in the sections above and to explain the interplay of the different models.

5.7 Results and discussion

5.7.1 Fluid dynamics

The first step in the simulation of hydrogen production through fermentation in the two configurations was to solve the two-phase flow field. In Fig. 5.5 the liquid-phase flow fields are shown by means of contour maps and vector fields where the color of the map indicates the velocity magnitude and the arrows indicate the direction of the liquid velocity.

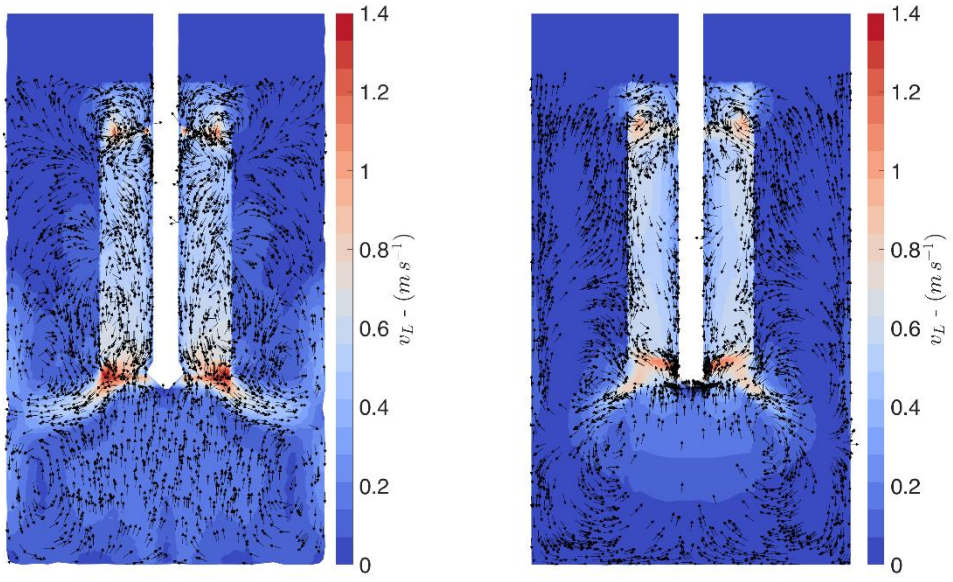

(a) (b)

Fig. 5.5 - Liquid flow field for the configuration with the supports inside (a) and outside (b) the draft tube. The contour maps indicate the liquid velocity magnitude, whereas the fixed-length vectors indicate just the local direction of the flow.

The vectors are shown in a plane passing through the vertical axis of the pipe for the recirculation of the gas-phase and, to improve the readability of the picture, the vectors have a fixed length. The arrows show that the fluid is pumped out of the draft tube at a high velocity (red color) and that the discharge jet of the lower impeller forms a 45° angle with the vertical and radial axis, approximately.

This is in agreement with what one would have expected, since the PBT is a mixed flow impeller (radial and axial flow) and its blades are tilted by 45°. The liquid pumped from the lower impeller forms two recirculation loops, one above and one below the impingement point.

The liquid then moves towards the top of the reactor with a small mean velocity and it enters the draft tube from the holes located just above the upper PBT. The upper impeller, then, forces the liquid towards the lower PBT.

In Fig. 5.5a, the liquid velocity field in the configuration with the supports inside the draft tube is shown, while Fig. 5.5b shows the configuration with the supports outside the draft tube. The mean velocity field is very similar, but few differences are noticeable. In Fig. 5.5b, the supports located in front of the lower PBT interact with the discharge jet of the lower impeller and the recirculation loops are smaller with respect to Fig. 5.5a. The interaction between lower discharge jet and supports produces a backward flow towards the impeller that results in some of the liquid being pumped upwards, close to the shaft. The porous structures channel the flow, limiting the misalignment of the velocity vectors. As a result, the velocity vectors are more aligned in the upward motion outside the draft tube (Fig. 5.5b), as well as in the downward motion inside the draft tube (Fig. 5.5a), with respect to the opposite configurations.

The peculiar configuration of the reactor generates a gas flow from the outer part of the tank to the internal one, where the impellers motion produces a vortex that ingests the gas phase and it disperses the bubbles in the liquid. The fluid dynamics of the reactor with the supports located inside the draft tube was previously characterized by Montante, et al. (2013a) and the reader is referred to the publication for further information. The predicted gas flow rate circulating from outside the draft tube to the inside, through the external pipe, is $7.82 Lh^{-1}$ for the configuration with the supports inside the draft tube and $7.36 Lh^{-1}$ for the other configuration, meaning that small but noticeable differences are distinguishable in the two configurations

when the impellers rotate at $N = 360 rpm$. One possible explanation is that the interaction between lower discharge jet and supports affects the drawdown efficiency of the impellers. The importance of the lower impeller in the gas recirculation was pointed out in a previous study. In fact, Montante, et al. (2013a) tested a number of impeller types, sized and clearances and concluded that the bottom impeller had to be chosen carefully, since a nonoptimal impeller geometry can result in failure of gas circulation. The reactor two-phase fluid dynamics analysis together with the validation of the CFD models with experimental data for the configuration with the supports inside the draft tube were already completed by Montante, et al. (2013b), therefore no further results concerning the two-phase fluid dynamics are reported in this work.

Being the power consumption an important process variable, we calculated the power draw as obtained by the simulations with the supports inside and outside the draft tube. For the first configuration the power drawn by the impellers is 3.20 *W*, whereas for the latter is 3.24 *W*. In a previous experimental work (Montante, et al., 2013a), the power drawn by the impellers for the bioreactor configuration with the supports inside the draft tube was measured at 350 *rpm* and resulted equal to 2.99 *W*. The real and simulated values of the power consumption for the configuration with the supports inside the draft tube are in good agreement and the configuration with the supports outside the draft tube does not appreciably change the power consumption.

5.7.2 Mass transfer coefficients

The local liquid-side mass transfer coefficient and the local interfacial area distribution are easily calculated once the two-phase flow field is established, in fact these two quantities are fixed in time since we decoupled the solution of the flow field from the solution of the species transport. In Fig. 5.6, k_L and a are shown, as calculated for the bioreactor configuration with the supports inside the draft tube.

Solving Eq. (5.13) in the context of the turbulent two-fluid model entails calculating k_L in the whole volume of the reactor even though the liquid phase does not reach the top part of the geometry. This result is a consequence of the two-phase turbulence model used in this work, which considers a single turbulent field obtained

with local average quantities. As expected, the local liquid-side mass transfer coefficient is higher where the turbulent dissipation rate is higher, i.e. in the proximity of the two impellers. Inside the supports, k_L is subject to a sharp reduction due to the lower fluid velocities inside the porous structures.

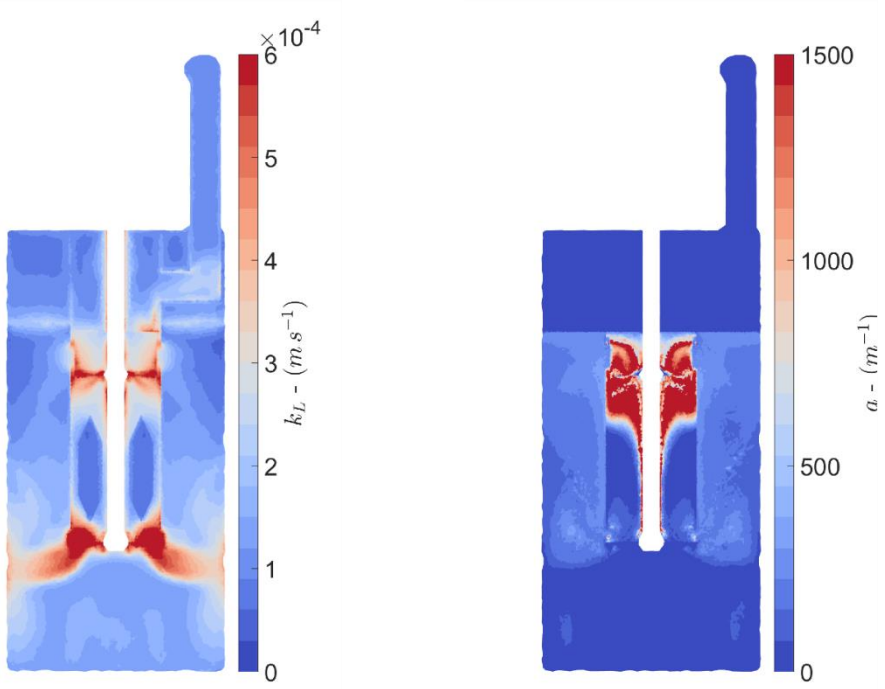

(a) (b)

Fig. 5.6 - k_L (a) and a (b) calculated from a fixed flow field, in the configuration with the supports inside the draft tube.

The interfacial area between the liquid phase and the gas bubbles basically follows the distribution of gas dissolved in the liquid phase, where the gas volume fraction is lower than α_G^{cr}, Eq. (5.14).

High gas hold-ups are located around the upper PBT, close to the ingesting-vortex, therefore high interfacial area values are calculated in this zone. The liquid flow drags the gas from the upper PBT to the lower PBT inside the draft tube, decelerating inside the porous structures (therefore decreasing the drag force on the bubbles) and allowing fraction of the gas phase to ascend the draft tube, towards the upper impeller. The liquid deceleration is just in part due to the porous support: as a matter of

fact, the liquid deceleration is also observed in the configuration with the supports outside the draft tube, Fig. 5.5b. As is well-known, just a fraction of the fluid pumped by the PBT impeller move towards the bottom of the tank, whereas the other fraction is recirculated towards the impeller, as the discharge jet hits the wall of the draft tube. Accounting for the mechanisms explained above, it is straightforward to explain that the lower velocities in the draft tube are generated by a lower fluid flow rate with respect to the flow rate overall pumped by the impeller. In the unobstructed outer part of the reactor, the interfacial area is almost uniform.

The considerations made for the geometry with the supports inside the draft tube also hold for the other configuration (Fig. 5.7).

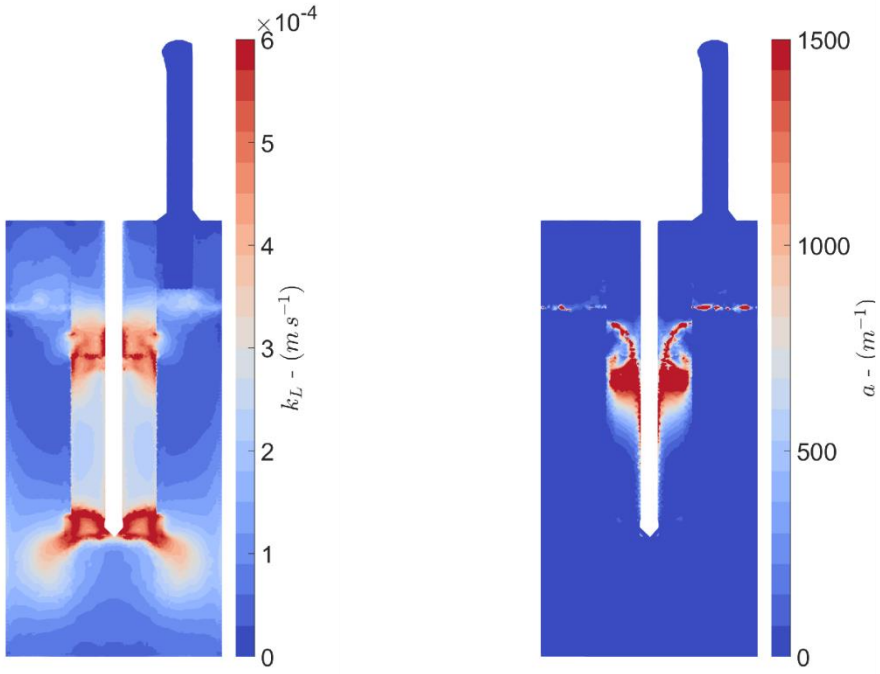

(a) (b)

Fig. 5.7 – k_L (a) and a (b) calculated from a fixed flow field, in the configuration with the supports outside the draft tube.

The liquid-side mass transfer coefficient inside the draft tube, Fig. 5.7a, assumes higher values, with respect to the same zone in Fig. 5.6, since here the flow field it is not disturbed by the porous supports. The interaction between lower discharge jet and the porous structures, however, impairs the impellers drawdown performance

and, as a result, less gas is dragged towards the lower PBT. It is important to keep in mind that the planes shown in this Section slice the porous support, therefore a lower interfacial area is expected in the zone outside the draft tube, with respect to the same zone in Fig. 5.6, as already seen for the supports placed inside the draft tube.

Fig. 5.8 compares the volumetric mass transfer coefficient (k_La, s^{-1}), that is the product between the liquid-side mass transfer coefficient and the interfacial area between the liquid phase and the gas bubbles) in the two different configurations.

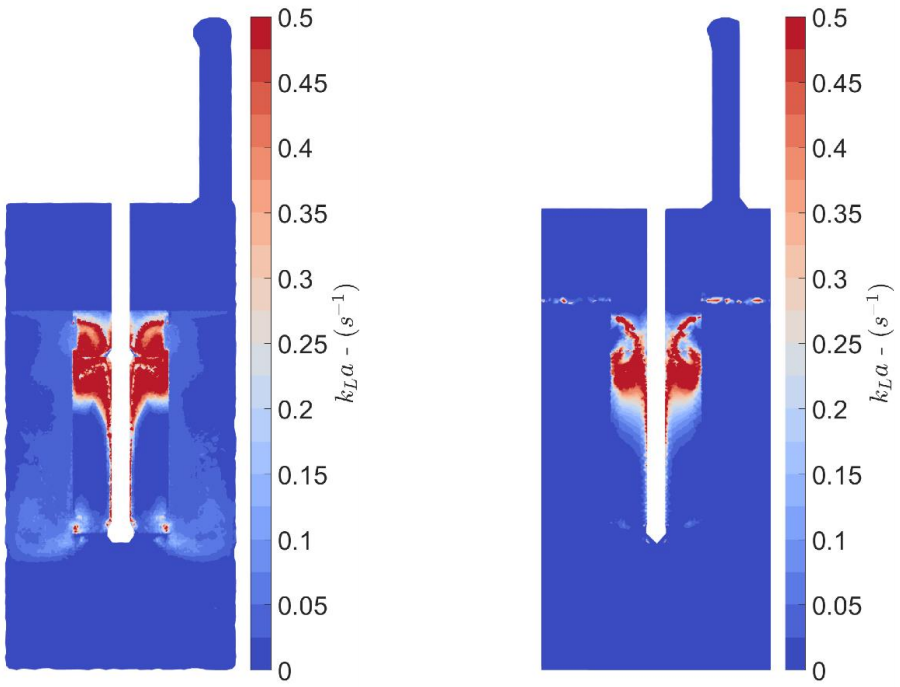

(a) (b)

Fig. 5.8 – k_La calculated from a fixed flow field, in the configuration with the supports inside the draft tube (a) and in the configuration with the supports outside the draft tube (b).

The figures illustrate that the spatial limiting factor is the interfacial area, in fact the contour map of k_Las closely resemble the contour maps of the interfacial areas (shown in Fig. 5.6b and Fig. 5.7b), meaning that just the reactor zones where the interfacial area is high produce high values of the volumetric mass transfer coefficient. Limited to the k_La analysis, it would seem that the reactor configuration with the supports inside the draft tube is the most efficient, however we have to assess the overall production of H_2 as well as the interphase molar flux of hydrogen from the

liquid to the gas phase, in order to evaluate the performances of the two configurations.

5.7.3 Hydrogen production and stripping: supports inside the draft tube

After obtaining the local volumetric mass transfer coefficients in both the configurations studied, we turned our attention to the hydrogen production and its removal from the liquid phase. As explained in Section 5.6, the above discussed data were obtained with a steady state solver, whereas data concerning the species transport had to be calculated through a time-dependent simulation.

In Fig. 5.9 a snapshot of the reactor with the porous supports inside the draft tube during the initial stage of the reaction ($t \approx 1s$) is presented.

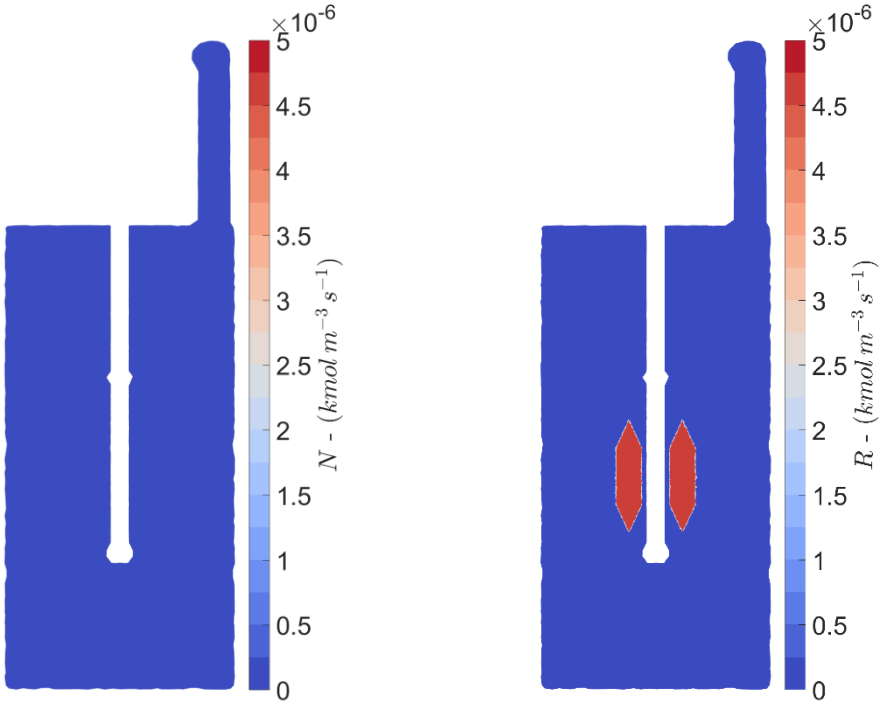

(a) (b)

Fig. 5.9 – Local interphase hydrogen molar flux (a) and chemical reaction rate (b) after 1s of simulated time, in the configuration with the supports inside the draft tube.

The contour map of the local mass transfer rate after 1s (Fig. 5.9a) and the contour map of the reaction rate (Fig. 5.9b) are compared with the same range of rates in the color map, to simplify the discussion.

At the very beginning of the process, the interphase mass transfer is considerably slower than the reaction rate due to the low H_2 concentration. The overall hydrogen mass transported from the liquid phase to the gas phase per unit time, in the whole volume, is $1.50E-13 kmol\ s^{-1}$, while the production of hydrogen at the beginning of the process is $1.12E-09 kmol\ s^{-1}$. From this analysis we can observe how, after few seconds since the beginning of the reaction with this reactor configuration, the N_2 cannot strip enough hydrogen from the aqueous phase and it starts to accumulate in the liquid.

As the concentration of hydrogen rises in the liquid, the interphase mass transfer driving force grows and, consequently, it boosts the overall mass transfer rate. After a little more than 3 minutes ($\approx 200s$), the accumulation of hydrogen in the system slows (Fig. 5.10), meaning that the production of hydrogen is partially compensated by the hydrogen removal.

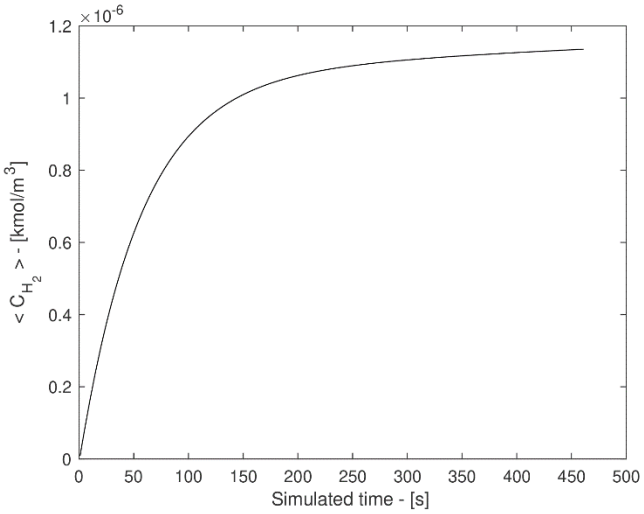

Fig. 5.10 – Mean molar concentration of H_2 *inside the reactor*

Examining Fig. 5.11a, we notice that most of the interphase mass transfer occurs in the proximity of the higher impeller, where the volumetric mass transfer coeffi-

cient is larger. Almost all the stripping of the hydrogen produced in the porous supports happens in this relatively small portion of the reactor, therefore most of the reactor volume is unexploited, if we limit our attention to the H_2 production and stripping. As expected, the reaction rate does not change appreciably in the first minutes of the process, Fig. 5.11b.

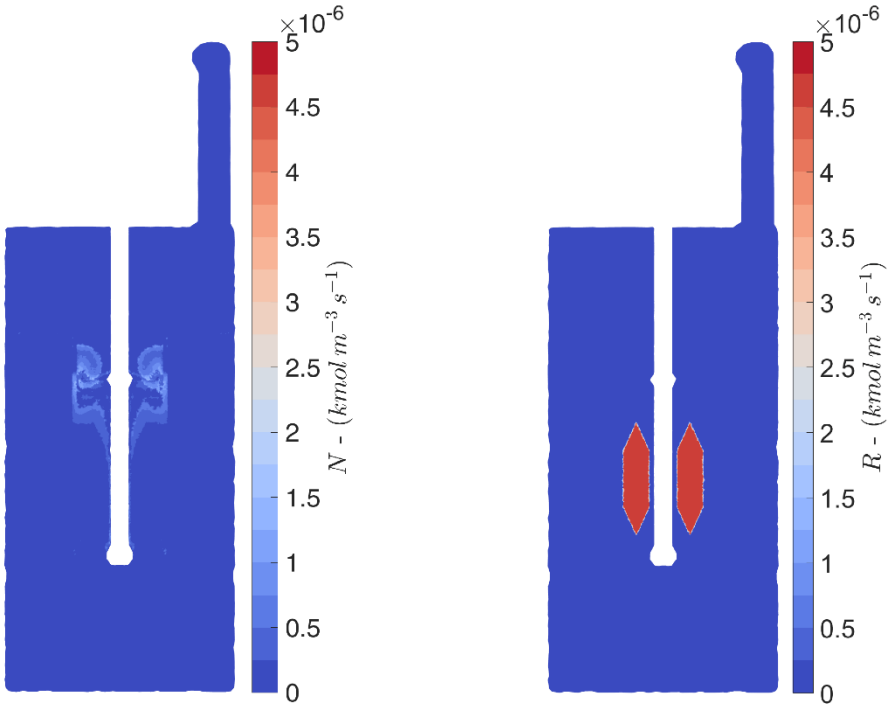

(a) (b)

Fig. 5.11 – Local interphase hydrogen molar flux (a) and chemical reaction rate (b) after 450s of simulated time, in the configuration with the supports inside the draft tube.

In Fig. 5.12 the hydrogen concentration in the liquid phase is reported and it is clear that the hydrogen has to recirculate from outside the draft tube to the inside, through the holes positioned in correspondence of the higher impeller, before being stripped by the recirculating nitrogen current.

This transport route is detrimental to the gas removal efficiency, since the hydrogen must travel through the bulk of the reactor (where k_La is low), before coming

into contact with the high volumetric transport coefficient zone. A possible solution would be to move the porous supports closer to the high $k_L a$ zone, close to the upper impeller, provided that this would not dramatically change the fluid dynamics.

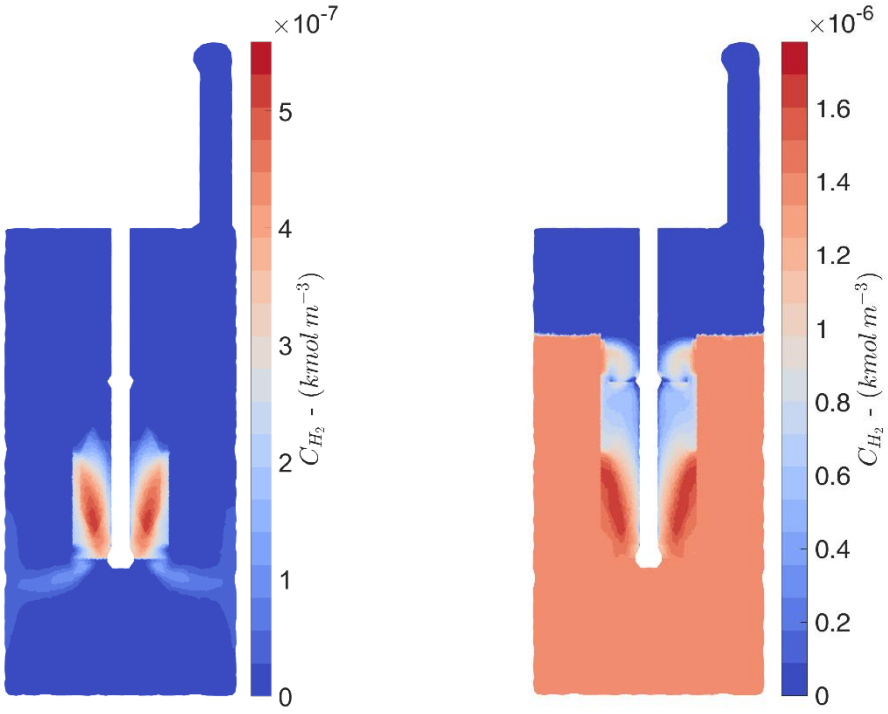

(a) $t = 1s$ (b) $t = 450s$

Fig. 5.12 – Local concentration of H_2 in the liquid phase at different simulated times, in the configuration with the supports inside the draft tube.

In Fig. 5.13, the dynamics of the integral interphase mass transfer rate and chemical reaction rate are shown.

It is possible to see the mass transfer rate slowing down after approximately 200 *s*, and to reach the steady state more than 38 *h* of simulated time are estimated, with a steady state molar rate of production/removal equal to $1.12E-09\ kmol\ s^{-1}$. The steady state volumetric flow rate of hydrogen is 1.4% of the nitrogen volumetric flow rate, therefore the hypothesis that we proposed in Section 5.6 (the product formation does not affect the two-phase flow field) may be acceptable.

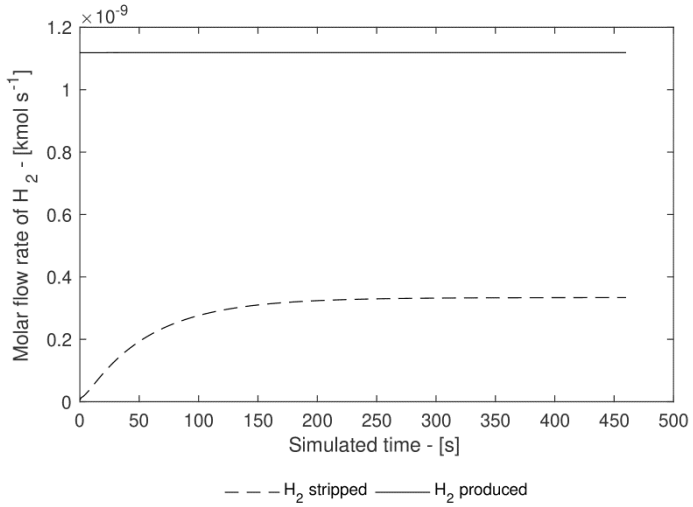

Fig. 5.13 – Integral interphase mass transfer rate and chemical reaction rate, in the configuration with the supports inside the draft tube.

5.7.4 Hydrogen production and stripping: supports outside the draft tube

Concerning the reactor configuration with the porous structures fixed outside the draft tube, after about 350*s* of simulated time the simulations did not reach a steady state (Fig. 5.14) and an optimistic evaluation identifies the steady state after more than 90 minutes of simulated time. After little more than 6*s*, the reactor with the supports outside the draft tube reached a mass transfer rate that matched the hypothesized steady state mass transfer rate in the other configuration. If the steady state projection were true, an interphase mass flow rate of $2.4E{-}08 kmol\ s^{-1}$ would be needed to ensure that all the hydrogen produced from the reaction is stripped. This predicted value is 32.9% of the nitrogen flow rate recirculated as the stripping gas, therefore decoupling the two-phase fluid dynamics from the species transport (the hypothesis proposed in Section 5.6), may produce inaccurate results.

Again, it should be borne in mind that the hydrogen production rate is more than an order of magnitude higher in the reactor configuration with the supports outside the draft tube, with respect to the other configuration.

Fig. 5.15 demonstrates how an efficient use of the reactor volume follows from placing the porous supports outside the draft tube.

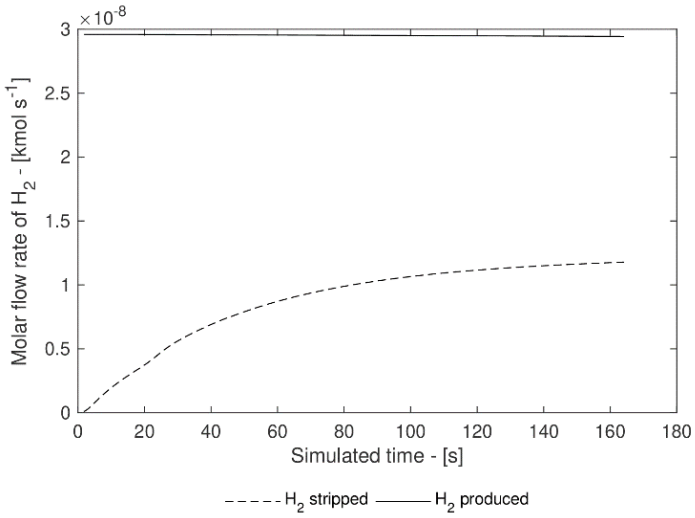

Fig. 5.14 – Integral interphase mass transfer rate and chemical reaction rate, in the configuration with the supports outside the draft tube.

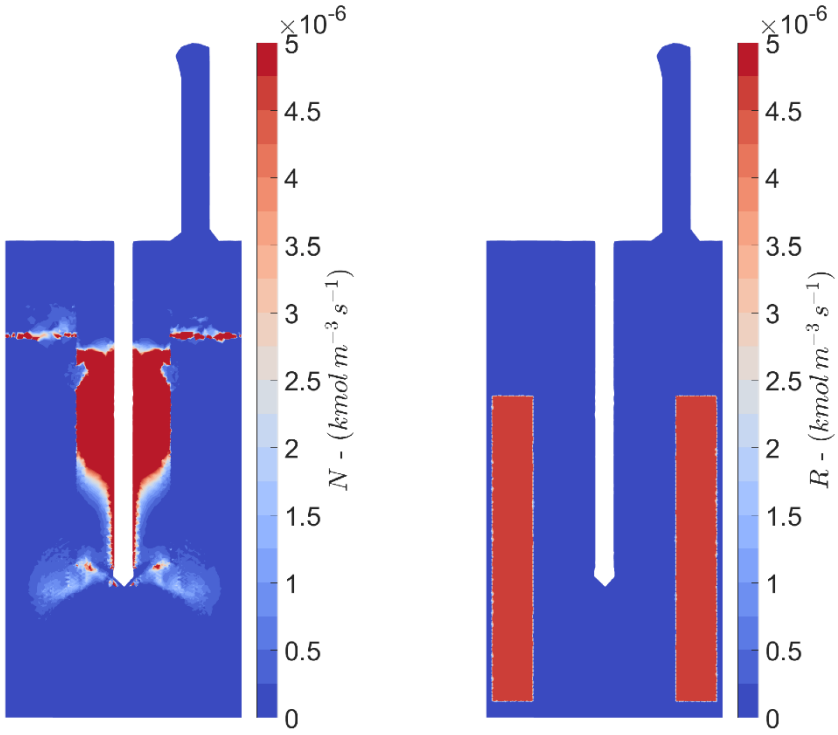

Fig. 5.15 – Local interphase hydrogen molar flux (a) and chemical reaction rate (b) after 350s of simulated time, in the configuration with the supports outside the draft tube.

In Fig. 5.15b we see that the production of hydrogen is confined in the zone outside the draft tube, whereas the majority of the interphase mass transfer occurs inside the draft tube. The hydrogen-rich liquid enters the inner volume from the holes in the draft tube and immediately encounters the high k_La zone where the largest part of the interphase mass transfer happens. Being the hydrogen concentration higher in this configuration (Fig. 5.16), with respect to the configuration with the supports inside the tube (Fig. 5.12), high interphase molar fluxes are also found in proximity of the lower PBT and at the interface, Fig. 5.15.

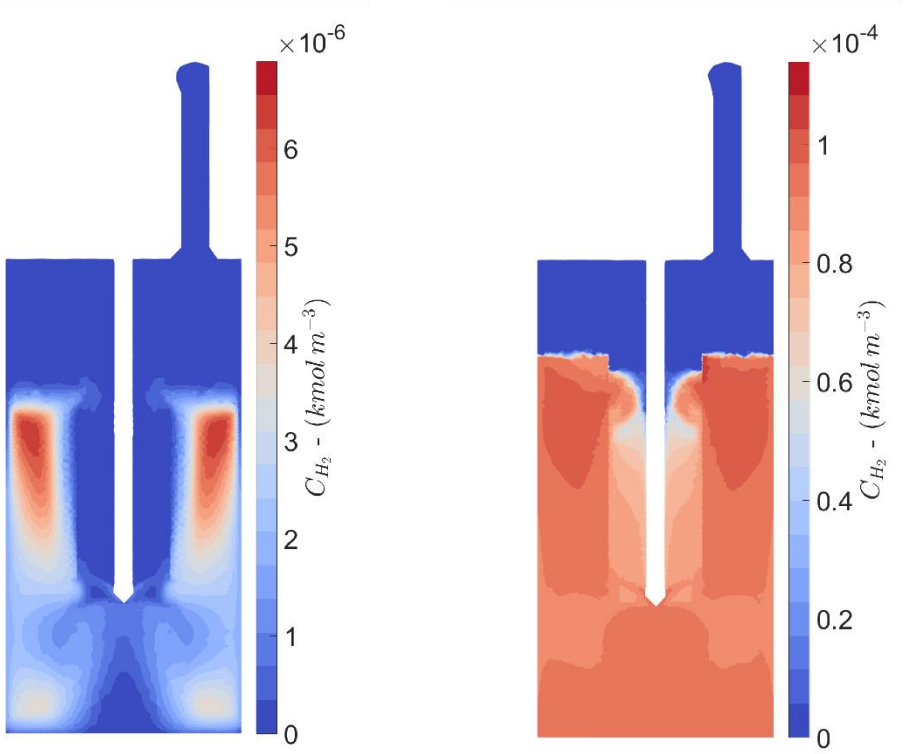

(a) *t = 1.7 s* (b) *t = 350 s*

Fig. 5.16 – Local concentration of H_2 in the liquid phase at different simulated times, in the configuration with the supports outside the draft tube.

Despite the high interphase fluxes, the chemical reaction rate is faster and hydrogen accumulates in the liquid phase. In Fig. 5.16b we can observe that the concentration of hydrogen in the liquid phase is lower where the mass transfer rate is higher.

Analyzing the hydrogen concentration in the gas phase of the reactor with the supports positioned outside the draft tube, Fig. 5.17, we notice how in the headspace inside the draft tube the product concentration is considerably high. A possible explanation is that just a portion of the gas that participates in the interphase mass transfer in the region close to the upper PBT is then entrained into the liquid towards the lower PBT, while the remaining part recirculates toward the top of the reactor. As a result, hydrogen accumulates in the gas head above the upper PBT. The gas current increases its concentration as the bubbles are transported in the liquid, meaning that hydrogen is being stripped from the aqueous environment.

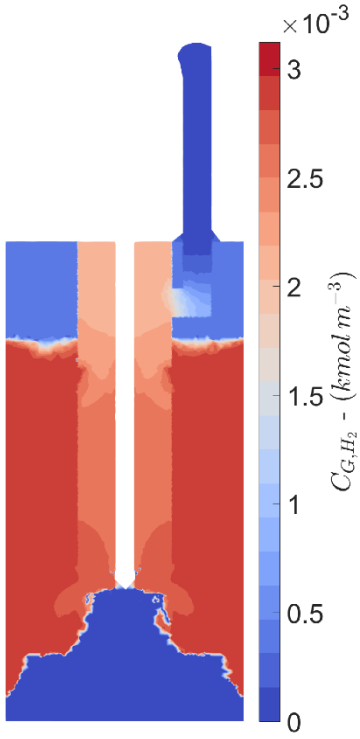

Fig. 5.17 – Local concentration of H_2 in the gas phase, after 350s of simulated time.

The concentration of hydrogen in the gas drops remarkably at the liquid-gas interface, since the hydrogen-rich gas flow rate bubbling from the liquid is diluted in the gas space that was initially devoid of hydrogen. To reduce the transitory phase required to increase the hydrogen concentration in the headspace outside the draft

tube, a possible improvement would be to reduce the volume of the reactor by decreasing the height of the tank, without overly reducing the headspace necessary for the gas-liquid disengagement. At the bottom of the reactor, there is a relatively large part of the equipment that does participate neither in the hydrogen production nor in the interphase mass transfer, Fig. 5.15. The dead zone is detrimental to the performance of the process and a potential solution would be to reduce the volume of the reactor by decreasing the length of the tank.

5.8 Conclusions

In this work, a CFD study of the biohydrogen production in a vortex-ingesting stirred tank reactor is proposed. The two-phase turbulent flow field of the reactor in two configurations (an existing one, which fluid dynamics was already experimentally characterized in literature, and a configuration proposed to maximize the biohydrogen production) was modelled with a two-fluid model approach.

A method to model the fermentative production and the stripping of biohydrogen in the self-ingesting stirred tank reactor was proposed and it can be easily extended to any more comprehensive kinetics and mass transfer models. A local model of the liquid-side mass transfer coefficient found in literature and a newly proposed interfacial area formulation for the two-fluid model were adopted, together with the Henry's gas law, to model the interphase flux of hydrogen. A substrate inhibition model for biohydrogen production by attached cells of the hyperthermophilic organism *Thermotoga neapolitana* in porous supports was selected to model the kinetic of a simplified biochemical reaction.

The CFD has proven helpful for the assessment of the performances of the reactors, allowing a local and an instantaneous analysis of the reaction rate, the interphase hydrogen fluxes and the other processes that take place inside the tank. We used the numerical simulations to study the hydrogen production and removal at different times, to evaluate the local behavior of the equipment and to propose geometrical changes, without the need to build the new porous supports and experimentally study the new configuration.

The analysis of the two different bioreactor configurations showed that the hydrogen stripping is successful in reducing the hydrogen concentration in the liquid

phase, the two-impeller configuration ensures the gas recirculation through the outer pipe, making this design suitable to be used with a gas separation system, to enhance recovery. Increasing the amount of biomass in the system results in an increased hydrogen production, but it can cause large H_2 supersaturation if the interphase mass transfer rate is not fast enough.

Future works will address the coupling between the fluid dynamics, the production and the removal of hydrogen and its effect on the overall performances of the reactor. A validation of the proposed model for the interfacial area with experimental data and the implementation of a more realistic kinetic for the biohydrogen production are aspects that may deserve further investigation.

5.9 Nomenclature

a	Interfacial area
C_2	Inertial resistance
CC	Cell concentration
C_D	Bubble drag coefficient
C_G	Molar concentration of H_2 in the gas phase
C_L	Molar concentration of H_2 in the liquid phase
C_L^I	Molar concentration of H_2 in the liquid at the L-G interface
C_L^S	Molar concentration of substrate in the liquid phase
d_B	Bubble diameter
D_i^k	Mass diffusion coefficient of the k^{th} species in the i^{th} phase
D_L	Diffusion coefficient of H_2 in the liquid phase
$\boldsymbol{F}_{drag}$	Interphase drag term
$\boldsymbol{g}$	Gravitational acceleration
H	Tank height
$\mathcal{H}$	Henry's constant
$\boldsymbol{J}_i^k$	Diffusion flux of the k^{th} species in the i^{th} phase
k	Turbulent kinetic energy
K	Eddy cell model constant
K_I	Inhibition constant
k_L	Liquid side mass transfer coefficient
$k_L a$	Volumetric mass transfer coefficient
K_S	Half saturation constant
$\dot{m}_{ij}^k$	Mass transfer of k^{th} species from the i^{th} to the j^{th} phase
$\dot{n}_{L\to G}^{H_2}$, N	Interphase H_2 molar flux from the liquid to the gas phase
P	Pressure
PM_{H_2}	H_2 molecular weight
$q_L^{H_2}$	H_2 specific production rate
$q_{L,max}^{H_2}$	Maximum H_2 specific production rate
R	Reaction rate
R_i^k	Net production rate of the k^{th} species in the i^{th} phase
$R_L^{H_2}$	H_2 production rate in the liquid phase
Re_p	Particle Reynolds number
S	Substrate concentration
S_i	Momentum sink for pressure drops inside the porous supports
Sc_t	Turbulent Schmidt number

t	Time
T	Tank diameter
$\boldsymbol{T_i}$	Viscous stress tensor of the i^{th} phase
$\boldsymbol{U_i}$	Velocity of the i^{th} phase
$\boldsymbol{U_S}$	Slip velocity
V_{cell}	Volume of the grid cell
Y_i^k	Mass fraction of the k^{th} species in the i^{th} phase

Greek letters

α_G	Gas volume fraction
$\alpha_G{}^{cr}$	Critical gas volume fraction
α_i	Volume fraction of the i^{th} phase
α_L	Liquid volume fraction
$1/\Gamma$	Viscous resistance
ϵ	Turbulent dissipation rate
ϵ_L	Turbulent dissipation rate in the liquid phase
μ_i	Dynamic viscosity of the i^{th} phase
μ_L	Liquid dynamic viscosity
μ_t	Turbulent viscosity
ν_L	Liquid kinematic viscosity
ρ_i	Density of the i^{th} phase
ρ_L	Liquid density
ρ_G	Gas density
$\boldsymbol{\tau^t_i}$	Reynolds stress tensor of the i^{th} phase

5.10 References

Alberini, A. (2013). *Produzione di bioidrogeno in dark fermentation da scarti dell'industria agroalimentale mediante l'impiego di batteri ipertermofili*. Alma Mater Studiorum – Università di Bologna. Retrieved from http://amsdottorato.unibo.it/5388/1/Alberini_Andrea_Tesi.pdf

Bach, C., Yang, J., Larsson, H., Stocks, S. M., Gernaey, K. V., Albaek, M. O., & Krühne, U. (2017). Evaluation of mixing and mass transfer in a stirred pilot scale bioreactor utilizing CFD. *Chemical Engineering Science*, *171*, 19–26. https://doi.org/10.1016/j.ces.2017.05.001

Bakonyi, P., Nemestóthy, N., Simon, V., & Bélafi-Bakó, K. (2014). Review on the start-up experiences of continuous fermentative hydrogen producing bioreactors. *Renewable and Sustainable Energy Reviews*, *40*, 806–813. https://doi.org/10.1016/j.rser.2014.08.014

Bakonyi, Péter, Buitrón, G., Valdez-Vazquez, I., Nemestóthy, N., & Bélafi-Bakó, K. (2017). A novel gas separation integrated membrane bioreactor to evaluate the impact of self-generated biogas recycling on continuous hydrogen fermentation. *Applied Energy*, *190*, 813–823. https://doi.org/10.1016/j.apenergy.2016.12.151

Bakonyi, Péter, Kumar, G., Koók, L., Tóth, G., Rózsenberszki, T., Bélafi-Bakó, K., & Nemestóthy, N. (2018). Microbial electrohydrogenesis linked to dark fermentation as integrated application for enhanced biohydrogen production: A review on process characteristics, experiences and lessons. *Bioresource Technology*, *251*, 381–389. https://doi.org/10.1016/j.biortech.2017.12.064

Bharathiraja, B., Sudharsanaa, T., Bharghavi, A., Jayamuthunagai, J., & Praveenkumar, R. (2016). Biohydrogen and Biogas – An overview on feedstocks and enhancement process. *Fuel*, *185*, 810–828. https://doi.org/10.1016/J.FUEL.2016.08.030

Cammack, R., Frey, M., & Robson, R. (2001). *Hydrogen as a fuel: learning from nature*. London: Taylor and Francis. Retrieved from http://citeseerx.ist.psu.edu/viewdoc/download?doi=10.1.1.474.9824&rep=rep1&type=pdf

Chang, J.-S., Lee, K.-S., & Lin, P.-J. (2002). Biohydrogen production with fixed-bed bioreactors. *International Journal of Hydrogen Energy*, *27*(11–12), 1167–1174. https://doi.org/10.1016/S0360-3199(02)00130-1

Cisneros-Pérez, C., Carrillo-Reyes, J., Celis, L. B., Alatriste-Mondragón, F., Etchebehere, C., & Razo-Flores, E. (2015). Inoculum pretreatment promotes differences in hydrogen production performance in EGSB reactors. *International Journal of Hydrogen Energy*, *40*(19), 6329–6339. https://doi.org/10.1016/j.ijhydene.2015.03.048

Danckwerts, P. V. (1951). Significance of Liquid-Film Coefficients in Gas Absorption. *Industrial & Engineering Chemistry*, *43*(6), 1460–1467.

https://doi.org/10.1021/ie50498a055

Delafosse, A., Collignon, M.-L., Calvo, S., Delvigne, F., Crine, M., Thonart, P., & Toye, D. (2014). CFD-based compartment model for description of mixing in bioreactors. *Chemical Engineering Science*, *106*, 76–85. https://doi.org/10.1016/j.ces.2013.11.033

Ding, J., Wang, X., Zhou, X.-F., Ren, N.-Q., & Guo, W.-Q. (2010). CFD optimization of continuous stirred-tank (CSTR) reactor for biohydrogen production. *Bioresource Technology*, *101*(18), 7016–7024. https://doi.org/10.1016/j.biortech.2010.03.146

Elqotbi, M., Vlaev, S. D., Montastruc, L., & Nikov, I. (2013). CFD modelling of two-phase stirred bioreaction systems by segregated solution of the Euler–Euler model. *Computers & Chemical Engineering*, *48*, 113–120. https://doi.org/10.1016/j.compchemeng.2012.08.005

Frascari, D., Cappelletti, M., Mendes, J. D. S., Alberini, A., Scimonelli, F., Manfreda, C., … Fedi, S. (2013). A kinetic study of biohydrogen production from glucose, molasses and cheese whey by suspended and attached cells of Thermotoga neapolitana. *Bioresource Technology*, *147*, 553–561. https://doi.org/10.1016/j.biortech.2013.08.047

Gimbun, J., Rielly, C. D., & Nagy, Z. K. (2009). Modelling of mass transfer in gas–liquid stirred tanks agitated by Rushton turbine and CD-6 impeller: A scale-up study. *Chemical Engineering Research and Design*, *87*(4), 437–451. https://doi.org/10.1016/j.cherd.2008.12.017

Guo, W.-Q., Ren, N.-Q., Wang, X.-J., Xiang, W.-S., Meng, Z.-H., Ding, J., … Zhang, L.-S. (2008). Biohydrogen production from ethanol-type fermentation of molasses in an expanded granular sludge bed (EGSB) reactor. *International Journal of Hydrogen Energy*, *33*(19), 4981–4988. https://doi.org/10.1016/j.ijhydene.2008.05.033

Guo, X. M., Trably, E., Latrille, E., Carrère, H., & Steyer, J.-P. (2010). Hydrogen production from agricultural waste by dark fermentation: A review. *International Journal of Hydrogen Energy*, *35*(19), 10660–10673. https://doi.org/10.1016/j.ijhydene.2010.03.008

Hänsch, S., Lucas, D., Krepper, E., & Höhne, T. (2012). A multi-field two-fluid concept for transitions between different scales of interfacial structures. *International Journal of Multiphase Flow*, *47*, 171–182. https://doi.org/10.1016/J.IJMULTIPHASEFLOW.2012.07.007

Kumar, G., & Buitrón, G. (2017). Fermentative biohydrogen production in fixed bed reactors using ceramic and polyethylene carriers as supporting material. *Energy Procedia*, *142*, 743–748. https://doi.org/10.1016/j.egypro.2017.12.121

Kumar, G., Mudhoo, A., Sivagurunathan, P., Nagarajan, D., Ghimire, A., Lay, C.-H., … Chang, J.-S. (2016). Recent insights into the cell immobilization technology applied for dark fermentative hydrogen production. *Bioresource Technology*, *219*, 725–737. https://doi.org/10.1016/j.biortech.2016.08.065

Lamont, J. C., & Scott, D. S. (1970). An eddy cell model of mass transfer into the surface of a turbulent liquid. *AIChE Journal*, *16*(4), 513–519.

https://doi.org/10.1002/aic.690160403

Li, C., & Fang, H. H. P. (2007). Fermentative Hydrogen Production From Wastewater and Solid Wastes by Mixed Cultures. *Critical Reviews in Environmental Science and Technology*, *37*(1), 1–39. https://doi.org/10.1080/10643380600729071

Łukajtis, R., Hołowacz, I., Kucharska, K., Glinka, M., Rybarczyk, P., Przyjazny, A., & Kamiński, M. (2018). Hydrogen production from biomass using dark fermentation. *Renewable and Sustainable Energy Reviews*, *91*, 665–694. https://doi.org/10.1016/j.rser.2018.04.043

Manish, S., & Banerjee, R. (2008). Comparison of biohydrogen production processes. *International Journal of Hydrogen Energy*, *33*(1), 279–286. https://doi.org/10.1016/j.ijhydene.2007.07.026

Markov, S. A. (2012). Hydrogen Production in Bioreactors: Current Trends. *Energy Procedia*, *29*, 394–400. https://doi.org/10.1016/j.egypro.2012.09.046

Mohsin, M., Rasheed, A. K., & Saidur, R. (2018). Economic viability and production capacity of wind generated renewable hydrogen. *International Journal of Hydrogen Energy*, *43*(5), 2621–2630. https://doi.org/10.1016/j.ijhydene.2017.12.113

Montante, G., Coroneo, M., & Francesconi, J. A. (2013). Computational Analysis of a Vortex Ingesting Bioreactor for Hydrogen Production. *CHEMICAL ENGINEERING TRANSACTIONS*, *32*(2012), 721–726. https://doi.org/10.3303/CET1332121

Montante, G., Magelli, F., & Paglianti, A. (2013). Fluid-dynamics characteristics of a vortex-ingesting stirred tank for biohydrogen production. *Chemical Engineering Research and Design*, *91*(11), 2198–2208. https://doi.org/10.1016/j.cherd.2013.04.008

Morchain, J., Gabelle, J.-C. C., & Cockx, A. (2014). A coupled population balance model and CFD approach for the simulation of mixing issues in lab-scale and industrial bioreactors. *AIChE Journal*, *60*(1), 27–40. https://doi.org/10.1002/aic.14238

Munro, S. A., Zinder, S. H., & Walker, L. P. (2009). The fermentation stoichiometry of Thermotoga neapolitana and influence of temperature, oxygen, and pH on hydrogen production. *Biotechnology Progress*, *25*(4), 1035–1042. https://doi.org/10.1002/btpr.201

Nathao, C., Sirisukpoka, U., & Pisutpaisal, N. (2013). Production of hydrogen and methane by one and two stage fermentation of food waste. *International Journal of Hydrogen Energy*, *38*(35), 15764–15769. https://doi.org/10.1016/j.ijhydene.2013.05.047

Nguyen, T.-A. D., Han, S. J., Kim, J. P., Kim, M. S., & Sim, S. J. (2010). Hydrogen production of the hyperthermophilic eubacterium, Thermotoga neapolitana under N2 sparging condition. *Bioresource Technology*, *101*(1), S38–S41. https://doi.org/10.1016/j.biortech.2009.03.041

Oh, S.-E., Iyer, P., Bruns, M. A., & Logan, B. E. (2004). Biological hydrogen production using a membrane bioreactor. *Biotechnology and Bioengineering*, *87*(1), 119–127.

https://doi.org/10.1002/bit.20127

Ren, N., Guo, W., Liu, B., Cao, G., & Ding, J. (2011). Biological hydrogen production by dark fermentation: challenges and prospects towards scaled-up production. *Current Opinion in Biotechnology*, *22*(3), 365–370. https://doi.org/10.1016/j.copbio.2011.04.022

Ri, P.-C., Ren, N.-Q., Ding, J., Kim, J.-S., & Guo, W.-Q. (2017). CFD optimization of horizontal continuous stirred-tank (HCSTR) reactor for bio-hydrogen production. *International Journal of Hydrogen Energy*, *42*(15), 9630–9640. https://doi.org/10.1016/j.ijhydene.2017.02.035

Show, K. Y., Zhang, Z. P., & Lee, D. J. (2008). Design of bioreactors for hydrogen production. *J. Sci. Ind. Res.*, *67*(11), 941–949. Retrieved from https://pdfs.semanticscholar.org/81f1/8b04b6a1118c665955be259edfc08016577f.pdf

Sivagurunathan, P., Kumar, G., Bakonyi, P., Kim, S.-H., Kobayashi, T., Xu, K. Q., … Bélafi-Bakó, K. (2016). A critical review on issues and overcoming strategies for the enhancement of dark fermentative hydrogen production in continuous systems. *International Journal of Hydrogen Energy*, *41*(6), 3820–3836. https://doi.org/10.1016/j.ijhydene.2015.12.081

Trad, Z., Fontaine, J.-P., Larroche, C., & Vial, C. (2016). Multiscale mixing analysis and modeling of biohydrogen production by dark fermentation. *Renewable Energy*, *98*, 264–282. https://doi.org/10.1016/j.renene.2016.03.094

Wang, X., Ding, J., Guo, W.-Q., & Ren, N.-Q. (2010). Scale-up and optimization of biohydrogen production reactor from laboratory-scale to industrial-scale on the basis of computational fluid dynamics simulation. *International Journal of Hydrogen Energy*, *35*(20), 10960–10966. https://doi.org/10.1016/j.ijhydene.2010.07.060

Wu, B. (2013). Advances in the use of CFD to characterize, design and optimize bioenergy systems. *Computers and Electronics in Agriculture*, *93*, 195–208. https://doi.org/10.1016/j.compag.2012.05.008

Chapter 6

Escherichia coli fermentation in bioreactors

A simple Interaction by Exchange with the Mean (IEM) mixing model is implemented to describe the glucose concentration segregations in industrial and laboratory scale bioreactors. This approach is coupled with a Population Balance Model (PBM) for the growth rate adaptation and a metabolic model dependent on the individuals state, both from the literature (Pigou & Morchain, 2015). The model formulation is validated against different published experiments and it is shown that the IEM model reduces the computational costs when just the segregation of few species is of interest. A model for the maintenance costs of *Escherichia coli* subject to glucose concentration fluctuation is also presented and implemented in the context of the IEM mixing model. A Eulerian formulation of the effects of the substrate fluctuations on the maintenance rate is proposed and tied to a more intuitive Lagrangian vision. The study of these metabolic changes due to substrate heterogeneities helps the understanding of the relationships between hydrodynamics and cells metabolism and it improves the agreement between numerical and experimental data.

6.1 Introduction

The effect of mixing on bioreactions has been identified many years ago by Hansford & Humphrey, (1966). Cultivating yeast in a continuous fermenter, these pioneers observed that the number and location of the injection points influence the glucose into biomass conversion yield. The highest yields were observed when multiple injection points located in the vicinity of the impeller were used. Dunlop & Ye, (1990) observed that the biomass dry weight in a continuous fermenter increases when glucose is fed through an inlet port characterized by a smaller Kolmogorov length scale. In other words, well-micromixed bioreactors allow higher yields whereas poorly micromixed devices lead to lower yields and favour by-product formation. It is remarkable that these conclusions perfectly match the modern vision of the interaction between reaction and mixing developed by Bourne, Bałdyga and Villermaux, among others, in the 80's (Baldyga & Bourne, 1992; Bourne, et al., 1981; Plasari, et al., 1978). The basic explanation is that mixing precedes the reaction. Since these two processes occur in series, the apparent rate of a chemical reaction as well as the formation of by-products are controlled by the rate of (turbulent) mixing. Following the microbiological explanation proposed by Hansford & Humphrey, (1966), Ye, (1985) explained that *cells which encountered region of high sugar concentration diverted [..] a greater proportion of substrate carbon into extracellular product via endogenous metabolism*. Thus, it appears that the substrate concentration distribution in a bioreactor impacts the yields as well as the rates of biochemical reactions. The interaction between mixing and bioreactions is although more complex than in chemical reactor in the sense that some additional metabolic pathways are triggered because of the repeated exposure to high and low concentrations (e.g. overflow metabolism for *Escherichia coli* or short-term Crabtree effect for yeasts). Nowadays, the commonly accepted idea regarding the effect of concentration heterogeneities is that they induce the activation of a large number of genes which causes an increase in the energy demand for maintenance as well as various metabolic responses, one of them being the formation of undesired by-products (Enfors et al., 2001; Lemoine, et al., 2015; Löffler et al., 2017; Takors, 2012). In order to investigate these effects, several lab scale experimental devices, reviewed by Neubauer & Junne, (2010), were used to mimic the fluctuat-

ing environment encountered by the cells along their trajectory in an imperfectly mixed bioreactor (Fowler & Dunlop, 1989; George, et al., 1993; Namdev, et al., 1992; Neubauer, et al., 1995). Among these, the most popular device is a two-stage bioreactor, generally a CSTR connected to a PFR. Displacing the feed point in one or the other reactor allows creating a variety of configurations leading to distinct biological responses.

The interaction between mixing and bioreactions has also been investigated by modelling methods. In the early 70's, a series of work from Tsai and co-workers investigated this question using the concepts of complete segregation and maximum mixedness (Fan, et al., 1971; Tsai, et al., 1969; Tsai, et al., 1971). In the work of Bajpai & Reuss, (1982) some refinements were introduced to account for the circulation time distribution. However, these authors considered an unstructured kinetic model for bioreaction that basically assumes that bioreaction rates are determined from local concentrations using constant biological parameters. Clearly, kinetic or metabolic structured models are mandatory for they introduce internal variables, linked to the biotic phase, which dynamically adapt to the external environment. Thus, bioreactions rate may now depend on the cell state also. Quite naturally, it appears necessary to consider some diversity among a population of living cells. This can be achieved using either probability density functions, PDF, (leading to continuous Population Balance Equations, PBE) (Henson, 2003; Mantzaris, et al., 1999; Morchain, et al., 2017) or discrete formulations (cell based models along with Monte Carlo techniques to deal with large cell ensembles) (Nieß, et al., 2017; Quedeville et al., 2018; Stamatakis, 2010).

Beside the description of the biological phase, one has to know about the heterogeneity of the concentration field. The trend, in the last decades was to rely upon Computational Fluid Dynamics (Hjertager & Morud, 1995; Morchain, et al., 2013; Schmalzriedt, et al., 2003) or Compartment Model Approach to do so (Alopaeus, et al., 2009; Delafosse et al., 2014; Nauha, et al., 2018; Pigou, 2018; Pigou & Morchain, 2015; Vrábel et al., 2001). In both cases, the spatial distribution of concentration is accessed. This knowledge, complemented with a Lagrangian particle tracking, can produce a temporal signal that is used as the boundary condition for a biological model (generally a set of ordinary differential equations) (Gernigon, et al., 2019; Haringa, et al., 2017; Siebler, et al., 2019). Thus, the effect of concentration fluctuations on the rate of biological reactions is obtained but the

reverse coupling (modification of the concentration field due to bioreactions) is computationally very demanding. However, in order to address the subject of interest here, i.e. the interaction between mixing and bioreaction, a full two-way coupling is necessary. This requires the transport of the biological phase in the three-dimensional space of the bioreactor. This is possible using a Eulerian description for the biological phase (transport of PDF) but the number of biological variables in the model is then limited (Pigou, 2018; Pigou & Morchain, 2015). So, the general trend is an ever-growing complexity, associated to a high level of expertise and prohibitively large numerical costs, which makes these modelling tools out of reach for most biochemical engineers.

In this work, we investigate the possibility to rely upon the statistical description of the concentration distribution only, disregarding the spatial dimensions. A popular model of this type is the Interaction by Exchange with the Mean model (IEM) originally introduced by Villermaux & Devillon, (1972) to address micromixing issues. In such models, the reacting volume is divided into two or more environments (or zones) and a characteristic time relative to mass exchange between the zones is introduced. Considering only two environments suggests that the concentration distribution will be approximated by two Delta functions. It was shown that this can constitute a fair approximation of the actual concentration PDF in the limit of fast reactions. In fed-batch bioreactors the characteristic time of substrate uptake generally decreases with time and becomes much smaller than the macromixing time (Morchain, 2017; Pigou & Morchain, 2015). Hence, a fed-batch fermenter subject to mixing issue is usually strongly segregated and exhibits a highly concentrated zone near the feed point and a very low concentration zone elsewhere.

Considering the various time scales of the biological response to concentration fluctuations, we developed and validated the idea that the disequilibrium between the uptake and utilization rates provides a good estimate of the flux of substrate that must be diverted into by-products (Morchain et al., 2013; Pigou & Morchain, 2015). However, up to now, the metabolic rate calculations assumed a growth rate dependent yield, namely a Pirt's law (Pirt, 1965), along with a constant maintenance rate. The idea of tying the maintenance rate to the process variables was already suggested by Holms, (1996) and by Meadows, et al., (2010), although they linked the maintenance rate to the growth rate. Since substrate fluctuations are known to produce a metabolic stress on bacteria and thus contribute to an increased

energy demand, it is proposed to relate the maintenance rate to the variance of the glucose concentration distribution. This rate being used to dynamically update the substrate into biomass yield, a coupling between the degree of mixing in the bioreactor and the glucose conversion efficiency is now introduced in the model.

This article presents the formulation of a segregation dependent maintenance rate. The Interaction by Exchange with the Mean (IEM) model is implemented in ADENON, an in-house developed bioreactor simulation software combining CMA, kinetic or mode based metabolic model and PBE approaches. Simulations results using the IEM model will be compared to the experimental observations published by Xu, et al., (1999) in a $20m^3$ reactor and by Neubauer et al., (1995) in a STR+PFR scale-down reactor. Spatially refined simulation using CMA (Pigou & Morchain, 2015) for the Xu experiment and a two-stage STR+PFR for the Neubauer experiment are also performed to serve as references. The challenges posed by the two sets of experiments considered in this work are related to the presence of spatial inhomogeneities or segregation that trigger a suboptimal operation of the fermentation process. In the Xu et al., (1999) experiment, the segregation is entirely due to the large scale of the reactor and the injection conditions that result in a poorly meso-mixed process. On the contrary, in the Neubauer et al., (1995) experiment, a segregated environment was purposely designed by means of a multi-stage reactor, with localized injections.

In the final part of this work, some details are given regarding the formulation of a Eulerian expression of the maintenance rate starting from a Lagrangian perspective. It is shown that one can reconcile the Lagrangian and Eulerian visions of the biological response to external fluctuations.

6.2 The experiments

In this work two different sets of experiments found in the literature were simulated, one studying a fed-batch culture in an industrial scale bioreactor, described by Xu et al., (1999) and lately simulated by Vrábel et al., (2001) and Pigou & Morchain, (2015), and one by Neubauer et al., (1995) dealing with a fed-batch culture in a pilot scale bioreactor.

Xu et al., (1999) investigated the acetate production in an industrial scale fed-batch bioreactor with *E. coli*. The fermentation was performed in a $20m^3$ stirred tank reactor stirred equipped with Rushton impellers. The initial concentration of glucose was equal to $0.29g_G/L$, the initial concentration of acetate was equal to zero and the initial biomass concentration was $X(t=0) = 0.1g_X/L$. After an initial batch phase of 0.92h, a feed solution of $454g_G/L$ of glucose was injected well above the upper impeller at variable flow rate with an exponential curve for 8.5h, changed to a constant value of 180L/h for 2.5h and then to 170L/h for 28.02h. The sampling of glucose, acetate and biomass concentration was performed at three different sampling points located at the top, in the middle and at the bottom of the reactor. Glucose gradients were identified as the result of insufficient mixing. Acetate was produced in the upper part of the reactor and a reduction of the glucose to biomass yield of 25% was observed with respect to the homogeneous 20L fermenter. This experimental observation could not be reproduced by Vrábel et al., (2001) but was correctly predicted by Pigou & Morchain, (2015) owing to the use of a Pirt's law with a maintenance rate equal to $0.250 mmol_G/g_X \cdot h$ ($45 mg_G/g_X \cdot h$).

Neubauer et al., (1995) investigated the *E. coli* responses to substrate fluctuations in a two-stages bioreactor of 10L consisting in a closed loop of a Stirred Tank Reactor (STR) connected to a Plug Flow Reactor (PFR) of 0.695L, Fig. 6.1. The glucose initial concentration was $10g_G/L$ and the system was operated in batch to the complete depletion of glucose (~8h). Once completed the batch phase, the system was operated in fed-batch for 8h, with the injection of glucose-rich solution ($600g_G/L$) at a constant flow rate of 50mL/h either in the STR or just before the PFR. The fed-batch results were collected for three different configurations: without the external PFR loop and injection in the STR (referred to as *Case A* or *Control*, in the publication, Fig. 6.1a) and with the external loop and injection in the PFR (referred to as *Case B* in the publication, Fig. 6.1b). The authors also investigated the use of oxygen enriched air as aeration gas in the PFR (Fig. 6.1c) to test the hypothesis that microaerobiosis would develop due to high substrate uptake. In the following we will refer to *Case B* configuration aerated with air as *Case B1*, Fig. 6.1b, and to the same configuration aerated with oxygen enriched air as *Case B2*, Fig. 6.1c. In each *Case*, the medium volume was kept constant to 10L. The biomass concentration and growth rate, as well as the glucose and acetate profiles in the PFR, were monitored in the Neubauer et al., (1995) experiment.

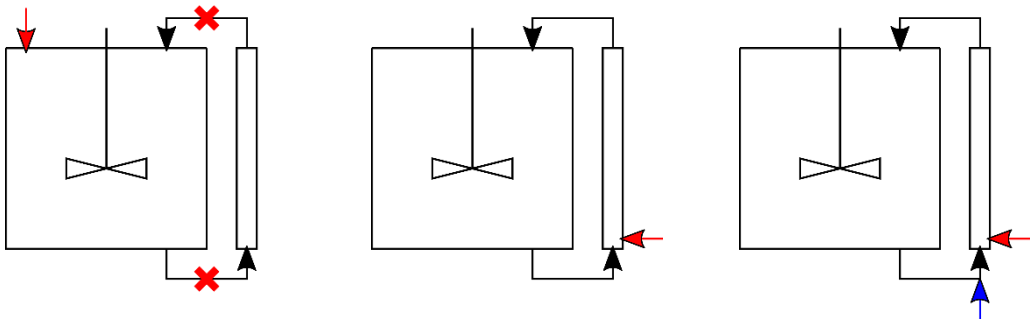

Fig. 6.1 - Schemes of the reactor configurations used in the Neubauer et al., (1995) *experiment: (a) injection of substrate (red arrow) in the STR operated without the PFR loop* Case A*, (b) STR+PFR with injection in the PFR,* Case B1*, (c) STR+PFR with substrate injection in the PFR and aeration with oxygen enriched air (blue arrow),* Case B2.

The residence time was 113s for the PFR, τ_{PFR}, and 27min for the STR, τ_{STR}. It was observed that the repeated exposure to high glucose concentration in the PFR, interrupted by prolonged periods of glucose limitations in the STR, led to an over-assimilation of glucose at the PFR inlet coupled with acetate production due to overflow metabolism and a reduced glucose to biomass yield in comparison to the homogeneous *Case A.* Some acetate was also produced in the upper part of the PFR because of oxygen limitation (fermentative catabolism). The addition of enriched air, *Case B2*, did not change the initial response at the PFR inlet but led to a lower formation of acetate in the upper part and a yield similar to that observed in *Case A.* As far as the authors know, these experimental results have not been simulated to date.

6.3 Mathematical model

6.3.1 General aspects

A detailed explanation of the population balance model and the metabolic model formulations, the solution strategies and their implementation in ADENON were already published in previous works (Morchain, 2017; Morchain, et al., 2014;

Morchain et al., 2013; Pigou & Morchain, 2015). However, they are briefly outlined here to allow a clear identification of the novelties provided in this work. The mass balance equation for a generic k component in a generic homogeneous control volume, V, reads:

$$\frac{dC_k}{dt} = \frac{1}{V}\left(\int_\Omega C_k^{in} \mid v \mid^{in} \cdot d\omega - \int_\Omega C_k \mid v \mid^{out} \cdot d\omega\right) + R_k \tag{6.1}$$

where C_k is the concentration, Ω is the surface enveloping the control volume, $\mid v \mid^{in}$ and $\mid v \mid^{out}$ are the norms of the velocity vector entering and exiting the control volume, respectively, and R_k is the volumetric reaction rate. Velocities in Eq. (6.1) come out from the solution of a hydrodynamic model. The Compartment Model Approach (CMA) falls into this category and the fluxes are calculated either from general considerations on the fluid dynamics of the system (Pigou & Morchain, 2015; Vrábel et al., 2001) or retrieved from the CFD simulations (Alopaeus et al., 2009; Delafosse et al., 2014; Nauha et al., 2018; Pigou, 2018).

The microbial population is considered as segregated with respect to the specific growth rate μ. Hence, the volumetric reaction rate in Eq. (6.1) is expressed as an integral over the μ space:

$$R_k = \int_0^\infty r_k(\mu, \boldsymbol{C}) X(\mu) d\mu \tag{6.2}$$

where $X(\mu)d\mu$ is the mass of cells able to grow at μ per unit volume, r_k represents the net specific reaction rate and $\boldsymbol{C}$ is the concentration vector of the species.

The equation for the cell density function $X(\mu)$ is obtained under the assumptions that daughter cells inherit the growth rate of their mother (Morchain & Fonade, 2009).

$$\frac{\partial X(\mu,t)}{\partial t} = -\frac{\partial}{\partial \mu}[X(\mu,t)\zeta(\mu)] + \mu X(\mu,t) \tag{6.3}$$

where the rate of change of X in the μ-space, $\zeta(\mu)$, in its general form is:

$$\zeta(\mu) \propto \frac{1}{T^{u/d}}(\mu^* - \mu) \tag{6.4}$$

with $T^{u/d}$ being a time constant which value depends on the direction of the rate of change of the specific growth rate and μ^* being the growth rate at equilibrium that generally takes the form of a Monod equation. The adoption of a segregated model with the growth rate capability as the internal coordinate, Eq. (6.3), was introduced to decouple the actual growth rate of the population from the local reactant concentrations, Eq. (6.4). This decoupling introduces an out-of-equilibrium metabolic behavior resulting in the production/depletion of by-products. The net reaction rate r_k results from a call to a metabolic model that can be regarded as a function f.

$$r_k = f\left(\mu, \boldsymbol{C}, Y_{k,l\neq k}\right) \tag{6.5}$$

where $Y_{k,l\neq k}$ is the generic yield coefficient expressing the k^{th} species to l^{th} species yield. The metabolic model adopted in this work corresponds to that already presented in Pigou & Morchain, (2015) and combines mass and energy balances. It considers four categories of biological reactions namely the production of biomass through substrate and energy consumption (*Anabolism*), energy production either by means of an oxidative pathway (*Oxidative catabolism*) or by fermentation (*Fermentative catabolism*) and the production of acetate due to the overconsumption of glucose (*Overflow metabolism*) or fermentative metabolism. It is worth recalling here that acetate production takes place either if the energetic need for growth is not fulfilled through the oxidative pathway (acetate production through fermentation) or if a cell uptakes more glucose than the amount used in the anabolic reactions (acetate production though overflow metabolism). The essential feature of our metabolic approach is that the maximum value for the anabolic reaction rate is the cell property μ. In a given environment some cells may be limited and some others not. Indeed, any limitation is actually relative to the cell state rather than defined in an absolute manner through concentration thresholds. In case of insufficient resources, the actual growth rate of some cells, μ^a, may be limited to a lower value than their growth rate capability ($\mu^a < \mu$). The term r_k consists of a summation of the specific reaction rates for each of the aforementioned biological reaction, weighted by the corresponding stoichiometric coefficients. Among these coefficients, the substrate to biomass yield was up to now determined using the

well-known Pirt's law (Pirt, 1965), Eq. (6.6), leading to a growth-dependent glucose to biomass yield, $Y_{XG}(\mu^a, m)$.

$$\frac{1}{Y_{XG}(\mu^a, m)} = \frac{m}{\mu^a} + \frac{1}{Y_{XG}^{max}} \tag{6.6}$$

In Eq. (6.6), Y_{XG}^{max} is the maximum conversion yield of glucose in biomass and m is the maintenance rate, treated as a constant.

6.3.2 New considerations

6.3.2.a Effect of substrate fluctuations on the maintenance rate

Having in mind the effects of imperfect mixing on cell physiology mentioned earlier, it is proposed to introduce a variable maintenance rate and express it as a function of the variance of the substrate concentration distribution in the system.

$$\overline{m} = m_0 + \alpha \int p(C_G)(C_G - <C_G>)^2 dC_G \tag{6.7}$$

where m_0 is the minimum maintenance rate of the cells, α is the model parameter, C_G is the substrate concentration, $<C_G>$ is the volume average of the substrate concentration in the fermenter and $p(C_G)dC_G$ is the volume fraction of the reactor with a concentration equal to C_G. Hypothesizing that the cells are uniformly distributed inside the reactor volume and dividing the reactor into N_C sub-volumes of equal size, a discrete expression for Eq. (6.7) can be formulated:

$$\overline{m} = m_0 + \alpha \frac{1}{N_C} \sum_{i=1}^{N_C} \left(C_{G,i} - <C_G>\right)^2 \tag{6.8}$$

Eq. (6.8) provides an Eulerian integral correlation between the sub-volumes concentration deviation from the volumetric average in the whole reactor and the average maintenance rate of any cell travelling in an heterogeneous concentration field. The derivation of Eq. (6.8) from the effects of substrate fluctuations on a single cell and on a swarm of Lagrangian cells is described in Section 6.6.

6.3.2.b The Interaction by Exchange with the Mean mixing model

In the IEM approach, the composition space of the species is discretized rather than the physical space of the reactor. The space of composition can be divided into two or more environments, Fig. 6.2b, that interact due to mixing.

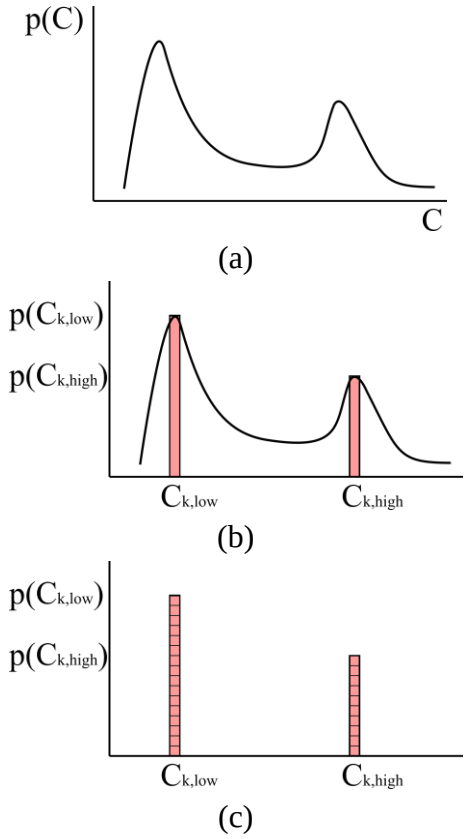

Fig. 6.2 – Hypothesized concentration distribution in a fed-batch reactor (a), its description by means of two environments (b) and discretization through elementary probability units (c).

In the experiments presented, the bioreactors are strongly segregated, and a description of the concentration distribution based on two environments (with high and low substrate concentration) constitutes a reasonable approximation. Let us consider a generic concentration distribution inside a reactor during a fed-batch fermentation, Fig. 6.2a. In this distribution it is possible to encounter two different

peaks, one at a lower concentration, $C_{k,low}$, with a higher probability, $p(C_{k,low})$, and one at a higher concentration, $C_{k,high}$, with a lower probability, $p(C_{k,high})$, corresponding to the bulk of the reactor and the poorly meso-mixed region in the vicinity of the species injection, respectively. The interaction of the species compositions in the different environments occurs by means of a mixing model (Fox, 2003).

The environments can be discretized in a number of elementary probability units, Fig. 6.2c, that can be thought as presumed sub-volumes in case the environments probabilities remain constant in time. A fundamental assumption in the IEM model is that each elementary sub-volume has the same probability to exchange mass with each and every elementary sub-volume, including those of the same environment. Therefore, the results of these exchanges can be represented by a single exchange with a fictitious sub-volume at the volume average concentration $<C_k>$. The resulting equations for the segregated species are:

$$\frac{dC_{k,low}}{dt} = \frac{1}{\tau_m}(<C_k> - C_{k,low}) + R_{k,low} \quad (6.9)$$

$$\frac{dC_{k,high}}{dt} = \frac{1}{\tau_m}(<C_k> - C_{k,high}) + R_{k,high} + S_k \quad (6.10)$$

with S_k being a source term representing the feed. The volume average concentration of any distributed species is computed as:

$$<C_k> = p(C_{k,low})C_{k,low} + p(C_{k,high})C_{k,high} \quad (6.11)$$

Having described the inhomogeneities in the system in terms of concentration space segregation instead of physical space segregation, the term τ_m is the only parameter of the model and it is related to some mixing time constant defining the characteristic time at which the exchange between sub-volumes happens.

The IEM model distributes just the species that cannot be considered as homogeneously dispersed in the volume. The reaction rates are calculated in each sub-volume and the concentrations of the homogeneously dispersed species are then volume-averaged to retain just one value per species. The concentration of the homogeneously dispersed species is then a composition of all the concentrations in the sub-volumes (which change differently due to the different reaction rates),

whereas the concentration of the distributed species is a vector with as many elements as the total number of sub-volumes.

6.3.3 Implementation in ADENON

All simulations were performed with ADENON, a simulation software developed in the MATLAB R2016a environment by this research group. The software focus is mostly directed at the simulation of bioreactors, by solving biological models within a fluid dynamics framework (compartment models, plug-flow reactors, stirred tank reactors, interconnected multi-stage reactors, batch or fed-batch cultures as well as accelerostat cultures). ADENON formulates a system of ODEs in terms of mass and volume balances, based on the user defined case configuration. This set of ODEs is then solved using the Runge-Kutta 2,3 explicit scheme for time integration.

In the previous section, two environments were considered. Dividing each of these environments into elementary sub-volumes of the same size allows a direct calculation of the probabilities $p(C_{k,low})$ and $p(C_{k,high})$ as the ratio of the number of sub-volumes in each environment to the total number of sub-volumes, N_C.

$$p(C_{low}) = \frac{N_C^{low}}{N_C} \tag{6.12a}$$

$$p(C_{high}) = \frac{N_C^{high}}{N_C} \tag{6.12b}$$

In this work we hypothesized that the environment probabilities remain constant during the fermentation.

Each environment being made of a collection of identical elementary sub-volumes, the average concentration now reads:

$$<C_k> = \frac{1}{N_C} \sum_{i=1}^{N_C} C_{k,i} \tag{6.13}$$

The implementation of the IEM model in the framework a compartment-based code is presented in Fig. 6.3.

As an illustration, the system consists of $N_C = 20$ sub-volumes (the 20 square squares composing the larger square) and two environments, corresponding to the

fraction of the total volume at a given composition (represented by the total number of red, N_C^{high}, and the total number of white squares, N_C^{low}).

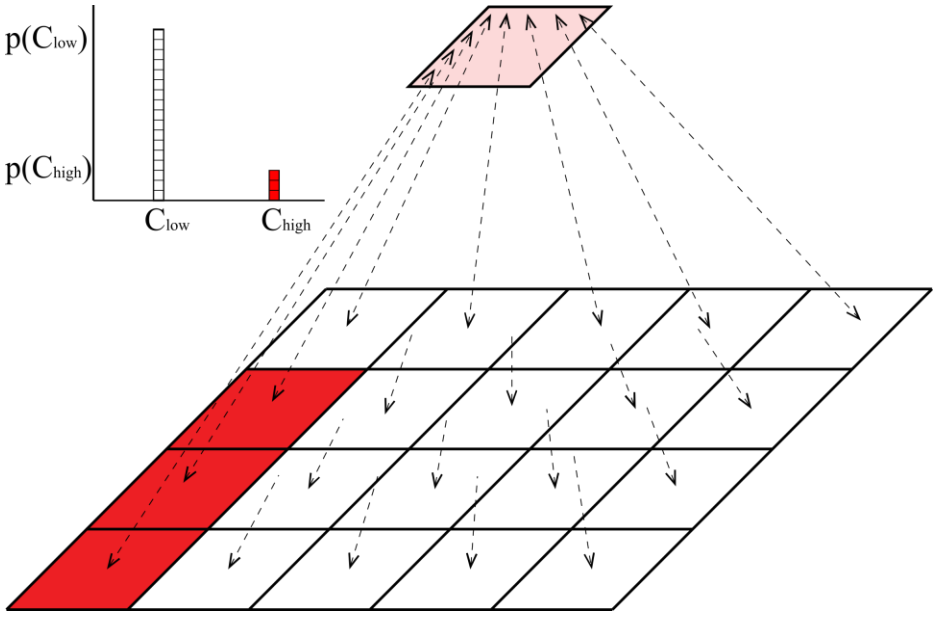

Fig. 6.3 – Scheme of an Interaction by Exchange with the Mean model. The scheme represents the two environments made of a collection of sub-volumes that exchange with their mean at the top. For any sub-volume, the total mass exchanged with the other sub-volumes is equivalent to the mass exchanged with a single fictitious volume at the mean concentration. In the top left corner, the concentration distribution described by means of two environments discretized through elementary probability units.

The arrows represent the exchange between each sub-volume and the mean. The corresponding environment distribution is represented as well. By changing the number of sub-volumes in which there is an injection, N_C^{high}, and the number of total sub-volumes, N_C, the probabilities of the environments with low and high concentration can be adjusted to any experimental configuration.

Implementing the IEM model as a collection of sub-volumes is of practical interest, being in the framework of a multicompartment based simulator. At first sight, solving N_C equations instead of two looks like a waste of resources, a step back due to the code structure. However, the benefit is that all simulations presented in this work, irrespective of the hydrodynamic model (CMA or IEM), are performed under the same modeling framework, using the same models for population and metabolic aspects of the problem.

6.4 Simulation set-up

6.4.1 Large scale fed-batch

The 20m^3 fed-batch experiment was simulated using the CMA with 70 compartments (as in Pigou & Morchain, (2015) and Vrábel et al., (2001)) in order to compare the IEM model against it. The initial conditions of the simulation were set to replicate the experiment and the initial biomass concentration was initialized at $\mu(t = 0) = 0.63\text{h}^{-1}$. Xu et al., (1999) reported that "*the dissolved oxygen signal did not show any oxygen limitation*" but hypothesized that the acid production was due to high substrate concentration inducing local oxygen limitations. Simulation due to Pigou & Morchain, (2015) showed that the acetic acid was indeed produced through the overflow metabolism rather than through fermentative pathways. Consequently, the oxygen inter-phase mass transfer rate was neglected and the concentration of the dissolved oxygen in the liquid was always considered at saturation ($\sim$10mg$_O$/L).

In our IEM simulation, the injection occurred in 1 of 70 sub-volumes, in the same way as Vrábel et al., (2001) and Pigou & Morchain, (2015) did in the context of a compartment model. Simulating the Xu et al., (1999) mixing time experiment with the IEM model allows the identification of τ_m leading to the same macromixing time of 250s, Fig. 6.4. The IEM model, of course, loses the spatial information regarding the tracer concentration, but, using an IEM model parameter equal to τ_m = 36s, it is able to reproduce the macromixing time.

In Fig. 6.4 the evolution of the tracer concentration at the three monitored locations as predicted by Pigou & Morchain, (2015) is shown.

The macromixing time is calculated as the time needed by the tracer to reach a concentration of $\pm 5\%$ of the final concentration and Fig. 6.4 shows that the non-dimensional concentration at the bottom probe reaches the $\pm 5\%$ interval after ~250s.

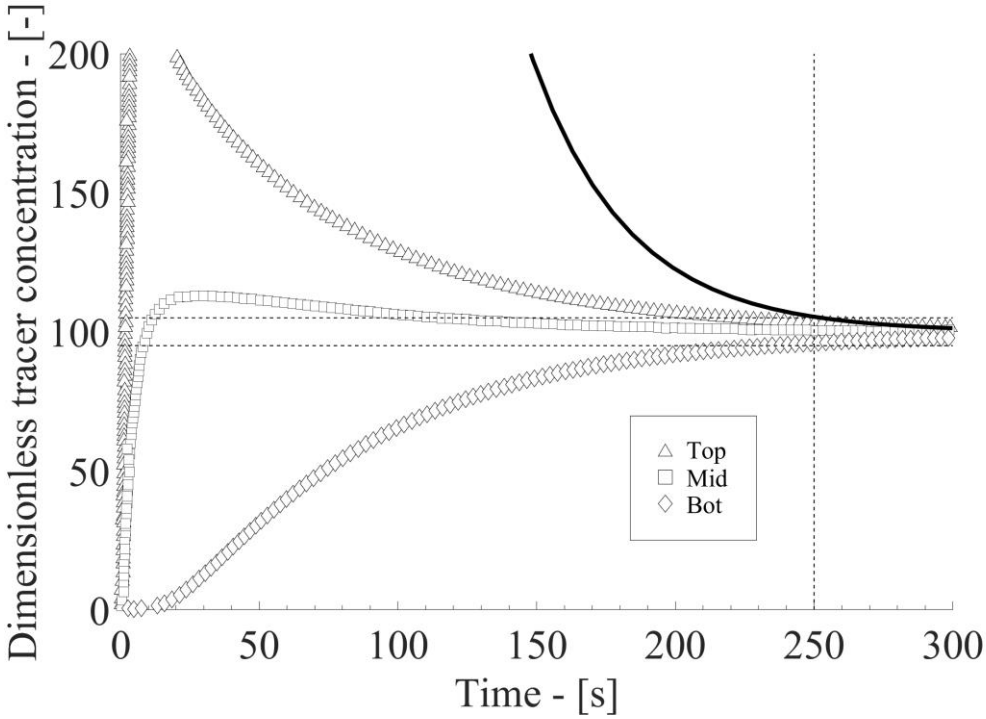

*Fig. 6.4 – The open symbols represent the passive tracer evolution in time at the top (*top*), middle (*mid*) and bottom (*bot*) of the fermenter as predicted by* Pigou & Morchain, (2015) *with the CMA. The tracer evolution in time as predicted by the IEM is plotted with the solid line and the mixing time of 250s is highlighted by the dashed line.*

6.4.2 Two stage bioreactor STR+PFR

Considering the Neubauer et al., (1995) experiment, the reference case is a spatially refined simulation performed considering a STR connected to a PFR. The initial conditions were set to replicate the experiments and the initial biomass concentration was initialized at $\mu(t=0) = 0.65\text{h}^{-1}$. When the IEM model is used, the biomass, the acetate and the oxygen were treated as perfectly mixed species. The oxygen inter-phase mass transfer rate was neglected (as in the simulation of the Xu et al., (1999) experiment) considering the concentration of the dissolved oxygen in the liquid always at saturation (~$10\text{mg}_O/\text{L}$). This condition, according to the authors, would be valid for most of their experimentally characterized reactor configurations. The injection being located in the PFR, Fig. 6.5a, this configuration resembles a poorly mesomixed fed-batch in a stirred tank reactor in which the injec-

tion plume is segregated from the bulk of the volume and the fresh substrate has to travel the whole length of the jet before being released in the bulk (zone model), Fig. 6.5b.

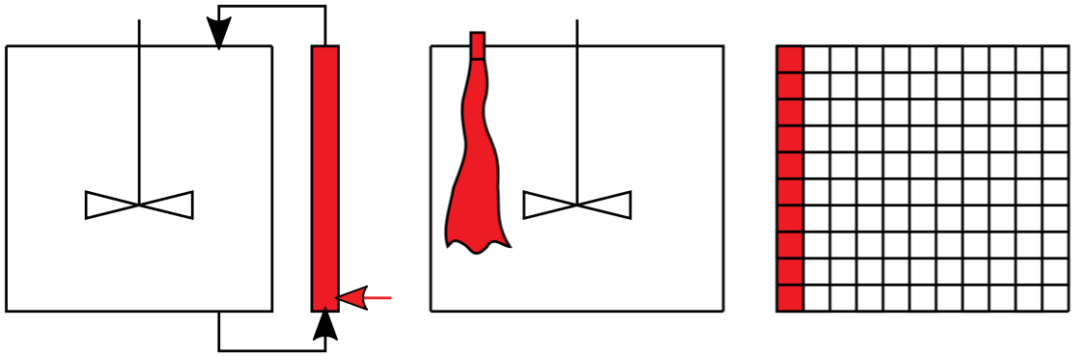

Fig. 6.5 – Reactor configuration of Case B *in* Neubauer et al., (1995) *experiment (a). Poorly mesomixed fed-batch in a stirred tank reactor (b) and its description by means of the IEM model (c).*

The IEM model, Fig. 6.5c, further simplifies the system dropping the spatial information. The model only deals with the two environments, the plume and the bulk with high and low substrate concentration respectively and assumes that the characteristic interaction time between these two environments is equal to the PFR residence time, equal to 113s, therefore this time was chosen for τ_m. A total number of 187 sub-volumes was defined in the simulations and the injection in the PFR was reproduced through a source term in 13 sub-volumes, obtaining a ratio of 13/187 = 0.0695 that closely matches the ratio between the experimental volumes 0.695L/10L = 0.0695.

6.4.3 Biological constants

All simulations are performed using the same metabolic model. A detailed presentation of the model can be found in the Appendix A of Pigou & Morchain, (2015). The same notation is used in this work. In that previous study, the constants for the Xu et al., (1999) experiment were determined and their values are used in this work. The constants of the Neubauer et al., (1995) experiment were tuned to match the *Case A* results. A sensitivity analysis was performed on the most influential constants shown in Tab. 6.1 and it is reported in Appendix A. The constants

that have the highest influence on the results of the simulations considered in this work are:

- ϕ_O^{max}, the maximum oxygen uptake rate;
- $K_{i,A}$, the acetate inhibition constant (in the expression of growth on glucose);
- $K_{i,A}^o$, the oxygen inhibition constant (in the oxygen uptake rate);
- m, the maintenance rate (see Eq. (6.6));
- Y_{AG}, the glucose to acetate conversion yield (see Eq. (6.5));
- Y_{XG}^{max}, the maximum glucose to biomass conversion yield (see Eq. (6.6));

And the constant values for the two sets of simulations are reported in Tab. 6.1.

Tab. 6.1 – Model constants and their values used to simulate the Xu et al., (1999) *experiment and the* Case A *of the* Neubauer et al., (1995) *experiment.*

Constant	Xu et al., (1999)	Neubauer et al., (1995)	Units
ϕ_O^{max}	15.60	14.00	$mmol_O/g_X \cdot h$
$K_{i,A}$	3.00	3.50	g_A/L
$K_{i,A}^o$	4.00	4.00	g_A/L
m	0.250	0.150	$mmol_G/g_X \cdot h$
${}^*Y_{AG}^{ferm}$	3.00	3.00	mol_A/mol_G
${}^*Y_{AG}^{over}$		2.00	mol_A/mol_G
Y_{XG}^{max}	1.32	1.50	mol_X/mol_G

**The conversion yield of glucose in acetate in the Neubauer et al., (1995) experiment was divided depending on the acetate production mechanism, i.e. fermentation (ferm) and overflow (over)*

6.5 Results

In this Section the results obtained with the IEM model in the two experimental set-ups described in Section 6.2 are shown and compared with the experimental data and the results from the compartment model (Pigou & Morchain, 2015). Results obtained considering the reactor as perfectly homogeneous are shown as well.

The dimensions of the spaces used in the simulations of the experiments are presented in Tab. 6.2. The first set of results corresponds to a constant maintenance rate while the second set is obtained with a variable maintenance rate.

Tab. 6.2 – Dimensions of the spaces used in the simulations

	Physical space	**μ-space**	**C-space**
Homogeneous model	0	1	0
Compartment model	3	1	0
IEM model	0	1	1

6.5.1 Constant maintenance rate

6.5.1.a Simulating the Xu experiment

Fig. 6.6 shows the average biomass, the glucose and the acetate concentration time evolution obtained with a maintenance rate equal to $0.250 mmol_G/g_X \cdot h$.

Concerning the average biomass concentration, Fig. 6.6a, all the three modelling strategies achieve a satisfactorily agreement with the experimental data. Taking into account spatial heterogeneities and biological diversity is not critical in predicting the total biomass. Indeed, the total amount of biomass is essentially driven by the substrate feed rate and the substrate into biomass conversion yield. Minor differences in the biomass concentrations are however observed because different amounts of acetate are produced and re-consumed depending on the substrate heterogeneity. In Fig. 6.6b, the evolution of the substrate concentration is reported. The glucose concentration profiles of the IEM, compartment and even the homogeneous case up to ~7h perfectly overlap.

As the spatial inhomogeneities become more important, three trends appear in the compartment model, depending on the sampling position. This aspect is overlooked by the IEM model, nonetheless, it produces results that are the same order of magnitude as the compartment model results and the use of this simplified model does not worsen the agreement with the experimental data, with respect to the more accurate compartment model.

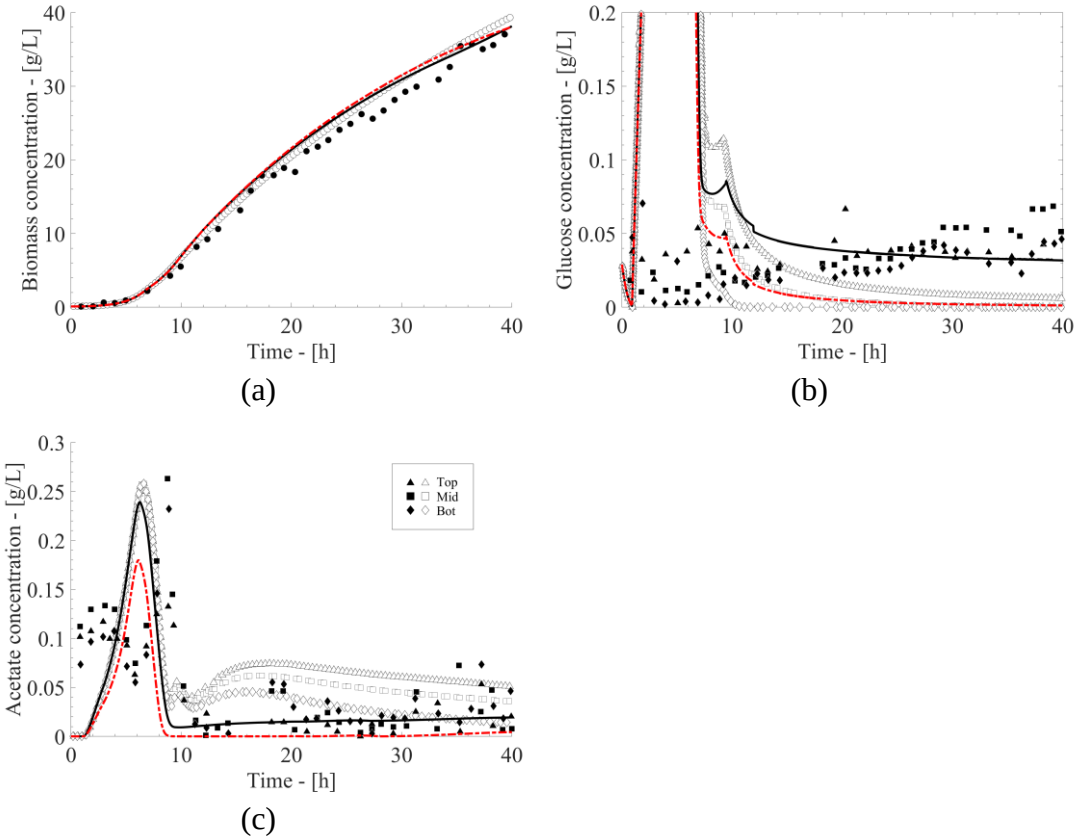

Fig. 6.6 – Average Biomass (a), Glucose (b) and Acetate (c) concentration evolution in the Xu et al., (1999) *experiment. Experimental data (filled symbols) and Compartment model results (open symbols) are collected at the top (*top*), middle (*mid*) and bottom (*bot*) of the fermenter, IEM model results (solid line) and homogeneous case (dashed line). All the numerical data are obtained with* $m = 0.250\ mmol_G/g_X \cdot h$.

Fig. 6.6c shows the time evolution of the concentration of acetate. IEM and compartment model results are in good agreement up to ~8h and, as for the data in Fig. 6.6b, the agreement between experimental and numerical concentration profile as predicted by the compartment and IEM model does not change appreciably. Considering the system as perfectly mixed, on the other hand, lead to an underestimation of the acetate concentration that is identically zero between 9h and 32h from the beginning of the process. This latter result is in line with the fact that acetate is produced by overflow metabolism which results from the cell exposure to concentration heterogeneities only.

The results obtained from the numerical simulation of the Xu et al., (1999) experiment show that the IEM model produces results that are in substantial agreement with the averaged global experimental data, while the homogeneous model results deviate appreciably but not significantly from the IEM and compartment models, with the largest differences found in the production of acetate. This latter result confirms that acetate is produced through overflow metabolism. In the model, the metabolic response is due to the local disequilibrium between uptake and growth rates. Therefore, the local disequilibrium between uptake and growth rates must be considered, either from a spatial point of view (CMA) or a statistical point of view (IEM), to account for by-product formation.

6.5.1.b Simulating the Neubauer experiment

The experimental results of Neubauer et al., (1995) and the simulation results are shown in Fig. 6.7. Fig. 6.7a, shows the evolution of the biomass concentration in the bioreactor for the *Case A* and *Case B*. The single STR *Case A* is simulated using a homogeneous model, while the *Case B* is simulated using either a two-stage bioreactor (STR+PFR) or the IEM model. The constants of the metabolic model reported in Tab. 6.1 were tuned in order to reach a better agreement between the perfectly mixed *Case A* and the homogeneous case. As explained in Appendix A, the most influential parameters are, with little surprise, the maintenance rate and the maximum glucose into biomass yield. Thanks to this tuning, the numerical results of the homogeneous model closely match the perfectly mixed experimental data. It is interesting to note that the constant maintenance rate is now equal to $0.150 mmol_G/g_X \cdot h$, much lower than the value necessary to simulate the highly segregated fed-batch of Xu et al., (1999). Regarding the simulation of *Case B*, the biomass concentration profiles as predicted by the IEM and the STR+PFR models almost perfectly overlap, indicating that considering the biomass as perfectly mixed could be an acceptable hypothesis when examining integral results, even in this reactor configuration.

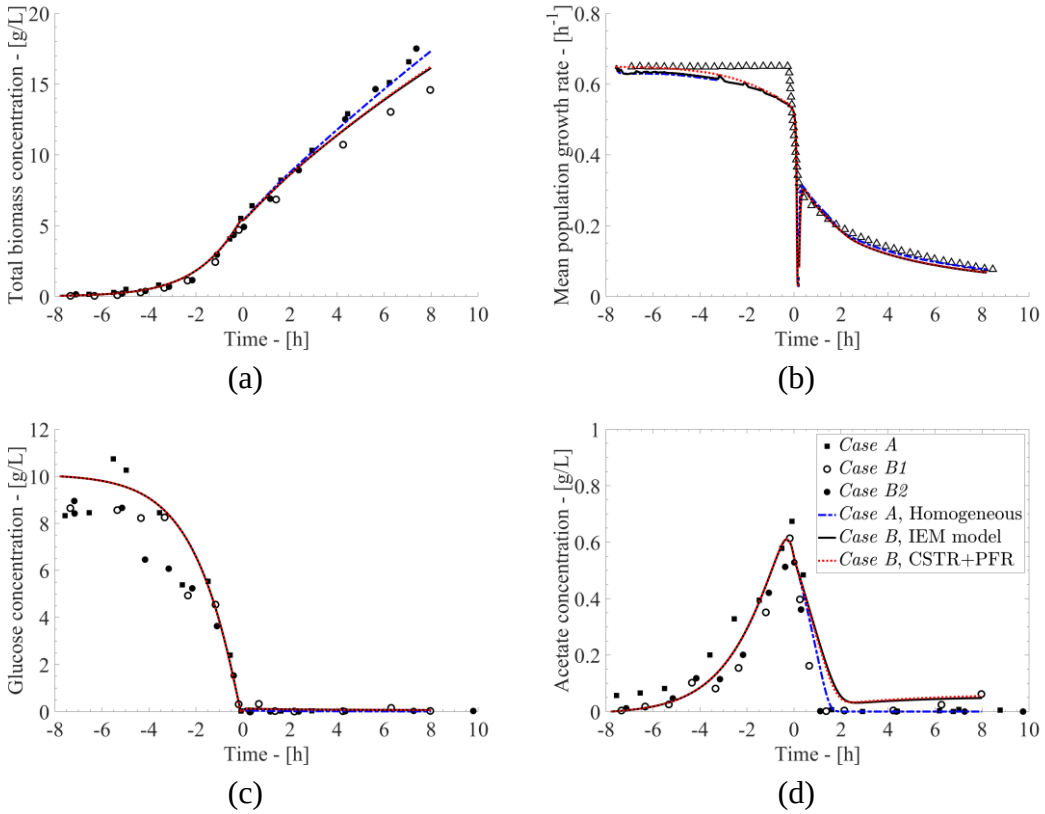

Fig. 6.7 – Biomass (a), Growth rate (b), Glucose (c) and Acetate (d) concentration evolution in the Neubauer et al., (1995) *experiments. Experimental data of* Case A *(squares) and* B *(circles) are shown together with the results of the homogeneous simulations (dashed line), the CSTR+PFR model (dotted line) and the IEM model (solid line). All the numerical data are obtained with* $m = 0.150\ mmol_G/g_X \cdot h$.

The IEM and the CSTR+PFR model, on the other hand, over-predict the amount of biomass produced in *Case B1* (open circles) during the fed-batch phase, although exhibiting a trend that qualitatively agrees with this experimental set-up, i.e. a non-linear reduced production of biomass in time.

The mean growth rate evolution in time is shown in Fig. 6.7b, where a very good agreement between the experimental and numerical results is achieved throughout most of the process. Between t=-5h and t=0 a noticeable deviation between the numerical and experimental data occurs, but, considering the strongly non-linear biomass growth in the same time interval Fig. 6.7a, this deviation can be explained by the fact that a constant growth was hypothesized during the batch phase by the authors of the experiment.

Considering the glucose consumption dynamics, shown in Fig. 6.7c, the overall trend and the quantitative agreement in the fermentation is very convincing. In the overall growth rate evolution and in the glucose consumption almost no differences exist between the homogeneous, the IEM and the CSTR+PFR models. Nonetheless, a deviation between experiments and simulations appears between the beginning of the process and ~ -3h. In Neubauer et al., (1995), it is said that the culture medium used for the batch phase of the fermentation contained 10.0g of glucose per liter, whereas the experimental data are slightly lower. Therefore, the misalignment between simulated and experimental data may be due to inaccuracies in the acquisition of the latter set of data.

Concerning the evolution of the acetate concentration, Fig. 6.7d shows two distinct trends. The acetate produced during the batch phase is rapidly re-consumed when the residual concentration of glucose becomes low. During the fed-batch phase, no acetate is produced in the *Case A*, whereas it accumulates when the injection is performed in the PFR. As stated earlier in the description of experiments, acetate is produced through overflow metabolism when cells enter the PFR and face a high glucose concentration. It is also produced through fermentation at the end of the PFR because of oxygen limitation, *Case B1*. This second source of acetate production vanishes if enriched air is used in the PFR *Case B2*. In any case, acetate is also re-consumed in the STR where the glucose concentration is low. These multiple sources of acetate production and re-consumption are taken into account in our metabolic model. In our simulations, the acetate in the homogeneous model is completely depleted after few hours from the beginning of the fresh substrate injection. This is a consequence of our metabolic model which considers that acetate is uptaken if the amount of glucose is insufficient to satisfy the cell needs for growth. The initial re-consumption also takes place in *Case B* and is correctly represented by the IEM and the STR+PFR models. Moreover, both models predict a remaining low but not negligible amount of acetate that is confirmed by the experimental data collected in the *Case B1* configuration.

One of the major unresolved aspects in the discussion presented above is the over-prediction of biomass in the *Case B1* of the Neubauer et al., (1995) experiment. Neubauer et al., (1995) report a slightly reduction of the conversion yield of glucose in biomass, Y_{XG}, from 0.5 to $0.38 g_X/g_G$ (-25% roughly). Similarly, Xu et al., (1999) had to reduce the value of Y_{XG} identified in a homogeneous lab scale

reactor in order to fit their results in the heterogeneous large scale fed-batch bioreactor. As a matter of fact, despite the description of the spatial inhomogeneities in the reactor, a constant m value, fitted from the perfectly mixed case data, proved to be inadequate in capturing the loss in biomass production observed in segregated bioreactors.

To sum up, it is possible to reproduce the experimental results using the IEM model with the same accuracy as spatially refined models. However, whatever the approach (spatial or statistical) it is necessary to increase the maintenance rate (or reduce Y_{XG}) in order to account for the effect of concentration heterogeneities on the substrate to biomass yield. These considerations led us to consider that the maintenance rate might increase with the heterogeneity of the glucose concentration field.

6.5.2 Changes in the maintenance rate

As stated in Section 6.3.2.a, substrate gradients may be responsible for the increased maintenance costs and, as seen in Tab. 6.1 and in Tab. A. 6.2, m is the constant that is subject to the largest changes due to mixing effects. As proposed in Section 6.3.2.a, Eq. (6.8) was implemented in the code obtaining an on-line calculation of the maintenance rate. The two constants in this law are identified as follows. The $m_0$value is set to $0.150\, mmol_G/g_X \cdot h$, having hypothesized that in the most homogeneous conditions (such as the *Case A* of the Neubauer et al., (1995) experiment) this value represents a base level for m. Exploiting the data collected from the fed-batch simulations of the large scale fed-batch reactor, the variance of the substrate distribution was computed and its time averaged value used to set to $\alpha = 4.86 \times 10^4 L^2/g_X \cdot mmol_G \cdot h$ such that the resulting maintenance rate is $\overline{m} = 0.250 mmol_G/g_X \cdot h$. All the simulations were performed again, with the $\overline{m}$ value linked to the degree of mixing in the bioreactor and compared to those using a constant value, fitted for each case study. Results of the Xu et al., (1999) experiment coupled with Eq. (6.8) are shown in Fig. 6.8.

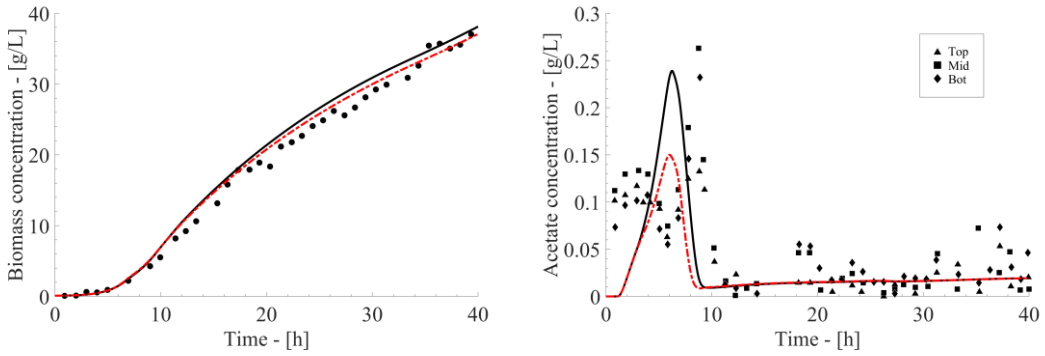

(a) (b)

Fig. 6.8 – Average Biomass (a) and Acetate (b) concentration evolution in the Xu et al., (1999) *experiment. Experimental data (symbols) are collected at the top (*top*), middle (*mid*) and bottom (*bot*) of the fermenter. IEM model results are reported for simulations with constant (solid line) and variable (dashed line) maintenance rate.*

Fig. 6.8 shows that tying the local mean substrate concentration fluctuations to the maintenance rate does not produce substantial changes in the biomass concentration, shown in Fig. 6.8a, where noticeable but small differences exist between the data obtained with a constant value of m or with a variable $\overline{m}$. Fig. 6.8b shows that different acetate profiles are obtained between about 3h and 9h from the beginning of the simulation. Before and after this time interval, the two acetate profiles obtained with constant and variable $\overline{m}$ perfectly overlap. In particular, the simulation where the maintenance rate could change due to the substrate fluctuation produced a lower peak concentration of acetate, due to a reduced fermentation rate. Indeed, Pigou & Morchain, (2015) showed that substrate gradients develop from 7h onward as the substrate consumption characteristic time gets smaller than the mixing time. The bioreactor is quite homogeneous up to 9h and the maintenance rate as predicted by Eq. (6.8) is about $0.150 mmol_G/g_X \cdot h$, much lower than the value used for the constant maintenance rate simulations ($0.250 mmol_G/g_X \cdot h$). Therefore, less glucose is needed by the cells that find more oxygen to catabolize the substrate, resulting in less acetate production. The glucose concentration profiles as obtained with a constant and a variable value of maintenance rate are not shown since they almost perfectly overlap.

The benefit of using a variable maintenance rate is more obvious when simulating the Neubauer et al., (1995) experiment, mainly because the cultivation con-

sists in a batch (homogeneous) and a fed-batch (segregated) period of equal duration. The results are shown in Fig. 6.9.

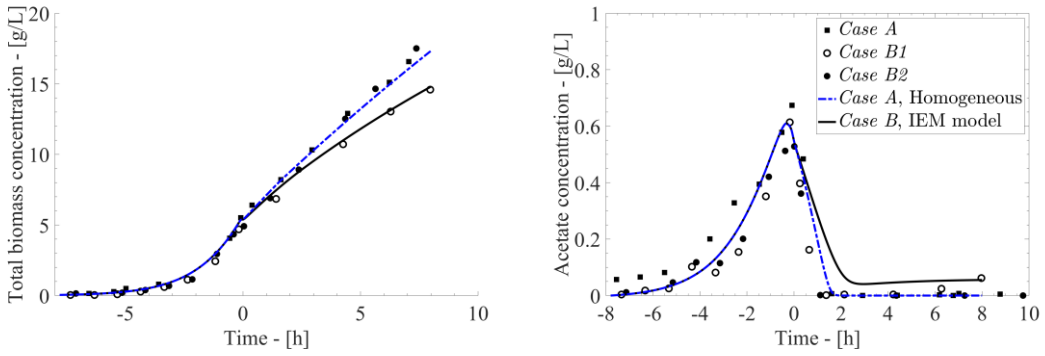

(a) (b)

Fig. 6.9 – Total biomass (a) and Acetate (b) concentration evolution in the Neubauer et al., (1995)*experiment. Experimental data (symbols) and IEM model results obtained with variable* $\overline{m}$ *for the* Case A *(dashed line) and* B *(solid line) experimental set-ups.*

The biomass concentration profiles as obtained from the IEM model coupled with Eq. (6.8) for the three different configurations described in Neubauer et al., (1995) and the corresponding experimental data are shown in Fig. 6.9a. The coupling of Eq. (6.8) does not substantially affect the biomass concentration profiles of *Case A*. In fact, the high concentration feed plume is rapidly dispersed in the bulk of the STR, leading to $\overline{m} \sim m_0 = constant$. Considering the biomass concentration profile in *Case B*, the IEM model coupled with Eq. (6.8) significantly improves the agreement between numerical and experimental results. In this case, the injection in the small plug flow reactor volume produces high local concentration peaks that are not promptly relieved. The acetate concentration profiles for the *Cases A* and *B* are shown in Fig. 6.9b and no relevant differences are found with respect to the numerical simulations with constant maintenance rate. Also, with a variable maintenance rate, the residual acetate concentration is consistently predicted for the *Case B*, which is found in the *Case B1* experiments as well.

6.6 Discussion

6.6.1 Time evolution of the maintenance rate

In Fig. 6.10, the evolution of $\overline{m}$ in time is shown for the Xu et al., (1999) and *Case B* of the Neubauer et al., (1995) experiment.

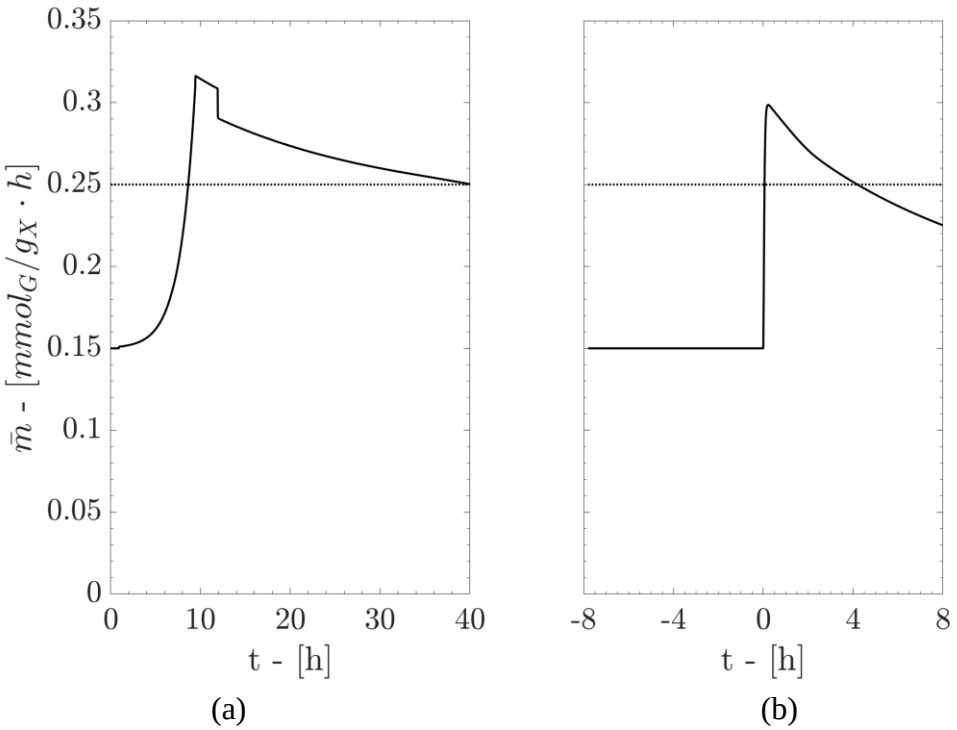

Fig. 6.10 – $\overline{m}$, solid line, as obtained from Eq. (6.8) for the Xu et al., (1999) *experiment (a) and* Case B *of the* Neubauer et al., (1995) *experiment(b). The dotted line is at a constant value of* $m = 0.25 mmol_G/g_X \cdot h$.

In the Xu et al., (1999) experiment, Fig. 6.10a, assuming a constant value of $\overline{m} = 0.250 mmol_G/g_X \cdot h$ leads to an over-prediction of $\overline{m}$ in the first ~9h of fermentation and a under-prediction of the mean maintenance rate in the last part of the process. Ultimately, the overall over- and under-predictions cancel out and considering $\overline{m}$ constant and equal to $m = 0.250 mmol_G/g_X \cdot h$ does not lead to substantial global differences.

On the other hand, $\overline{m}$ in *Case B* of the Neubauer et al., (1995) experiment, Fig. 6.10b, exhibit two different behaviors. During the batch phase (negative times), the maintenance rate is constant and equal to its value at rest: $\overline{m} = 0.150 mmol_G/g_X \cdot h$. Right after the injection, high glucose inhomogeneities develop in the multistage reactor resulting in a sharp peak in the mean maintenance rate profile that is slowly relieved in the following part of the fermentation. Hypothesizing a constant value of $m = 0.250 mmol_G/g_X \cdot h$ leads to an important over-prediction of the maintenance cost in the batch phase that results in a lower biomass production during this phase. Conversely, during the fed batch phase, a constant $\overline{m} = 0.250 mmol_G/g_X \cdot h$ seems to be an acceptable fit, with an overall under- and over-prediction that, as in the Xu et al., (1999) experiment, cancels out. On the other hand, hypothesizing a constant value of $m = 0.150 mmol_G/g_X \cdot h$ works fine when the bioreactor is actually homogeneous (*Case A* of the Neubauer et al., (1995) experiment), it also perfectly describes the batch phase but highly underestimates the mean maintenance cost, resulting in a higher final biomass production (as shown in Fig. 6.7a). The very short batch phase in the Xu et al., (1999) experiment results in an overall negligible effect of the over-prediction of the maintenance cost when considering a constant $\overline{m} = 0.250 mmol_G/g_X \cdot h$, whereas, due to a longer batch phase, a single constant value for the batch and fed-batch phase proved to be inadequate in describing *Case B* of the Neubauer et al., (1995) experiment.

The comparisons between the Xu et al., (1999) and Neubauer et al., (1995) experiments and the numerical simulations proves that disregarding the state of mixing and the inhomogeneities leads to inaccurate results, especially in terms of total biomass and acetate concentration. The results obtained with the IEM model closely match those obtained with the more accurate and more computational expensive compartment model, proving that the description of the segregations with a simplified approach may be enough when the growth rate distribution is spatially homogeneous. An accurate biomass prediction heavily depends on the correct estimation of the glucose into biomass yield, which must take into account the increased maintenance due to concentration gradients. Further considerations on the metabolic response, such as overflow, are needed to account for the acetate production. However, the metabolic responses leading to the formation of by-products cannot, by themselves, explain the loss of biomass productivity evidenced in the experiments. Thus, gradients affect the cell on two different levels: the first being the de-

creased yield and the second being the production/consumption of acetate. A simple kinetic model using a variable yield given by Eq. (6.8) suffice in describing the first effects whereas the addition of a metabolic model is needed to account for the by-product formation.

6.6.2 Lagrangian formulation of the $\overline{m}$ model

Following a single cell in its path inside the bioreactor, it was hypothesized that the cell, subject to instantaneous and localized glucose fluctuations, changes its maintenance rate according to Eq. (6.14), following the formulation proposed by Pigou, (2018) for the cell stresses.

$$\frac{dm}{dt} = \frac{K}{T_\sigma} \times \left(C_G(t) - \frac{1}{T_{bio}} \int_{t-T_{bio}}^{t} C_G(\tau) d\tau \right)^2 - \frac{m - m_0}{T_{rec}} \tag{6.14}$$

In Eq. (6.14), C_G refers to the instantaneous local concentration of glucose found by the cell along its path, K is a model constant representing the unit change in maintenance rate due to a unit change in the driving force (i.e. the squared concentration fluctuations), T_σ is a response time of the cell to external concentration fluctuations, the squared term in parentheses represents the driving force of the change in the maintenance rate, m_0 is the minimum maintenance rate of the cells and T_{rec} is a relaxation time towards the minimum maintenance rate m_0. The expression $\frac{1}{T_{bio}} \int_{t-T_{bio}}^{t} C_G(\tau) d\tau$ is a time average of the concentrations previously encountered by the cell. This integral quantity is introduced to account for a "memory effect", the fact that previously encountered concentrations contributed to set the present cell state (including its maintenance rate). It represents in some way an estimate of the concentration value to which the cell is accustomed. From that angle, T_{bio} can be interpreted as the time scale of long-term metabolic adaptation. The term in parentheses therefore measures how much the local environment is different from the past conditions and thus be perceived as stressing from the cell point of view. In a homogeneous bioreactor, the time average is actually constant, equal to C_G, the environment is stressless and the maintenance rate would relax toward the base level m_0 with a dynamic defined by the characteristic time T_{rec}. In a heterogeneous bioreactor, the value of the time average concentration depends on the

ratio between the mixing time and T_{bio}. If the mixing time is smaller than T_{bio}, the time average concentration can be regarded as the volume average $<C_G>$.

In addition, changes in the maintenance rate are certainly much slower than the rate of change of substrate concentration along the cell trajectory, because the former is a consequence of the latter. Thus, in the limit of the derivative dm/dt being negligibly small and Eq. (6.14) simplifies to:

$$m = m_0 + \alpha(C_G(t) - <C_G(t)>)^2 \tag{6.15}$$

Where the only parameter α, already introduced in Eq. (6.7), is equal to $\frac{K \times T_{rec}}{T_\sigma}$. Quite logically, α results from the cell responsiveness, its response time and its recovery time to external fluctuations. As such, the cell based Lagrangian vision helps understanding the integral Eulerian model for $\overline{m}$.

A fruitful parallel can be made between equation Eq. (6.14) and Eq. (6.4): in both cases a difference between the local conditions (μ^* or C_G) and a cell state variable (μ or $\frac{1}{T_{bio}}\int_{t-T_{bio}}^{t} C_G(\tau)d\tau$) is used to identify and quantify a cascade of biological responses. The short-term metabolic response leading to overflow, the induced effects resulting in an increased maintenance rate and finally the long-term response driving the population growth rate adaptation are accounted for at a minimal expense in terms of the number of internal cell variables

In order to gain knowledge on the rate of change of maintenance rate for a population of cells, Eq. (6.15) should be extended to a large number of particles. Ensemble averaging Eq. (6.15) over the total number of cells in the reactor, N_{cells}, yields to:

$$\overline{m} = m_0 + \alpha \frac{1}{N_{cells}} \sum_{j=1}^{N_{cells}} \left(C_G^j - <C_G>\right)^2 \tag{6.16}$$

where $\overline{m}$ is the ensemble average maintenance rate and C_G^j is the substrate concentration along the trajectory of the j^{th} cell. Eq. (6.8) is readily derived from Eq. (6.16) since N_{cells} is large enough to sample the whole volume. The summation in Eq. (6.16) is indeed a Monte Carlo calculation of the integral term presented in Eq. (6.7).

The parameters introduced in Eq. (6.14) are a modelling choice aimed at describing in the most accurate way the different phenomena occurring in a cell subject to substrate concentration fluctuation, without adding constitutive equations for each of them. A comprehensive description of the effect of the substrate concentration fluctuations on the cell metabolism would require *ad hoc* experiments and insight on the single cell metabolic responses (such as in Löffler et al., (2017), Nieß et al., (2017) and Simen et al., (2017)), that is beyond the scope of this work. The modelling of the metabolic changes due to substrate concentration fluctuations put forward in this work has the goal to implement a simple Eulerian integral description for the numerical simulations of heterogeneous bioreactors.

The single cell equation, Eq. (6.14) was solved for the Xu et al., (1999) and for *Case B* of the Neubauer et al., (1995) experiments and, in both cases, it was hypothesized that the cell spent a time exactly equal to $\tau_{C_{S,max}}$ at higher substrate concentration and $\tau_{C_{S,min}}$ at lower substrate concentration. Ideally, a distribution of residence times in the low concentration zone should be considered. The time trace of the glucose concentration experienced by these ideal cells is shown in Fig. 6.11. Having divided the substrate concentration space in 70 sub-volumes and occurring the injection of fresh substrate in just one of the sub-volumes, $\tau_{C_{S,max}}$ was assumed equal to ~3.6s for the Xu et al., (1999) experiment, being this time equal to one seventieth of the macro-mixing time, and $\tau_{C_{S,min}}$ equal to ~246.4 s. In the numerical study concerning *Case B* of the Neubauer et al., (1995) experiment, $\tau_{C_{S,max}}$ was assumed equal to , τ_{PFR} = 113s and $\tau_{C_{S,min}}$ equal to τ_{STR} = 27min. The maximum $C_{S,max}$, , and minimum, $C_{S,min}$ concentration in each simulation were assumed constant and equal to the whole-process-time average of the substrate concentration in the injection sub-volume(s) and in the remaining sub-volumes respectively. The time trace of the glucose concentration just introduced was used as $C_G(t)$ in Eq. (6.14) and the other constants are reported in Tab. 6.3. The characteristic time needed by the cell to adapt its metabolism to the substrate concentration in the surrounding environment, T_{bio}, was hypothesized to be long with respect to the other biological time scales as well as the fluid dynamics time scales. The values of the other constants should be determined from dedicated experiments, that is why, in this discussion, a systematic analysis of the constants of Eq. (6.14) is overlooked.

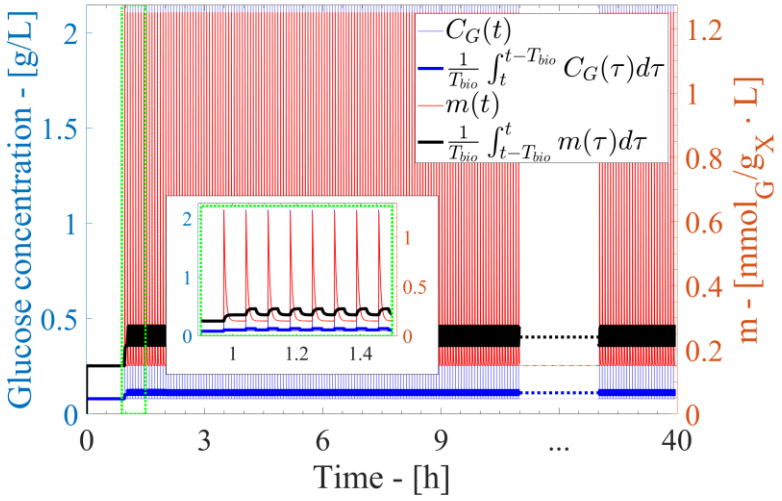

(a)

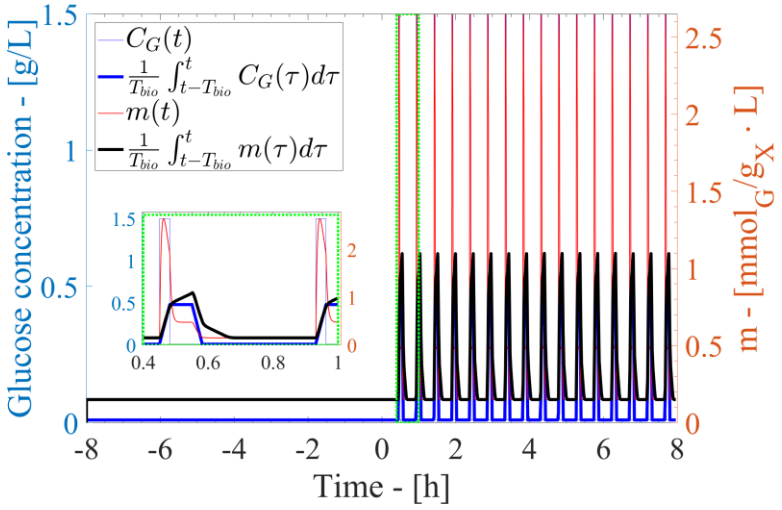

(b)

Fig. 6.11 – Instantaneous and averaged evolution of the glucose concentration experienced by the cells (left y-axis) and instantaneous and averaged maintenance rate (right y-axis). The simulations were devised to test the change in the maintenance rate due to substrate fluctuations for the Xu et al., (1999) *experiment (a) and for the* Neubauer et al., (1995) *experiment (b).*

The constants K, T_σ and T_{rec} and their ratio mostly influence the magnitude of the resulting m. The constants were set in order to get $\alpha = \frac{K \times T_{rec}}{T_\sigma}$ equal to $\alpha =$

$5.00 \times 10^4 L^2/g_X \cdot mmol_G \cdot h$, close to the value of $\alpha = 4.86 \times 10^4 L^2/g_X \cdot mmol_G \cdot h$ identified through experiments in Section 6.5.2.

Tab. 6.3 – Constants used in the solution of Eq. (6.14)

Constant	Value	Units
K	5×10^3	$L^2/g_X \cdot mmol_G \cdot h$
T_σ	5×10^{-4}	h
T_{bio}	0.1	h
m_0	0.150	$mmol_G/g_X \cdot h$
T_{rec}	5×10^{-3}	h

The constant T_{bio} and especially the ratio between T_{bio} and the interval between two consecutive fluctuations is what changes the overall integral behavior of m. The solution of Eq. (6.14) for the two experiments is shown in Fig. 6.11.

From Fig. 6.11a, in the zoomed drawing encircled with the dashed line, it is possible to see that the instantaneous maintenance rate obtained with the parameters in Tab. 6.3 for the Xu et al., (1999) experiment, $m(t)$, is subject to periodic peaks (due to the concentration fluctuations) after which it recovers its value at rest, m_0. Interestingly, the average m obtained over a T_{bio} time interval is almost constant during the fermentation, except for a short initial adjustment time immediately after the beginning of the fed-batch phase. As already mentioned, averaging in time over T_{bio} is equivalent to averaging over the volume or ensemble averaging over the entire microbial population. Remarkably, the averaged value of m is correctly predicted in this Lagrangian formulation, with the same value of $\alpha = \frac{K \times T_{rec}}{T_\sigma}$ derived from a Eulerian view.

On the other hand, the zoomed drawing encircled with the dashed line in Fig. 6.11b shows that in *Case B* of the Neubauer et al., (1995) experiment the fluctuation characteristic time is longer with respect to Xu et al., (1999). In fact, the presence of the large STR with low substrate concentration adds a long residence time between two consecutive glucose fluctuations. During this time, the cells have time to adapt to the new low-concentration environment, producing metabolic changes that affect the instantaneous maintenance rate as well as its averaged value. When the cells are transported to the high glucose concentration environment the concen-

tration difference triggers a higher metabolic stress with respect to the previous case. This behavior is caught by the model in terms of average glucose concentration (thick blue line) that is almost constant in Fig. 6.11a whereas it pulses due to the fluctuations in Fig. 6.11b. Another important aspect is the duration of the concentration fluctuation that in *Case B* of the Neubauer et al., (1995) experiment is two orders of magnitude larger than in the Xu et al., (1999) experiment. This longer exposure to high concentration allows the cell to adjust to the new high concentration environment, allowing for a small m recovery in the high concentration environment. The single cell behavior convoluted with the residence time distribution in the STR explains the increased maintenance at the population scale leading to a reduced production of biomass with respect to *Case A* of the same experiment.

6.6.3 Further considerations on the coupling with oxygen availability

In our simulations, the dissolved oxygen concentration is constant and equal to $\sim 10 \mathrm{mg_O/L}$, and fermentative metabolism could only take place because of a reduced oxygen uptake rate due to inhibition by acetate. Having set $K_{i,A}^{o} = 4 \mathrm{g_A/L}$ and obtaining a residual acetate concentration below $10 \mathrm{mg_A/L}$, acetate does not inhibit the oxygen uptake and therefore fermentation does not happen. Thus, the mixed-acid metabolism is not responsible for the reduced yield. The reduction was entirely attributed to an increased maintenance rate as a result of gradient induced stresses. This possible explanation was already proposed in most studies mentioned in the introduction. However, several authors also argued that an exposure to insufficient oxygen levels would trigger the mixed-acid fermentation pathways resulting in the production of lactate, formate and succinate from pyruvate. These pathways compete with the central metabolism pathway.

Neubauer et al., (1995) interpreted the reduced production of biomass in *Case B1* as a result of a suboptimal oxygen concentration that induced an acetate production through fermentation at the end of the PFR. To support this, they performed *Case B2* experiment (with oxygen enriched air injection in the PFR). The initial acetate production due to overflow metabolism was maintained but acetate formation due to fermentation was eliminated. Also, the production of biomass matched the biomass production in *Case A.* This suggests that overflow is not the main cause of yield reduction. Repeating the Neubauer et al., (1995) experiments,

Xu et al., (1999) measured that the various acids are re-assimilated almost completely in the aerated STR. They explained that the repeated production and re-assimilation may be a contributing factor causing biomass loss upon scale-up. Even though the oxygen sensor did not reveal limiting levels in the $20m^3$ experiments, they concluded that oxygen limitation was certainly present or perceived by the microorganisms. In the end, mixed-acid fermentation lead to small amounts of by-products (a few mg/L) which cannot quantitatively explain a decrease in biomass production of several g/L.

A possible explanation of this experimental observation is that the bacteria subject to intense substrate fluctuation almost instantaneously convert up to 30% of the substrate into CO_2 with a specific uptake rate of O_2 that was very similar to the specific rate of CO_2 excretion (Sunya, et al., 2012). This indicates that the oxygen demand increases as a result of over-assimilation. If enough oxygen is available, the massive excretion of CO_2 limits the substrate flood in the central metabolism and this mechanism therefore contributes to a reduction of the metabolic stresses, i.e. lower $\overline{m}$ values. If the oxygen availability is insufficient (or the oxidative capacity of the cells is saturated) mixed-acid fermentation is triggered as well as a cascade of genetic and enzymatic bioprocesses which contribute to an increased energetic *cost of living* from the cell point of view. It is therefore promising to consider that both substrate and oxygen distribution can contribute to a modification of the maintenance rate and extend the proposed approach to multiple nutrients.

6.7 Conclusions

In this work a two-environments IEM mixing model was implemented in the context of the software ADENON to describe the substrate inhomogeneities in two experimental fed-batch processes found in literature.

Numerical simulations were performed to compare results obtained with the IEM model to numerical results obtained with a compartment model from literature and to the experimental results. A very good agreement was reached between the results obtained with the IEM and the compartment model, proving that a simplified description of the state of mixing could suffice when just substrate concentration spatial gradients are important. The agreement between the experimental and

the numerical results is not worsened by the adoption of the simplified IEM model, in both the experimental set-ups found in literature.

In comparison to other approaches (CFD and CMA), the use of an IEM model allows a fast and inexpensive simulation of highly segregated heterogeneous bioreactors.

Considerations on the increase of the maintenance rate due to concentration fluctuations were necessary to improve the agreement with the experimental data. A modification to the Pirt's law introducing a dependence of the cell maintenance on the variance of the concentration distribution was hypothesized, validated against experimental data and discussed both from a Lagrangian and from a Eulerian perspective. This proposition constitutes a very simple and presumably general framework to connect concentration gradients to the maintenance rate.

To sum up, the cost of living in an imperfectly mixed bioreactor increases with the variance of the concentration distribution.

6.8 Appendix A

A sensitivity study on the constants range highlighted that 6 constants of the metabolic model had the highest effects on the Neubauer et al., (1995) results. The constants and their values can be found in Tab. A. 6.1.

Tab. A. 6.1 – Model constants and their values used in the sensitivity study.

Constant	-30% (-1)	Xu et al., (1999) value	+30% (+1)	Units
ϕ_O^{max}	10.92	15.60	20.28	$mmol_O/g_X \cdot h$
$K_{i,A}$	2.10	3.00	3.90	g_A/L
$K_{i,A}^o$	2.80	4.00	5.20	g_A/L
$\overline{m}$	0.175	0.250	0.325	$mmol_G/g_X \cdot h$
Y_{AG}	2.10	3.00	3.90	mol_A/mol_G
Y_{XG}^{max}	0.92	1.32	1.72	mol_X/mol_G

A ±30% deviation from the values proposed by Pigou & Morchain, (2015) to simulate the Xu et al., (1999) experiment was studied, to map the sensitivity of the Neubauer et al., (1995) results on the variations. Three response variables were observed, namely, the biomass concentration at the end of the fed-batch process, the maximum concentration of acetate found in the system during the whole process and the time needed to deplete the initial amount of glucose and therefore end the batch phase. The effects of the constants change on the response variables are shown if Fig. A. 6.1, where the constant normalized values of ±1 indicate a variation of ±30% from the default values and the y-axis values are the percent change of the response variables with respect to the simulations with the default constants values (0).

Fig. A. 6.1 shows that just a decrease in the maintenance rate, m, or an increase in the maximum conversion yield of glucose in biomass, Y_{XG}^{max}, may lead to an increase of the final concentration of biomass. Both constants appear in the Pirt's formulation of the glucose to biomass conversion yield, Eq. (6.6), but m is related both to the bacteria and to the operating conditions, whereas Y_{XG}^{max} is presented as a maximum limit only dependent on the selected strain. Increasing the biomass con-

centration at the end of the fed-batch phase by changing the two constants presented above lead to a relatively large variation in the production of acetate, that can be adjusted with a variation of the other constants.

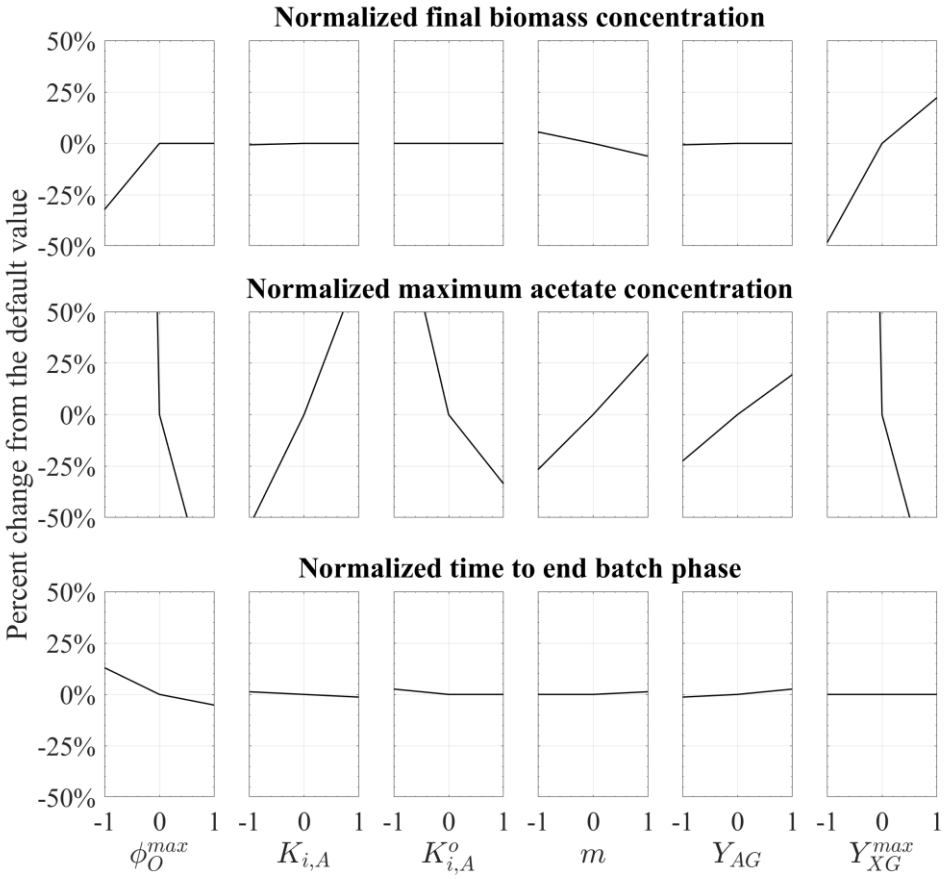

Fig. A. 6.1 – Effect of the constants ±30% variation on the response variables.

The sensitivity study was instrumental in tuning the constants in Tab. 6.1 for the *Case A* of the Neubauer et al., (1995) experiment. In Tab. A. 6.2 the percent change of the constant values tuned for the Neubauer et al., (1995) experiment with respect to the values proposed by (Pigou & Morchain, 2015) to simulate the Xu et al., (1999) experiment is reported. The constant values for the two experiments are reported in Tab. 6.1.

Tab. A. 6.2 shows that the maintenance rate is subject to the largest absolute value variation, pointing to the fact that a model to account for the change of m in the two sets of experiments may be needed.

Tab. A. 6.2 – Model constants and their values used to improve the agreement with the Case A *of the* Neubauer et al., (1995) *experiment.*

Constant	Percent change
ϕ_O^{max}	-10.3%
$K_{i,A}$	+16.7%
$K_{i,A}^o$	0.0%
m	-40.0%
Y_{AG}^{ferm} Y_{AG}^{over}	**-7.0%
Y_{XG}^{max}	+13.6%

** *The average Y_{AG} weighted on the acetate production mechanism is 2.79 mol_A/mol_G*

6.9 Nomenclature

$\boldsymbol{C}$	Species vector concentration
C_G	Glucose concentration
$<C_G>$	Volume average glucose concentration
C_G^j	Substrate concentration along the trajectory of the j^{th} cell
C_k	Concentration of the k^{th} species
$<C_k>$	Volume average concentration of the k^{th} species
$C_{S,max}$	Substrate concentration in the injection sub-volumes
$C_{S,min}$	Substrate concentration in the bulk sub-volumes
K	Unit change in m due to a unit change in the driving force
$K_{i,A}$	Acetate inhibition constant
$K_{i,A}^o$	Acetate inhibition constant in the oxygen uptake rate
m	Maintenance rate
$\overline{m}$	Variable maintenance rate of the cell population
m_0	Maintenance rate of the cells at rest
N_C	Number of sub-volumes
N_{cells}	Number of cells in the reactor
$p(C_k)$	Probability to find C_k in the control volume
r_k	Specific reaction rate of the k^{th} species
R_k	Volumetric reaction rate of the k^{th} species
S_k	Feed source term for the k^{th} species
t	Time
T_{bio}	Time scale of long-term metabolic adaptation
T_{rec}	Maintenance rate relaxation characteristic time
$T^{u/d}$	Adaptation time of the rate of change of μ
T_σ	Response time of the cell to external concentration fluctuations
V	Control volume
$\mid v \mid^{in}$	Norm of the velocity vector entering the control volume
$\mid v \mid^{out}$	Norm of the velocity vector exiting the control volume
X	Biomass concentration
Y_{AG}	Conversion yield of glucose in acetate
Y_{AG}^{ferm}	Conversion yield of glucose in acetate through fermentation
Y_{AG}^{over}	Conversion yield of glucose in acetate through overflow
$Y_{k,l\neq k}$	Conversion yield of the l^{th} into the k^{th} species
Y_{XG}	Conversion yield of glucose in biomass
Y_{XG}^{max}	Maximum conversion yield of glucose in biomass

Greek letters

α	Parameter for the integral formulation of $\overline{m}$
ζ	Rate of change of the specific growth rate
μ	Specific growth rate of the cell
μ^*	Equilibrium specific growth rate
μ^a	Actual specific growth rate
τ_m	IEM model parameter
τ_{PFR}	Residence time in the PFR
$\tau_{C_{S,max}}$	Time spent in the injection sub-volume(s) by an ideal cell
$\tau_{C_{S,min}}$	Time spent in the bulk sub-volume(s) by an ideal cell
τ_{STR}	Residence time in the STR
ϕ_O^{max}	Maximum oxygen uptake rate
Ω	Surface enveloping the control volume
ω, τ	Free variables of integration

6.10 References

Alopaeus, V., Moilanen, P., & Laakkonen, M. (2009). Analysis of stirred tanks with two-zone models. *AIChE Journal*, *55*(10), 2545–2552. https://doi.org/10.1002/aic.11850

Bajpai, R. K., & Reuss, M. (1982). Coupling of mixing and microbial kinetics for evaluating the performance of bioreactors. *The Canadian Journal of Chemical Engineering*, *60*(3), 384–392. https://doi.org/10.1002/cjce.5450600308

Baldyga, J., & Bourne, J. R. (1992). Interactions between mixing on various scales in stirred tank reactors. *Chemical Engineering Science*, *47*(8), 1839–1848. https://doi.org/10.1016/0009-2509(92)80302-S

Bourne, J. R., Kozicki, F., & Rys, P. (1981). Mixing and fast chemical reaction—I. *Chemical Engineering Science*, *36*(10), 1643–1648. https://doi.org/10.1016/0009-2509(81)80008-5

Delafosse, A., Collignon, M.-L., Calvo, S., Delvigne, F., Crine, M., Thonart, P., & Toye, D. (2014). CFD-based compartment model for description of mixing in bioreactors. *Chemical Engineering Science*, *106*, 76–85. https://doi.org/10.1016/j.ces.2013.11.033

Dunlop, E. H., & Ye, S. J. (1990). Micromixing in fermentors: Metabolic changes inSaccharomyces cerevisiae and their relationship to fluid turbulence. *Biotechnology and Bioengineering*, *36*(8), 854–864. https://doi.org/10.1002/bit.260360816

Enfors, S. O., Jahic, M., Rozkov, A., Xu, B., Hecker, M., Jürgen, B., … Manelius, A. (2001). Physiological responses to mixing in large scale bioreactors. *Journal of Biotechnology*, *85*(2), 175–185. https://doi.org/10.1016/S0168-1656(00)00365-5

Fan, L. T., Tsai, B. I., & Erickson, L. E. (1971). Simultaneous effect of macromixing and micromixing on growth processes. *AIChE Journal*, *17*(3), 689–696. https://doi.org/10.1002/aic.690170336

Fowler, J. D., & Dunlop, E. H. (1989). Effects of reactant heterogeneity and mixing on catabolite repression in cultures ofSaccharomyces cerevisiae. *Biotechnology and Bioengineering*, *33*(8), 1039–1046. https://doi.org/10.1002/bit.260330813

Fox, R. O. (2003). *Computational Models for Turbulent Reacting Flows*. *Computational Models for Turbulent Reacting Flows*. Cambridge: Cambridge University Press. https://doi.org/10.1017/CBO9780511610103

George, S., Larsson, G., & Enfors, S.-O. (1993). A scale-down two-compartment reactor with controlled substrate oscillations: Metabolic response of Saccharomyces

cerevisiae. *Bioprocess Engineering*, *9*(6), 249–257. https://doi.org/10.1007/BF01061530

Gernigon, V., Chekroun, M. A., Cockx, A., Guiraud, P., & Morchain, J. (2019). How Mixing and Light Heterogeneity Impact the Overall Growth Rate in Photobioreactors. *Chemical Engineering & Technology*, *42*(8), ceat.201900102. https://doi.org/10.1002/ceat.201900102

Hansford, G. S., & Humphrey, A. E. (1966). The effect of equipment scale and degree of mixing on continuous fermentation yield at low dilution rates. *Biotechnology and Bioengineering*, *8*(1), 85–96. https://doi.org/10.1002/bit.260080108

Haringa, C., Deshmukh, A. T., Mudde, R. F., & Noorman, H. J. (2017). Euler-Lagrange analysis towards representative down-scaling of a 22 m 3 aerobic S. cerevisiae fermentation. *Chemical Engineering Science*, *170*, 653–669. https://doi.org/10.1016/j.ces.2017.01.014

Henson, M. A. (2003). Dynamic modeling of microbial cell populations. *Current Opinion in Biotechnology*, *14*(5), 460–467. https://doi.org/10.1016/S0958-1669(03)00104-6

Hjertager, B. H., & Morud, K. (1995). Computational fluid dynamics simulation of bioreactors. *Modeling, Identification and Control: A Norwegian Research Bulletin*, *16*(4), 177–191. https://doi.org/10.4173/mic.1995.4.1

Holms, H. (1996). Flux analysis and control of the central metabolic pathways in Escherichia coli. *FEMS Microbiology Reviews*, *19*(2), 85–116. https://doi.org/10.1016/S0168-6445(96)00026-5

Lemoine, A., Maya Martinez-Iturralde, N., Spann, R., Neubauer, P., & Junne, S. (2015). Response of Corynebacterium glutamicum exposed to oscillating cultivation conditions in a two- and a novel three-compartment scale-down bioreactor. *Biotechnology and Bioengineering*, *112*(6), 1220–1231. https://doi.org/10.1002/bit.25543

Löffler, M., Simen, J. D., Müller, J., Jäger, G., Laghrami, S., Schäferhoff, K., … Takors, R. (2017). Switching between nitrogen and glucose limitation: Unraveling transcriptional dynamics in Escherichia coli. *Journal of Biotechnology*, *258*, 2–12. https://doi.org/10.1016/j.jbiotec.2017.04.011

Mantzaris, N. V., Liou, J.-J., Daoutidis, P., & Srienc, F. (1999). Numerical solution of a mass structured cell population balance model in an environment of changing substrate concentration. *Journal of Biotechnology*, *71*(1–3), 157–174. https://doi.org/10.1016/S0168-1656(99)00020-6

Meadows, A. L., Karnik, R., Lam, H., Forestell, S., & Snedecor, B. (2010). Application of dynamic flux balance analysis to an industrial Escherichia coli fermentation.

Metabolic Engineering, *12*(2), 150–160. https://doi.org/10.1016/j.ymben.2009.07.006

Morchain, Jerome. (2017). *Bioreactor Modeling : Interactions between Hydrodynamics and Biology*. London/Oxford: ISTE Press Ltd/Elsevier Ltd. Retrieved from https://books.google.ca/books?hl=en&lr=&id=-w4TDgAAQBAJ&oi=fnd&pg=PP1&dq=%22bioreactor+modeling%22+morchain&ots=9i_q_CCmQa&sig=traN3Vbx1rvQzoKFPxLPonBbb8E#v=onepage&q=%22bioreactor modeling%22 morchain&f=false

Morchain, Jérôme, & Fonade, C. (2009). A structured model for the simulation of bioreactors under transient conditions. *AIChE Journal*, *55*(11), 2973–2984. https://doi.org/10.1002/aic.11906

Morchain, Jérôme, Gabelle, J.-C. C., & Cockx, A. (2014). A coupled population balance model and CFD approach for the simulation of mixing issues in lab-scale and industrial bioreactors. *AIChE Journal*, *60*(1), 27–40. https://doi.org/10.1002/aic.14238

Morchain, Jérôme, Gabelle, J. C., & Cockx, A. (2013). Coupling of biokinetic and population balance models to account for biological heterogeneity in bioreactors. *AIChE Journal*, *59*(2), 369–379. https://doi.org/10.1002/aic.13820

Morchain, Jérôme, Pigou, M., & Lebaz, N. (2017). A population balance model for bioreactors combining interdivision time distributions and micromixing concepts. *Biochemical Engineering Journal*, *126*, 135–145. https://doi.org/10.1016/j.bej.2016.09.005

Namdev, P. K., Thompson, B. G., & Gray, M. R. (1992). Effect of feed zone in fed-batch fermentations of Saccharomyces cerevisiae. *Biotechnology and Bioengineering*, *40*(2), 235–246. https://doi.org/10.1002/bit.260400207

Nauha, E. K., Kálal, Z., Ali, J. M., & Alopaeus, V. (2018). Compartmental modeling of large stirred tank bioreactors with high gas volume fractions. *Chemical Engineering Journal*, *334*, 2319–2334. https://doi.org/10.1016/j.cej.2017.11.182

Neubauer, P., Häggström, L., & Enfors, S.-O. (1995). Influence of substrate oscillations on acetate formation and growth yield in Escherichia coli glucose limited fed-batch cultivations. *Biotechnology and Bioengineering*, *47*(2), 139–146. https://doi.org/10.1002/bit.260470204

Neubauer, Peter, & Junne, S. (2010). Scale-down simulators for metabolic analysis of large-scale bioprocesses. *Current Opinion in Biotechnology*, *21*(1), 114–121. https://doi.org/10.1016/j.copbio.2010.02.001

Nieß, A., Löffler, M., Simen, J. D., & Takors, R. (2017). Repetitive Short-Term Stimuli Imposed in Poor Mixing Zones Induce Long-Term Adaptation of E. coli Cultures

in Large-Scale Bioreactors: Experimental Evidence and Mathematical Model. *Frontiers in Microbiology*, *8*(JUN), 1195. https://doi.org/10.3389/fmicb.2017.01195

Pigou, M. (2018). *Modélisation du comportement cinétique, des phénomènes de mélange et de transfert locaux, et des effets d'hétérogénéité de population dans les fermenteurs industriels*. *http://www.theses.fr*. Toulouse, INSA. Retrieved from https://www.theses.fr/2018ISAT0038

Pigou, M., & Morchain, J. (2015). Investigating the interactions between physical and biological heterogeneities in bioreactors using compartment, population balance and metabolic models. *Chemical Engineering Science*, *126*, 267–282. https://doi.org/10.1016/j.ces.2014.11.035

Pirt, S. (1965). The maintenance energy of bacteria in growing cultures. *Proceedings of the Royal Society of London. Series B. Biological Sciences*, *163*(991), 224–231. https://doi.org/10.1098/rspb.1965.0069

Plasari, E., David, R., & Villermaux, J. (1978). Micromixing Phenomena in Continuous Stirred Reactors Using a Michaelis-Menten Reaction in the Liquid Phase (pp. 125–139). https://doi.org/10.1021/bk-1978-0065.ch011

Quedeville, V., Ouazaite, H., Polizzi, B., Fox, R. O., Villedieu, P., Fede, P., … Morchain, J. (2018). A two-dimensional population balance model for cell growth including multiple uptake systems. *Chemical Engineering Research and Design*, *132*, 966–981. https://doi.org/10.1016/j.cherd.2018.02.025

Schmalzriedt, S., Jenne, M., Mauch, K., & Reuss, M. (2003). Integration of Physiology and Fluid Dynamics. In *Process Integration in Biochemical Engineering. Advances in Biochemical Engineering/Biotechnology* (pp. 19–68). Springer, Berlin, Heidelberg. https://doi.org/10.1007/3-540-36782-9_2

Siebler, F., Lapin, A., Hermann, M., & Takors, R. (2019). The impact of CO gradients on C. ljungdahlii in a 125 m3 bubble column: Mass transfer, circulation time and lifeline analysis. *Chemical Engineering Science*, *207*, 410–423. https://doi.org/10.1016/j.ces.2019.06.018

Simen, J. D., Löffler, M., Jäger, G., Schäferhoff, K., Freund, A., Matthes, J., … Takors, R. (2017). Transcriptional response of Escherichia coli to ammonia and glucose fluctuations. *Microbial Biotechnology*, *10*(4), 858–872. https://doi.org/10.1111/1751-7915.12713

Stamatakis, M. (2010). Cell population balance, ensemble and continuum modeling frameworks: Conditional equivalence and hybrid approaches. *Chemical Engineering Science*, *65*(2), 1008–1015. https://doi.org/10.1016/j.ces.2009.09.054

Sunya, S., Delvigne, F., Uribelarrea, J.-L., Molina-Jouve, C., & Gorret, N. (2012). Comparison of the transient responses of Escherichia coli to a glucose pulse of various intensities. *Applied Microbiology and Biotechnology*, *95*(4), 1021–1034. https://doi.org/10.1007/s00253-012-3938-y

Takors, R. (2012). Scale-up of microbial processes: Impacts, tools and open questions. *Journal of Biotechnology*, *160*(1–2), 3–9. https://doi.org/10.1016/j.jbiotec.2011.12.010

Tsai, B. I., Erickson, L. E., & Fan, L. T. (1969). The effect of micromixing on growth processes. *Biotechnology and Bioengineering*, *11*(2), 181–205. https://doi.org/10.1002/bit.260110206

Tsai, B. I., Fan, L. T., Erickson, L. E., & Chen, M. S. K. (1971). The reversed two-environment model of micromixing and growth processes. *Journal of Applied Chemistry and Biotechnology*, *21*(10), 307–312. https://doi.org/10.1002/jctb.5020211008

Villermaux, J., & Devillon, J. C. (1972). Representation of the coalescence and the redispersion of the fields of segregation in a fluid by a model of phenomenologic interaction. In *Chemical Reaction Engineering: Proceedings of the Fifth European/Second International Symposium on Chemical Reaction Engineering* (pp. B1-13). Amsterdam: New York, Elsevier Pub. Co.

Vrábel, P., Van der Lans, R. G. J. M., Van der Schot, F. N., Luyben, K. C. A. M., Xu, B., & Enfors, S. O. (2001). CMA: Integration of fluid dynamics and microbial kinetics in modelling of large-scale fermentations. *Chemical Engineering Journal*, *84*(3), 463–474. https://doi.org/10.1016/S1385-8947(00)00271-0

Xu, B., Jahic, M., Blomsten, G., & Enfors, S.-O. (1999). Glucose overflow metabolism and mixed-acid fermentation in aerobic large-scale fed-batch processes with Escherichia coli. *Applied Microbiology and Biotechnology*, *51*(5), 564–571. https://doi.org/10.1007/s002530051433

Ye, S. J. (1985). *Micromixing in saccharomyces cerevisiae aerobic fermentation*. Washington University, Saint Louis, Missouri. Retrieved from http://crelonweb.eec.wustl.edu/theses/S. Ye.pdf

Chapter 7

Conclusions

The goal of the research presented in this PhD thesis was to investigate different turbulent two-phase processes in mechanically stirred tanks and bioreactors by means of numerical simulations.

Different phenomena were studied in the context of the RANS-TFM approach, in which the segregation of the phases required specific modelling of the different closure terms to describe the fluid dynamics behavior, the interphase interactions and the effects within each single phase, such as the biomass metabolism or the evolution of the drop diameters.

The investigation concerned different laboratory scale equipment involving dispersed particle/droplets/bubbles in a continuous liquid phase, with the purpose in mind to identify a modelling method for industrial-scale equipment for each specific system. As a result, the direct resolution at all turbulent length and time scales, the entire particle-fluid interface, the particle-fluid interaction forces, the particle-particle collision and particle-wall collision events is not possible. In this realm, the major strength of the TFM model is the viability of application at indus-

trial scale with a realistic representation of the equipment geometry, that is the target of any design and geometrical optimization method.

Strengths and limitations of the TFM model for the investigate two-phase flows are different depending on the main physical characteristics of the specific turbulent multiphase equipment under investigation, namely: the dispersed phase mean volume fraction, the dispersed phase volume fraction distribution in the equipment volume, the dispersed phase size distribution, the operating mode for the dispersed phase (batch as in the case of droplets and particles, continuous for bubbles). In addition, possible inter-phase mass transfer, chemical or biochemical reactions, if present, must be considered.

For those processes that are critically affected by the turbulent flow field of the continuous phase (e.g. bubble/droplet breakage and coalescence) the same limitations of single-phase RANS-based simulations and the same attention to numerical verification that are already well known from previous investigations have to be kept in mind.

The dispersed phase mean and local volume fraction determines the level of interactions.

- In case of one-way coupling, as in the investigated liquid-liquid stirred tank, fluid-particle interaction models for TFM models are generally well established, provided that a realistic size of the dispersed phase is either know a-priori (as is the case of inert solid particles or narrow size distribution of bubbles or droplets) or determined by population balance models in case of wide size distribution. In this latter case, limitations are mainly concerned with the breakage and coalescence models and with the RANS-based prediction of the liquid phase turbulent flow field, due to the dependency of breakage and coalescence mechanisms on the turbulent field. A method for partially overcoming this limitation is identified in the liquid-liquid study.
- In case of two-way coupling the effect of the dispersed phase on the turbulent field may have a significant impact, either enhancing or dumping turbulent fluctuations. In the incomplete suspension of dense solid-liquid mixtures, for instance, the lack of an established turbulence dumping model due to the settled layer of particles leads to an overprediction of an interphase

term, resulting in incorrect suspension of the solids from the bottom of the tank.

- In case of four-way coupling the interactions between particles, such as collisions, are modelled as ensemble averaged phenomena. Collisions of particles in dense solid-liquid suspensions in fully turbulent stirred tanks proved to have a negligible contribution in predicting the volume fraction distribution of the dispersed phase above N_{JS}. On the other hand, a related phenomenon as the particle packing is essential in correctly predict the suspension, but its modelling relies on a numerical approach.
- For very large dispersed phase concentration, the dominant flow regime may change due to phase inversion, inter-particle collisions, enhanced aggregation phenomena, etc. In these conditions, the Euler-Euler model limits are pushed, and a reliable prediction of the flow fields needs additional models to take the changed physics into account. This is the case of unsuspended solids on the tanks bottom, where inter-particle collision is the main momentum exchange mechanism and the effect of interstitial fluid becomes less important, thus becoming a granular flow regime.

The validation of the numerical results with experimental data has been systematically performed and either confirmed the goodness of the models and the modelling techniques (such as in the case of Liquid-Liquid turbulent field, in the solid volume fraction profiles in complete suspension conditions, in the bioreactor fluid dynamics and in the chemical species evolution in time as predicted by the metabolic model) or it was instrumental in understanding the limits and the uncertainties of the model formulations (as, for instance, in the prediction of the DSD of diesel fuel in water and in the solid volume fraction profiles in incomplete suspension conditions) helping in some cases the development of new models (for example in the implementation of a TFM interfacial model for the mass transfer of gas in water and in the formulation of the maintenance rate dependence on the substrate fluctuations).

The main specific results achieved in the thesis are summarized in the following.

Conclusions

- Liquid-Liquid dispersions in stirred tanks:
    - experimental data confirmed that, in the investigated system and operating conditions, the diluted dispersed phase has a negligible impact on the mean and fluctuating variables of the continuous phase;
    - RANS-TFM predictions of the turbulent field satisfactorily agree with single-phase results from the literature;
    - the simulations underpredict the DSD, suggesting that specific tuning of the breakup kernel parameters is needed;
    - grid effects are relevant and need to be properly addressed beforehand;
    - a novel scalar correction for the breakup kernel derived from local quantities is proposed.

- Solid-Liquid suspension in stirred tanks:
    - in the operating conditions considered, the so-called granular model formulation did not provide any contribution to the TFM in the prediction of the solid distribution in the stirred tank for solid volume fractions up to 0.15, provided that a packing limit was included;
    - in complete suspension conditions the coupling between TFM and the proper interphase forces provided reliable radial profiles of solid volume fraction;
    - in the investigated incomplete suspension conditions the accuracy of the numerical radial concentration profiles was unsatisfactory;
    - the turbulent dispersion force significantly contributes to the solid suspension and distribution in the stirred tank;
    - specific models to account for particle-particle interactions and advances in the modelling of the effects of the solid phase on the liquid turbulent field and of the turbulent dispersion in the incomplete suspension of solids are needed.

Conclusions

- Biohydrogen production in stirred fermenters:
    - a modelling strategy for the fermentative production and stripping of biohydrogen in the self-ingesting stirred tank reactor was implemented;
    - the interphase flux of hydrogen was modelled with a local mass transfer coefficient from the literature, a novel interfacial area formulation for the TFM and the Henry's gas law;
    - the kinetics of a simplified biochemical reaction for hydrogen production was described with a substrate inhibition model and implemented in porous supports for attached growth biomass;
    - the performances of two reactor configurations were tested with a local and an instantaneous analysis of the reaction rate, the interphase hydrogen fluxes and the two-phase fluid dynamics;
    - geometrical changes were proposed based on the local behaviour of the bioreactor;
    - the two-impeller configuration allows the circulation of stripping gas to enhance recovery.

- *Escherichia coli* fermentation in bioreactors:
    - a probabilistic mixing model was derived and implemented in the context of the software ADENON to describe the substrate inhomogeneities in fed-batch systems;
    - results from the IEM and the compartment model agree, proving that a simplified mixing model could suffice when just substrate segregation is important.
    - the adoption of the simplified IEM model does not worsen the agreement with the experiments from the literature;
    - the simulation with an IEM model of highly segregated heterogeneous bioreactors is faster and computationally cheaper than CFD and CMA;
    - a simplified model tying the maintenance rate of a population to the variance of the substrate concentration distribution was developed, implemented, validated against experimental data and discussed both from a Lagrangian and from a Eulerian perspective;

- introducing in the Pirt's law a dependence of the cell maintenance costs on the substrate concentration fluctuations improved the agreement with the experimental data.

Future development work will aim at extending the prediction capabilities of the RANS-TFM simulations of liquid-liquid mixture in more concentrated conditions, studying the drawdown mechanism and, possibly, implementing hybrid techniques to account for the simultaneous presence of large agglomerates and finely dispersed droplets. The coupling between fluid-dynamics and bioreactions will be further investigated, working on the development of robust and computationally viable methods to describe both the two-phase flow and the cells metabolism, to simulate bioreactors of industrial interest.